Institute of Physics, Polish Academy of Sciences

Division of Physics and Technology of Wide Band Gap Semiconductor Nanostructures

Synthesis and physicochemical properties of novel, tungsten-oxide double perovskites and their derivatives doped with selected rare-earth ions.

Damian Włodarczyk

A thesis presented for the degree of

Doctor of Philosophy

Supervisor:

Prof. Dr hab. Andrzej Suchocki

Warsaw, 2023

Acknowledgments

I want to express my deepest gratitude towards several people who, in particular, helped me through this extensive research:

My supervisor, **Prof. Dr hab. Andrzej Suchocki** (IP PAS) for his valuable guidelines, insightful remarks during numerous discussions, and patience while proofreading this elaborate dissertation;

Prof. dr hab. Krystyna Lawniczak-Jablonska (IP PAS) for teaching me valuable lessons about fundamental X-ray analysis that lead me to initial success in planning and interpreting the results for further self-supported development.

Prof. dr hab. Hanka Przybylinska (IP PAS), whose professional EPR expertise not only led to a breakthrough in an actual interpretation of a not-well-understood physicochemical phenomenon that we encountered in our materials but also pinpointed us into the right direction in terms of finally derived conclusions.

Dr eng. Mikolaj Amilusik (IHP PAS) and **Prof. dr hab. Michal Bockowski** (IHP PAS) for granting the access to irreplaceable, sophisticated, high-temperature furnaces filled with a wide variety of media, without which none of these novel materials would have ever been made.

Dr eng. Maciej J. Chrunik (MUT), who taught me the basics of synthesis methods with the occasional provision of sparsely needed reactants during the first stages of work.

Dr hab. Michal Strankowski (PG) for his time performing helpful DSC and TG analysis which contributed significantly to the first stages of my research regarding performance and stability issues.

Dr eng. Katarzyna M. Kosyl (IP PAS) and **Dr Roman Minikayev** (IP PAS) for teaching me the basics of XRD analysis with CIF construction and interpretation. **Prof. dr hab. Wojciech Paszkowicz** (IP PAS) for related, valuable hints.

Dr Lev-Ivan Bulyk (IP PAS) and **Dr Volodymyr Tsiumra** (IP PAS) for their help and assistance in more challenging and engaging laboratory experiments concerning LT luminescence.

Last but not least, I acknowledge the financial support of the **Polish National Science Centre** through Preludium grant no. **2019/33/N/ST5/02317** directly supervised by me and related to topics investigated here; and the **Ministry of Education and Science** project no. **1/SOL/2021/2 supporting** the development and conservation of the SOLARIS National Synchrotron Radiation Centre in Cracow, where all synchrotron measurements were performed.

Table of Content

List of abbreviations

XRD - X-ray Diffraction,
NPD – Neutron Powder Diffraction,
XPS - X-ray Photoelectron Spectroscopy,
XAS - X-ray Absorption Spectroscopy,
EPR - Electron Paramagnetic resonance,
FTIR – Furrier Transform Infrared,
DSC – Differential Scanning Calorimetry,
TG – Thermogravimetry,
DPs – double perovskites,
GS – Goldschmidt factor,
mGS – modified/modern Goldschmidt factor by Bartel et al.,
NUV – Near Ultraviolet,
NIR – Near Infrared,
CCD – Charge Coupled Device,
NA – Numerical aperture,
FWHM – Full Width at Half Maximum;
Cp – Heat Capacity,
SEM – Scanning Electron Microscopy;
HP – High Pressure,
DAC – Diamond Anvil Cell,
V_o – Oxygen vacancy,
O_i – interstitial oxygen,
PTM – Pressure Transmitting Medium,
RT – Room Temperature
LT – Low Temperature,
TEY – Total Electron Yield
SDD – Silicon Drift Detector
HT- High Temperature,
BCW – Ba_2CeWO_6,
CCWO – $Ca_3Ce_2W_2O_{12}$;
BPW – Ba_2PrWO_6
SCWO – $Sr_9Ce_2W_4O_{24}$
SG – Space Group,
ICSD – Inorganic Crystal Structure Database,
CCDC – Cambridge Crystallographic Data Centre
JCPDS – Joint Committee on Powder Diffraction Standards,
RE – rare-earth (ions or atoms),
PL – Photoluminescence,
IR – Infrared,
DFT – Density Functional Theory,
BE – Binding Energy,
E_g – Energy gap
E_a – Activation energy
E_F – Fermi energy
CB – Conduction Band
VB – Valence Band
CTB – Charge transfer band
SSR – Solid State Reaction;

Abstract (Angielski)

This comprehensive work showcases four novel rock-salt type compounds as amphoteric rare-earth tungstates $A_xRE_yW_zO_{6z}$. Two of them belong to classic double perovskites, and the other two are more related to so-called ilmenites or garnets. All of them are acquired as microcrystalline powders via high-temperature solid-state reactions of pellets in inert atmospheres. This work aims to create and thoroughly describe novel materials that could possess superior optical or scintillating properties to their scheelite predecessors, like $BaWO_4$:Ce/Pr. Furthermore, due to precursors' unique PL behavior & polymorphism, a high chance of finding an efficient energy convertor or radiation temperature sensor was anticipated. Therefore, 3 of the investigated compounds were chosen to host cerates at their RE occupation sites (RE=Ce) and the remaining one in the form of praseodymate (RE=Pr). The former group was targeted to be double perovskites varying only by alkaline 2+ atoms (A= Ba, Sr, Ca^{2+}). However, due to significant ionic radii differences, the last two turned out to be rather large, tilted, and less ordered structures. Ilmenites and garnets are popular side products during the double perovskite production process but are also worth investigating. Regarding praseodymium, only the barium variant was attempted – mainly to comprehensively compare original properties and unique phenomena acquired later during the investigation process from the nearest isostructural member. Also, barium turned out to be the only large-enough ion to produce good quality, double perovskite matrix.

Presented studies will have fundamental meaning and focus on synthesis descriptions and experimental details regarding used methods and related equipment. The second chapter will present an essential physicochemical characterization of undoped structures at ambient conditions using: powder XRD patterns & SEM projections, FTIR with Raman spectra, and XPS joined with complementary XAS data. Thirdly, results from non-ambient (temperature versus pressure) conditions will be shown concerning possible polymorphism (Raman spectroscopy), structural diversity (XRD, XPS, XAS), stability (in inert gases), and decomposition (air-sensitivity) using DSC and TG. Lastly, EPR measurements concerning magnetically-active content properties will open a gateway into the fourth chapter concerning optical measurements and unexpectedly decaying emission spectra of barium double perovskites related to charge transfer and interstitial oxygen evolution. Other results regarding the time-resolved photoluminescence of doped and undoped samples, excitation, absorption, theoretical and experimental band-gap form estimations are also present. Chosen dopants concern mostly Yb^{3+} and Ce or Pr^{3+} depending on discussed material – cerate-tungstates hold Pr, praseodymates Ce. All were selected in favor of creating a friendly environment for long-range, far down-converting energy transfer towards infrared and Yb^{3+}: (sensitizer Ce/Pr) NUV→UV-VIS (mediator WO_x)→NIR (activator Yb).

The final verdict about this research, based on all justifiable evidence collected so far, is that all these materials are relatively weak phosphors – barium praseodymate being the most photosensitive in matters of intensity but short-lived just as his cerate cousin; Sr and Ca-related cerium-tungstates being, on the contrary, weak but stable and persistent sources of light. They do not possess good enough capabilities to function as efficient, long-term down-converters, especially if they overheat and decompose in the air due to the extensive power applied by the lasers. They carry, however, very interesting charge-transfer capabilities related to photobleaching and internal oxygen evolution that might be at value for some NUV or deeper radiation one-time sensors - they are unfortunately unrecoverable. Use-and-forget manner makes them a one-way sensor. Nevertheless, these new matrices open many new possibilities and routes for future scientific research, i.e., in terms of magnetism or other RE dopants if they possess such shallow charge-transfer states just below the 5d conduction band. This work may continue beyond the scope of a Ph.D. dissertation or serve as an inspiration for others later on.

Streszczenie (Polish)

Praca ta w lapidarny sposób przedstawi 4 nowe materiały w postaci amfoterycznych proszków wolframianowych opartych na ziemiach rzadkich - o wzorze ogólnym $A_xRE_yW_zO_{6z}$. Dwa z nich klasyfikują się do klasycznych, podwójnych perowskitów, a dwa pozostałe to są bliżej spokrewnione z tzw. ilmenitami czy granatami. Wszystkie są uzyskiwane w wyniku wysokotemperaturowych reakcji w ciele stałym przeprowadzanych na skompresowanych pastylkach umieszczonych w atmosferze gazów obojętnych. Pierwotnym celem badań było stworzenie i dokładne opisanie owych materiałów, które powinny posiadać względnie lepsze właściwości optoelektroniczne, czy nawet scyntylacyjne w stosunku do swojego pierwowzoru jakim był $BaWO_4$:Ce/Pr. Co więcej, ze względu na unikalny polimorfizm oraz świecenie owego prekursora, istniała również duża szansa na wynalezienie efektywnego konwertera energii czy też wytworzenie radiacyjnego sensora czułego w niskich temperaturach. W związku z tym 3 z badanych związków zostały wybrane jako nośniki ceru w miejscach oznakowanych jako RE (cerany), a czwarty jako host prazeodymu (prazeodymiany). Pierwsza grupa docelowo miała należeć do rodziny podwójnych perowskitów różniących się jedynie jonami alkaicznymi (A= Ba, Sr, Ca)$^{2+}$, jednak ze względu na duże różnice w promieniach jonowych, dwa ostatnie kationy okazały się tworzyć duże, pochyłe i mniej uporządkowane struktury. Są one popularnymi produktami ubocznymi w procesie produkcji ww. związków i też szeroko bada się ich naturę z równych powodów (głównie w celach eliminacji). W przypadku prazeodymowego związku, stworzono go, gdyż chciano podjąć próbę potwierdzenia - na zasadzie kompleksowego porównania - oryginalnych właściwości ceranu baru z czymś potencjalnie izostrukturalnym, co mogłoby wykazać się czymś o równie unikatowych właściwościach, Bar jest też jedynym pierwiastkiem, który okazał się być wystarczająco duży by tworzyć struktury podwójnych perowskitów zatem wybór dla kolejnego sąsiada w układzie chemicznym wydawał się być oczywisty.

Prezentowane badania mają fundamentalny charakter i pierwszy rozdział skoncentruje się głównie na szczegółowych opisach syntez i eksperymentalnych metod oraz powiązanego z nimi sprzętu. W drugim rozdziale zaprezentowana zostanie podstawowa charakterystyka fizykochemiczna struktur niedomieszkowanych w warunkach otoczenia z wykorzystaniem: proszkowej dyfrakcji XRD i zdjęć SEM. Spektroskopia FTIR zestawiona z komplementarny sposób wraz z widmami Ramana posłuży do stworzenia tzw. odcisków palca – charakterystycznych widm używanych w toku dalszych analiz strukturalnych. Dane z XPS oraz XAS ukażą równocześnie dualistyczny charakter jonowy wszystkich związków w obrębie typowych podpowłok i ich krawędzi absorpcji (głównie RE i W). Rozdział trzeci przedstawi wyniki z rozmaitych technik uzyskanych w warunkach innych niż pokojowych – głównie w funkcji temperatury oraz ciśnienia – by zbadać złożone kwestie polimorfizmu (spektroskopią Ramana), spornego zróżnicowania strukturalnego (XRD, XPS, XAS), czy stabilności (w gazach obojętnych) i ewentualnego rozkładu (wrażliwość na powietrze) przy użyciu technik DSC i TG. Ostatecznie niecodzienne wyniki pomiarowe EPR, zainspirowane istnieniem podstawowych form paramagnetycznych w związkach, otworzą drzwi ku czwartemu rozdziałowi, który dotyczyć będzie pomiarów optycznych. Tam zostanie uwypuklone zjawisko czasówo-zależnego zaniku emisji ziem rzadkich wśród barowych podwójnych perowskitów związane najpewniej z przenoszeniem ładunku do W czy międzywęzłowego tlenu pod wpływem promieniowania. Znajdują się tam również inne wyniki dotyczące porównania fotoluminescencji próbek domieszkowanych i niedomieszkowanych, absorpcji i emisji, teoretyczne i eksperymentalne przewidywania szerokości domniemanych (prostych) przerw energetycznych. Wybrane domieszki to głównie Yb^{3+} i Ce lub Pr^{3+} w zależności od omawianego materiału – wolframiany cerowe zawierać będą Pr, prazeodymiany zaś Ce. Wszystkie dobrane tak by stworzyć korzystne warunki do zaistnienia zjawiska przekazu energii dalekiego zasięgu w kierunku iterbu i podczerwieni: (donory hν Ce/Pr) NUV→UV-VIS (pośrednik WO_x)→NIR (akceptor hν Yb).

W świetle wszystkich wykonanych i zebranych do tej pory wyników badań można rzec, że wynalezione materiały są stosunkowo słabymi luminoforami – prazeodymian baru jest najlepszy pod względem intensywności, ale jego emisja jest nietrwała, podobnie jak w izostrukturalnym ceranie; Obydwa związki wydają się być wysoce podatne na światło (nietrwałe). Wolframiany ceru związane ze strontem czy wapniem są bardziej trwałymi i długoterminowymi emiterami, ale znacznie słabszymi. Związki nie wykazują zatem wystarczających możliwości czy też zdolności, aby funkcjonować jako wydajne konwertery promieniowania, zwłaszcza jeśli mogą ulec szybkiemu przegrzaniu i rozkładowi z powodu przyłożonej dużej mocy laserowej w atmosferze tlenowej. Posiadają one jednak inne, bardzo interesujące właściwości takie jak możliwość przenoszenia ładunku powiązaną pośrednio ze zjawiskiem fotowybielania i ewolucji wewnętrznie zgromadzonego, międzywęzłowego tlenu. Może to nieść wartościowy potencjał dla konstrukcji czujników promieniowania NUV lub głębszego (bardziej energetycznego), ale w sposób nieodwracalny – niestety są one raczej jednorazowego użytku. Niemniej jednak wszystkie wyżej wymienione matryce otwierają wiele nowych możliwości i ścieżek dla rozwoju przyszłych badań naukowych, np. w zakresie magnetyzmu lub innych z zastosowaniem różnorakich domieszek ziem rzadkich. Ta praca może być równie dobrze kontynuowana po doktoracie lub posłużyć innym jako inspiracja do dalszego rozwoju.

Introduction and Aims

This study thoroughly describes four novel RE-tungstate materials, their crystallographic structure, physicochemical properties in various conditions, polymorphism, stability, and some basic optical phenomena related to luminescence, like charge and energy transfer. At first, undoped materials will be shown to create a base for further deliberation. Dopants like Cerium, Praseodymium, and Ytterbium 3+ will be introduced later to assess the potential for creating efficient NUV (Ce/Pr) → UV-Vis (WO_x) →NIR (Yb) down-converters or NUV sensors related to thermometry far below 0°C.

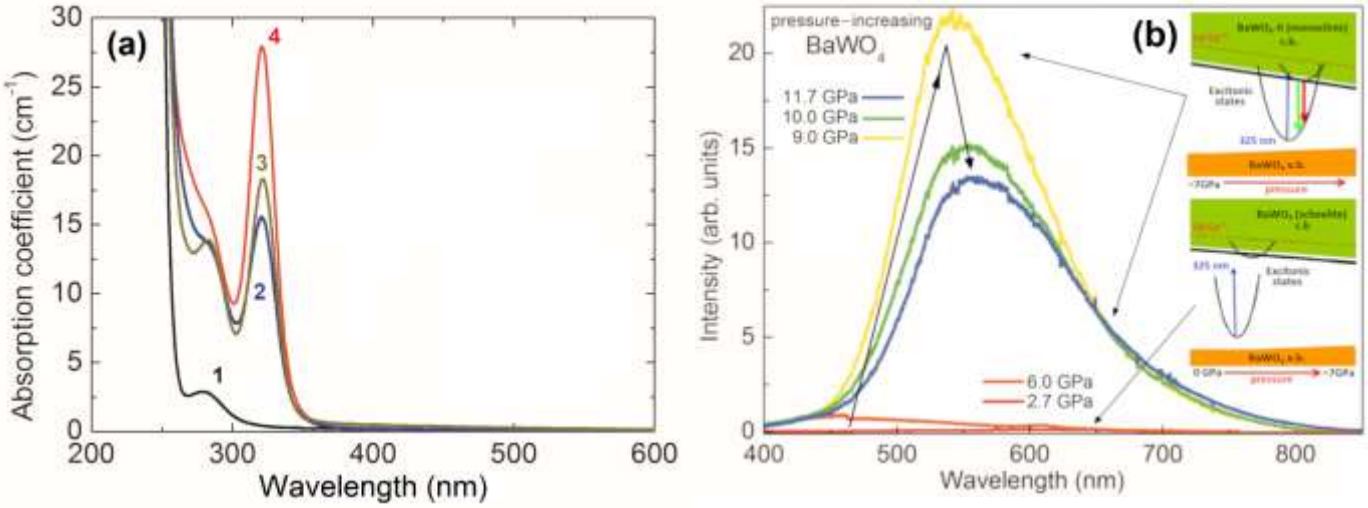

Figure 1 (a) Ambient absorption spectra of (1) pure $BaWO_4$, doped with 0.5 atom % Ce^{3+} along (2) [100] or (3) [001] crystallographic axes, and (4) additionally codoped with 1 atom % Na^+ to compensate for any additional vacancies. Scheme (b) shows pressure-influenced PL properties of $BaWO_4$ crystals during excitation with 325 nm laser wavelength.

The research was inspired by a previous $BaWO_4$ study where this famous scintillator, known for elaborate polymorphism (& synthesized using the Czochralski method),[1] activates its optical capabilities during compression while being excited by NUV, 325 or even deeper 275 nm laser light – as *Figure 1*.[2] During that process emerging, intense, yellowish-green PL bands cover a broad visible range of emission making these crystals potentially attractive sensitizers for stimulating any artificially implanted NIR activators as shown in *Figure 2*.[3]

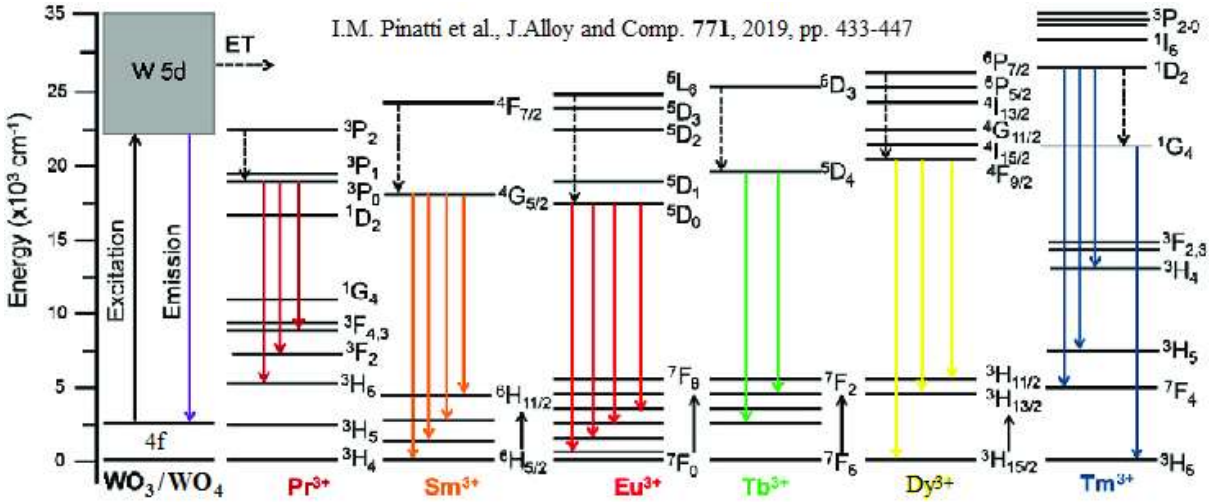

Figure 2 Diagram of an energy transfer mechanism for rare-earth doped tungstates excited with 350 nm or shorter laser light showing potential for future sensitizing ions.

On the basis of theoretical and experimental studies, several authors suggest that the origin of this greenish emission is an extrinsic mix related either to (WO_3 + F) centers[4–7] or some oxygen-deficient complexes (WO_3 + V_O), which can emit orange light.[8] Others consider the interference of defect centers containing interstitial oxygen (WO_4 + O_i)[9–11] or intrinsic distortions in the $(WO_4)^{2-}$ tetrahedra as a source of the initially expected green light being artificially redshifted.[12] Theoretical studies performed by us,[2] Campos[13] and Longo et al.[14] attribute this PL response to various interstitial vacancies and subtle intrinsic oxygen distortions creating vast complexes within convoluted tungsten WO_x matrix. That is the most plausible answer, given the data gathered below. The activation mechanism of recorded emission initially presents itself by simple band-gap shrinkage (by lowering the top 5d W^{6+} state) while pressure is being applied - like in the pictograms shown to the right of *Figure 1b*.[2,15,16] At those circumstances, the scheelite unit cell ($I4_1/a$)[17–21] structurally changes at ~7 GPa through so-called second-order phase-transition to a metastable $I2/a$ fergusonite state,[15,22–26] to finally form a monoclinic $P2_1/n$ phase above ~9 GPa,[27–31] as depicted in *Figure 3*.

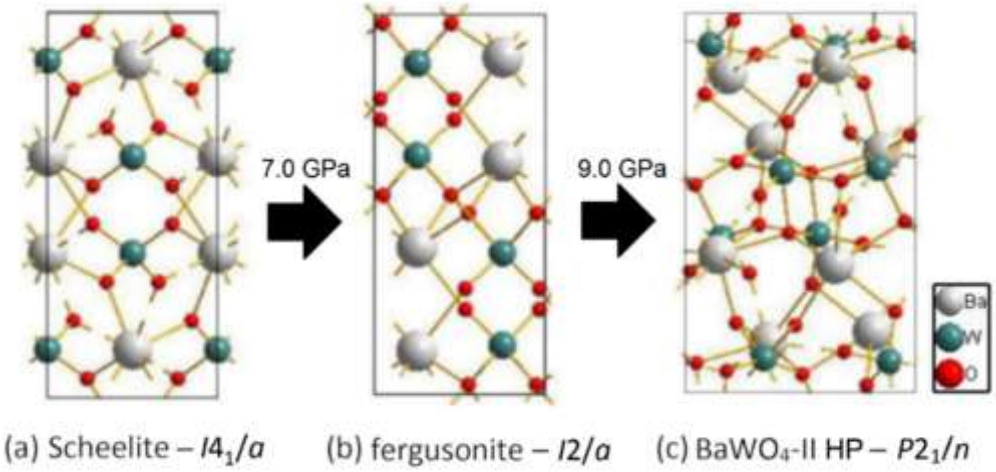

Figure 3 Three crystallographic structures of $BaWO_4$: (a) ambient- and low-temperature scheelite; intermediate (7−9 GPa) fergusonite (b); high-pressure (+9 GPa) monoclinic $BaWO_4$-II phase (c).

The evidence of such reversible behavior, although with large ~4 GPa hysteresis, was provided by Raman spectra in *Figure 4*. (Appendix *Figure A1* provides more insight about related peak versus pressure position dependencies during compression). Nevertheless, the emission of the scintillator is affected analogically – *Figure 5*a,b. The response was much more potent (regarding intensity) with a carefully chosen set of RE dopants, as seen in *Figure 5*c,d. Ideologically, Ba^{2+} should be substituted with RE ions (not W) hosting NUV sensitizers like Ce or Pr^{3+} ions, further reinforcing the PL-related effects by a couple of additional multisites. This must be done carefully since some additionally introduced (O-related) defects could hamper their intended influence. Already present, defective reddish component (band) from aforementioned V_o or O_i intrusions visualized in *Figure 6* might, however, come in handy later when exciting other NIR energy acceptors.[2,32,33] To control their effective presence, smaller ions like Na^+ or Li^+ were introduced as co-dopants – mainly to compensate for differences in the Ba-RE ionic radii as convenient space fillers and to relieve the tension or negative internal stresses developing within matrices mentioned above.[34–36]

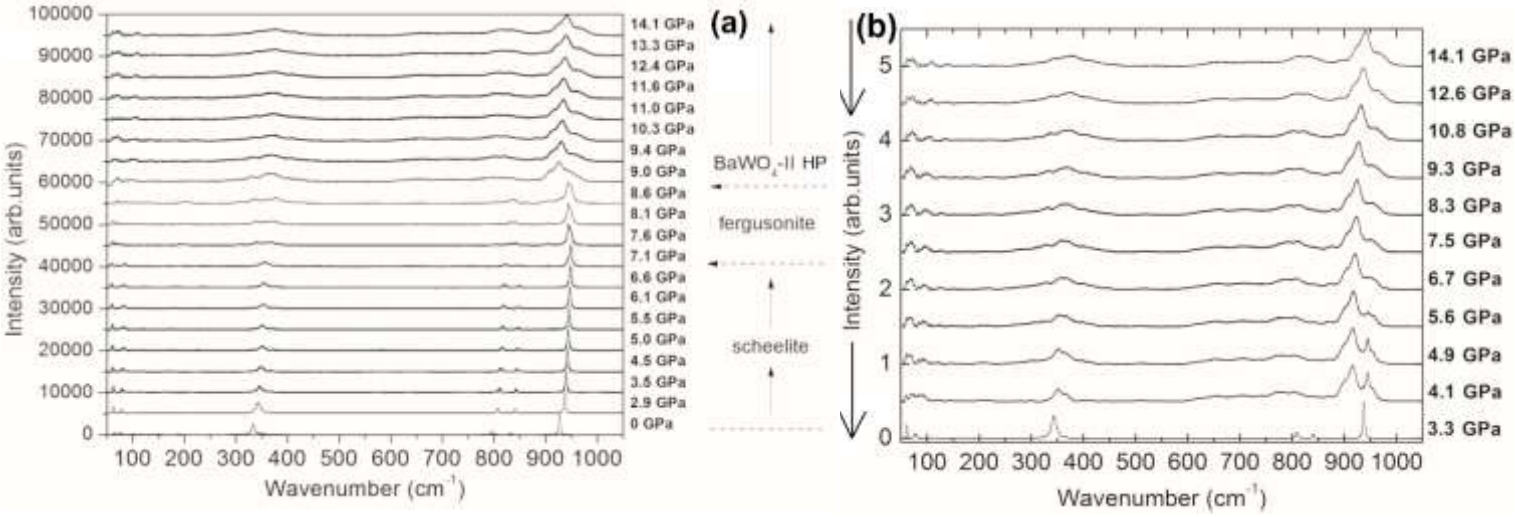

Figure 4 (a) Pressure-dependent, room-temperature Raman spectra of $BaWO_4$ doped with 0.5 atom % Ce^{3+} and 1 atom % Na^+, oriented along [100] axis. Phase transitions are noticeable at 7.1 GPa (to the metastable fergusonite phase) and 9.0 GPa to monoclinic HP $BaWO_4$-II. Picture (b) contains data collected during pressure release. The reverse transition from the HP $BaWO_4$-II to the scheelite phase occurs between 4.9 and 4.1 GPa. Arrows guide the eye.

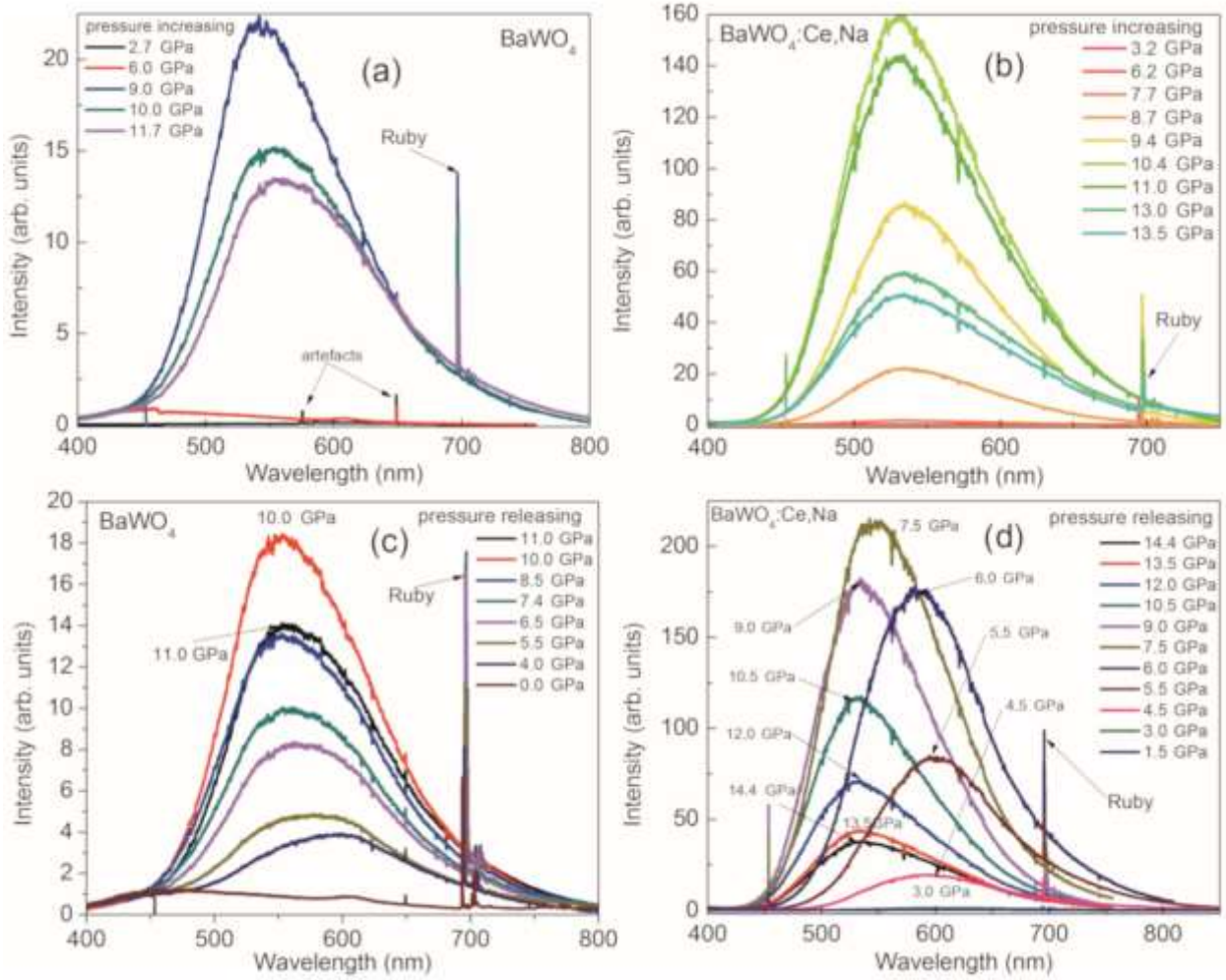

Figure 5 Luminescence of pure $BaWO_4$ and $BaWO_4$:Ce^{3+} (0.5 atom %), Na^+ (1 atom %) as a function of pressure increase (a, b) and release (c, d) at 293 K. Excitation wavelength: 325 nm.

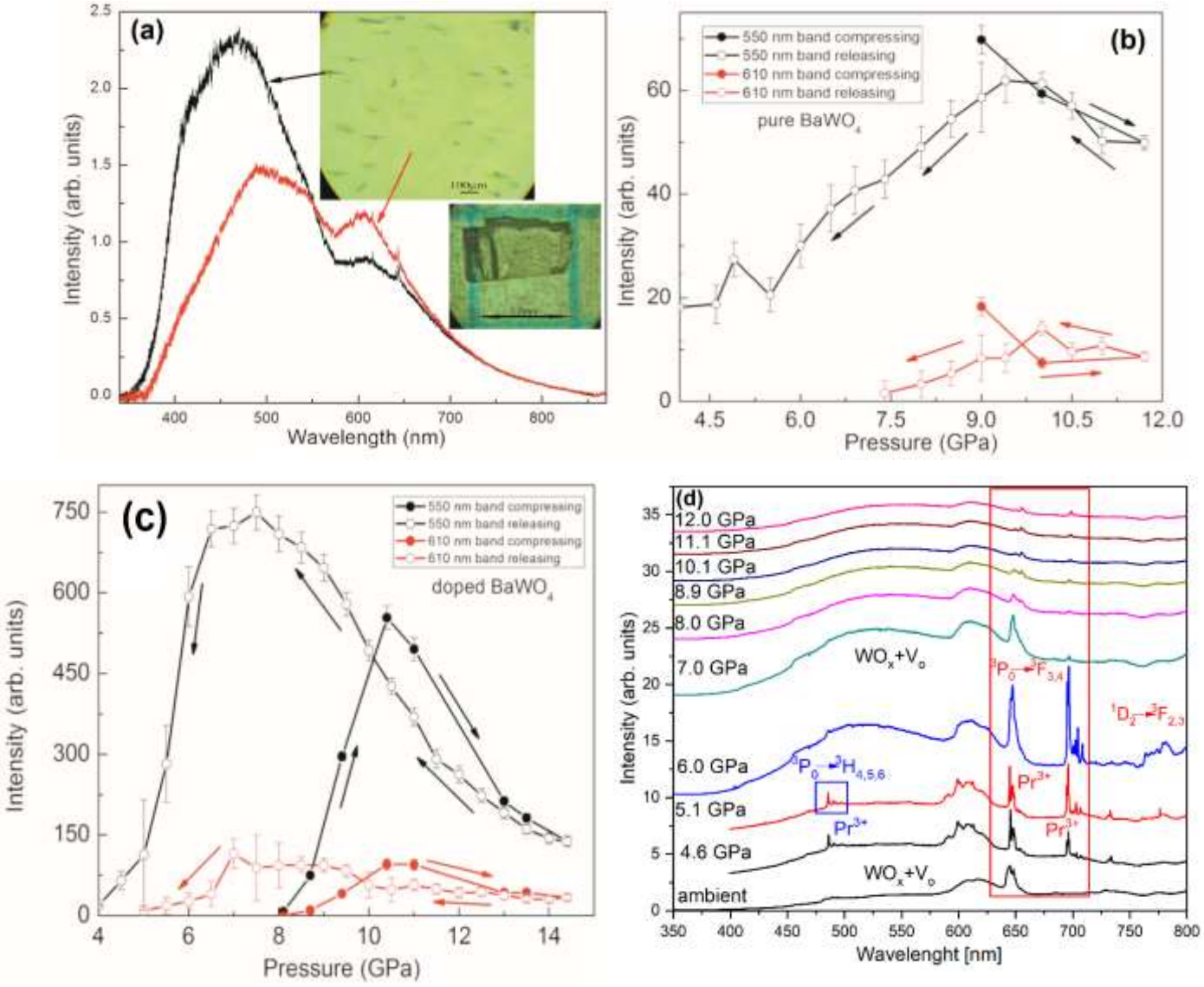

Figure 6 Luminescence of a $BaWO_4$ single crystal at 70 K under 275 nm excitation is shown in figure (a), where it reaches the maximum output. The red PL spectrum stems from blackish inclusions, which are actually empty regions, while the black spectrum is from a homogeneous crystal without any inclusions as visible in the insets. Intensity vs. pressure dependence of greenish-yellow 550 nm (black symbols) and weak, orange 610 nm (red symbols) PL bands are visualized in figure (b) for pure and (c) doped $BaWO_4:Ce^{3+}$ (0.5 atom %), Na^+ (1 atom %), single crystals measured at 10 K under 325 nm excitation. The direction of pressure changes is indicated using color-specific arrows. Figure (d) shows high-pressure luminescence spectra of $BaWO_4:Pr^{3+}$(0.5%), Na^+(1%) under 302.5 nm laser excitation. One can witness Pr and WO_x bands evolution during compression through metastable (fergusonite) phase above 6 GPa, where the emission briefly intensifies and later quenches after a brief transition to monoclinic $P2_1/n$ SG.

So, basing on initial $BaWO_4$:RE data, aforementioned literature,[1-35] and some theoretical projections presented below, an assumption was made. Naturally available materials and their chemical stoichiometry suggested that the formula would expand towards a double perovskite if RE were fully introduced into the matrix, not as dopants but as genuinely integrated

constituents.[37] Perovskites alone are a group of rock-salt type minerals discovered by Lev Perovski in late 1839 by the Ural mountain range.[38] Their natural occurrence in Earth's mantle was associated with primordial processes initially started in dimming stars. There, the depletion of Ti in the photosphere signified the transition from M to L-type brown dwarfs at their final stages of existence, which is also the primary ingredient of Perovskite predecessors.[39] Generally, they possess a straightforward, empiric formula – $^{XII}A^{VI}BX_3$, where A is a 12-times-coordinated, 2+ alkali ion. B is a 6-times-coordinated, d- or f-block cation of various charge states. X is obviously a charge-compensating anion that could vary depending on the environment or desired usage if synthesized artificially. It could be Br^-, I^-, Cl^-, F^-, S^{2-},[40,41] but foremostly, popular O^{2-} - just like in its archetype, $CaTiO_3$.[42,43] Barium titanate was later used by Megaw et al.[44] to describe the structure in detail using XRD – and so, the knopite was distinguished as a rare-earth-bearing sub-derivative bearing close resemblance to our barium compounds. Since many different cations could be embedded into those knopite-like structures, a large variety of materials could be theoretically tailored & further developed into specific applications. A popular subject of interest is nowadays: optoelectronics,[37] piezoelectric sensors;[45–47] Widely considered magnetism[48,49] associated with antiferro-[50,51] or ferrimagnetism,[52,53] memory-storage devices,[54] supported by superconductivity;[55–58] photocatalysts[59–61] used in energy conservation just like fuel- [62–64] or solar cells[65–67] are also at grasping range. Such broad technological scope withholds a large field of compounds ranging from metallic, semiconducting to even insulating properties using different dopants at adjustable temperatures.[37,54,68] It would be a shame not to explore them.

Double perovskites function on the same or even broader scale. They are something in shape and form similar to a natural perovskite, but the unit cell size is usually doubled ($A_2BB'X_6$). The evenly spread, corner-shared clusters hosting central ions of various ionic radii (and type, B =/= B') surrounded by many electro-accepting ions keep them together.[37] Their numbers and general space group affiliation are usually dictated by several rules: ionic radii, bonding type/electronegativity associated with its coordination number, and an overall compendium of Glazer tilt systems that encompass registered distortions in a comprehensive encyclopedia.[69,70] These systems could be further connected to one another by mutual structural dependencies based on group theory and DFT calculations suggesting possible coexistence or polymorphism if a proper stimulus is applied.[71,72] Firstly, however, one must predict if considered formations are available at all. Several offhand methods were derived to accommodate such matters. The most common one is Victor Goldschmidt's factor from 1926.[73] Basing on chosen A, B, and X-site cations, their ionic radii and coordination number one can estimate (with ~75% accuracy) if the chosen material will fall into the favorable range of synthesis where a quite-ordered structure will manifest itself. Ideal theoretical values range from 0.85÷1.05 but of course, the closer one gets to the border, the more tilted structure will be, finally resulting in other, semi-related SG of a monoclinic or elongated rhombohedral kind – scientists usually strive to achieve a perfect cuboid. To compensate for subtle details, numerous discrete structural changes and dependencies now coming into view (thanks to modern techniques and statistical overview after almost a century) a more accurate (~92%) and sophisticated GS factor formula has been established by Bartel et al.[74] In theory, it should provide more information and distinguish better ordered-vs-disordered crystallographic

systems in the region of interest, but the ideology behind it is still the same. The desired acceptability values change from **0.825÷1.059** regarding (GS) to $\tau <$ **4.18** (in mGS), but only if $r_A > r_B$ rule is still maintained. So, considering the general formula of our desired double perovskites to be $^{XII}A_2{}^{VI}BB'{}^{II}X_6$, where ^{XII}A = Ba, Sr or Ca^{2+}; ^{VI}B = RE = Ce/$Pr^{3/4+}$; ^{VI}B = $W^{4/5/6+}$; and ^{II}X = O^{2-} the aimed structures present themselves theoretically in range of values shown in *Table 1* below.

Table 1 Classic (GS)[73] and modernized (mGS)[74] Goldschmidt parameters were fashioned into calculating theoretical factors predicting the existence of discussed, newly-developed materials. The ions have been paired in such a way to respect the preferable B-site (8+ or 9+) charge balance within those structures. *Red* color marks worse GS/mGS factor, *green* better values. **Bold** fonts mark the best (top) and worst (bottom) of them all.

	Ionic radii [Å]				
$^{XII}A^{2+}$	**^{VI}B-site (Ce/Pr)**	**^{VI}B'-site (W)**	**^{II}X (O^{2-})**	**t (GS)**	**τ (mGS)**
Ba 1.61	Ce^{4+} 0.87	W^{4+} 0.66	1.35	**0.989**	**3.421**
	Ce^{3+} 1.01	W^{5+} 0.62		0.967	3.460
	Pr^{4+} 0.99	W^{4+} 0.66		0.962	3.474
	Pr^{3+} 1.13	W^{5+} 0.62		0.941	3.578
Sr 1.44	Ce^{4+} 0.87	W^{5+} 0.62		0.942	3.678
	Ce^{3+} 1.01	W^{6+} 0.60		0.916	3.829
Ca 1.34	Ce^{4+} 0.87	W^{5+} 0.62		0.908	3.940
	Ce^{3+} 1.01	W^{6+} 0.60		**0.883**	**4.210**

So for mGS ($= \frac{r_X}{r_{BB'}} - n_A\left[n_A - \frac{r_A}{r_B \times \ln(r_A/r_B)}\right]$), the lower the number, the better the result. In old GS ($= \frac{r_A + r_X}{\sqrt{2}(r_{BB'} + r_X)}$), the further you go from ideal 1.00, the worse - more discrepancies in the form of alternating, non-cubic space groups might transpire.[37] That withholds the most truth for the lower border-line of classic GS where substitution with a smaller alkaline atom contracts the unit cell far more than B-site atoms exchange, creating, as a result, vast cationic vacancies. If they are, by chance, periodically ordered, several cases could, in proper circumstances, create an opportunity to produce compounds such as quaternary perovskites. Ideologically aforementioned materials host complex, 4a×4a×4a multilayered cubic (*Fm*-3*m*) superstructures where 'a' is denoted as a primitive cubic unit cell dimension.[75] Of course, since the GS parameter is lower in them, an enlarged number of defects changes A/B-site occupation to even below 50%. The mechanism derived from this archetype showcases a modification of most 6-times coordinated B-site octahedra to tetrahedra sites shared with chosen alkaline (A) atoms.[76] That is why most of these derivatives have been found in alternating tetragonal SGs. Furthermore, the scientific community is widely interested in them since they possess a large variety of yet unidentified capabilities as a new group of minerals. Some postulate intriguing relations between the elements of crystallographic structure and the emission spectra (concerning selectively chosen dopants & regularly placed defects that artificially modulate or even enhance the luminescence toward its persistent character); however, no concrete evidence towards a specific mechanism has been proposed yet.[77–79] Fairly justifying other prosperities by their experimental results, some of them exhibit large magnetoresistivity,[68,80] dielectricity,[81–83] superconductivity, or even antiferromagnetism in cryogenic temperatures.[55,84] But first, let the community dispute whether or not these structures are really stable & belong to perovskites or other garnet-like SGs.

Various by-products could occur just above and below the classic GS comfort zone – from aforementioned garnets (i.e., $Mg_3Al_2Si_3O_{12}$) to a mix of unrelated salts and oxides.[37,74,85,86] But, the most popular of them would probably be the ilmenites. They resemble a rigid titanium ore mineral with a more distorted, large, rhombohedral SG of tubular shape. Their idealized archetype would be trigonal $FeTiO_3$ with alternating layers tilted along the one (c) axis.[87,88] It was originally discovered by William Gregor in 1791 in a river by the Russian Ilmansky mountain range.[89,90] It could also be found (much later) on the Moon or Pluto.[91,92] It is a widespread by-product of dying blue supergiant stars. Usually is highly anisotropic, brownish-gray, and exhibits weak magnetic properties. Due to immorphable, disordered structure riddled with many defects, ilmenites did not find many applications in today's world – some are sparsely used in paints, inks, fabric and plastic dyes, paper, food coloring, sunscreen, and cosmetics.[93–95] They are also used in heavy industry extreme refinement to extract Fe and Ti, but these processes seem to fade into history.[96–99]

Table 2 $A_2BB'O_6$ materials with A^{2+} = Ca, Sr, Ba composition, reported in the literature since 1950 by Vasala and Karppinen.[37] Left column represents the B cation, and the top row the B' cation. The green color indicates perovskite compounds successfully synthesized at ambient pressure. Purple - DP stabilized using either high-pressure / oxygen-partial-pressure conditions. Compounds with hexagonal non-perovskite structures like ilmenites or garnets are yellow. Cases where no coherent structures or phases related to the $A_2BB'O_6$ composition formed are marked as red. White boxes are yet uninvestigated options. X marks with possible color outcomes (according to the previous GS discussion) mark the spots of the work currently conducted work in this dissertation.

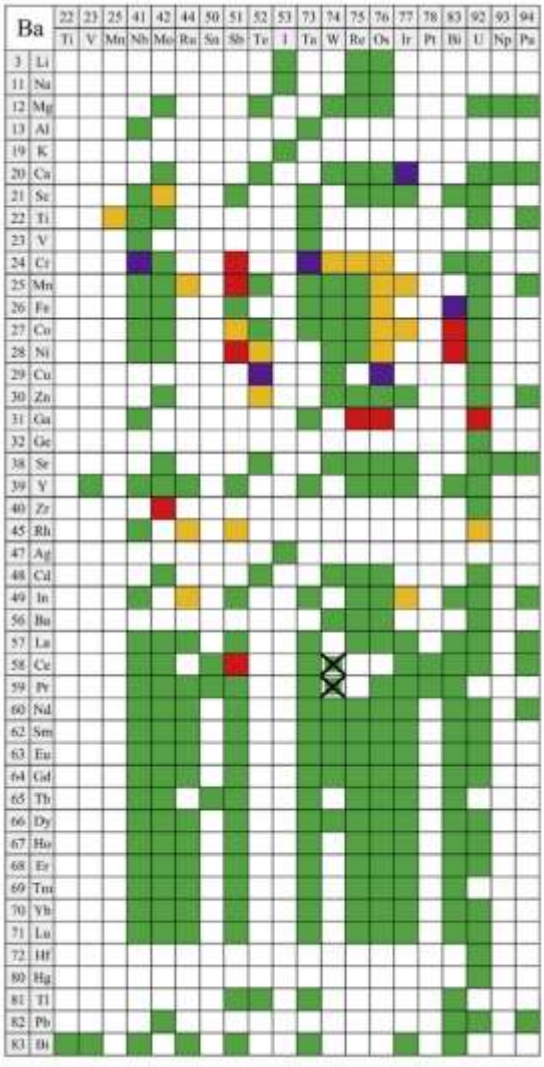

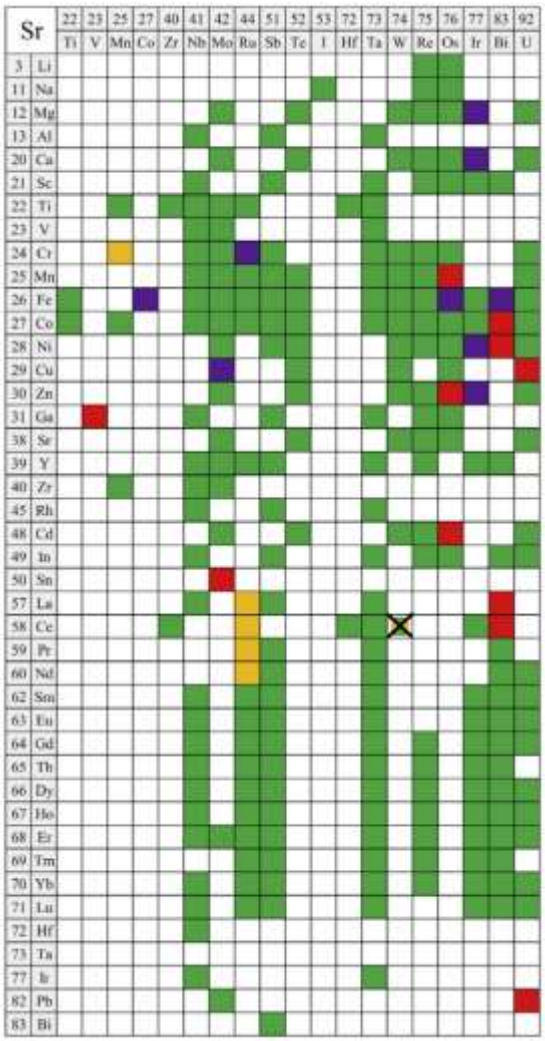

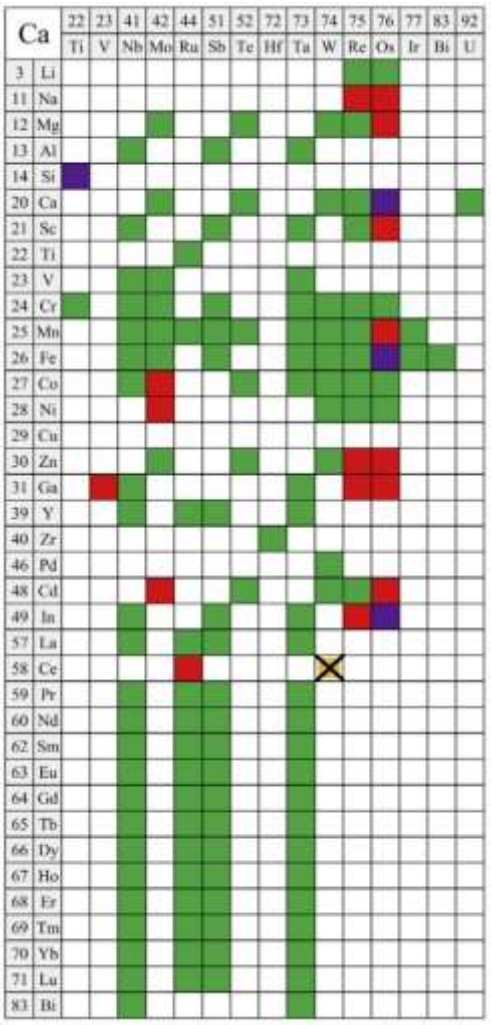

Given all the by-products that can transpire during sole double perovskite synthesis while GS factor lowers down, a brief statistical review of available space groups [37,41,71,72] and Glazer tilt systems[69] is required to understand the current product placement of newly created materials as shown in *Table 2*. There, a summary of all double perovskite creation attempts is gathered to the best knowledge since late 1950 to the year 2015. Amongst all the green and violet squares, meaning successful and HP-aided syntheses, and yellow with red marks, suggesting the creation of other phases (such as ilmenites) or total failures in the form of mixed, inhomogeneous salts and oxides, black X's are placed. These were the indigenous spots that this research is trying to fulfill. Ba, Sr, and Ca (double) perovskites of Ce/W or Pr/W. The actual results will be discussed in Research and Discussion *chapter 2,* however, at this rate, one can estimate, by calculated GS, that their outcome would be as suggested by colors provided in the insets near inner X edges. Barium Ce, Pr/W compilation having GS > 0.94 should appear as relatively good DPs. Strontium Ce/W pairing is still above 0.90, so we could assume some type of order in the form of perovskites – maybe quaternary or more disordered shapes. Calcium is relatively small and operates at the lower borderline of the tolerance factor, where statistics are not that promising. In terms of sheer numbers, they could turn out as ilmenites or, at worst, a mix of oxides and tungstate salts. Nevertheless, omitting statistical discouragement presented in *Figure 7,* one should still aim for the best outcome. BCW and BPW are relatively close to the ideal GS = 1.00 and are in the most packed, SG-rich range. Here cubic (*Fm*-3*m*), rhombohedral (*R*-3), tetragonal (*I*4/*m*), and monoclinic groups transpire – a little less *I*2/*m* or more tilted $P2_1/n$. Since shrinkage of the unit cells (lowering GS) promotes $P2_1/n$ distortion and inflation of cubical *Fm*-3*m* SG, all future projections should be focused solely on the remaining rhombohedral, tetragonal, and monoclinic groups. The lower we go (GS-wise) towards SCWO and CCWO, the monoclinic systems seem to be more prevalent. While *I*2/*m* is visually set in the background, the chance for a cubic unit cell does not fade as rapidly as for the other SG. The pattern is, however, rather distinct and not likely. CCWO has clear dominance over $P2_1/n$ SG chance but with such low GS, materials could easily turn into other disordered systems falling out of double perovskites charts - *Figure 8*.

A wider scope of DP SG projection parameters should be considered, not solely based on simple GS values. Mainly speaking, the difference between inserted BB'-site ionic radii ($\Delta r_{BB'}$) and cationic charge states ($\Delta Z_{BB'}$) which have further connections to such factors like: Degree of order (S) being defined as $2g_{BB'}$-1,[100–102] where $g_{BB'}$ is the occupancy declared by XRD measurements at B-site cations (correctly occupying designated sites without any sharing). (S=1 means complete order; 0 long-range disorder); and generally known as

Madelung's Free Energy.[103,104] Madelung energy of ordering is an empirical value (not only for perovskites), which states that with the increasing charge difference and change in central ions ionic radii, the electrostatic repulsion should overcome the entropic issues inside any unit cell and cations should order properly given the exact amount of free interatomic space.[103–105] This parameter is also proportional to ~ $\Delta Z_{BB'}$, and $\Delta Z_{BB'}$, in consequence, imposes a direct dependence on $\Delta r_{BB'}$. The larger the ΔZ, the better internal order one will get. To have a proper perspective, if $\Delta Z=0$, it is highly inconvenient. This value upsets the stereotypical 8+ balance of DPs & there is no energy gain between cations. They repulse each other pretty strongly, prompting higher disorder.[106,107] Ionic radius is the only directly-related parameter that could strongly correlate with changing cationic charge/structure imbalance. While changing, it behaves in a proportional manner when quantified with some structure-specific constants. Generally, the larger the difference between central B & B' sites, the more probable the long-range ordering is.[107,108] According to provided statements, the $\Delta r_{BB'}$ difference higher than 17% (or rather 20% given the statistics) would increase lattice strain that, in consequence, would overcome entropic influence, and the structure would come out genuinely ordered. *Table 3* contains all possible options and annotations from literature gathered by Vasala & Karppinen, with red marks pinpointing the range of existence for our newly-developed materials.

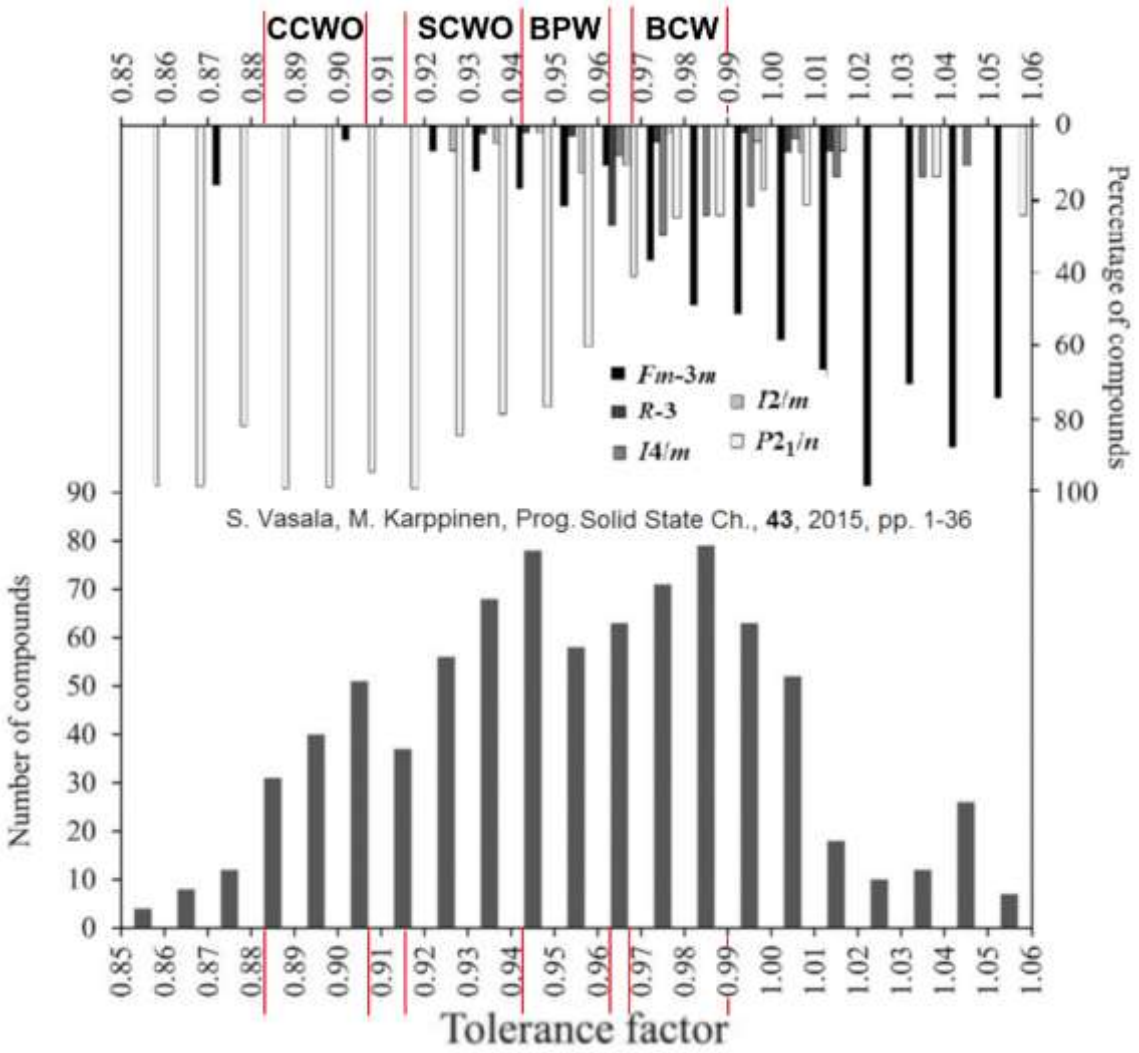

Figure 7 Number of $A_2BB'O_6$ compounds reported with different values of GS factor and percentages of ordered compounds hosting different space groups merged together from graphs presented in Vasala's & Karppinen's review.[37] Red color lines mark the borderline values of each investigated material, taking into account different B-site ions mentioned in *Table 1*.

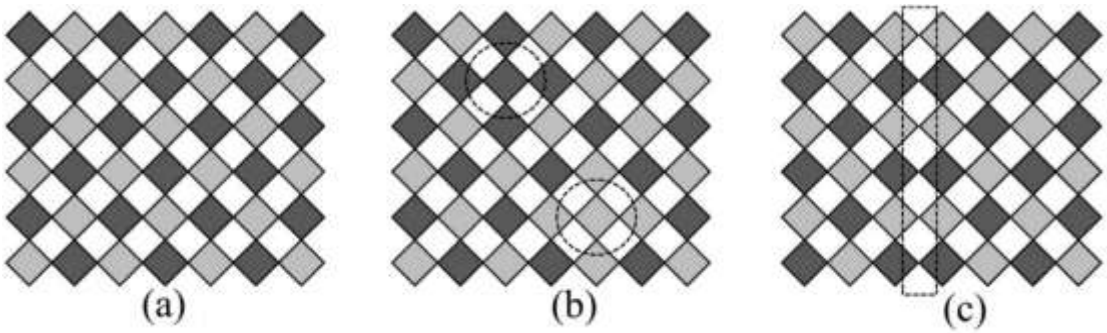

Figure 8 Schemes of probable B-site cation order in perovskites: (a) completely ordered, (b) antisite disorder, and (c) the antiphase boundary case.[37]

Table 3 Summary of cation orderings found in different $A_2BB'O_6$ double perovskites made by Vasala & Karppinen.[37] Red color marks ideologically desired ionic structures.

$\Delta Z_{BB'}$	Ionic structure	Ordering	$\Delta r_{BB'}$ [Å]
0	$A^{2+}{}_2B^{4+}B'^{4+}O_6$	Disordered with $\Delta r_{BB'} < 0.17$ Å	$\Delta r_{CeW}=0.21$; $\Delta r_{PrW}=0.33$
	$A^{3+}{}_2B^{3+}B'^{3+}O_6$	Disordered	
	$A^{+}{}_2B^{4+}B'^{6+}O_6$	Ordered	
2	$A^{2+}{}_2B^{3+}B'^{5+}O_6$	Mostly disordered, ordered if $\Delta r_{BB'} >> 0.17$ Å	$\Delta r_{CeW}=0.39$; $\Delta r_{PrW}=0.51$
	$A^{3+}{}_2B^{2+}B'^{4+}O_6$	Most partially ordered	
4	$A^{2+}{}_2B^{2+}B'^{6+}O_6$	Mostly highly ordered	
	$A^{3+}{}_2B^{+}B^{5+}O_6$	Ordered	
6	$A^{2+}{}_2B^{+}B'^{7+}O_6$	Ordered	

Researchers were fully aware of unfavorable (low) ΔZ_{BB} values making their choices during pure-lattice modeling, as seen in *Table 3*. However, future experimentations showed that high enough Δr_{BB} with additional inclusions hosting mixed $\Delta r_{Ce^{4+}/W^{5+}} = 0.25$ Å and $\Delta r_{Ce^{3+}/W^{6+}} = 0.41$ Å pairs (appearing spontaneously) hold great promise in terms of autoregulation. That phenomenon bestows more promising GS factors for the overall matrix but is challenging to control. That is probably why no one has yet divulged into this group of compounds considering problematic synthesis and its incoming, meticulous optimization/control.

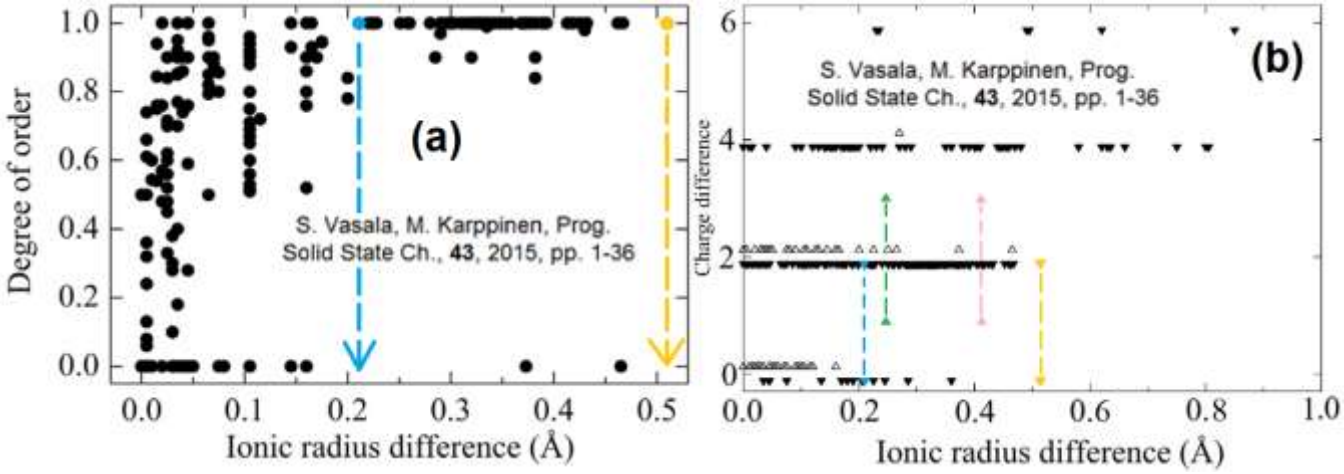

Figure 9 Statistical overview of (a) B-site cation's degree order for $A^{2+}{}_2B^{3+}B'^{5+}O_6$ perovskites, and (b) charge difference as a function of B-site cation radius divergence made by Vasala and Karppinen.[37] In Figure (b), disordered compounds (hollow triangles) have been moved up, and ordered (black triangles) slightly lowered for clarity/legibility reasons. Blue and yellow symbols with dashed arrows guide the eye in the range of possible placement of our newly-discovered materials – their stretch depends on Ce^{3+}/W^{5+} and Ce^{4+}/W^{4+} fractions/ ratios of intermediate pairing. Green and pink marks account for unusual, mixed ion couples that might transpire between the two sets mentioned above, possibly creating other disordered compounds like ilmenites. The 'pairing' refers to the batch's whole (scattered) volume, not the immediate crystallographic neighborhood.

Knowing all three Madelung parameters, one can now crudely project newly modeled materials into the compiled statistical charts montaged by Vasala and Karppinen[37] in *Figure 9*. There, some ideal, borderline points of order have been displayed according to currently chosen, 100% pure cationic options (Ce blue and Pr yellow). A broader range should be set regarding possible intermediate outcomes emerging from the chaotically mixed charge states (green Ce and Pr pink) due to the unideal dispersion of ions naturally upsetting the perfect balance. This uncertainty might be narrowed down by carefully-planned XRD, NPD, XPS, or XAS experiments; however, considering synthesis conditions, everything needs to be perfectly repetitive and stable, which is often not the case.[37] Charge disproportionation[109–113] and A/B-site mixing[114–117] are phenomena that are not easily controlled but might lead to some exotic oxidation states or properties that are not conventionally available. However, discretely balanced and stable ions inside a unique matrix are something to strive for. Compared to cation ordering, the charge balancing process is quite often quick & chaotic in rock-salt type materials – many factors can upset it. Sometimes fast cooling (freezing) is required to prevent minor phases from appearing in more significant amounts – kinetic barriers often limit such $A_2BB'O_6$ perovskites from appearing (influencing their $ABO_3{\times}AB'O_3$ cluster fusion). [118–121] This procedure often leads to discrete, temporary-frozen B-site balance (sometimes uneven) but is necessary to maintain the delicate 8+ charge state of internal DP ions. This procedure is, unfortunately, not typically recommended since it counters slow (but crucial) ionic diffusion during solid-state reaction & has a bad influence on the overall mix - even a small anion displacement can leave lattice strains & empty spaces for interstitial inclusions (like O). These phenomena would usually lead to later oxidation & facilitate unnecessary electron transfer from unknown sources. Some say that freezing is cheating nature by compensating the difference in space with artificial defects – the material should be freely self-balancing from a long-range perspective. Electron movement should not be obstructed then, but it is a highly disputed subject here.[53,71,82,101,102] Schools of synthesis are different because charge ordering is not always complete, and ideal chemical formulae are not ideal integers – usually, fractions with a surplus of anions are added to meet the needs of many just to have satisfying purity.[37] This ideology is highly dependent on synthesis temperature, as one will see in upcoming experiments in the air or our syntheses' based on this 'so-called' rapid cool-down.[122–125] High-pressure, of course, plays a role in it too but is not as prominent – more in terms of moderating such properties like excessive evaporation and final SG duality (RT polymorphism).[126–128] The last subject is a fight between 2 competing processes associated with mixed valency[105,110] and partial substitution (A/B-site crossover), as shown in *Figure 10*. That causes a lot of mayhem but also the emergence of interesting properties in terms of electric conductivity.[56,129] Mixing of A/B states is slowed chiefly down but still transpires at different rates at each occupation site. Trans ionic migration is not commonly desired since it is the primary perpetrator of minor SG inclusions or even total failure in achieving a clean, homogenous product by breaking DP into oxides and salts/garnets – as portrayed in *Table 2* by all visible red spots. However, as one will see in matters of A=Ca, Sr, and B=Ce, even with such processes, compounds such as quaternary perovskites or ilmenites could still commonly appear.

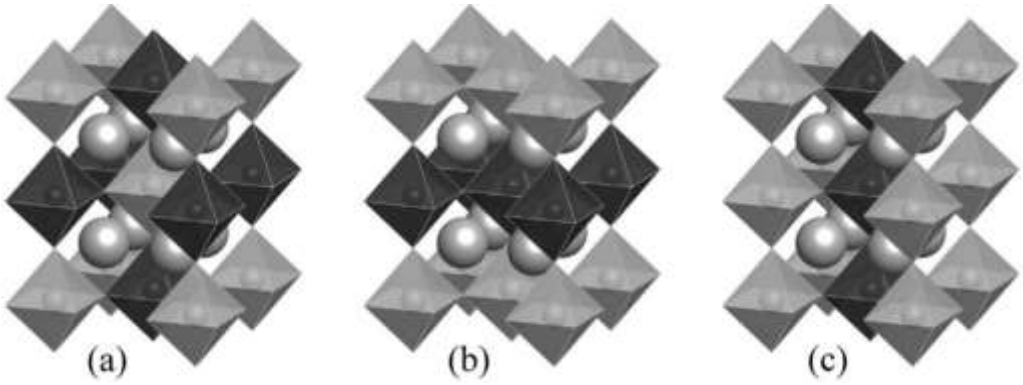

Figure 10 Different A/B-site cation orderings found in $A_2BB'O_6$ DPs: (a) rock-salt, (b) layered, and (c) column types as foretold by Vasala and Karppinen.[37]

Of course, other perovskite systems exist, like so-called triple-deckers. Very useful, layered heterostructures of semiconductors (inorganics) enclosed by atomically thin organic (mainly insulating) sheets usually grown from solid solutions and withheld by van der Waals forces could be tailored into a wide range of optoelectronic applications.[130] Inspired by the discovery of 2D graphene and efficient encapsulation, those crystalline solids could also be used for energy storage and IT technologies. That is, only if interfaces are neatly stacked & well-defined thin films, which is a time-consuming and tedious procedure to maintain.[131] By contrast, layered perovskites could also be seen as analogs of weakly bonded 3D lattices stabilized by organic molecules in Pb-based solar cells.[132,133] Authors like Aubrey[134] have already noticed that, with current (organic perovskite) fabrication technology, this family of compounds could be exploited as a template for modeling white light emission with control of electrical conduction on a macro scale. Their optical experiments and computational modeling have also shown nice quantum effects worth further pursuit in 'topological' electronic states leading to spatially dependent conductivity.[130,133]

Our team worked once on substructures derived from triple-deckers. So-called Ruddlesden-Popper matrices - atomically thin inorganic sodium titanate 2D lattices co-assembled from different Ln = La^{3+} (x=0.005), Gd^{3+} (x=) ions doped with Pr^{3+} ($Na_2Ln_{2-x}Pr_xTi_3O_{10}$) for self-calibrated, low-temperature, optical thermometry.[135,136] This project has proven to be a valuable experience regarding synthesis regimes and foreseeable Pr radiative transitions. Despite my work being mainly restricted to high-pressure polymorphism and Raman spectra (peak vs. pressure/temperature relations – see *Figure A2* for reference) one could witness greenish-blue ($^3P_0 \rightarrow {}^3H_5/{}^3F_2$) and, more important, orangish-red light ($^3P_0 \rightarrow {}^3F_4$ which could be used towards Yb^{3+} NIR excitation. Behaviorism such as this during compression served as another inspiration for this work.[137] The idea of incorporating Pr^{3+} as an efficient transmitter was established having in mind the advantage of non-radiative $^3P_0 \rightarrow {}^1D_2$ overpass and controlled luminescence quenching via shallow traps (vacancies) – a possible transition mechanism suggested by Aumüller et al.[138] Nevertheless, those layered perovskite-oxide compounds, expressed by a general $A_2A'_{n-1}B_nO_{3n+1}$ formula, where the perovskite $A'_{n-1}B_nO_{3n-1}$ two-dimensional, micro-spaced decks possess octahedra formed by slicing typical, perovskite structures alongside one of orthogonal, cubic directions interleaved by A cations as shown in *Figure 11* were too complicated for commercial implementation, so I have decided to turn my sight to something simpler (maybe more profitable).[139,140]

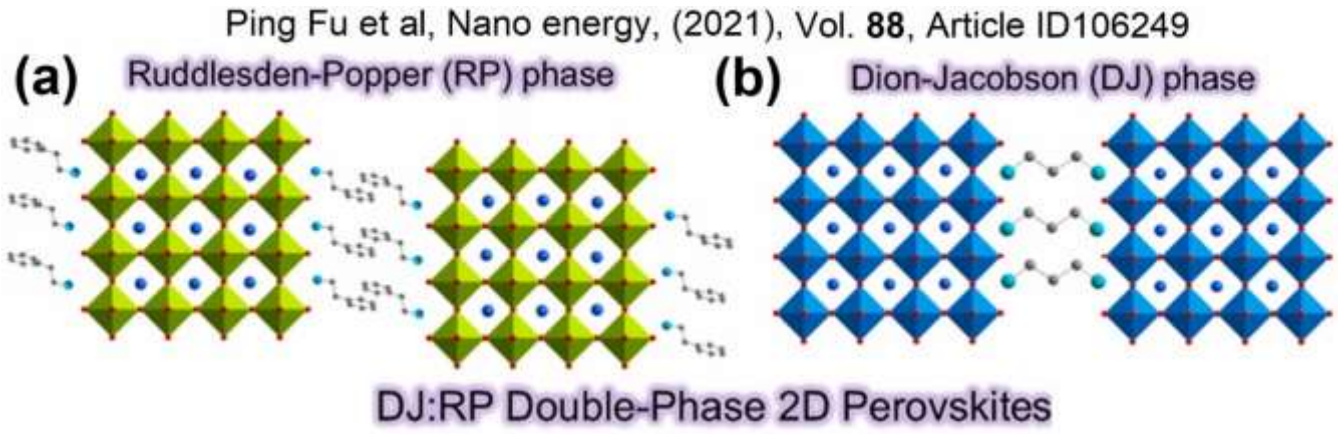

Figure 11 Structural manifestation of 2D-3D triple-decker perovskites phases – Ruddlesden-Popper (a), and Dion-Jacobson (b) as described by Ping Fu et al.[141]

Worth mentioning are the other Dion-Jacobson phase perovskites. They have also been proven to be more stable than 3D-based solar cells. These double-phased perovskites (not double perovskites) are composed of diammonium matrices often mixed with large organic ions (interlayered slabs), preventing local relaxation.[141] Compared to mono ammonium counterparts, they suppress charge recombination and e^- transport (charge transfer) by improving energy converters' efficiency and stability, introducing some local distortions into the crystallographic structure.[141–143] Those robust, harsh matrices have stressed lattice crucial in controlling cation migration by passive defects and distortions in 3D space. That is why those materials are considered mixed 2D:3D type cells, while the 2D aspect is rather crucial.[144–146] Engineering such substances is rather complex and involves nucleation of the Ruddlesden-Popper phase first as an archetype due to lower formation energy. However, they possess immense potential in constructing stable, futuristic solar panels if only the designers choose proper spacers to effectively control thermal-related stresses in environmentally changing relative humidity.[132,147] Now, one can see why some people (like me) decided to fast-cool (freeze) their materials during the last stages of solid-state reaction.

Research & Discussion

1. Experimental Section

1.1 Equipment & Instrumentation

Powder X-ray diffraction (XRD) data were collected on an X'pert MPD (Panalytical) diffractometer equipped with a Cu (Kα) lamp (40 kV, 30 mA) involving Johansson type germanium monochromator and semiconducting strip-detector of resolution close to 0.05°. Broad patterns (from 10 up to 150° 2θ) were collected within a 3 to 12h window with setup working in Bragg-Brentano geometry. Rietveld refinement was performed on FullProf Suite.[148]

Confocal micro-Raman spectra were registered on Monovista CRS+ spectrometer provided by S&I Gmbh having: 0.75 m Acton-Princeton monochromator; back-thinned, deep-depleted PyLoN system, nitrogen-cooled (-125°C) CCD camera (1340×100 - 20μm per pixel array); computer-controlled Olympus XYZ IX71 inverted stage equipped with Moticam (1280×1204) camera and long working distance objectives such as 50× (NA 0.9, ambient conditions), 10× (NA 0.23, high-pressures – HP, & temperatures - HT) and 5× (NA 0.12, low temperatures - LT) magnifications were used during various studies. Used lasers were grey-filtered (power managed by automated Trivista software). Green, diode-pumped Cobolt Samba 04-01 series emitting 532 nm wavelength was used in junction with 2400 grooves per mm holographic grating in monochromator; and NIR Torsana StarBright L series 785nm laser was used together with 1500 grooves per mm grating. After passing through a 50/50 fused silica broadband beam splitter, the Rayleigh line was low-pass filtered from the Stokes signal up to ~60 cm^{-1}. The monochromator entrance slit had 100 μm, and the final resolution was 0.88 cm^{-1} for green, and 0.49 cm^{-1} for NIR laser, respectively. The acquisition time was growing from 40 min to 2h since both samples strongly absorbed the light and overheated quickly – in order not to burn them in varying gas and p(T) conditions, all samples' power density was set within the range of 0.217÷1.12 $mW/\mu m^2$.

Complementary Furrier Transform Infrared (FTIR) reflection spectra were collected using Nicolet 8700 spectrometer from ThermoElectron Corp working in Attenuated Total Reflectance mode. 64 scans, 1 s each, were registered between 400-4500 cm^{-1} with a resolution set of ~ 1 cm^{-1}.

Electron Paramagnetic Resonance (EPR) data was acquired via a Dual channel Bruker ESR300 spectrometer working on X band (9.33 GHz), with a precision of around 100 mG between 1 to 8.6 kGausses. Powders were placed in 4 mm thin wall quartz tubes of 250 mm length provided by WilmadLabGlass through Merck SA.

Synchrotron radiation experiments – X-ray Absorption Spectroscopy (XAS) - were performed on pellets at the SOLARIS NSRC facility in Poland, Cracow. The bending magnet (1.31 T) at the BL04 beamline used Total Electron Yield detection (TEY) mode at RT & Silicon Drift Detector (SDD) at LT. The synchrotron worked at electron energy of 1.50 GeV. An ultra-high vacuum of ~1.5×10^{-9} mbar was applied. The beam spot size was roughly ϕ=2.5 mm. No specific polarization was used. The resolution was set in between 75 (Ca $L_{2,3}$-edge, O K-edge) to 150 meV (Ba, Ce $M_{4,5}$-edges), depending on the choice of specific edge. The total working range was 150÷1700 eV. Samples in the form of compressed powder pellets

were placed on Mo holders & tighten up using screws with pins. Background measurements on empty holders were also performed.

X-ray photoelectron spectroscopy (XPS) measurements were performed after XAS by applying powders to Prevac setup equipped with Scienta R4000 hemispherical analyzer (pass energy 200 eV) and monochromatic X-ray tube (Al Kα - 1486.7 eV source). The Full width at half maximum (FWHM) of the reference $4f_{7/2}$ Au line measured at room condition was 0.6 eV. The orbitals O 1s (K), W 4f ($N_{6,7}$), Ce 3d ($M_{4,5}$), Ba 3d ($M_{4,5}$) or Ca 2p ($L_{2,3}$), spin-orbit doublets were measured. Spectra were analyzed using the commercial CASA XPS software package (Casa Software Ltd, version 2.3.17) using Shirley background curves. Spectra were fitted with a mixed Gaussian-Lorentzian function. Mounting proper electrical contact between low-conducting powder and the instrument was ensured by the incorporation of carbon tape.

Differential Scanning Calorimetry (DSC) & Heat Capacity (Cp) were taken on Netzsch Phoenix DSC apparatus, model DSC 204 F1. Temperature scans ranged from room conditions to 873K at a heating rate of 10K per min. A three-staged, heating–cooling–heating system was set in inert-inert-air conditions to assess the particular behavior of each sample in specific environments. The heat capacity (C_p) reference was Saphire. Crucibles hosting investigated powders were made out of concave Al pans.

Thermogravimetry (TG) was subsequently carried out in nitrogen and air conditions - 20 ml per min of nitrogen flow – using Netzsch Tarsus, model TG 209 F3 at temperatures ranging from 293K to 1273K. The heating/cooling rate was roughly 10K per min. The mass of each powdery sample placed in a small corundum crucible had approximately 10 mg.

A Hitachi SU-70 SFE scanning electron microscope with a dispersive radiation detector (EDX) and cathodoluminescence system GATAN Mono CL3 was used to take SEM images. Powders' images were additionally processed for statistical purposes using ImageJ software.

High-pressure (HP) measurements were performed up to 20 GPa via hydraulic drive in Almax easyLab diamond anvil cell (DAC) using diamonds with 0.45 mm II-as standard design culets. Gaskets with 0.15 mm holes were made from Inconel x750 alloy and filled up to 50% with powder. The applied pressure transmitting medium (PTM) was argon, and ruby (α-Al_2O_3:Cr^{3+}) was used as a pressure gauge applying the principles divulged by Syassen and Mao et al.[149,150] An exemplary compression cascade showcasing R1/R2 modes used for calculations is shown in *Figure A3*.

Low temperatures (LT ~5K) were maintained using continuous helium-flow, Oxford Instruments cryostat model CF1204. High-temperature measurements (up to 873K) were performed in an N_2 and air atmosphere using the LINKAM FTIR600 stage working together with the T95 controller and LNP95 water pump operated via PC LINK software & Pt103 thermocouple. Both instruments were equipped with NUV-permeable quartz windows.

UV-Vis-NIR absorption & reflection spectra were collected in the 250-900 nm range using Cary 5000 spectrophotometer equipped with a photomultiplier, a PbS detector, and a Quanta-phi integrating sphere attached to measure powders and pellets. The sphere is coated with Spectralon® 95% reflectance material, 2.5 μm thick, coupled with a double Littrow monochromator, Schwarzchild optics, and tungsten, halogen, or deuterium arc source. Experiments were executable in a photometric system working in double-beam mode operated by WinUV software.

Emission and excitation spectra were measured on Horiba Jobin-Yvon Fluorolog-3 spectrofluorometer working in FL-3-12 configuration with FluorEssence software. 450 W Xenon

lamp, joined with double (emission) or single (excitation) grating monochromator, works in tandem with two possible detectors: single-photon counting mode PMT Hamamatsu R928P (operational range 260-850 nm) or PbS for NIR range.

The EKSPA photoluminescence detection system known as an optical parametric oscillator (OPO) excitation source joined with a SpectraPro SP-2500 spectrometer provided by Princeton Instruments was used to separate incoming UV light for dopant, LT excitation wavelengths: from 212 nm, through 232, 252, 275, 325 to 360 and 431 nm. The multichannel detector head provided by Hamamatsu Photonics was controlled by MCD controller c7557-01. Slit alternated between 1 (doped) and 1.5 (undoped) mm while acquisition time varied from 2×5 (undoped) to 10×0.5 (doped) seconds. If any, the commonly used filter was only low-pass 400 nm.

1.2 Synthesis conditions and reactants

After meticulous optimization, substrates chosen for solid-state synthesis are summarized in *Table 4*. Process specifics are crudely summarized in an infographic labeled as *Figure 12*, however, the whole proceedings and remarks regarding the research and development of those paths will be the subject of discussion in this paragraph as well as all of the tested options and disregarded intermediate reactants or solutions.

Table 4 Summary and characteristics of substrates used in solid-state syntheses with their respectable providers, purity, and other valuable remarks regarding their proper safe-keeping.

Substrate	Product	Purity [%]	Provider	Remarks
$BaCO_3$	BCW & BPW	99.99	Strem Chemicals	Preheated to release H_2O
$CaCO_3$	CCWO	99.95		
$SrCO_3$	SCWO	99.94	Chemat/Alfa Aesar	
CeO_2	BCW, BPW	99.995	Strem Chemicals	CCWO & SCWO failed the test
$Ce_2(CO_3)_3 \times n\ (6)\ H_2O$	CCWO, SCWO	99		Preheated to release H_2O
$(NH_4)_2Ce(NO_3)_6$	BCW	99.99	Merck	Positively tested
WO_2	BCW, BPW	99.9		CCWO & SCWO tests failed
WO_{3-x} ($W_{18}O_{49}$)	BCW	94	Self-made	Positively tested Unstable
WO_3	CCWO, SCWO	99.995	Strem Chemicals	
Pr_6O_{11}	BPW	99.99	Chemat/Alfa Aesar	Pr_3O_5 ~6% Unstable in air
Pr_2O_3	All doped samples			
Yb_2O_3		99.9	Strem Chemicals	

The first syntheses were done using Pechini,[151] hydro-thermal & solvothermal methods[152] since they are much cleaner and provide better condition control with overall homogeneity within the structures. However, several issues led to a quick rejection of all previous attempts. Firstly, materials oxidized beyond desired proportions during calcination and drying in air, especially when polymer resin (mannitol) had to be thoroughly removed. Secondly, water is also a bad environment since it hosts a substantial amount of oxygen despite discovered substances being amphoteric -their precipitation was relatively easy, but elevated

O & OH content was substantial. Furthermore, in terms of protecting vital, not-fully-oxidized, amphoteric reactants like Ce^{3+}, $W^{4+}O_2$, or $W^{4/5+}{}_{18}O_{49}$, acid was essential to be added, which often boosts the oxidation. Thirdly, using any good alkalized (NaOH) organic (alcohol) mixture with surfactants (like EDTA or DTPA) in mild temperatures (considering being stored below 180÷200°C in a pressurized autoclave to 6÷8 atm.) inevitably always results in the formation of high 20÷30% content of other, highly undesired luminescent-active impurities[2,5,153,154] like A_2WO_4, A_2WO_5 or even AWO_4 mixed with (A=Ba/Ca^{2+}) cerates or just simple ceria rendering further experiments useless. That led the team to believe that actual, slow migration control of well-mixed components during pressurized solid-state reaction in an inert atmosphere is actually the key.

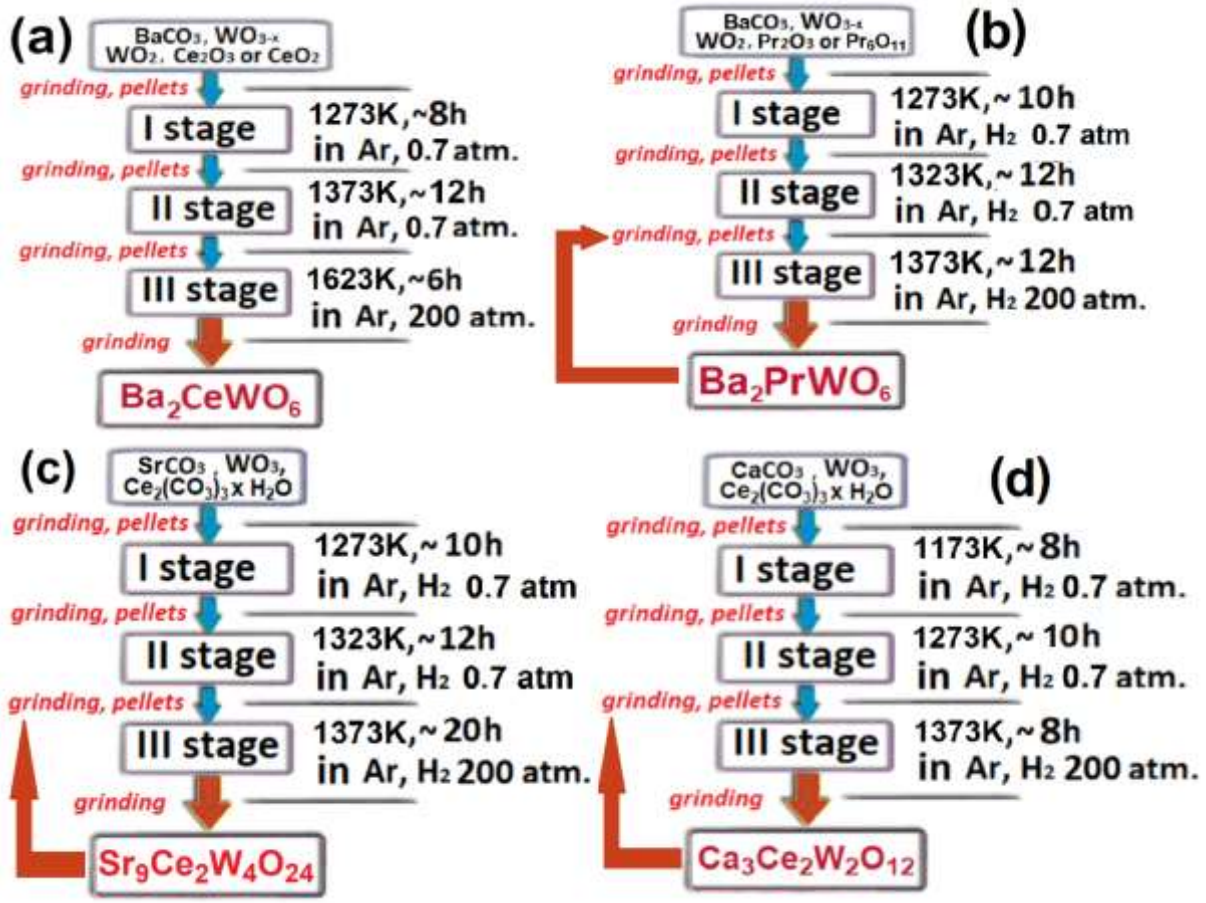

Figure 12 Ideological scheme depicting all optimized solid-state syntheses of investigated tungstates: (a) for BCW; and (b) BPW double perovskites, respectively; (c) for SCWO, which came out as something in the shape of quaternary perovskite; and closely related (d) CCWO ilmenite.

Therefore, all materials (in the form of powders) were synthesized using high temperatures in an oxygen-depleted/airless atmosphere via solid-state reaction in constant-flow reactors at temperatures above 1173K. Initially, the pressure was lowered to 0.7 atm. to improve the flow of the inert medium and desorption of gases coming out from decomposing reactants pressed earlier into tight pellets (to 10 MPa, d~13mm). All of them were sintered in corundum crucibles after grinding with ethanol after each step. Later, the whole system was heated up (specifically to levels according to Tamman's rule)[155] and pressurized to ~200 atm. to increase the ionic diffusion rate of specific RE ions and ensure that the oxygen is being flushed out of the reactor. During 1st

stage, two intermittent (~15 min long) stops were made at 723 and 1173K due to the big release of H_2O, NH_3, and eventual NO_x, CO_2, respectively, depending on which reactants were used. The heat rate should not exceed ~10K/min, but cooling down below 1273K must be rapid to freeze the atoms in place so that oxides, cerates, and other simple $A_2WO_{4/5}$ tungstates would not form. This regime should be maintained using an inert atmosphere down to at least 393-373K - mainly to avoid any oxidation and moisture absorption since these materials will turn out to be oxygen- (evolution with temperature) and light- (time-resolved, deep UV) sensitive. They turn from weak semimetallic phosphors to other insulating scintillators via decomposition. In order to prevent such changes & keep them as they truly are for more than eight months, a vacuum exicator in a dim room without any strong sunlight is recommended. One might also add 1÷5‰ of H_2 to the synthesis mixture to neutralize any possible free radicals during the synthesis.[156,157] Sometimes, after grinding post-last stage and powder XRD check, a fourth round of synthesis was initiated, repeating everything mentioned in the last 3rd stage if some remaining reactants could be neutralized - depicted schemes were not just the bare minimum needed to achieve satisfying results. The crude nature of SSR already implies that sometimes a repetition might be needed even if all conditions are the same, however usually, it was enough – chemistry and internal processes could not be ideally controlled each and every time due to entropic reasons, but this was the average number of steps taken.[158–160] If one is exemplary lucky, BCW can occasionally form a big, dark crystal with a violet tinge encased inside a tightly-pressed pellet. However, that result was achieved only once (not repeatable), sacrificing a lot of powdery exterior towards unwanted CeO_{2-x} & $BaWO_4$ impurities. Usually, a minor 1÷2% surplus of WO_2 and inert gas with 2500+ atm. pressure is also needed.

Products that were actually aimed at are: Ba_2CeWO_6 (BCW), Ba_2PrWO_6 (BPW), Sr_2CeWO_6, and Ca_2CeWO_6 in the form of double perovskites. Unfortunately, the latter two turned out to be something different (as seen in *Figure 12*) due to naturally caused entropy arising from apparent elongation or rather tilt of shrinking and twisting alkaline-oxygen polyhedral along one axis.[37,69] First batches were inhomogeneous dualistic mixes of 50:50 desired phase versus those depicted in the aforementioned schemes. After many attempts, not much success was achieved in terms of thoroughly purifying them from all the extra content, but optimizing the conditions towards desired, 8+ BB'-charged double perovskites resulted in +93% purity – at least regarding barium. The other two, not so much. So, basing on pieces of information provided by Vasala and Karppinen,[37] a test was derived to see if the other 2 (Sr & Ca) compounds would be achievable in the other pure form given they naturally chose some different shape/stoichiometry. This side-tracking is common in DPs synthesis and is also worth pursuing according to science due to empirical investigations of structural disorder. The notes about the strontium-related compound at least state that it remains within the desired family of compounds but as a quaternary $Sr_9Ce_2W_4O_{24}$ (SCWO) perovskite.[75,77–79] The last, Calcium one, formed so-called ilmenite $Ca_3Ce_2W_2O_{12}$ (CCWO) derivative.[161–166] Both with massive unit cells preferring 9+ B-site ion charge balance.

All the findings were documented (in upcoming *chapters 2, 3 & 4*) using methods mentioned before in the experimental *section (1.1)*, however, one peculiar thing stood out. All materials seemed to show dualistic BB'-site ion charge, which transfer was difficult to control using conventional stimuli like temperature, pressure, time-resolved PL, or reheating in reduction atmosphere/gases. So, an attempt was made to utilize alternative resources in the form of intermediate oxides, other than conventionally

known WO_3, WO_2, CeO_2, or Pr_2O_3, to see whether or not something more homogeneous (or even exotic) will be easier to obtain & naturally balance itself out. Consequently, WO_{3-x} (idealistically $W_{18}O_{49}$ closest to non-existent W_2O_5), heat-pretreated $Ce_2(CO_3)_3$ hydrate (as unstable Ce_2O_3 substitution), and Pr_6O_{11} (nearing perfect, hard-to-achieve PrO_2 structure) were involved but, as it turned out, to no avail. Cationic balance, later described in *chapter 2.3*, approached the same discrete values with passing time but from the opposite angle or charge-state boundary conditions. Meaning ions were seeking the same ratios from a different perspective. That could be somehow irreversibly manipulated (especially later using deep-NUV or X-ray light) but with some dire structural consequences for barium structures. It seems like the B-site ions were trying to compensate for some local oxygen vacancies and defects but to no avail, hence all this disproportionation and not uncommon charge-mixing effect.[109–117]

As for Ce^{3+} ingredients, intercalated water in cerium (III) carbonate was assessed via TG and powder XRD patterns to show that it has mainly × $6H_2O$ with $CeOH(CO_3)$ & a small amount of >1% $Ce(CO_3)_2$. Decomposition and post-reduction of usual 4+ ceria gave worse results of CeO_{2-x} complexes (like Ce_7O_{12} or Ce_3O_5), so this original substance (Ce^{3+} donor) seemed to be a more practical solution in producing Ce^{3+}/W^{5+} phase (& dopants) in comparison to the other Ce^{4+}/W^{4+}.

Knowing that oxidizing Pr^{3+} oxides do not usually create pure PrO_2 but, instead, often host a complex mixture of Pr_nO_{2n-2} phases (analogical to the reduction of CeO_2 or decomposition of its bicarbonates resulting with, at worst, a mix of 5 RE^{4+} ingredients)[167] we have decided to try with Pr_6O_{11} since other remaining phases ($1.585<n<1.833$) rapidly interchange between each other with alternating temperature, moisture, and carbon dioxide content (charge transfer and much more).[168–171] It is the best, relatively stable Pr oxide having an equilibrium phase close to Pr^{4+}-rich PrO_2 hosting $4PrO_2 \times Pr_2O_3$.[172] With it, we could hope for the best Pr^{4+}/W^{4+} ratio with competing Pr^{3+}/W^{5+} set within the matrix. On behalf of this and the previous paragraph, one could genuinely deduce that BPW and BCW reactants will behave incongruently compared to SCWO & CCWO analogs, which are built up from much more stable, fully oxidized B-site ions.

To accommodate for the failed attempts of creating a complementary, pure RE^{3+}/W^{5+} phase (in comparison to RE^{4+}/W^{4+}, which resulted in a similar imbalance reaching the aforementioned discrete ratio but from the other side of the BB'-site spectrum), a W^{5+} carrier substance was created – at least as an intermediate solution for SSR. Early mentioned RE^{3+}/W^{5+} cationic pair could be made predominant according to previously displayed recipes in *Figure 12*. Conventionally affordable methods on a laboratory scale could be modified for use from such articles.[173–176] There, $W_{18}O_{49}$ has the best 4+/5+ ratio of ions in all WO_{3-x} family. Also known as $WO_{2.72}$, made by T. Fita-Chala et al.,[173] has the best reaction properties recorded due date. It is the closest formula to non-existent, perfect 5+ $W_2O_5/WO_{2.5}$ oxide that one could wish for but also the most unstable one. Slow oxidation, outside of suspension and protective environment, to W^{6+} is imminent; thus, we recommend using it no longer than 3-4 days after successful synthesis. W_2Cl_{10} alternative is not a good solution since it would contaminate structures with persistent chlorides even if it is truly stable.[177,178] Because of those problematic issues, and the aforementioned BB' self-balance that still maintains itself despite using different reactants and environments, I refrained from studying this family of samples and simply chose to stick with RE^{4+}/W^{4+} reactants. Simply because the one thing that changed was the balance of Ce^{3+}/Ce^{4+} to W^{5+}/W^{4+} - the properties remained the same. No pure (Ce^{4+}/W^{4+} or Ce^{3+}/W^{5+}) cationic phase was finally achieved during the nontrivial synthesis attempts, so there was no difference in where to start. Furthermore, not only the mixed pairing was unavoidable, but also, using unstable oxides turned out to introduce more contaminants into the samples – they had more unintegrated, distorted oxides, and W^{6+} appeared at the end, further complicating the structure, creating more vacancies, mixed B-site pairs, and highly-unwanted minor phase in the form of $A^{2+}WO_4$ scintillators. That is why one should stick to RE^{4+}/W^{4+} substrates.

2. Physicochemical characterization in ambient conditions

2.1 SEM imaging and morphology

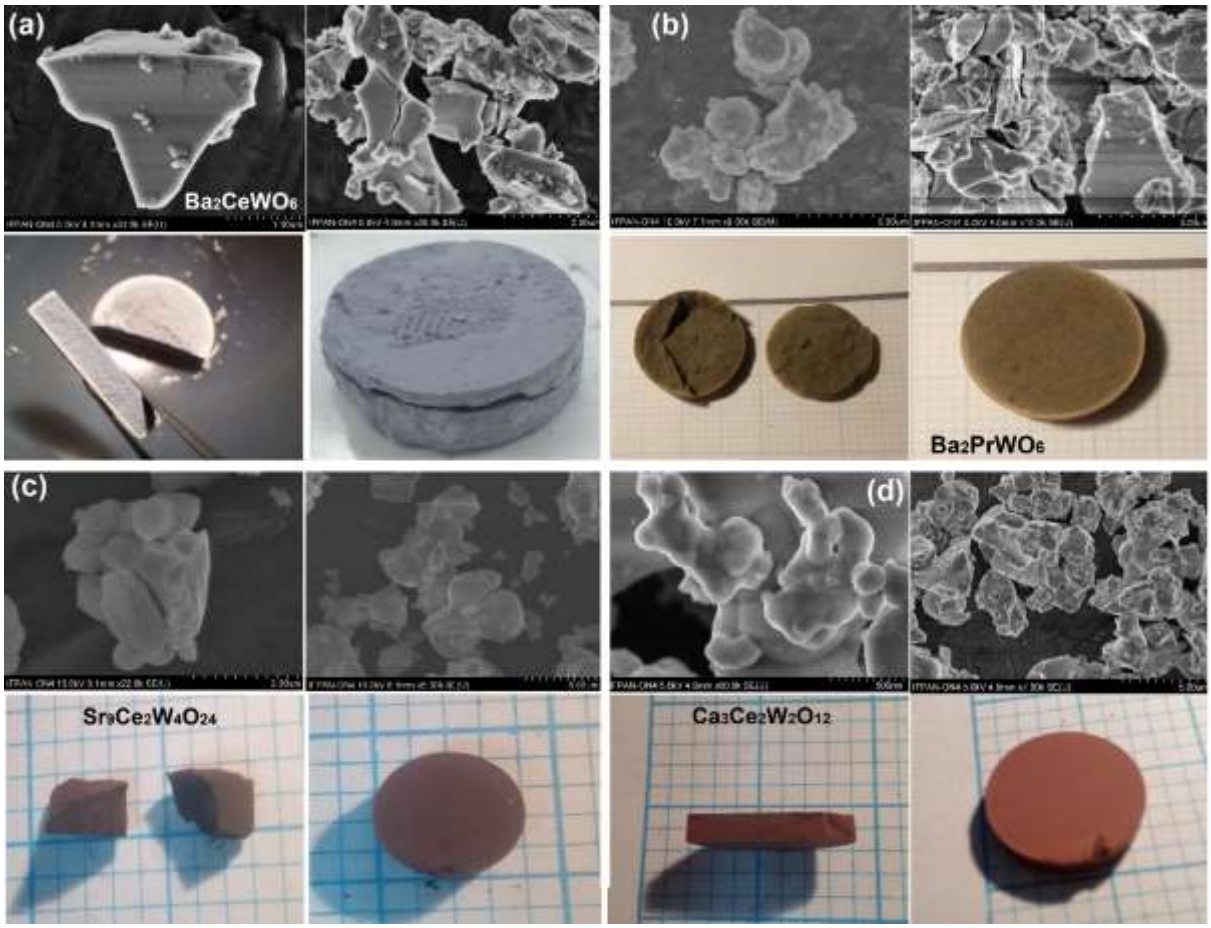

Figure 13 Micro (upper) and Macro (lower) -scopic photos of newly-created materials: dualistic (a) greyish-blue BCW; and (b) greenish-grey BPW double perovskites; with homogeneously brown (c) SCWO quaternary perovskite; and slightly lighter (d) CCWO ilmenite. One can notice that BCW & BPW have more defined microcrystalline structures, but their surface is riddled with defects. BCW's outer shell has a mostly unwanted, white, and brittle layer of ($BaO+CeO_{2-x}$). BPW, on the other hand, has a lighter crust containing $BPWO+Pr_2O_3$ intrusions.

Micro- and macro visualizations of all samples' final forms post-solid-state reaction are presented in *Figure 13,* where one can see that (a) BCW, just like its praseodymium counterpart (b) BPW, has more defined, smaller, polycrystalline structures, at least from the inside. Both double perovskites show dualistic nature and some pronounced discoloring on the outside. As it turns out, the brighter exterior shells are more defective and riddled with minor phases. Steel-grey color BCW crystalline polygons (a) are covered with a brittle ($BaO+CeO_{2-x}$)-rich layer that could be easily scraped. It occurs due to slow but inevitable WO_2 evaporation that could be mitigated by adding a slight surplus of that ingredient. BPW case (b) is less severe since the brighter layer contains more Pr^{3+} in the form of mixed $BaPr_2WO_7+Pr_2O_3$ impurity phases (majority in terms of total interior content is ~Pr^{4+}/W^{4+} pair as shown later in XPS/XAS related paragraph). SCWO (c) quaternary perovskite and (d)

CCWO ilmenite also share few similarities (being visibly different from the previous two materials) and are a lot more homogeneous. However, occasionally those two congruent substances form a darker hue on the surface - a very thin but grainy in touch, which is easy to remove even with a simple touch of a scalpel or tweezers – it is most probably a layer of W/WC ceramics originating from oxidized W and carbonate reactants. That is also why one should not use graphite crucibles as sample holders during HT synthesis. Both perovskite derivatives have brownish color – SCWO being slightly darker. Widely spread micro-to-nano-sized spherical particles are mostly cluttered together as fine dust, which is not easily separated and seems to attract each other statically; thus, each particle's size is much more difficult to assess. Before divulging into analytics, it is worth mentioning that all SEM experiments were performed on actual grains extracted from the middle of the pellets where the actual phase resided - XRD was also done on samples collected the same way. Outer layers were still mostly scraped off for a separate measurement after realizing the material's dual character shortly after cracking the pellet in half shortly post-synthesis. We also wanted to avoid eventual contamination from interior grains falling into the middle of the pellet while cracking them open.

A statistical overview done in Image J software on randomly-chosen, well-defined 20 grains (dAV20) is summarized in *Table 5*. Debey-Scherrer equation: $d_{AVDS} = \frac{K \times L}{FWHM \times \cos(\theta)}$ was also incorporated to provide some insight into this subject based on provided XRD patterns. According to tables in Langford, Willson, and Scherrer's work,[179] shape constants (K) were derived from 3 chosen, well-distinguished XRD peaks at higher 2Θ angles.[180] Their hkl's and FWHM's, alongside with some visual recognition, were crucial to estimate proper calculating factors; however, one must note that for grains larger than 200 nm, these Debey-Scherrer estimates are much less accurate. This highly depends on the limitations originating from the sheer size of used X-ray wavelength (L) – in our case, equal to Cu Kα.

Table 5 A summary of estimations and calculations performed respectfully on SEM images and powder XRD patterns to determine grains' actual size and shape parameters for all newly acquired rare-earth tungstate materials.

Material	d_{AV20} [nm]	$\pm\sigma_{AV20}$ [nm]	Shape K_{hkl}	Peak angle [2Θ]	Peak FWHM [Rad] $\times 10^{-3}$	d_{AVDS} [nm]	$\pm\sigma_{AVDS}$ [nm]
BCW	781.3	95.5	0.88÷0.90	134; 92.5; 69.6	3.2; 1.86; 1.4	861.6	48.0
BPW	854.6	90.6	0.88÷0.92	110; 69.8; 85.4	2.6; 1.9; 2.08	913.6	7.0
SCWO	1128.3	104.9	0.83÷0.86	81.3; 72.8; 44.1	1.6; 1.7; 1.5	972.9	42.6
CCWO	1035.8	114.7	0.84÷0.86	77.2; 44.6; 31.9	1.86; 1.5; 1.5	915.9	17.8

Sometimes the shape (K) and (dAV) of the particles were hard to assess because of joined conglomerates in large proportions hardly visible through SEM microscope, like in the case of SCWO and CCWO. This was most probably due to low contrast from low conductivity/charging effects and the aforementioned electrostaticity of the fine dust. However, some trends could be easily established based on just a few lone, widely scattered particles present on the edges of the browsed area, as seen in *Table 5*. Interior BCW and BPW microcrystals (which we should focus on due to lack of contaminants) are generally

slightly smaller, with BCW being the tiniest. Their shape is also more cuboidal (higher K constants) due to their polyhedral, polycrystalline nature. BCW also has more diverse crystal sizes, as can be deduced by average deviation factors (σAV). The last statement also stands for CCWO; however, alongside with SCWO, their characteristics open up a different group or rather a pair of conjoined similarities: they are substantially larger, as mentioned before, their particles attract each other like in fine dust; and finally, their shape is more spherical as showcased by the K value. SCWO is also the largest of them all. From a statistical standpoint, d & σ parameters established from SEM imaging (AV20) and XRD patterns (AVDS) do not differ that much on the nanometer scale and show the same tendency, where SCWO > CCWO > BPW > BCW. They provide different insights into the same phenomena that somehow complement each other. However, from an experimentalist point of view, regarding previous remarks about Debey-Scherrer equation limitations, SEM imaging seems to be a more reliable source, especially because one physically sees the nature of incoming results in a larger specimen group.

2.2 Powder XRD analysis

Ba_2CeWO_6 (BCW) and Ba_2PrWO_6 (BPW) double perovskites are identical in many crystallographic features, as seen in *Figures 14 & 15,* respectively. First, they turned out to be as planned in shape and form. The upcoming analysis is based on similar isostructural conclusions regarding SG assignment, polymorphism, changing axial constraints, and dualistic $RE^{3/4+}/W^{5/4+}$ ionic nature. Even in such doubtful subjects like overall appearance, impurities, degradation, and LT phase transitions, everything is connected, so it is just natural to start the discussion with those 2.[181–183]

According to ICSD crystallographic database, their isostructural predecessors are *Fm*-3*m* Ba_2BiYO_6 (record nr 65555) from Lenz et al.[184] work or Ba_2SrWO_6 (246108).[185] Other typical examples of such already-developed structures might be found amongst $Ba_2Ce_{3/4}\square SbO_6$ or $Ba_{1.75}\square_{0.25}BaWO_{5.75}\square_{0.25}$, where □ is a vacancy.[183,184,186,187] Garrido Barios event predicted such BPW creation and appearance using just DFT calculations.[188] Rietveld refinement, however, showed poor results regarding peaks' shapes vs. intensities ratio for this specific space group (BCW R_{wp} ~23.5%; BPW ~23.9%). BCW acquired first,[183] ideologically has an almost cuboid unit cell – slightly monoclinically tilted, straight β angle by 0.015° (at worst batch 0.04°). Similarly, BPW, but with an even more subtle tilt of ~0.01°. Best fittings (BCW R_{wp} ~ 20.9%; BPW ~17.5%) suggested that we have encountered a problematic case of mostly indistinguishable patterns: of *I*2/*m* (Glazer tilt system $a^0b^-b^-$)[69] shown above and alternative, *R*-3 (a-a-a-) SG stored in supplementary Figures *A4* & *A5*. Their refinement data were summarized in *Table 6* and *Table A1,* respectively. It does not mean that other possibilities were not explored - the rest of rejected SG matches and the whole meticulous fitting process are presented as insets of aforementioned *Figure A4*(a-d) (and refer to BPW processing too) but, without additional assets like neutron diffraction, or information about behavior outside of ambient conditions, gathered through, i.e., HP XRD, there was no way to ascertain the final point group matches at that point in time. Especially after all (4) applications for much-needed synchrotron time were rejected, the only possibility was to follow Lufaso[181] and Howard[71] et al. research where they saw *I*2/*m*↔*R*-3 interchanging into

one another at specific p(T) conditions – they state that both SG could coexist together at room temperature since their phase transition belongs to broad second order type later turning into more recognizable, monoclinic $P2_1/n$. To limit future discussion, let's focus more on the former, $I2/m$, since this SG assignment will be more accurate at the end of the discussion.

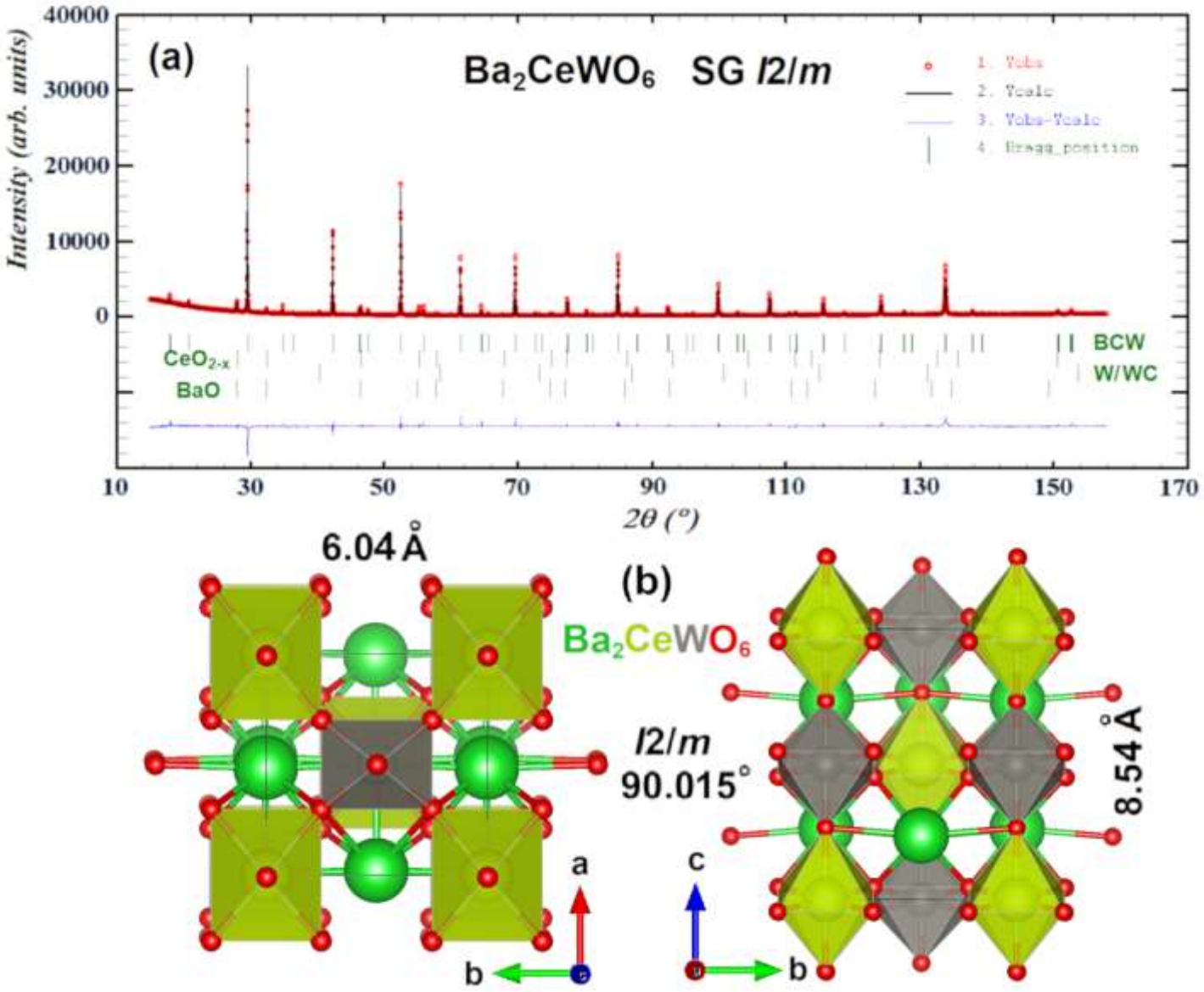

Figure 14 Original XRD pattern (a) acquired after Rietveld fitting and refinement of best, 95% pure $I2/m$ phase containing traces of BaO and highly-distorted CeO_{2-x} (probably Ce_7O_{12}) oxides alongside minor traces of W/WC phase. Red dots are the manifestation of a naturally observed pattern. A straight black line is a calculated fit. The blue line depicts the difference between them. Green vertical lines are specific Bragg positions assigned to specific phases. The unit cell is shown in partially ball-stick, partially polyhedral convention in figure (b) with some additional structural parameters alongside the 'c' (left) and 'a' (right) axes. Yellow spheres and polygons are ceria, red is oxygen, and grey is assigned to tungsten. Barium is depicted solely as green spheres to improve overall visibility since its dodecahedra would cover most of the view.

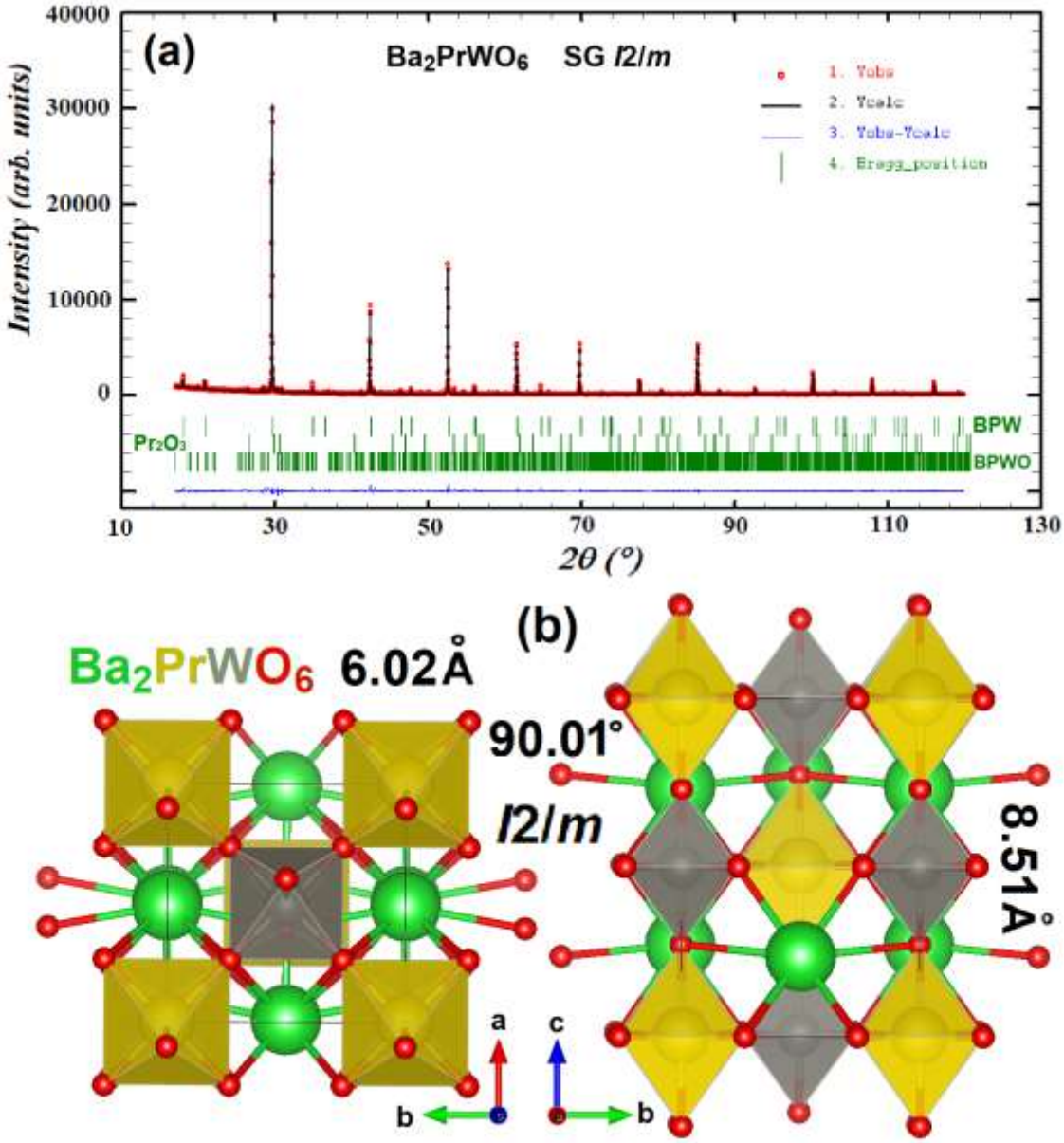

Figure 15 Original XRD pattern (a) acquired after Rietveld fitting and refinement of best, ~96% pure *I*2/*m* phase Ba_2PrWO_6 (BPW) containing traces of $BaPr_2WO_7$ (BPWO) and distorted Pr_2O_3 oxide impurities. Red dots are the manifestation of a naturally observed pattern. A straight black line is a calculated fit. The blue line depicts the difference between them. Green vertical lines are specific Bragg positions assigned to specific phases. The unit cell is shown in partially ball-stick, partially polyhedral convention in figure (b) with some additional structural parameters alongside the 'c' (left) and 'a' (right) axes. Yellow spheres and polygons are Pr ions. Red is oxygen, and grey is assigned to tungsten. Barium is depicted solely as green spheres to improve overall visibility since its dodecahedra would cover most of the view.

The unit cell of *I*2/*m* SG is generally pretty small and compact. The tilt is not even that visible. The same can be said about BPW – the only difference here is that Pr ions localized in central octahedra are slightly smaller due to the bigger electronegativity of the shrinking RE ionic radii and, consequently, the total volume compared to Ce.[189] That ultimately also influences the distortion of β angle, constricting the monoclinic cell more towards its perovskite-like cuboid character. All crystallographic parameters for this and other, mainly chosen SG are summarized

in *Table 7;* meanwhile, alternatives, like *R*-3 (which analysis would be analogical despite having larger axial distances and volume), are placed in supplementary *Table A2*.

Finally, synthesized double perovskites were not exactly pure. Much struggle has been experienced while optimizing the solid state reaction (SSR) via the shake & bake method – to improve batch from 86% to 94-95% of needed content. The most encountered impurities were sweated out RE oxides (BCW = CeO_2, BPW = Pr_2O_3) joined with their alkaline counterparts (BaO), seemingly trying to form some sort of distorted cerate in the case of BCW - *Figure A6*; or praseodymate – $BaPr_2WO_7$ regarding BPW (*Figure 15*).[190–193] Those minor phases resulted from bad RE ion migration dictated by Tamman's rule (connected to elevated melting points),[155] surface effects, and environmental exposure of the pellet's outside layers. Some RE are also known for their mixed valence character (in that case referring mainly to the substrates) like Ce_7O_{12} (ICSD 4113), Ce_3O_5 (621709)[194,195] or Pr_6O_{11} (69109), and Pr_5O_9 (105542).[196,197] Those exotic compounds like to form due to subtle chemical imbalance, lower enthalpy, and uncontrollable, time-dependent charge transfer partially influenced by atmospheric oxygen. That pronounces their occurrence to be problematic and somehow unavoidable. Though the judgment of XRD HighScore databank redirects us to Pr_2O_3 (61179)[198] in terms of BPW (*Figure 15*) and possibly Ce_7O_{12} species for BCW (*Figure A7*), all remarks mentioned above and in *Table 4* would suggest better reference those intermediate species as CeO_{2-x} or PrO_{2-x} group, where x: $0<x<0.5$ – mostly $0.167<x<0.286$.[169–171,194,196,199–201]

The other most common impurity is W or WC originating from graphite crucibles or contact between used carbonates with evaporating WO_2. As mentioned before, those ceramics are easily removable, but that instigates usage of a small surplus of WO_2 (not higher than 1÷2%) while creating a synthesis batch. Too much of it or the presence of residual oxygen (i.e., after not evacuating the furnace or not creating an inert atmosphere with slightly lowered pressure that enables the gas to come out of the compressed substates) will definitely result in creating excessive amounts of $BaWO_4$ – *Figure A8*. This will not only negatively affect Raman but also emission and excitation spectra creating false signals and covering more valuable, subtle bands of particular interest.[2,202,203] BCW and BPW could experience such intrusions because they are built up from $BaREO_3 \times BaWO_3$ as tungstate-based double perovskites. Already crystallographic inconsistencies in BaO and CeO_{2-x} lattice implied a try-hard fusion to $BaCeO_{3-x}$ species.

Table 6 Conventional Rietveld reliability factors for all investigated compounds and their minor phases present in the best, possibly purest batch. Data refers to diffractograms hosting Bragg contribution patterns corrected with the background to the most plausible, undoped SG. Alternates are presented in the supplement *Table A1*.

Formula	SG	Z	V [Å^3]	d_{cal} [g/cm^3]	R_B	R_P	R_{WP}	R_{EXP}	N_σ GoF	χ^2	Fract [%]
Ba_2CeWO_6	*I*2/*m*	2	311.342	7.410	13.5	23.6	20.9	4.36	1304.809	22.5	94.92
CeO_{2-x}	*Fm*-3*m*	4	164.194	6.963	43.2						2.39
BaO	*Fm*-3*m*	4	168.010	6.062	36.7						2.37
W(/WC)	*Im*-3*m*	2	31.695	19.264	98.9						0.32
Ba_2PrWO_6	*I*2/*m*	2	308.843	7.479	5.75	18.3	17.3	2.66	2674.274	42.2	95.71
$BaPr_2WO_7$	*P*112$_1$/*b*	4	623.818	7.613	28.5						3.97
Pr_2O_3	*P*-3*m*	1	77.676	7.051	57.9						0.32
$Sr_9Ce_2W_4O_{24}$	*I*4$_1$/*a*	4	2201.420	6.602	3.82	11.1	13.2	6.24	223.051	4.45	99.41
W(/WC)	*Im*-3*m*	2	31.677	19.257	72.4						0.59
$Ca_3Ce_2W_2O_{12}$	*R*-3*c*	18	4528.414	6.338	4.29	8.31	9.72	2.67	799.386	13.2	99.63
W(/WC)	*Im*-3*m*	2	31.683	19.261	67.0						0.37

Table 7 Crystallographic parameters obtained for all acquired structures regarding their mainly discussed, undoped space groups stored in CIF files hosted at the CCDC database. Alternative SG projections are shown in the appendix alongside with similar summary in *Table A2*.

Formula	Main SG	Unit cell axis length [Å]			Angles [°]			Volume [Å^3]
		a [100]	b [010]	c [001]	α	β	γ	
Ba_2CeWO_6	*I*2/*m*	6.0376(0)	6.0369(0)	8.5420(0)	90.000	9.015	90.000	311.34(2)
Ba_2PrWO_6	*I*2/*m*	6.0219(3)	6.0218(3)	8.5167(3)	90.000	9.010	90.000	308.84(3)
$Sr_9Ce_2W_4O_{24}$	*I*4$_1$/*a*	11.6220(9)		16.2980(1)		90.000		2202.42(0)
$Ca_3Ce_2W_2O_{12}$	*R*-3*c*	9,7258(3)		55.2793(0)	90.000		120.000	4528.41(4)

$Sr_9Ce_2W_4O_{24}$ quaternary perovskite (SCWO) has a larger, densely packed (over 345 atoms) unit cell riddled with many defects from shared Ce/Sr or half-occupied A-atom sites. Its complex nature, alongside with evenly unique XRD pattern, can be seen in *Figure 16.* Dimensional data is stored in *Table 7*. Though there is still much debate about the assignment of these freshly-classified compounds, finding a proper isostructural matrix was not yet an easy task among those few articles that reported on them. Smirnov was the first to discover $Sr_9La_2W_4O_{24}$ as an archetype in the late 80s.[204] His work has been, however, buried in time since he did not publish any relevant structural data in the form of CIF. Only after some time (the late 90s) Xie[79] and Bramnik[205] et al. developed their own $Sr_9RE_2W_4O_{24}$:Eu (RE=Gd, Y) structures (JCPDS 50–0375 and 49-0568 respectively)[206] on the basis of well-known $Sr_{11}W_4O_{24}$ and have noticed his input. The early 2000s brought us $Ba_9Ln_2W_4O_{24}$ and a wide variety of Sr-related compounds $Sr_9Ln_2W_4O_{24}$ (Ln = La, Nd, Eu, Gd, Y),[75,78,204,206–209] but the accurate description and debate came with the work about $Sr_{7/4}\square_{1/4}SrReO_6$ which referred to $Ba_{11}Os_4O_{24}$ as its ancestor.[210] The thing is, most of these compounds are cubic (*Fm*-3*m*) in nature and have neatly long-range order of defects stacked throughout enormous unit cells. Our SCWO falls out of that first assignment– it is undoubtedly tetragonal, *I*4$_1$/a, just like $BaWO_4$ and those last 2 Sr/Ba compounds. Its refinement data can be viewed in *Table 6* and confronted with the *Fm*-3*m* alternative in supplementary *Table A1*. The difference in R_{wp} (Tetragonal SG ~13.2% while cubic ~ 80.2%) will be astronomical, making the final choice rather obvious. *Figure A9* & *Table A2* also show those remaining doubtful SCWO projections with simplified dimensional parameters.

This compound is relatively pure and homogeneous despite generating much debate amongst scientists (mainly about the current compound assignment within the ilmenite/garnet subgroup, which connections are not clearly agreed upon). The only noticeable traces of impurities that were somehow distinguishable in a meaningful way from the background noise was W/WC ceramics present only at the surface. As mentioned before: very thin and easy to remove, at almost negligible content ~0.59% mass.

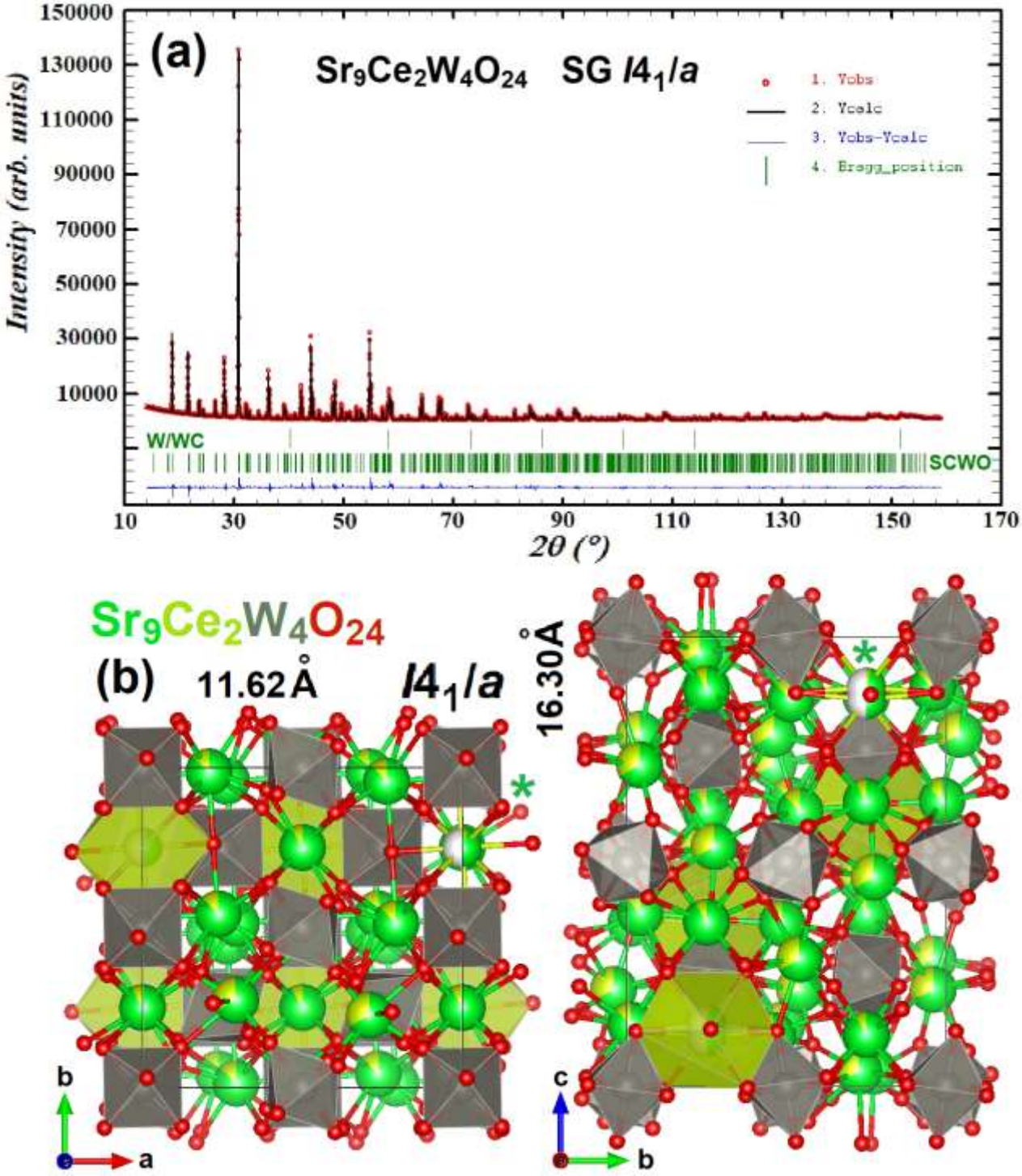

Figure 16 Original XRD pattern (a) acquired after Rietveld fitting and refinement of best, ~99% pure $I4_1/a$ phase $Sr_9Ce_2W_4O_{24}$ (SCWO) containing traces of W/WC impurities. Red dots are the manifestation of a naturally observed pattern. A straight black line is a calculated fit. The blue line depicts the difference between them. Green vertical lines are specific Bragg positions assigned to specific phases. The unit cell is shown in partially ball-stick, partially polyhedral convention in figure (b) with some additional structural parameters alongside the 'c' (left) and 'a' (right) axes. Green spheres are strontium atoms. Yellow is cerium. Red is oxygen, and grey is assigned to tungsten space filling. Some of the Sr and Ce polygon projections were omitted to improve the overall visibility. Green asterisks mark artificially removed polygons to showcase a unique feature of some neighboring, half-occupied Sr/Ce sites (0.497/0.03).

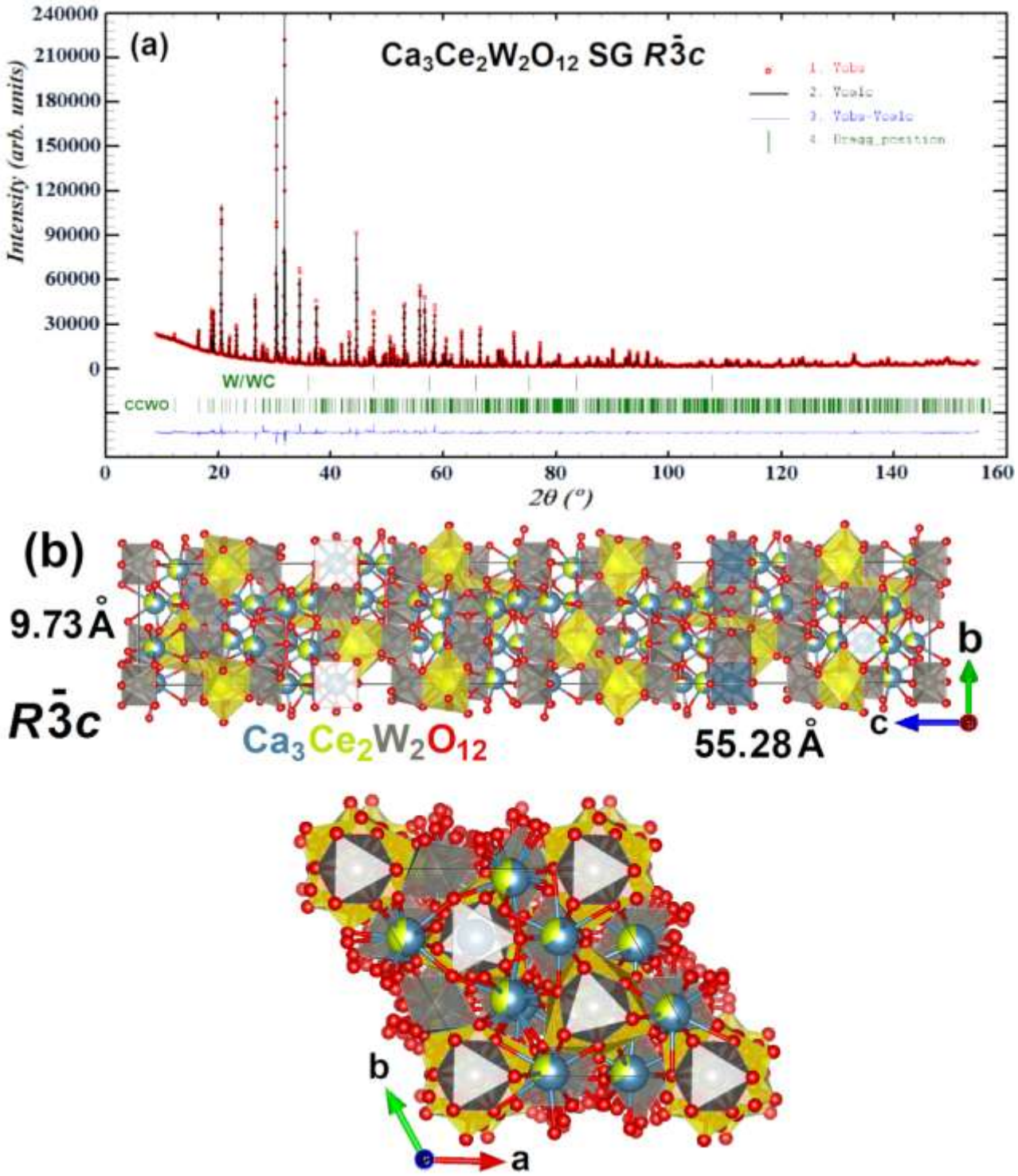

Figure 17 Original XRD pattern (a) acquired after Rietveld fitting and refinement of best, 99.7% pure *R*-3*c* phase containing only minor W/WC impurities. Red dots are the manifestation of a naturally observed pattern. A straight black line is a calculated fit. The blue line depicts the difference between them. Green vertical lines are specific Bragg positions assigned to specific phases. The unit cell is shown in partially ball-stick, partially polyhedral convention in figure (b) with some additional structural parameters alongside the 'c' (down) and 'a' (up) axes. One might notice that both calcium and cerium atoms partially share some sites, so only 2 of them (with different shapes and most pure occupation) were chosen to be depicted as polyhedral to maintain visibility. The remaining atoms are: yellow – cerium, *r*ed -oxygen, and grey – tungsten.

Similar statements are true for $Ca_3Ce_2W_2O_{12}$ (CCWO) ilmenite presented in *Figure 17* above. It even looks the same internally (giant unit cell with staggering 342 atoms additionally sharing A^{2+}/RE sites) and externally - it is in a slightly brighter shade of brown, as shown in *Figure 13*. The only impurity would be an identical, minuscule amount of W/WC phase (~0.37%) allocated on the surface. Furthermore, it behaves the same in various conditions and is only one atom short of typical garnets like $Mg_3Al_2Si_3O_{12}$.[211] So, it truly makes a point to give a question of whether or not CCWO is an ilmenite or a garnet - analogically to SCWO if it is really a quaternary perovskite or something else. Only more profound studies and statistical overview could tell. We definitely saw a lot of common features between them and garnets, so I support that statement.

CCWO is directly related to its isostructural counterpart in the form of already discovered $Ca_3La_2W_2O_{12}$ with JCPDS pattern no 49-0965.[163,164,166] This compound, however, was reported to have its own archetype – $Ca_5RE_2O_{12}$ made by Villars et al.[212] He, unfortunately, did not determine all lattice parameters through structural refinement so we were obliged to do and present them in *Table 8*.

Table 8 Unique structural details of newly acquired $Ca_3Ce_2W_2O_{12}$ structure, based on the Rietveld refinement of preferably chosen *R*-3*c* space group. Note that U_{iso} has been set to be the same for all O and W atoms, respectively.

Site	***x***	***y***	***z***	U_{iso} **[Å^2]**	**Occ. (<1)**
Ca1	0.0093(2)	0.35914(19)	0.18694(2)	0.0033(4)	0.678(2)
Ce1	0.0093(2)	0.35914(19)	0.18694(2)	0.0033(4)	0.322(2)
Ca2	0.37275(16)	0.04466(14)	0.04948(2)	0.0017(3)	0.5541(19)
Ce2	0.37275(16)	0.04466(14)	0.04948(2)	0.0017(3)	0.4459(19)
Ca3	0	0	0.10415(3)	0.0007(6)	0.303(6)
Ce3	0	0	0.10415(3)	0.0007(6)	0.697(6)
Ca4	0	0	0.25	0.043(2)	
W1	0.33174(11)	0	0.25	−0.00009(14)	
W2	0	0	0.162812(18)	−0.00009(14)	
W3	0	0	0	−0.00009(14)	
O1	−0.0035(14)	0.1863(10)	0.22340(15)	0.0025(9)	
O2	0.0036(13)	0.1713(11)	0.02094(14)	0.0025(9)	
O3	0.1355(10)	0.1911(11)	0.17969(16)	0.0025(9)	
O4	0.1863(10)	0.0745(11)	0.14022(15)	0.0025(9)	
O5	0.1927(10)	0.3107(12)	0.10760(14)	0.0025(9)	
O6	0.2460(8)	0.1049(9)	0.0836(2)	0.0025(9)	

As seen above, the disputed unit cell is huge and rhombohedral – a straightforward assignment. The only problem is whether SG is centrosymmetric (*R*-3*c*) or not (*R*3*c*). Again, in the case of powder XRD, they are indistinguishable. Even their VESTA/CIF projections do not show any visual differences at first glance, given that those cells are so complicated and densely packed. They exhibit the same *hkl* parameters hence *R*3*c* projection was omitted. The presence of a symmetry center could be confirmed by more sophisticated techniques like high-resolution single-crystal XRD or NPD; yet again, we had not received access to those facilities (rejection of proposals during Covid), nor was crystal form of this substance achievable at Polish institutes. The other possibility was to reach out to the Kharkiv Institute of Single-Crystal, but the war came. However, upcoming sections about Raman spectroscopy

and polymorphism outside ambient conditions slightly turn the balance towards *R*-3*c* SG. Again, all conventional refinement reliability factors with structural parameters for chosen SG are stored consecutively in *Tables 6* & *7,* whereas alternatives in appendix *Tables A1 & A2.*

The repeatable occurrence of shared multisites is worth mentioning, but now only between Ca and Ce – similar to shared Ca/La sites in Li, Hirrle, and Autenrieth et al. cases.[163,164,166] No noticeable vacancies and half-occupied sites, in any case. However, the material is still defective, which will be showcased later in the luminescence chapters. That should not be a surprise since the volume of CCWO is approximately two times bigger than SCWO. That inflammation might be responsible for better internal distribution of atoms in a longer perspective. More details about exact occupancies – their sites, position, neighborhood, and percentages can be viewed online via CCDC CIF file repositories. That applies not only to precedencies' of CCWO and SCWO but also to more simplified structures like BCW and BPW.

Doped materials look genuinely the same and will be shown and discussed only, referring to the preferred SG. The main concern were the impurities – will chosen RE dopants fully integrate with the matrix given theoretically chosen substitution places? First of all, cerium-tungstates, so BCW, CCWO, and SCWO, were substituted with Pr^{3+} and/or Yb^{3+} to accommodate planned NUV→VIS→NIR energy transfer. The amounts of chosen dopants to (ideologically) swap with Ce^{3+} were 0.5, 2.5, and 5%, respectively. These values refer not to the total amount but to the amount of each RE ion if stacked together. That way $Ba_2Ce_{0.99}Pr_{0.005}Yb_{0.005}O_6$, $Ca_3Ce_{1.9}Pr_{0.05}Yb_{0.05}W_2O_{12}$, and $Sr_9Ce_{1.8}Pr_{0.1}Yb_{0.1}W_4O_{24}$ were acquired. Of course, since Ca and Sr partially share sites with Ce, the intentional substitutional effect is also mixed – resembling much Ba^{2+}/Ce exchange in $BaWO_4$:Ce mentioned at the beginning of introduction[2] - Yb/Pr could be lodged there as well. Regarding sole praseodymium tungstate BPW instead of Pr constituent, a 7.5% amount of Ce was introduced.

The other thing were the minor phases that can occur outside of already reported ones in pure matrices. So in all cases ubiquitous W/WC; in BCW – something else than BaO, CeO_{2-x} (samples with $BaWO_4$ were automatically discarded due to substantial PL interference & misleading Raman response); $Ba_2Pr_{0.925}Ce_{0.075}WO_6$ would have BPWO and PrO_{2-x} intrusions. The presence of those REO_{2-x} oxides was most unfortunate from the beginning, however, not entirely avoidable. There PL interference was to be expected, yet, after 1.5 years of optimization, experiments must still have been tried out - the only solution was to be sure that Yb_2O_3 would not fall out of the matrices just like $Ce^{3/4+}$ oxides in BPW or $Pr^{3/4+}$ in BCW, SCWO or CCWO. Thus, it did not, as seen in *Figure 18* and related to it *Table 9*.

Table 9 Conventional Rietveld reliability factors for all investigated compounds and their minor phases present in the best possible batch. Data refers to diffractograms hosting Bragg contribution patterns corrected with the background to the most plausible, doped SG.

Formula	SG	Z	V [Å^3]	d_{cal} [g/cm^3]	R_B	R_P	R_{WP}	R_{EXP}	N_σ GoF	χ^2	Fract [%]
BCW:Pr,Yb	*I*2/*m*	2	311.342	7.423	13.4						94.49
CeO_{2-x}	*Fm*-3*m*	4	168.103	6.802	25.9	28.4	19.4	3.95	1488.539	24.0	2.89
BaO	*Fm*-3*m*	4	168.846	6.033	29.9						2.62
BPW:Ce	*I*2/*m*	2	308.918	7.477	6.41						95.01
$BaPr_2WO_7$	*P*11$2_1$/*b*	4	624.984	7.599	41.1	26.4	25.2	10.82	245.779	5.44	4.47
Pr_2O_3	*P*-3*m*	1	77.893	7.032	65.7						0.52
SCWO:Pr,Yb	*I*4$_1$/*a*	4	2202.314	6.600	5.39	12.1	14.9	3.69	992.835	16.2	99.29
W(/WC)	*Im*-3*m*	2	31.698	19.211	64.6						0.71
CCWO:Pr,Yb	*R*-3*c*	18	4522.411	6.357	6.66	12.3	13.2	4.49	510.730	8.69	99.58
W(/WC)	*Im*-3*m*	2	31.669	19.211	64.9						0.42

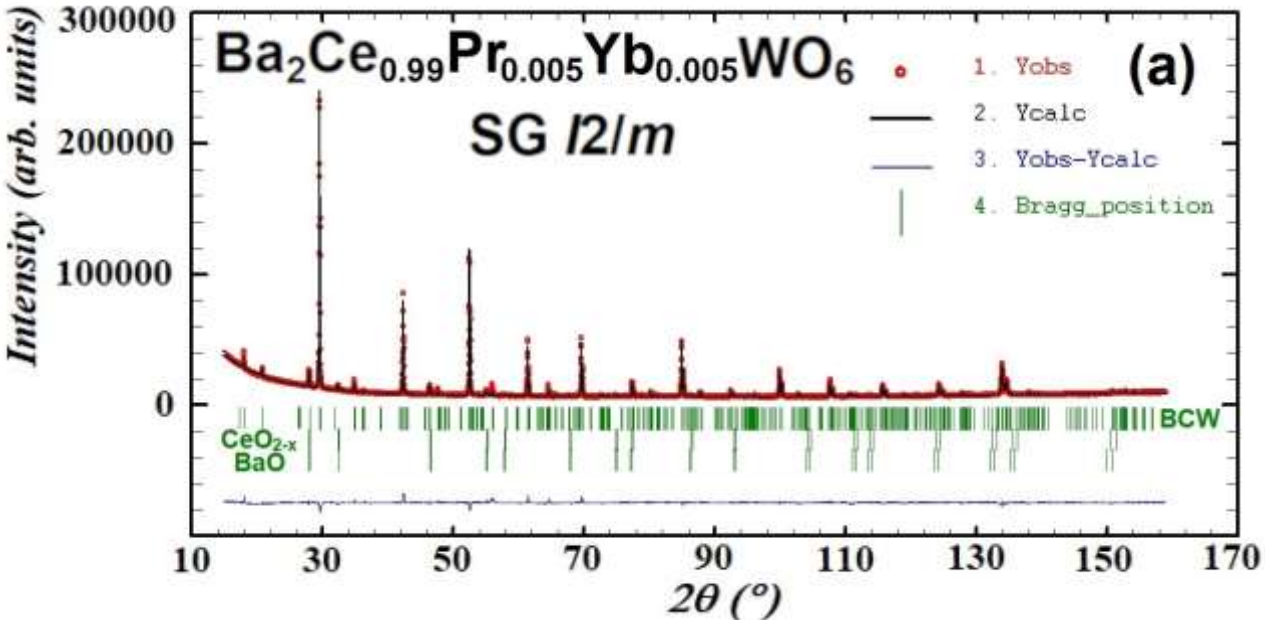

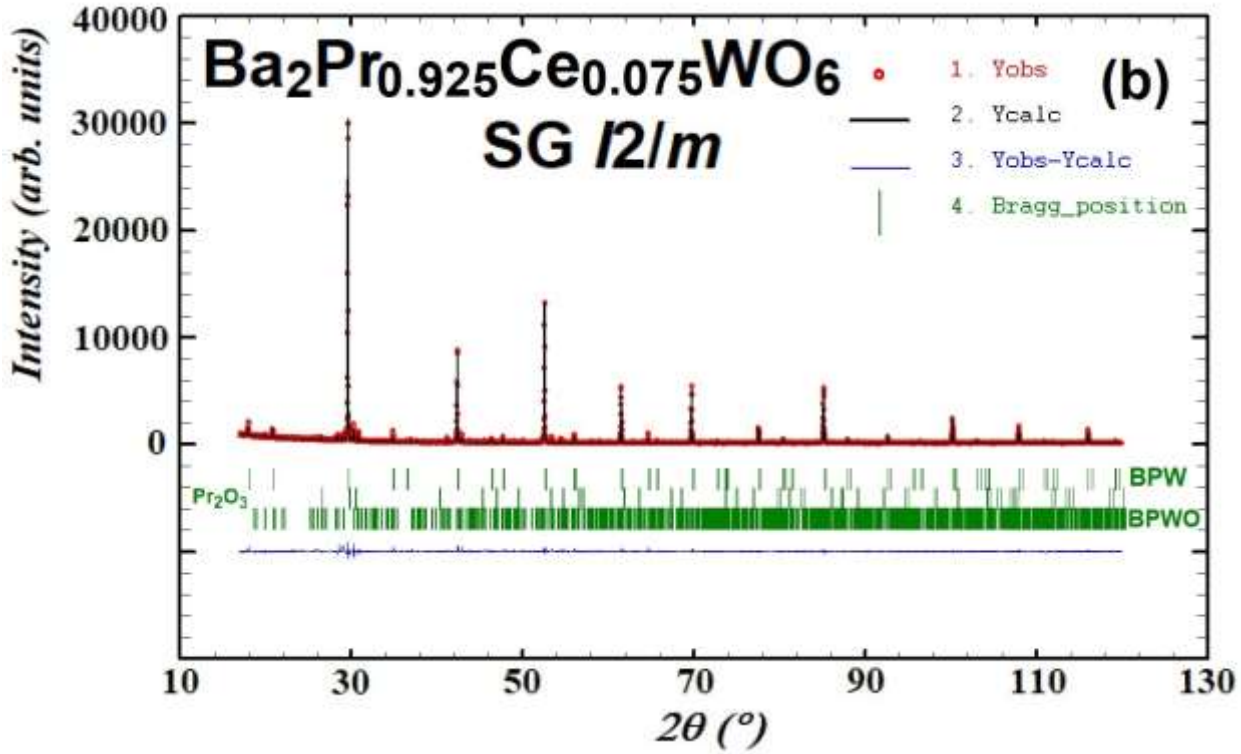

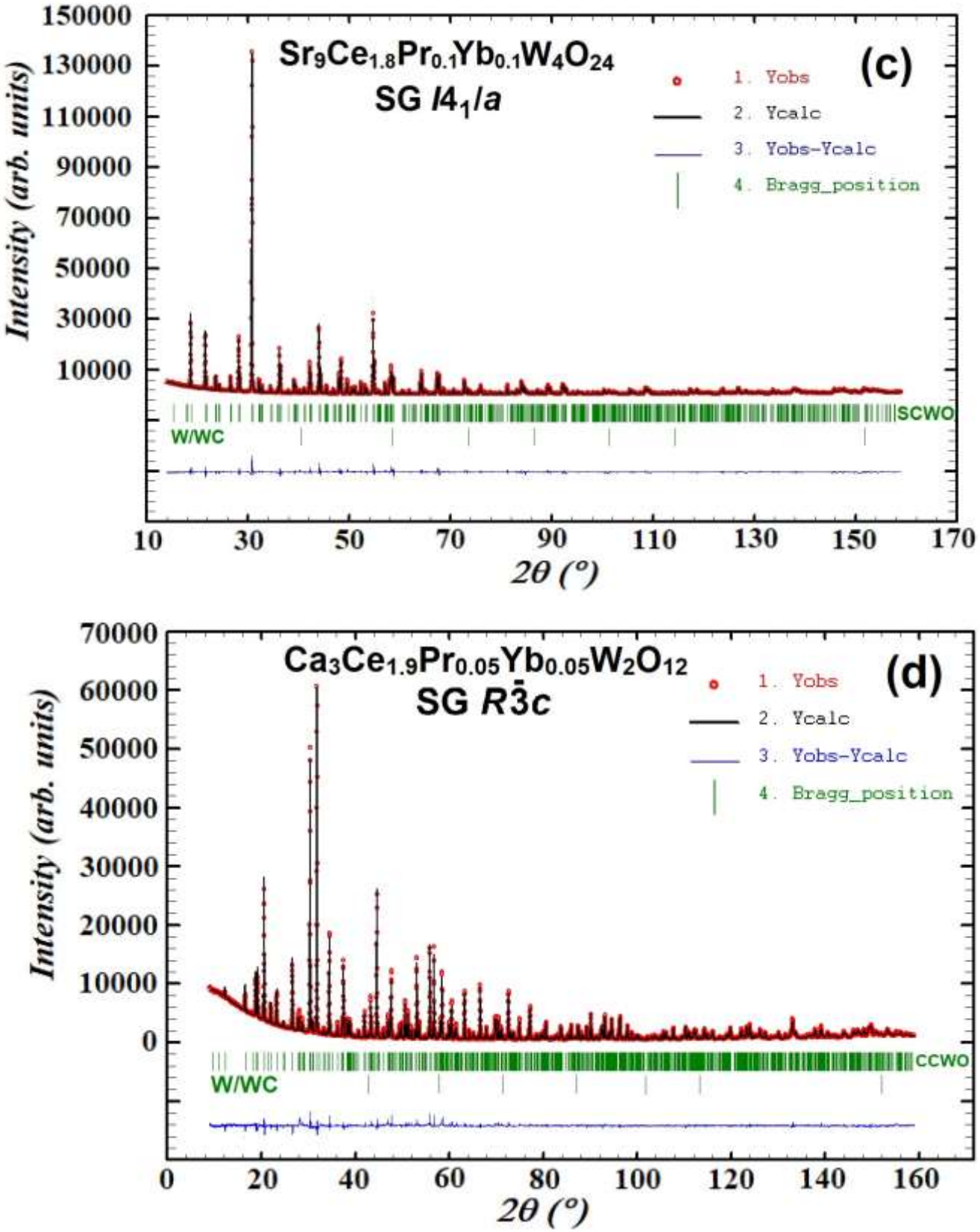

Figure 18 Refined XRD patterns of doped: (a) BCW:Pr,Yb (0.5%); (b) BPW:Ce (7.5%); (c) SCWO:Pr,Yb (5%); and (d) CCWO:Pr,Yb (2.5%). Red dots are the manifestation of a naturally observed pattern. A straight black line is a calculated fit. The blue line depicts the difference between them. Green vertical lines are specific Bragg positions assigned to specific phases.

2.3 X-ray spectral characterization (XPS & XAS)

The application of other complementary X-ray analytic techniques was necessary to estimate the actual content of our powderish materials. This means assessing the cation diversity for carefully balanced structural or stoichiometric purposes and regarding optical properties.[213] It is a well-known fact that only a few ions having specific electron configurations in unique bonding states (i.e., non-empty valence shells, paired mesomeric systems in short or long-range conjunction with good excitations sources) possess proper radiative response if built in a suitable matrix of sufficient crystallographic field strength.[214,215] Furthermore, BB'-site substrates used here have from 2 (RE) to 3 (W) different charges available that might change into one another during the synthesis (such is their unstable nature), so their ratio and appearance must be examined. Shortly speaking, optically active Ce/Pr^{3+} could easily change to naked-shell 4+, rendering them partially useless.[167,195,196] The same stands for W 4 or 5+, which should be semi-metallic and provide a small band gap compared to W^{6+}, which is more insulating.[216,217] These things are crucial to monitor when developing novel, PL-active matrices while searching for an eventual explanation of synthesis/property failure, incoherent behavior outside ambient conditions, or simple defect probation. Characteristics of other applied ions could also help in optimizing various processes, establishing hypotheses, confirm or debunk many questions taking into account that this study is also fundamental in its origin, so oxygen and alkali ions (such as Ba, Sr, and Ca)$^{2+}$ will also be briefly discussed further. For now, let's just shift our focus to the most important RE cations presented in *Figure 19,* where XAS (deep penetrating technique) & XPS (more surface-related) measurements seem to show some coherent postprocessing results.

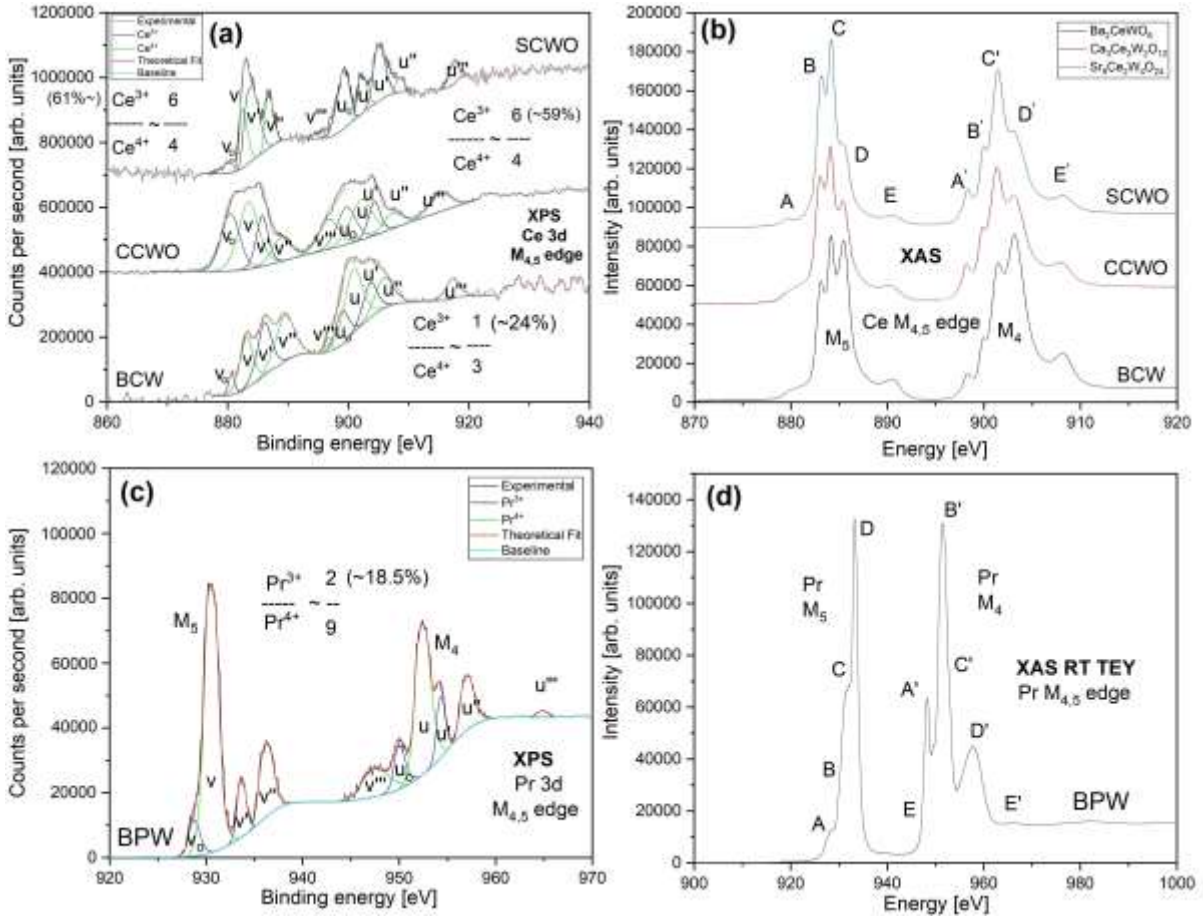

Figure 19 Crucial X-Ray Spectra collected at room temperature and ultra-high vacuum for B-site rare-earth 3d atom shells such as Ce for BCW, CCWO, and SCWO using (a) XPS and (b) complementary XAS techniques. Figures (c) and (d) feature the same methods in respective order but for Pr in BPW.

Cerium and Praseodymium 3d spin-orbit shell and $M_{4,5}$ absorption edges show complex, multiplet band structures at their respective energies (880-915 and 925-965 eV, respectively). The versatility of ionic forms could be assessed by careful and simple deconvolution, knowing need-to-know basics from the literature and reference spectra collected pure substrates at own leisure, as shown in appendix *Figure A10*. Two sets of five XPS peaks ($3d_{5/2}$ v, v_o, v', v'', v''') and $3d_{3/2}$ (u, u_o, u', u'', u''') could be found at the beginning ($3d_{5/2}$) or end ($3d_{3/2}$) of each range mentioned previously.[218–231] Despite having slightly different principles, intensities, and ratios, XAS presents its content the same way - shallower M_5 edge being the first set (A-E) while deeper M_4 edge (A'-E') is shown later, at higher energies. The spectrum of pure Ce^{4+} (i.e., CeO_2) should consist of three multiplets related to $4f^n$ (n = 0,1,2) electron interactions denoted as v, v'' and v''' components in $d_{5/2}$ shell (marked as green)[227,231–234] similarly to B, D, E peaks in XAS. Separated by an 18.5 eV gap and typical 1.5 v/u intensity ratio should be mirrored by a $d_{3/2}$ set (u, u'', and u''') withholding analogical meaning – in XAS: B', D' and E'.[235–237] The rest of the peaks are denoted to Ce^{3+} in the same manner (and marked as blue), so $4f^n$ (n = 1,2) XPS (XAS) modes related to $d_{5/2}$ component (M_5) are marked as v_o and v' (A,C) while $d_{3/2}$ (M_4) as u_o and u' (A',C').[219,225,228,229,234,238,239] Knowing this, establishing proper positioning, peak area, and FWHM could be used for calculating the actual Ce^{3+}/Ce^{4+} ratio from totally added content. $Pr^{3/4+}$ signals sets are interpreted somehow analogically but at higher energy ranges.[220–223,240] Apart from the information provided in the insets of *Figure 19*, one can view them collectively in summary provided in *Table 10,* but for now, the true aim is to establish whether or not B and B'-site ions (Ce/Pr and W) can balance each other out in the core – could they be coexisting nearby in subtle, charge-balanced octahedral sites showing some explicit dependencies, and, if so, will they explain eventual discrepancies in future optical or polymorphism studies? Or possibly justify the existence of other perovskite derivatives?

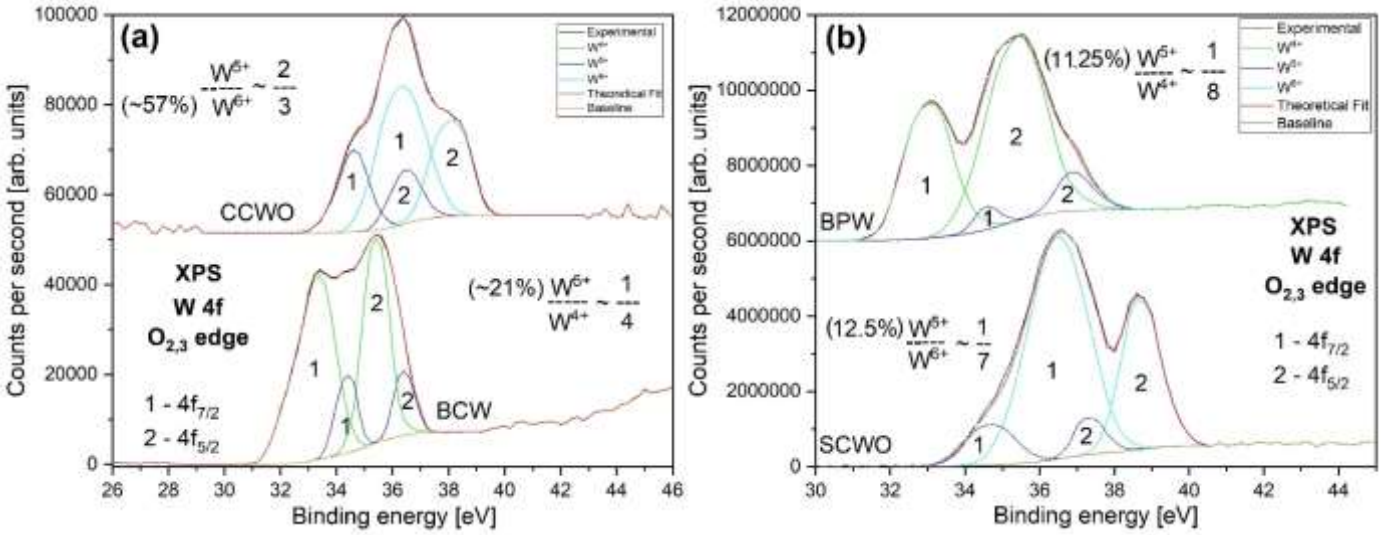

Figure 20 XPS 4f-shell spectra taken at ambient conditions for all four investigated materials regarding the other B'-site ion, tungsten. Figure (a) refers to BCW and CCWO, respectively, hosting fully balanced 8+ or 9+ composition to their Ce counterparts, while (b) presents uneven BPW and SCWO.

Hence, the joint quantitative analysis with W 4f ($O_{2,3}$ edge) presented in *Figure 20*. Such grouping is not coincidental. Both Ba_2CeWO_6 (BCW) and $Ca_3Ce_2W_2O_{12}$ (CCWO) in *Figure 20a* have very close, complementary content to their RE counterparts showcasing structural balance in pronounced ionic duality within the matrix. Double perovskites seem to prefer 8+ BB'-site core balance compared to derivatives, such as ilmenites, where this number is higher by one, 9+. That fact is satisfied by: the Ce^{3+}/Ce^{4+} ratio in BCW, equal to roughly 1/3 (24/76%), while $W^{5/4+}$ does not fall far behind with its 21/79% values meaning, consequently, that Ce^{3+} should accommodate for its neighbor W^{5+}

maintaining aforementioned 8+ balance. Thus, creating a phase sustaining ~1/5 to 1/4 of total content. The rest, ~75÷80%, would create Ce^{4+}/W^{4+} 'artificial' pairs. Artificial because this scenario seems somewhat idealistic – there is no way of telling whether or not this type of segregation is genuinely taking place in the nearest neighborhood - rather not. The ions are mostly spread apart, not ideally – distanced, compensating the charge only throughout the whole volume of the sample. In powders, this phenomenon would create a lot of local defects and vacancies via not perfectly balanced multisites, which are undoubtedly present. Future discussion will tell us more on that matter, but what is most important for now is that 'pairings' and 'couples' will be used loosely to abbreviate such conditions as stated above to shorten an already elaborate discussion.

So, CCWO follows close the same patterns as Barium DPs but 2/3 of Ce^{4+}/Ce^{3+} (41/59%) ions are joined by W^{5+}/W^{6+} 'pairs' (43/57%) featuring the same 2/3 combination of 9+ phases. This would analogically form ~60% of the Ce^{3+}/W^{6+} matrix while the rest would be scattered as Ce^{4+}/W^{5+} environment. Again, not essentially well mixed or agglomerated, as PL behavior would also suggest (in future *chapter 4*). The situation complicates for the other pair in *Figure 20b* and requires some extensive commentary because of the prolific lack of W^{5+} in comparison to Ce^{3+}/Ce^{4+} content. That suggests many possible problems in the form of gaps, vacancies, or other distortions forming within the unit cell and creates an opportunity to elaborate more on the nature of XPS 4f shell build. In each picture, two sets of overlapping $4f_{7/2}$ (1 -lower energy) and $4f_{5/2}$ (2 - higher energy) spin-orbit doublets are visible – between 30 and 40 eV per sample. The lowest pair (green) is denoted to W^{4+} and usually mismatches the WO_2 reference not exceeding ±0.5 eV.[241] Another set (blue) was first thought to be W^{6+} (later colored as cyan), however, the WO_3 reference has shown that its peaks are localized much higher. After much research, the discrepancy matched other WO_{3-x} species containing some exotic W^{5+} ions.[242–245] That was a pleasant surprise considering their high instability (no pure W_2O_{10} in existence); however, compared to the other XPS-related articles showcasing materials like W_2Cl_{10} as a reference, there was at least some proof to justify the existence of such cations with some additional, future evidence. The position mismatch was also small – not bigger than ±0.2÷0.3 eV.[246,247] Next, all cyan W^{6+} signals were firm enough that their characteristics and positioning did not cause any interpretation issues. Fitting WO_3 reference perfectly, the only concern was big FWHM which suggested a lot of scattered multisites and interference from ionic mismatches scattered throughout a complicated, powderish matrix.[244,248–250] Again, the analyzed parameters are summarized in *Table 10*. Pure, metallic W (impurity detected by XRD) would also be visible here in between 31÷33 eV, just below W^{4+} doublets; however, possibly due to low (<1%) content, it was not detectable, especially if it was primarily present as scrapable WC ceramics localized on the surface of originally acquired pellets.[251–254]

Focusing solely now on Ba_2PrWO_6 (BPW) and $Sr_9Ce_2W_4O_{24}$ (SCWO) content, Pr/Ce vs. W ratios vaguely suggest the same conclusions as for BCW and CCWO regarding 8 and 9+ charge balance. However, the concentration of exotic W^{5+} ions seems to be upset – the proportions are 1/8 and 1/7, respectively, compared to their predominant W^{4+} and W^{6+} counterparts. This pronounced mismatch is so significant that it is not safe to say whether or not (18.5%) Pr^{3+}/W^{5+} (11.25%), (81.5%) Pr^{4+}/W^{4+} (88.5%) in BPW; or (39%) Ce^{4+}/W^{5+} (12.5%), with (61%) Ce^{3+}/W^{6+} (87.5%) phases in SCWO actually form. There is a distinct probability in BPW, though. Both materials would try to compensate for such distortions in some shape or form. Since, according to powder XRD, SCWO is riddled with a lot of A^{2+} half-occupied vacancies, this W^{5+} deficiency would be highly responsible for all eventual V_o holes or gaps. To some extent, this also stands true for BPW, which hosts a considerable amount of interstitial oxygen (O_i) but more about that in future EPR and optical chapters regarding charge-transfer phenomena.

Lastly, it is worth mentioning that XAS spectra of W were unavailable to provide any support since the capabilities of BL04 beamline's equipment exceeded noteworthy edges (just outside of provided energy range or due to detector limitations).

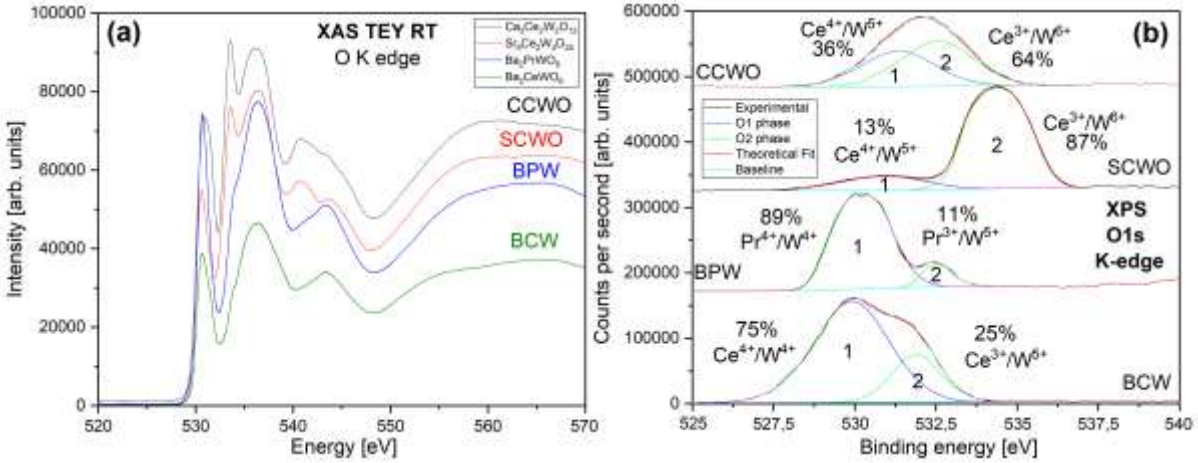

Figure 21 Convoluted oxygen K-edge XAS (a), and simple XPS O1s spectra (b) taken at ambient conditions for all tungstates to depict their actual characteristics and compare various interatomic bondings and reoccurring matrix interactions.

Figure 21 showcases data about numerous oxygen σ-π bondings present within investigated cerates/tungstates/praseodymates and oxygen interactions with the local chemical environment. Since all materials were made using all kinds of oxides, this element's shell or edge could tell us some crude but valuable information about overall interactions, polarity, vacancies, and interjections within these systems. It serves as a unique fingerprint to justify eventual material group assignment; however, many features will also naturally but inevitably repeat themselves.[255,256]

XAS K absorption edges in *Figure 21a* are more complex and, after deconvolution, tell more about the materials, so it is good to start with them. Several bands are grouped in well-defined regions and will be interpreted and compared collectively according to the literature[257–260] since precise DFT calculations without information from additional NPD measurements would be just pure guessing. All edges start with an abrupt onset at around 530 eV assigned to the antibonding π* bond. The rest peaks onward are just different σ* bonds of various origins. Second, weakly developed shoulder might appear in derivatives, more visible in SCWO and CCWO, since hybridized antibonding O2p÷B-site d-molecular orbitals might differentiate from the other, second B'-site 'pair' like RE or $W^{6/5+}$ (in CCWO ~6:4 ratio) and hypothetically $W^{5/4+}$ ions (weaker in BCW ~2:8). More critical is the 533 eV mode typical for ilmenites (significantly weaker in BCW or BPW structures). Its intensity/ratio is not so prominent even for SCWO, but, for sure, this material is more like CCWO in terms of internal structure - truly an intermittent (in between perovskite-ilmenite like) material riddled with a lot of multisites, vacancies, and defects affecting the structure via distorted A^{2+}/RE-O-W bonds via dislocated dangling (O^-) or interstitially trapped (O_i) oxygen. In derivatives, it is undoubtedly related to alkaline atom partially-substituted or half-occupied site trying to break off the current symmetry. Moderately distinguishable features at 534-538 eV seem to be simultaneously visible in all the structures. They describe interactions between A^{2+} ions, oxygen, and chosen d-block type states, i.e., 5d W-O-Sr 4s / Ba 6s or 5d/4f Ce-O-Sr 4s/ Ba 6s. However, they show little to no changes in terms of structural displacement after deconvolution. The literature does not state anything out of the ordinary in this region, but at least the lack of sharper peaks still supports partial substitution influencing local amorphization of the structure. Hybridization difference is mainly driven here by the bonding angle of the central ions controlling the bandwidth. That is why the region near 540-545 eV in core structures

of higher symmetry would show some prolific differences. According to it, alongside the peak around 533 eV, dissociating derivatives from double perovskites is more plausible. Not only does the outside appearance support this claim, but also later spectral appearance and SG changes (HT, LT) and assignment through Howard et al. research.[71,72] Shared, substituted A, and B-sites with prominent vacancies contribute to signals closer to 540 eV. Many different interactions at B-sites make those bands more distinguished; however, corner-sharing arrangements in perovskite cells also tend to have two reinforced oxygen bands visible in that region – although at slightly higher energies (at the end of the energy range mentioned above ~545 eV). It is due to highly-induced, short-range coordination associated with the formation of triply coordinated oxygen and self-achieved long-range periodicity of joined double triclusters ($2\times ABO_3$). After this, the edge creates an extensive loss feature.[261,262]

Complementary XPS spectra are depicted in *Figure 21b*. Although less detailed, all of them show two unevenly split bands telling us still enough about two types of oxygen bridges currently available - between various B-site W-O-Ce and W-O-Pr ion species in both derivatives (with predominant Ce^{3+}/W^{6+} against Ce^{4+}/W^{5+} 9+ balanced 'couples') and double perovskites (containing mainly 8+ RE^{4+}/W^{4+} vs. RE^{3+}/W^{5+} 'pairs', RE = Pr/Ce).[263–266] In BPW and BCW, the first strong band, localized at ~530 eV, is surely related to the main RE^{4+}/W^{4+} phase having ionic difference $\Delta Z=0$, hence the lowest polarization and binging energy. Formation of the second, broader band at higher positions fits more +8 ionic Re^{3+}/W^{5+} 'couple' with $\Delta Z=2$. Such disfigured shape could accommodate for the amount of proportionally stored interstitially oxygen that would not only distort the structure but also introduce more oxidized tungsten ions – mainly responsible for W^{5+} appearance, which actually also limits (the visibility of) this exotic phase by shear deficiency of that ion. That holds especially true for BPW considering future data presented at EPR vs. PL chapters. Overall, the same relations could be told for both derivatives.[267,268] Both modes relate to present RE-O-W bridges with charges balanced around 9+ BB'site total balance. Signals are localized at slightly higher energies (532-535 eV) since ΔZ also grew from 0÷2 to (Ce^{4+}/W^{5+}) 1÷3 (Ce^{3+}/W^{6+}). Major XPS signals related to W^{6+} phases probably also host oxygen related to trapped or symmetry-breaking oxygen defects (V_o) - see FWHM's, precise positions and final stoichiometric formulae in *Table 10* with insets of *Figure 21b* for reference.[269–272]

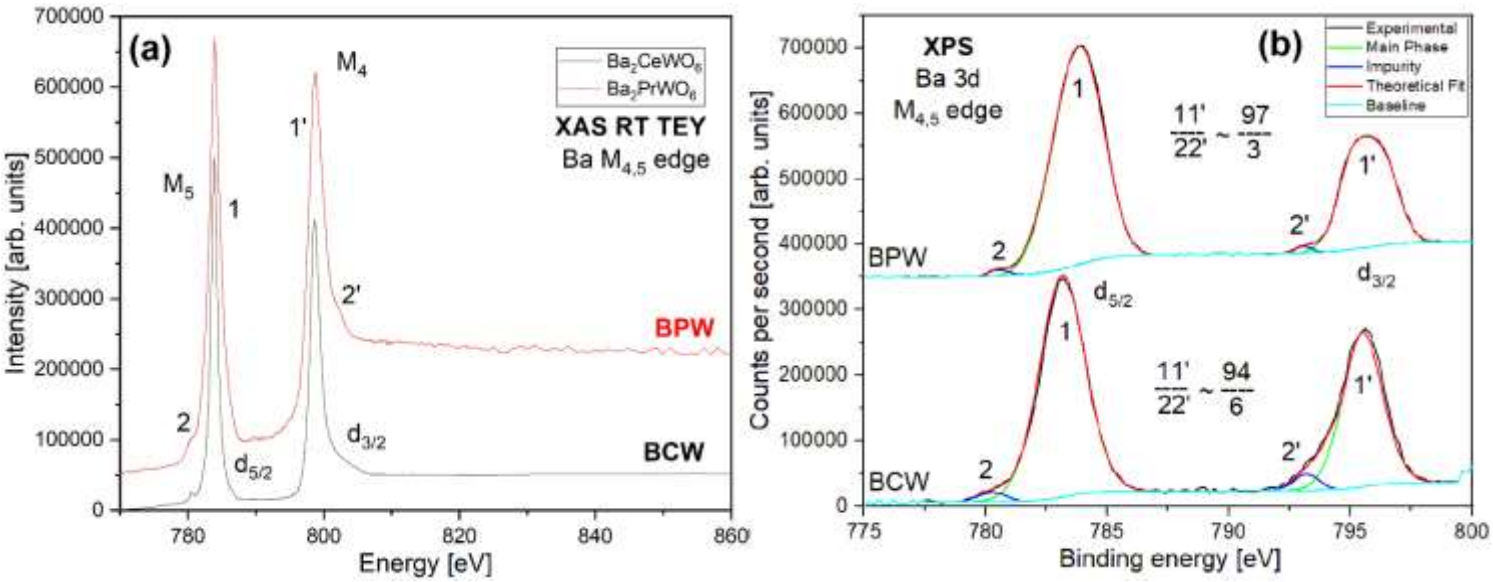

Figure 22 Barium (a) XAS M-edge, and (b) XPS 3d spectra collected at ambient conditions showcasing main (1) phase and secondary (2) phases related most likely to impurities such as BaO (in BCW) or BPWO (in BPW) in double perovskites. The strange, non-symmetric occurrence of both shoulder bands in XAS vs. XPS spectra is worth noting for yet unknown reasons.

BCW and BPW barium absorption edges with 3d shell spectra - low energy 5/2 (M_5) & 3/2 (M_4) localized higher - are presented in *Figure 22*. Both are quite straightforward in interpretation and possess one main peak, related to the primary phase, accompanied by a small shoulder designated to impurities – to BaO and $BaPr_2WO_7$ (BPWO) in BCW and BPW, respectively.[273–275] While considering their suitable match with the content of XRD diffractograms, a strange, non-symmetric occurrence of both 22' shoulder bands should be noted in XAS – *Figure 22a*. Their spectra are mirrored in contrast to typical, repeatable XPS configuration for yet unknown reasons - just like in our previous work.[183] BPW peaks are separated by subsequently ~3.3 and 2.3 eV gaps from the main peaks.[276,277] In BCW first value slightly decreased to 2.8 eV.[183] This might advocate the statement that the distorted $Ba^{(+1)}O$ suboxides trying to fully oxidize (+2) & merge into different species like BPWO or $BaCeO_{3-x}$ due to REO_{2-x} separation during synthesis. However, the main peaks do not fall much behind their referral positions by ±1.5 eV.[278,279] All read-out and calculated parameters are gathered with the rest of the XPS data in *Table 10*.

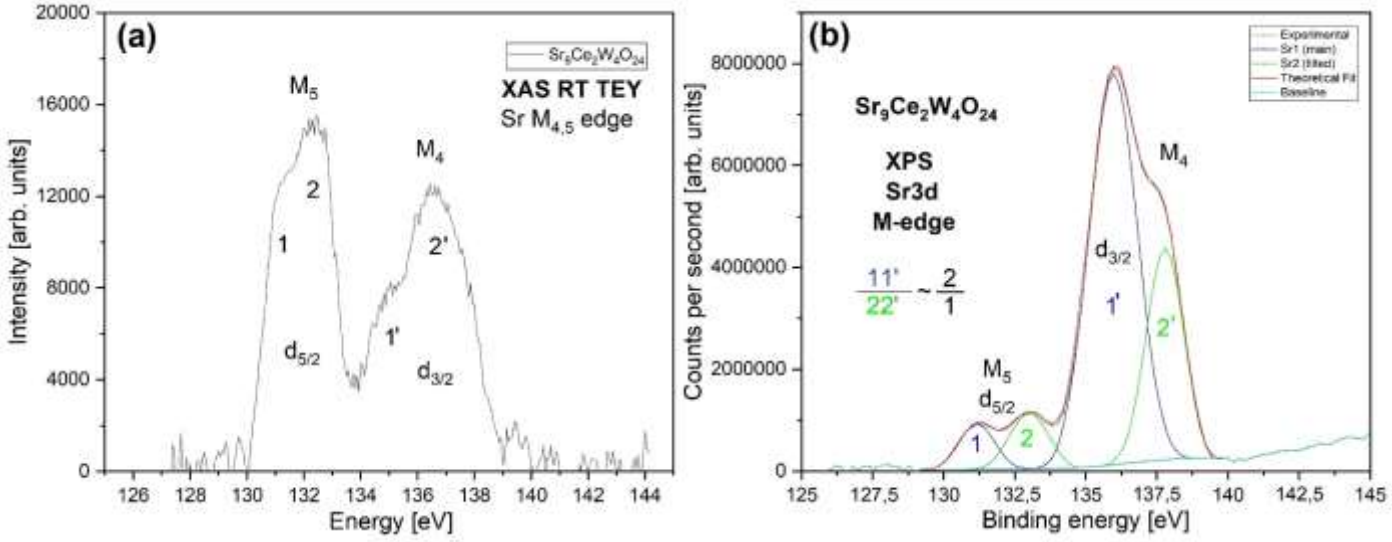

Figure 23 Strontium (a) XAS M-edge, and (b) XPS 3d-shell spectra collected at ambient conditions from SCWO quaternary perovskite featuring the main phase (1) with secondary peak (2) related most likely to symmetry breaking strontium ions escaping their regular sites towards RE positions due to prominent tilting.

Strontium $M_{4,5}$-edges in *Figure 23a* were tricky to collect on XAS due to the detector's bottom energy limit (~100eV) and high noise-to-signal ratio. However, a quick comparison was made to 3d XPS spectra in *Figure 23b*. After applying a proper baseline and filtrating off all other low-energy edges, the same set of signals was separated from the background. This means that XPS would also be more reliable than XAS, but still, based on variable intensity and noise, a strong correlation can be found between each 3d set of M_5 edges. $3d_{5/2}$ 131.2 & 133.0 eV XPS peaks are positioned analogically to M_4 ($3d_{3/2}$ 136 & 137.6 eV) bands. Compared to the referral positions, the discrepancy between registered signals is around ±1.0 eV – slightly smaller than for barium.[278,280–282] Signals' duality is also surely unrelated to impurities since SCWO had no Sr-related minor phases (only W/WC). The other possibility, supported by literature, would be defective $Sr^{(+1)}$-O bonding present due to current tilt and unit-cell packing defects caused by symmetry breakage featuring partial substitutions and prominent vacancies.[256,282,283] They are definitely noticeable quantities to report since the 11'/22' area ratio is close to 2:1. Yet, again, some strange phenomenon has been observed between XAS and XPS spectra – peaks 1,2 and 1',2' have been flipped around regarding the area and intensity ratio for a yet unknown reason -

just like in barium.[274,278,280,284] The interpretation stays the same, however. Worth adding is a comment about symmetry breakage - here, concern is the small disproportions in the overall stoichiometric formula of this quaternary perovskite which is close to 4× the standard formula of $A_2BB'O_6$.[270–272,285] Strictly speaking, $Sr_9Ce_2W_4O_{24}$ has some distinct resemblance to $Sr_8Ce_4W_4O_{24}$ which after division (by 4) would give Sr_2CeWO_6 double perovskite. The same statement concerns $Ca_3Ce_2W_2O_{12}$ below when divided by two, would give Ca_2CeWO_6 if not for the unfortunate lack of squeezed-out 1 Ca atom.[183]

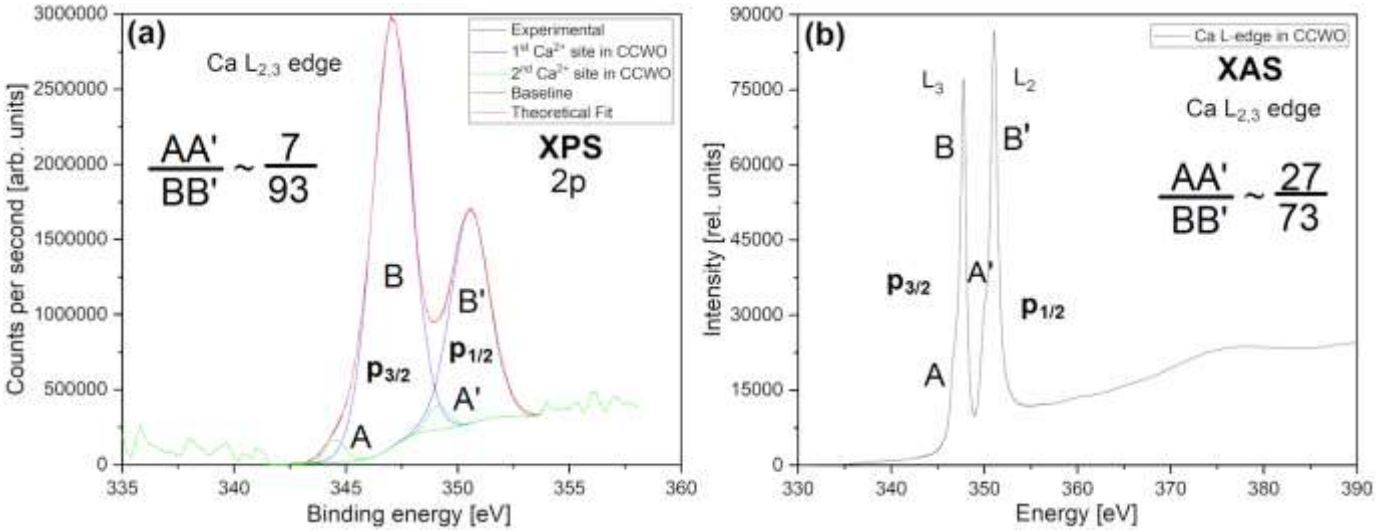

Figure 24 (a) XPS spectra of Ca $2p_{3/2}$ and $2p_{1/2}$ shell within CCWO ilmenite matrix alongside (b) XAS Ca L-edge measurements showing main symmetry-breaking interactions at room conditions and ultra-high vacuum.

Calcium $2p_{3/2}$ and $2p_{1/2}$ levels seem to correspond well to symmetrical $L_{2,3}$ edges in *Figure 24*. The only issue is the intensity/ratio discrepancy between the satellites – in XAS, the area covered by them is much bigger (27:73%) than on XPS (only 7 to 93%). Although the origin of those bands is not a mystery, their disproportionate values can cause confusion, especially knowing that none match the aforementioned Ce^{3+}/Ce^{4+} (59/41%) content – XAS is much more reliable due to deep penetration. Nevertheless, both sets should be interpreted the same way as SCWO: AA' shoulders as tilted, broken symmetry sites with $Ca^{(+1)}$-O suboxide interactions while dominating BB' bands correspond to the primary phase and its bridging RE-O-Ca-O-W bonds.[286–289] The issue here is surely not related to impurities like in barium double perovskites since the purity of CCWO is ~99% & less than 1% is related to W/WC. Worth noting is the displacement of the main XAS and XPS bands against the referral values by ±1.5 eV – this might be an issue related to calibration, but the separation between peaks and their satellites is an issue purely related to chemical interactions and their origin.[290,291] Here, shoulders are spread apart from their bigger neighbors by approximately 2 eV, which further supports $Ca^{(+1)}$-O interpretation, but the shape of the peaks (their FWHM) and their individual AA' gap reaching 4.3 eV implies high disorder and a lot of scattered multisites involved in their contribution. Generally, the gaps are more significant than in barium double perovskite edges (which are more ordered structures), so this conclusion is reasonable.[273,292]

Table 10 Summary of all crucial core level information experimentally investigated on XPS: their content, characteristics, and stoichiometric formulae based on total atomic ratios for both BCW & BPW double perovskites (normalized to W); and the other two SCWO & CCWO derivatives (normalized to Ce).

Material	Core level	s-o split	Position [eV]	FWHM [eV]	Total Atom [%]	Fraction
BCW	W4f	7/2	33.4 ; 34.4	1.65 ; 0.86	8.96	1
		5/2	35.4 ; 36.4	1.13 ; 0.88		
	O1s	---	529.9 ; 531.8	1.78 ; 2.68	61.01	6.81
	Ba3d	5/2	780.4 ; 783.2	2.21 ; 1.47	19.46	2.17
		3/2	793.2 ; 795.5	1.16 ; 1.88		
	Ce3d	5/2	880.6;883.1 886;2;889.6;896.0	1.08;2.20 2.56;3.64;1.03	10.57	1.18
		3/2	898.6;900.8 904.0;906.6;917.3	1.91;2.63 2.31;3.09;2.51		
BPW	W4f	7/2	33.1 ; 34.6	1.76 ; 0.62	8.69	1
		5/2	35.4 ; 36.9	1.89 ; 1.13		
	O1s	---	530.2 ; 532.6	2.47 ; 1.05	62.95	7.24
	Ba3d	5/2	780.5 ; 783.9	0.89 ; 2.41	18.15	2.09
		3/2	793.4 ; 795.7	0.79 ; 3.04		
	Pr3d	5/2	928.8;930.5;933.6 936.2;947.5	1.32;1.73;1.04 1.61;2.91	10.21	1.17
		3/2	949.9;952.4;954.4 957.0; 964.8	1.26;1.78;0.98 1.52;1.42		
SCWO	W4f	7/2	34.7 ; 36.5	1.47 ; 1.89	9.49	3.82
		5/2	37.3 ; 38.5	0.90 ; 1.25		
	Sr3d	5/2	131.2 ; 133.0	1.45 ; 1.60	22.91	9.22
		3/2	136.0 ; 137.6	1.98 ; 1.55		
	O1s	---	531.0 ; 534.4	3.03 ; 3.01	62.63	25.20
	Ce3d	5/2	880.4;882.7;885.1 887.8;896.4	2.28;1.39;2.52 1.68;1.80	4.97	2
		3/2	899.5;901.6;904.6 907.8;917.2	2.15;1.72;2.18 1.62;1.92		
CCWO	W4f	7/2	34.6 ; 36.4	1.27 ; 1.96	9.56	1.92
		5/2	36.5 ; 38.1	1.39 ; 1.76		
	Ca2p	3/2	345.8 ; 347.2	1.23 ; 2.00	15.56	3.12
		1/2	349.2 ; 350.7	1.03 ; 1.94		
	O1s	---	531.4 ; 532.6	1.59 ; 2.60	64.92	13.04
	Ce3d	5/2	880.5;883.4 885.8;889.0;896.8	3.53;3.66 2.26;2.85;3.17	9.96	2
		3/2	899.8;901.8;904.8 907.6;916.4	3.22;3.72;3.02 3.07;2.84		

After extensive data gathering and qualitative analysis of provided atomic shells and edges, one can pursue quantitative calculations based on *Table 10* to estimate the actual stoichiometric proportions of all our compounds and confront them with references from the XRD database. It is a well-known fact that there are always some discrepancies between ideal, isostructural formula, and realistic composition, but the proper ratios need to be

established in order to: push the overall work onward; evaluate the product quality, arrangement, and mineral assignment; check for eventual mishaps and plan optimizing procedures for future reference. So in the case of barium double perovskites, both rare-earth tungstates were normalized to their respective d-block tungsten. The idea is to always choose a central, most crucial ion or an atom closest to the least common multiple. In that case, both criteria fit W, so the total atomic ratios calculated from XPS spectra turned out to be $Ba_{2.17}Ce_{1.18}WO_{6.81}$ and $Ba_{2.09}Pr_{1.17}WO_{7.24}$ in comparison to idealistic Ba_2CeWO_6 (BCW) and Ba_2PrWO_6 (BPW). These values are not far from the goal considering slow WO_2 evaporation (amended by ~2% surplus of the substrate). There is undoubtedly more Ba due to BaO and BPWO impurities involved in messing around the perfect deconvolution alongside REO_{2-x} species. If gathered together, they could support the case of creating distorted (single) perovskites like $Ba_{0.17}Ce_{0.09}O_{0.51}$, but that is just a long shot. The remaining CeO_{2-x} and Pr_2O_3 phases would still exist. More critical is the surplus of oxygen, which signifies a possibility of interstitial oxygen traps and vacancies that could be responsible for slight oxidation experienced with $W^{4+} \rightarrow W^{5/6+}$ during synthesis despite using inert Ar gas (with a slight addition of 1-5‰ of H_2). This will influence band gaps, future PL measurements, and energy transfer properties if not attended to.

Derivatives also have more oxygen - not only ideal but in absolute configuration. Since they have more W in their configuration (SCWO ~4), the least common multiple for jointly present ions would be 2. for Cerium, so that was the chosen basis of multiplication and division. As can be deduced from the lower half of *Table 10*, $Sr_9Ce_2W_4O_{24}$ (SCWO) turned out to be $Sr_{9.22}Ce_2W_{3.82}O_{25.2}$ and $Ca_3Ce_2W_2O_{12}$ (CCWO) ~ $Ca_{3.12}Ce_2W_{1.92}O_{13.04}$. Tungsten deficiency has been noted (for the reasons already stated before). The only difference would be Ca and Sr, which surplus could not be accommodated by any impurities. Their abundance would presumably influence symmetry-breaking interactions and the eventual occurrence of vacancies/half-occupied sites by tilting those giant, densely-packed unit cells.[256,269–272,285]

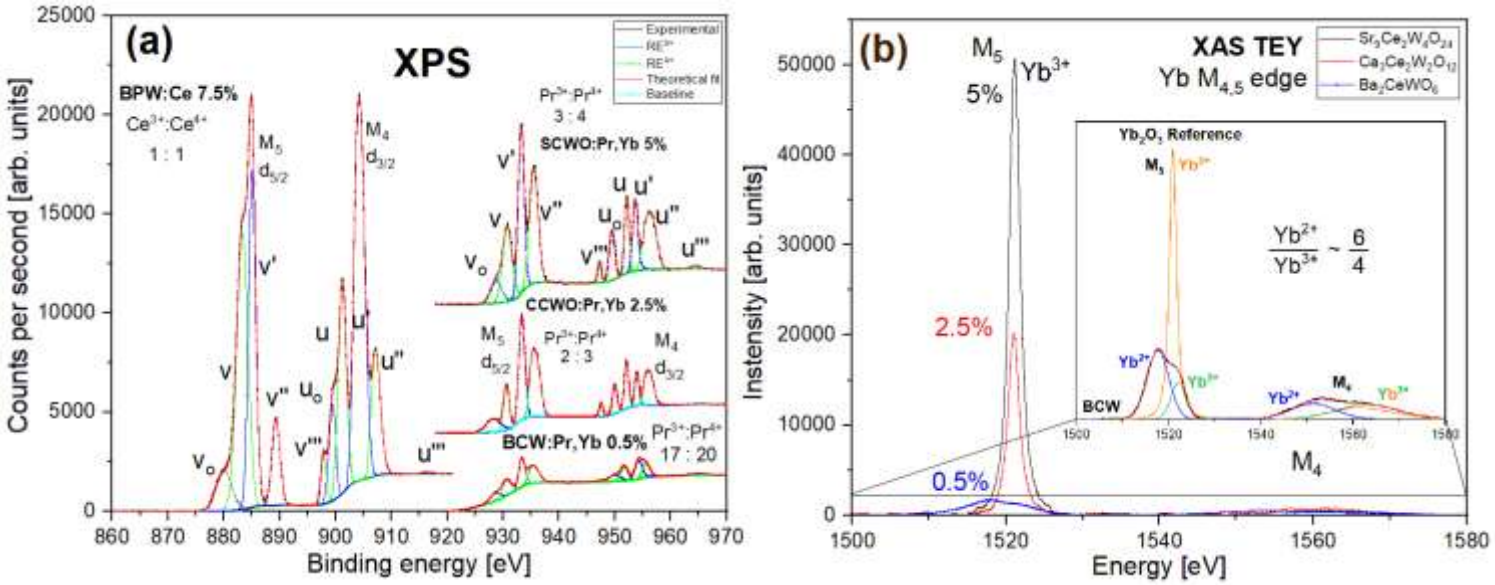

Figure 25 Room temperature X-ray spectra for all doped materials with selectively chosen RE ions: (a) XPS focuses on Ce/Pr 3d shell, while (b) XAS on Yb. Insets provide additional data about content features such as deconvoluted peaks or eventual ratios compared to some RE-oxide references.

A brief comment should be made on the dopants since, till now, all discussion focused solely on pure matrices. Firstly, they were doped evenly, so every stated percentage amounts concern all cations separately but equally. Secondly, both graphs in *Figure 25* are crucial in determining the factual content of PL-active dopant concentration after introducing them to the matrices. Chosen amounts of RE^{3+} cations substituted other RE oxides in various degrees since they possess unstable nature and usually are mixed with some other, differently charged atoms.[169,171,195,196,199,200,292] That is why the true values of excitable centers are always lower than expected - it is good to account for that loss or just accept the benefit of lower PL quenching factors. Thirdly, the quantitative assessment of such phenomena might help in predicting future emission and (Ce,Pr NUV sensitizers →NIR Yb activators) energy transfer properties, not to mention damage control (eventual influence from defects).[293–298] Such research data from neighboring edges of: (a) energy emitters like Pr doped cerates or Ce-hosting praseodymates; [220–231,240,299] and (b) energy-accepting Yb ions,[300,301] were gathered in *Table 11* below. Fourthly, the interpretation is consistent and follows the analysis & conclusions presented previously for constituent Pr/Ce ions.

Table 11 XPS deconvolution data sampling actual content of PL-active RE dopants stored within investigated phosphors previously mentioned in *Figure 25*.

Abbreviation	**Ideally planned stoichiometric formula**	**Total percentage of each introduced dopant [%]**	**Sensitizer ratio $(Ce/Pr)^{3+}$ / $(Ce/Pr)^{4+}$**	**Real sensitizer RE^{3+} content [%]**	**Activator Yb^{2+} / Yb^{3+} ratio**	**Real activator Yb^{3+} content [%]**
BCW:Pr,Yb	$Ba_2Ce_{0.99}Pr_{0.005}Yb_{0.005}O_6$	0.5	17:20	0.23	6:4	0.20
CCWO:Pr,Yb	$Ca_3Ce_{1.9}Pr_{0.05}Yb_{0.05}W_2O_{12}$	2.5	2:3	1.00	0:1	5.00
SCWO:Pr,Yb	$Sr_9Ce_{1.8}Pr_{0.1}Yb_{0.1}W_4O_{24}$	5.0	3:4	2.14	0:1	2.50
BPW:Ce	$Ba_2Pr_{0.925}Ce_{0.075}WO_6$	7.5	1:1	3.75	---	---

An unusual disproportion was noticed for Yb. Just like W^{5+}, a less common ion in the form of Yb^{2+} was found in BCW. Unintentionally and unbeknownst to researchers who just added Yb_2O_3 (presented in the inset of *Figure 25b*), this discovery was surprisingly intriguing. The origin is probably the same as the appearance of W^{5+}, but here some unintentional charge transfer must have occurred between B-site or maybe partially from evacuated O^{2-} ions during SSR creating residual, interstitial oxygen while kept in $Ar:H_2$ atmosphere. It gives an unprecedented opportunity to look into this nontrivially charged element; however, Yb^{3+} is an ion with which we will be most invested since the goal was to create an efficient downconverter emitting white light or NIR radiation. Furthermore, unfortunately, Yb^{2+} has [XE] $4f^{14}$ $6s^2$ electron configuration, which is optically inactive.[302–305] This means that we will eventually try to switch it back to Yb^{3+} (through HT annealing or light-induced reverse charge transfer) to improve the odds of emission by increasing the receiver's concentration, thus improving the photon's absorption cross-section.[3,163,306,307]

2.4 Raman and FTIR spectroscopy

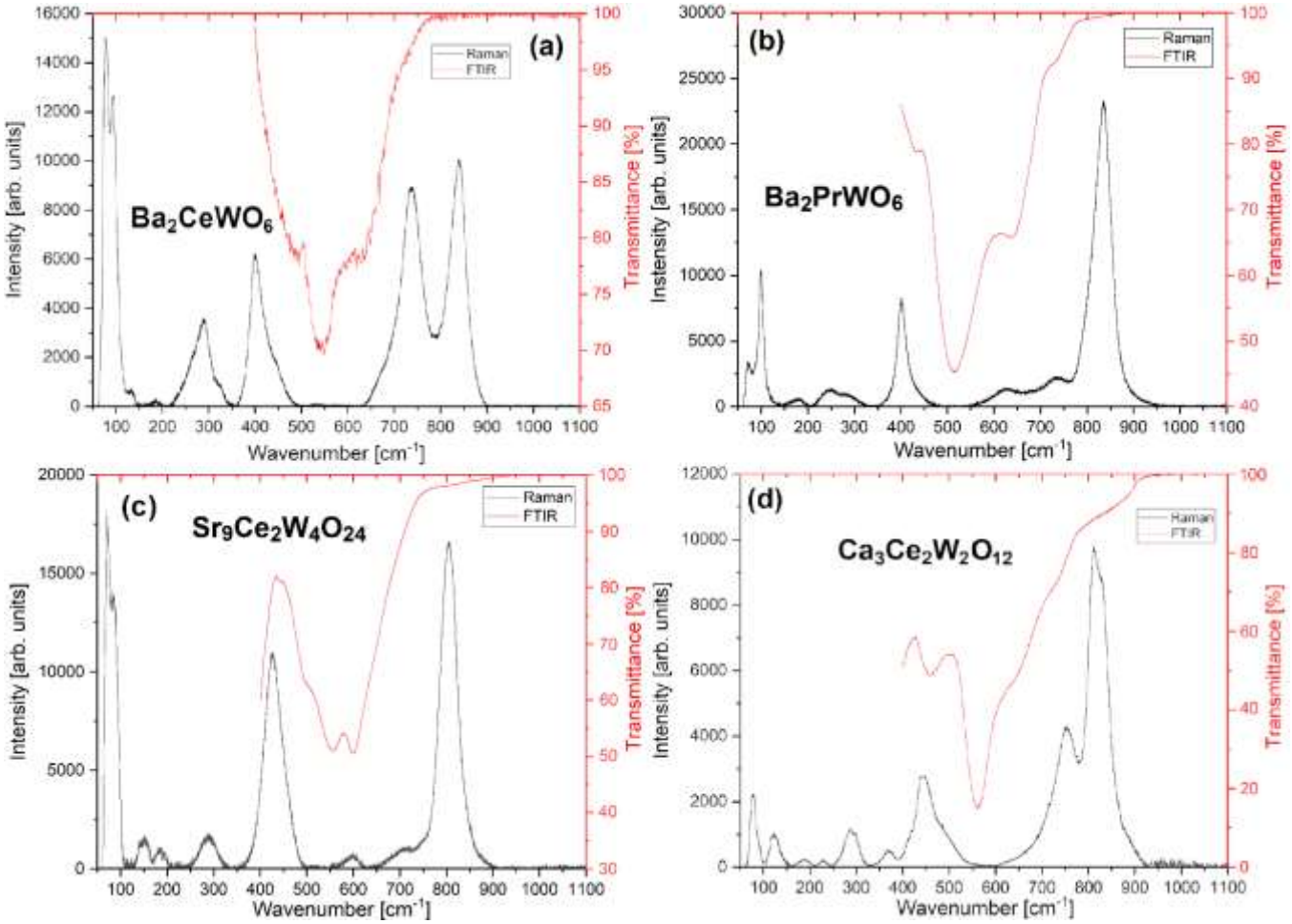

Figure 26 Joined Raman (down-black) and FTIR (up-red) spectra of undoped (a) BCW, (b) BPW double perovskites, and two other (c) SCWO, (d) CCWO derivatives. Data were collected at ambient room conditions in the region of interest - no additional signals were detected between 1100 cm^{-1} and 4000 cm^{-1}.

Techniques such as FTIR and (more importantly) Raman spectroscopies were involved in clearing up any doubts originating from XRD SG selection. Knowing their complementary factor in analysis through group theory calculations, one could support crystallographical findings by matching the number of currently visible modes to assigned phases in various conditions (ambient vs. HP, HT, LT changes). However, a fundamental base must be established to evaluate a well-described fingerprint region for upcoming polymorphism studies. Sometimes this is enough to clear any initial discrepancies (unfortunately, not here).

Based solely on XRD data, a preemptive selection of SG has been made in *section 2.2*. More ordered BCW and BPW double perovskites were assigned to slightly tilted cuboid (monoclinic β angle) *I*2/*m*. Derivatives like SCWO quaternary perovskite and CCWO ilmenite to $I4_1/a$ and *R*-3*c,* respectively. The results of group theory calculations for these choices are presented in *Table 12*. Factors for alternatives like *R*-3 (BCW, BPW), *Fm*-3*m* (SCWO), and *R*3*c* (CCWO) were gathered in supplementary *Table A3*. Together, all the data can be confronted with the experimental results shown in *Figure 26*.

Table 12 Factor group analysis for all mainly chosen space groups of discussed tungstates.

Material (SG)	Ion	Wyckoff Positions	Point Symmetry	Red. Representation
BCW **BPW** ***I2/m*** ***(C_{2h})***	A^{2+} (Ba)	4i	C_s	$2A_{1g}+A_u+B_g+2B_u$
	$B^{3+/4+}$ (Ce/Pr)	2a	C_{2h}	A_u+2B_u
	$B'^{4+/5+}$ (W)	2d	C_{2h}	A_u+2B_u
	O_1^{2-}	4i	C_s	$2A_{1g}+A_u+B_g+2B_u$
	O_2^{2-}	8j	C_1	$3A_{1g}+3A_u+3B_g+3B_u$
$\Gamma_{TOTAL} = 7A_{1g}+7A_u+5B_g+11B_u$; $\Gamma_{ACUSTIC} = A_u+2B_u$; $\Gamma_{IR} = 6A_u+9B_u$; $\Gamma_{Raman} = 7A_{1g}+5B_g$				
SCWO ***$I4_1/a$*** ***(C_{4h})***	A^{2+} (Sr)	8e, 16f	C_2, C_1	$4A_g+4A_u+4B_g+5^1E_g+5^1E_u+5^2E_g+5^2E_u$
	$B^{3/4+}$ (Ce)	8e, 16f	C_2, C_1	$4A_g+4A_u+4B_g+5^1E_g+5^1E_u+5^2E_g+5^2E_u$
	$B'^{6/5+}$ (W)	8c, 8d	C_i	$6A_u+6^1E_u+6^2E_u$
	O^{2-}	16f	C_1	$3A_g+3A_u+3B_g+3^1E_g+3^1E_u+3^2E_g+3^2E_u$
$\Gamma_{TOTAL} = 11A_g+17A_u+11B_g+13^1E_g+19^1E_u+13^2E_g+19^2E_u$; $\Gamma_{ACUSTIC} = A_u+^1E_u+^2E_u$; $\Gamma_{IR} = 16A_u+18^1E_u+18^2E_u$; $\Gamma_{Raman} = 11A_g+11B_g+13^1E_g+13^2E_g$				
CCWO ***R-3c*** ***($D3_d$)***	A^{2+} (Ca)	2a, 4c, 12f	C_1, C_3, D_3	$4A_{1g}+5A_{2u}+9E_u+9E_g$
	$B^{3/4+}$ (Ce)	4c, 12f	C_1, C_3	$4A_{1g}+4A_{2u}+8E_u+8E_g$
	$B'^{6/5+}$ (W)	6e, 4c, 2b	C_2, C_3, C_{3i},	$2A_{1g}+4A_{2u}+7E_u+5E_g$
	O^{2-}	12f	C_1	$3A_{1g}+3A_{2u}+6E_u+6E_g$
$\Gamma_{TOTAL} = 13A_{1g}+28E_g+16A_{2u}+30E_u$; $\Gamma_{ACUSTIC} = A_{2u}+E_u$; $\Gamma_{IR} = 15A_{2u}+29E_u$; $\Gamma_{Raman} = 13A_{1g}+28E_g$				

Unfortunately, both barium double perovskites have space groups hosting coincidentally the same number of modes for Raman – 12 (*I2/m* $7A_{1g}+5B_g$ or $4A_g+4^1E_g+4^2E_g$ for *R*-3). Furthermore, even if a befitting number of peaks was an issue (usually +2÷4 more counting the defects and probable impurities), all spectra seem eerily identical considering shape and form. Even comparing with derivatives bearing many different stoichiometric formulae. FWHM is considerably large, ~36÷50 cm^{-1} wide. Those problematic similarities could be attributed to various disordered $(Ce,Pr)^{3/4+}/W^{4/5/6+}$ ion 'pairings' manifesting themselves in indigenous multisites – different charges, V_o defects, scattered throughout the matrix contributing to a specific stretch or bending. All materials harbor some kind of BB'-site ionic balance – BPW & BCW 8+, SCWO, and CCWO 9+. Keeping this order in mind, careful theoretical interpretation denoted with unique modal characteristics were gathered in *Tables 13 & 14* with support from the literature.[308–313]

Table 13 Conjoined experimental Raman data collected at ambient conditions with literature-verified phonon assignments emphasizing observable differences and similarities for both BCW and BPW double perovskites.[308–313] Asterisks mark modes that could also be associated with REO_{2-x} impurities according to previous XRD results & some theoretical energy-scattering calculations.[321,324]

Wavenumber ω_0 [cm^{-1}]		*Signal assignment & Characteristics*	
Ba_2CeWO_6	**Ba_2PrWO_6**		
78.6	72.2	BaO_6 multisite complex lattice deformations at A-sites of mixed B_g and $^1E_g/^2E_g$ origin signifying disorder & divergence from a perfect cuboid structure.	BCW s, sh BPW mw, sh, left shoulder
96.5	99.5		BCW s, sh BPW m, sh
134,1	163.1		BCW w, sh. right shoulder BPW w, br
182.8	179.8		BCW w, br BPW w, br
231.2	247.4	In-plane σ_ρ & out-of-plane σ_τ bending in REO_6 and WO_6 clusters of mixed B_g and $^1E_g/^2E_g$ origin between shared and not shared B-sites of various 3/4/5+ charges. *possible REO_{2-x} O^{2-} vacancy (V_o) interference	BCW, w, sh, left shoulder BPW mw, br
267.0*	---		mw, sh, left shoulder
288.3	280.0		BCW m, sh BPW mw, br
320.3	315.7		BCW mw, sh, right shoulder BPW w, br
---	367.1	In-plane σ_{sc} & out-of-plane σ_ω bending in REO_6 and WO_6 clusters of mixed B_g And ^1E_g origin between shared and not shared B-site cations of various charges.	BPW w, br, left shoulder
400.1	401.2		BCW m, sh BPW m, sh
441.9	434.8		BCW mw, sh, right shoulder BPW mw, sh, left shoulder
459.9	458.2	Distorted impurity of v_{sym} REO_2, (F_{2g})	mw, sh, right shoulder
532.5*	564.4*	Transverse REO_6 and WO_6 motion of mixed A_{1g}, and A_g character between shared and not shared B-sites of cations having different charge / *REO_{2-x} complex lattice V_o distortions (RE^{3+}:RE^{4+})O_7.	w, br
576*	625.8*		BCW w, br BPW mw, br
667.2	678.7		BCW mw, sh, left shoulder BPW mw, br, left shoulder
733.5	734.5		BCW s, sh BPW mw, br
814.5	791.3	v_{asym} & v_{sym} stretches of REO_6 & WO_6 clusters of A_{1g} and A_g for various Wyckoff sites not only partially occupied but also hosting B-site RE/W ions bearing different charges.	BCW m, sh, left shoulder BPW m, sh, left shoulder
838.9	835.1		BCW s, sh BPW s, sh
---	851.6		BPW s, sh, right shoulder

w-weak; m-medium; s-strong; sh-sharp; br-broad; v_{sym} – symmetric stretching; v_{asym} – asymmetric stretching; σ_{sc} – scissoring deformation; σ_ω – wagging deformation; σ_τ – twisting deformation; σ_ρ – rocking deformation; V_o – oxygen vacancy; RE – neighboring rare-earth (Pr/Ce) oxide clusters

As for derivatives, they both have way too few peaks to be simply assigned to either phase: SCWO tetragonal group has 48 (A_g+B_g+^1E_g+^2E_g) modes in total while cubic 25 (A_{1g}+E_g+T_{2g}). The difference is less severe for the latter group (by 8 than 31), yet still, it does not explicitly clarify anything about the other SG. Accounting for all the strontium-exclusive sites being half-occupied or others riddled with vacancies after partial substitution with $Ce^{3/4+}$, that maybe should not surprise. This statement is also true for CCWO, where more suitable noncentrosymmetric SG hosting 21 (A_1+E) peaks is pointed against the chosen *R*-3*c* with 41 (A_{1g}+E_g) modes. Without NPD measurements, only polymorphism measurements outside of ambient conditions could help.[71,72]

Table 14 Conjoined experimental Raman data collected at ambient conditions with literature-verified phonon assignments emphasizing both observable differences and similarities in SCWO and CCWO perovskite derivatives.[308–313]

Wavenumber ω_0 [cm^{-1}]		*Signal assignment & Characteristics*	
$Sr_9Ce_2W_4O_{24}$	**$Ca_3Ce_2W_2O_{12}$**		
71.1	81.3	CaO_6 & SrO_6 multisite complex lattice deformations at A-site of mixed B_g/E_g origin signifying disorder & divergence from a perfect cuboid structure.	SCWO s, sh CCWO m,sh
85.0	92.4		SCWO s, sh, right shoulder CCWO mw, sh
141.5	123.5		SCWO w, sh, left shoulder CCWO mw, sh
150.9	---		SCWO mw, br
186.5	186.3		SCWO w, br CCWO w, br
---	228.3	In-plane σ_ρ & out-of-plane σ_τ bending in CeO_6 and WO_6 clusters of mixed B_g/E_g origin between shared and not shared B-sites of various 3/4/5/6+ charges.	w, br
---	261.7		w, br, right shoulder
289.3	288.6		SCWO mw, br CCWO mw, sh
---	297.7		mw, sh
391.3	370.8	In-plane σ_{sc} & out-of-plane σ_ω bending in CeO_6 and WO_6 clusters of mixed B_g/E_g origin between shared and not shared B-site cations of various charges.	SCWO mw, sh, left shoulder CCWO mw, sh
411.4	414.5		SCWO m, sh, left shoulder CCWO mw, sh, left shoulder
426.0	445		SCWO m, sh CCWO m, sh
---	499.3	Transverse CeO_6 and WO_6 motion of mixed A_{1g}/E_g character between shared and not shared B-sites of cations having different charges.	mw, sh, right shoulder
557.6	---		w, br, left shoulder
598.7	626.7		SCWO w, br CCWO w. br, right shoulder
710.9	710.8		SCWO mw, br CCWO mw, sh, left shoulder
749.2	753.2	ν_{asym} & ν_{sym} stretches of CeO_6 & WO_6 clusters of A_1 and A_{1g} for various Wyckoff sites not only partially occupied but also hosting B-site RE/W ions bearing different charges.	SCWO mw, sh, left shoulder CCWO m, sh
784.7	812.8		SCWO m, sh, left shoulder CCWO s, sh
805.6	828.3		SCWO s, sh CCWO s, sh
844.2	888.1		SCWO mw, br, right shoulder CCWO mw, sh, right shoulder

w-weak; m-medium; s-strong; sh-sharp; br-broad; ν_{sym} – symmetric stretching; ν_{asym} – asymmetric stretching; σ_{sc} – scissoring deformation; σ_ω – wagging deformation; σ_τ – twisting deformation; σ_ρ – rocking deformation;

FTIR did not provide much support either, given it showed not only that the signals were much broader (+64 cm^{-1}) FWHM but also that many of the B_u/E_u modes were cut off below 400 cm^{-1} limit (considering filters and air interference). Data in a similarly ordered fashion is presented in *Table 15,* giving interpretation support from the literature.[313–319]

Table 15 Conjoined experimental data and literature phonon assignment collected at ambient conditions using confocal, reflective FTIR spectroscopy for all investigated compounds to emphasize observable differences and similarities.[313–319]

Wavenumber ω_0 [cm^{-1}]				*Characteristics*	*Assignment*
BCW	**BPW**	**SCWO**	**CCWO**		
	435	445	459	m, sh, left shoulder	In- and out-of-plane bending WO_6 bands and partially substituted REO_6 clusters of $E_u/^2E_u$ origin down to 100 cm^{-1}
476		497		m, sh, left shoulder	
554	514.5	554	560	s, sh	ν_{sym} stretch of both WO_6, and partially substituted REO_6 clusters of A_u/A_{2u} origin.
		599		s, sh	
632	639	648.5		m, sh, right shoulder	
	731.5	797	722	mw, sh, right shoulder	ν_{asym} stretch of both WO_6, and partially substituted REO_6 clusters of A_u/A_{2u} origin.
	834	874	855	w, br	

w-weak; m-medium; s-strong; sh-sharp; br-broad; ν_{sym} – symmetric stretching; ν_{asym} – asymmetric stretching; RE – neighboring rare-earth (Pr/Ce) oxide clusters

Worth mentioning are a few peaks of debatable origin or modes clearly related to impurities, such as not-negligible shoulder present at ~460 cm^{-1} in most double perovskites. That band is often denoted as stretching mode F_{2g} of fully oxidized CeO_2.[320,321] Assuming PrO_2 would be slightly heavier, appearance should follow shortly after at lower wavenumbers. Another sight to monitor is a weak set of broad peaks occasionally appearing near 550 - 600cm^{-1} – visible as hashtags in zoomed insets alongside other remarked peaks in *Figure A11*. Some articles refer collectively to them as deficient CeO_{2-x} V_o modes where $0<x<0.5$ could cause additional lattice deformations around 230÷250 cm^{-1}.[321–324] Here, most likely PrO_{2-x} analogs of Ce_7O_{12} or Ce_3O_5 like Pr_3O_5 or Pr_6O_{11} could also occur.[325–327] This supports the statement that Raman spectroscopy is truly a surface-based analytic tool (together with XRD diffractograms and manual examination of pellets confirm REO_{2-x} influence), but the contribution from the actual structure could not be fully discarded here. The appearance of those modes could account for the same differently-charged Pr/Ce-O-W/Ba bridges forming inside the rich-in-defects lattice.[183] At this point, only further HP & LT Raman studies could tell. Finally, one should critically avoid $BaWO_4$ easily emerging from the matrix if an excessive amount of oxygen (atmospheric or interstitial) is present (marked as asterisks in *Figure A11a*). Not only does this tungstate have very strong scattering signals, but it also has prominent PL as a scintillator promoting by its quantum efficiency false results covering the true, more subtle ones from the originally developed matrices.[2,202,203,328]

3. Pressure and temperature studies of polymorphism and stability

3.1 Raman pressure vs. temperature dependencies

In search of possible (indirect) SG confirmation via the eventual track of phase-transitions at various conditions, as documented in the vast perovskite literature,[37,71,72] an approach was taken to investigate polymorphism using all on-sight available assets. Given the limitations of accessible techniques (XRD, XPS), more detailed results could be obtained with the use of European synchrotron beamlines (like HP, LT XRD & NPD - they would help to assess not only the nature of eventual changes but also establish a set of bulk moduli with respectable Grüneisen parameters)[329–332] the only resort left was to use the technique that our scientific team specialized in – Raman spectroscopy incorporating cryostats and DAC. Sparked out of curiosity, this first small research out of RT boundaries led to an extensive investigation elaborating on the unusual behaviorism of the samples conjuring more non-trivial questions with time (about stability and sensory capabilities featuring charge transfer, oxidization, and photobleaching phenomena) which will be answered at the conclusions after all the evidence presented in this (*section 3*) in upcoming (*section 4*) chapters.

Starting from HP, all samples were submerged in quasi hydrostatic Ar PTM, creating soft, butter-like jelly when compressed under nitrogen-level temperatures up to ~15 GPa.[333,334] Together with all surrounding air and moisture, a mild interference in the form of weak but sharp signals could be seen in the range up to 140 cm^{-1} – see supplemental *Figure A12* for reference. Those modes do not shift or change their intensity during the experiment and are usually easily distinguished and filtered out by the software if visible.[335,336] That is because they usually are swallowed by good scattering responses from the investigated materials. The initial goal was to reach at least 20 GPa – at that point, 0.45 mm diamonds would withstand the pressure with inert Ar inside without risk of breaking, and the samples would probably not be exploited above that threshold. Other, more compressible, and hydrostatic PTMs like oils and alcohol mixtures affect double perovskite structures to some degree (intercalar amorphization), so this option was omitted until absolutely necessary.[337,338]

Barium double perovskites were the first to be investigated. Their compression and decompression cascades are presented in *Figure 27*. As arrows guide the eye, nothing remarkable happens – typical slow red-shift of the bands (previously registered and categorized at RT in *Figure 26ab* & *Table 13*) is observed at various rates with gradual amorphization, but no phase transition occurs.[339,340] Some of them are so weak they fade and reappear spontaneously in the spectra – that concerns, especially those debatable ones related to CeO_{2-x} defects (featured in *Figure A11*).[323–326] Wavenumber vs. pressure dependencies and all accountable coefficients are presented for BCW & BPW in *Figure 28* and *Table 16,* respectively. *Fm*-3*m* SG would transform several times by now (up to 20 GPa) compared to *I*2/*m* or *R*-3, the monoclinic tilt would be unquestionably apparent.[37,71,72,341–343] Higher transition thresholds could not be disqualified for the other two; however,[344–346] both materials seem quite stable in these conditions as hysteresis during release is not higher than 2 GPa.[183] Nevertheless, the experiments must have been halted at some point since, as predicted, the Ni750 gasket would not withstand such elevated pressures – average deformations from the original indentation state can be viewed in appendix *Figure A13*.

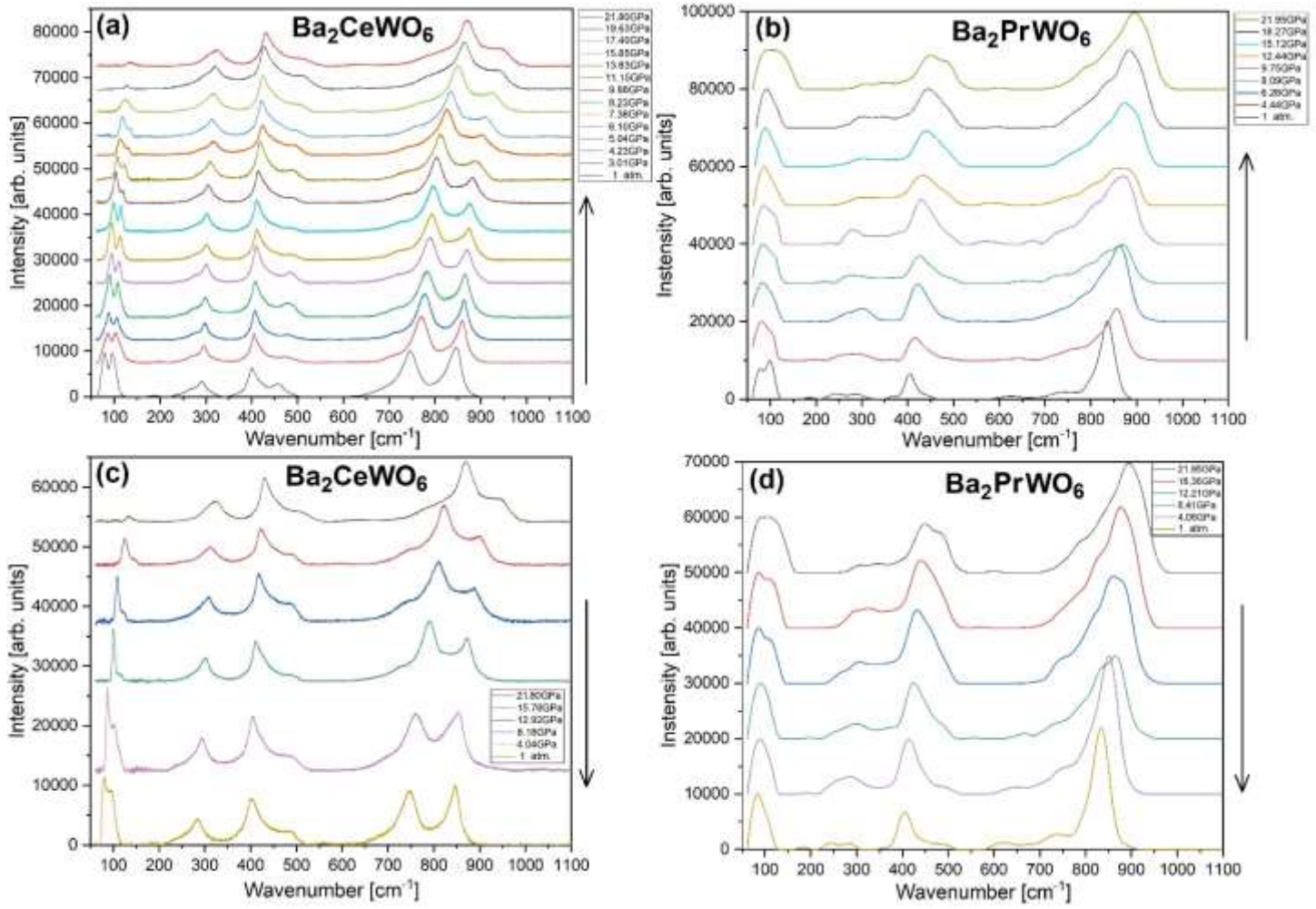

Figure 27 Raman spectra collected under hydrostatic argon PTM while using consecutive compression (top) − decompression (bottom) cycles for barium double perovskites BCW (left), and BPW (right). Arrows guide the eye. Despite apparent, slow amorphization accompanied by red-shifting peaks no phase transitions were denoted.

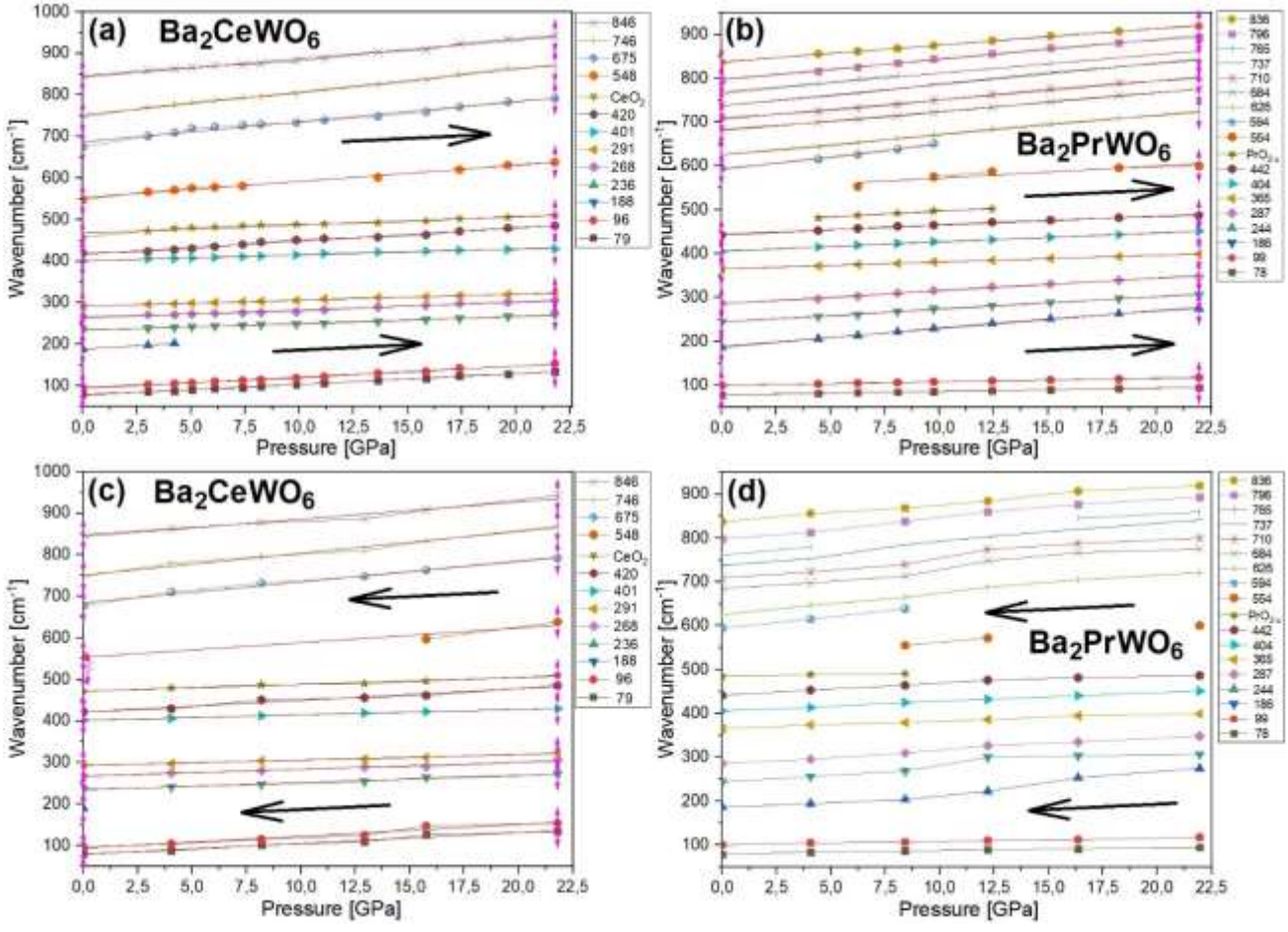

Figure 28 Raman peak position vs. pressure relations for double perovskite modes showcased in previous *Figure 27*. Presented similarly, compression is shown on the top, while decompression dependencies are on the bottom. BCW to the left, BPW to the right. Inserted right and left arrows guide the eye. Pink anchors mark the areas of linear fits. Error bars are too small to be legible.

Table 16 Room temperature wavenumbers vs. pressure coefficients of Raman lines presented previously in Figure 28 compression cycles for both BCW and BPW double perovskites.

Ba_2CeWO_6			**Ba_2PrWO_6**		
ω_0 [cm^{-1}]	$d\omega/dP$ [cm^{-1}/GPa]	R^2	ω_0 [cm^{-1}]	$d\omega/dP$ [cm^{-1}/GPa]	R^2
79	2.57 ± 0.04	0.99	78	0.76 ± 0.01	0.99
96	2.66 ± 0.07	0.99	99	0.82 ± 0.01	0.99
188	3.27 ± 0.17	0.99	186	4.08 ± 0.09	0.99
236	1.65 ± 0.05	0.98	244	2.89 ± 0.06	0.99
268	1.87 ± 0.10	0.96	287	2.91 ± 0.09	0.99
291	1.45 ± 0.03	0.99			
			365	1.55 ± 0.02	0.99
401	1.40 ± 0.05	0.98	404	2.07 ± 0.04	0.99
420	3.15 ± 0.11	0.98	442	2.06 ± 0.08	0.98
548	3.90 ± 0.13	0.99	554	2.77 ± 0.61	0.83
			594	5.74 ± 0.40	0.98
			626	4.52 ± 0.13	0.99
675	4.82 ± 0.22	0.97	684	4.30 ± 0.09	0.99
			710	4.35 ± 0.12	0.99
746	5.52 ± 0.14	0.99	737	4.86 ± 0.10	0.99
			765	4.26 ± 0.21	0.98
			796	4.54 ± 0.12	0.99
846	4.45 ± 0.16	0.98	836	3.80 ± 0.06	0.99

On the other hand, both tungstate derivatives (SCWO & CCWO) show more noticeable changes at HP, as seen in *Figure 29*. A set of new peaks appear in the range of 500-700 cm^{-1} with some exceptions at the 250 or 1050 cm^{-1} (in SCWO), showcasing emerging defects or worsening symmetry. Those modes alongside originally registered peaks swing in place, losing their linearity before adjusting to new ω(p) trends. For CCWO, the process starts at 11 GPa, and for SCWO, as far as 15 GPa – those are also the limits till which the linear coefficients were calculated in *Table 17*. Those changes could be entirely dismissed as decomposition since they are completely reversible,[347–349] however, past this point, a noticeable hysteresis could be noted - reaching ± 3÷3.5 GPa in comparison to BCW & BPW (0÷0.5 GPa). Below them, at 9 (CCWO) & ~12 GPa (SCWO), no delayed response was noted. It is not likely to fully and truly ascertain the nature of those transitions without access to other, more sophisticated HP techniques (XRD), but with the literature mentioned above and some analogy to neighboring structures that previously had their DFT calculations done. When followed thoroughly, peak vs. pressure dependencies in *Figure 30* feature a slow, intermittent zone of fluctuations that could be distinguished while samples transition to a new form suggesting a (Landau-Ginzburg) second-order phase transition as disputed by Howard et al.[71,72] Those two derivatives surely lower their symmetry given common tilt systems, wildly spread defects, and partially substituted A^{2+}/$B(RE^{3/4+})$ sites – materials usually transition to a monoclinic *C*2/*c* (CCWO & SCWO) or *C*2/*m* (SCWO) SG – yet still, it is to be confirmed in the future given lack of HP XRD data and denoted slight hysteresis (typical for first-order).[350–354]

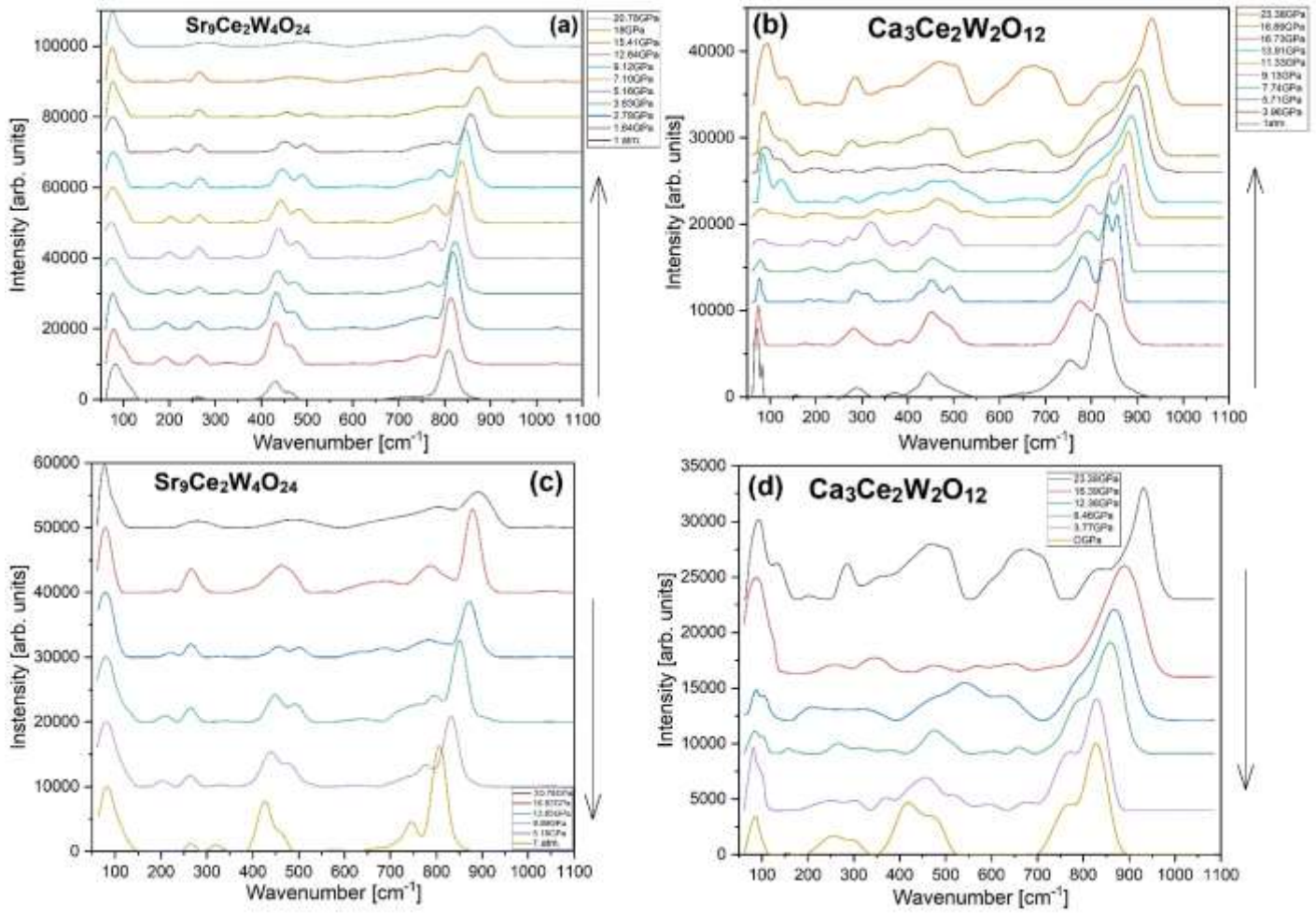

Figure 29 Raman spectra collected under hydrostatic argon PTM while using consecutive compression (top) − decompression (bottom) cycles for both SCWO (left) and CCWO (right) derivatives. Arrows guide the eye. Red vertical lines cut the pressure range into sections where theoretically reported second-order phase transition transpires.

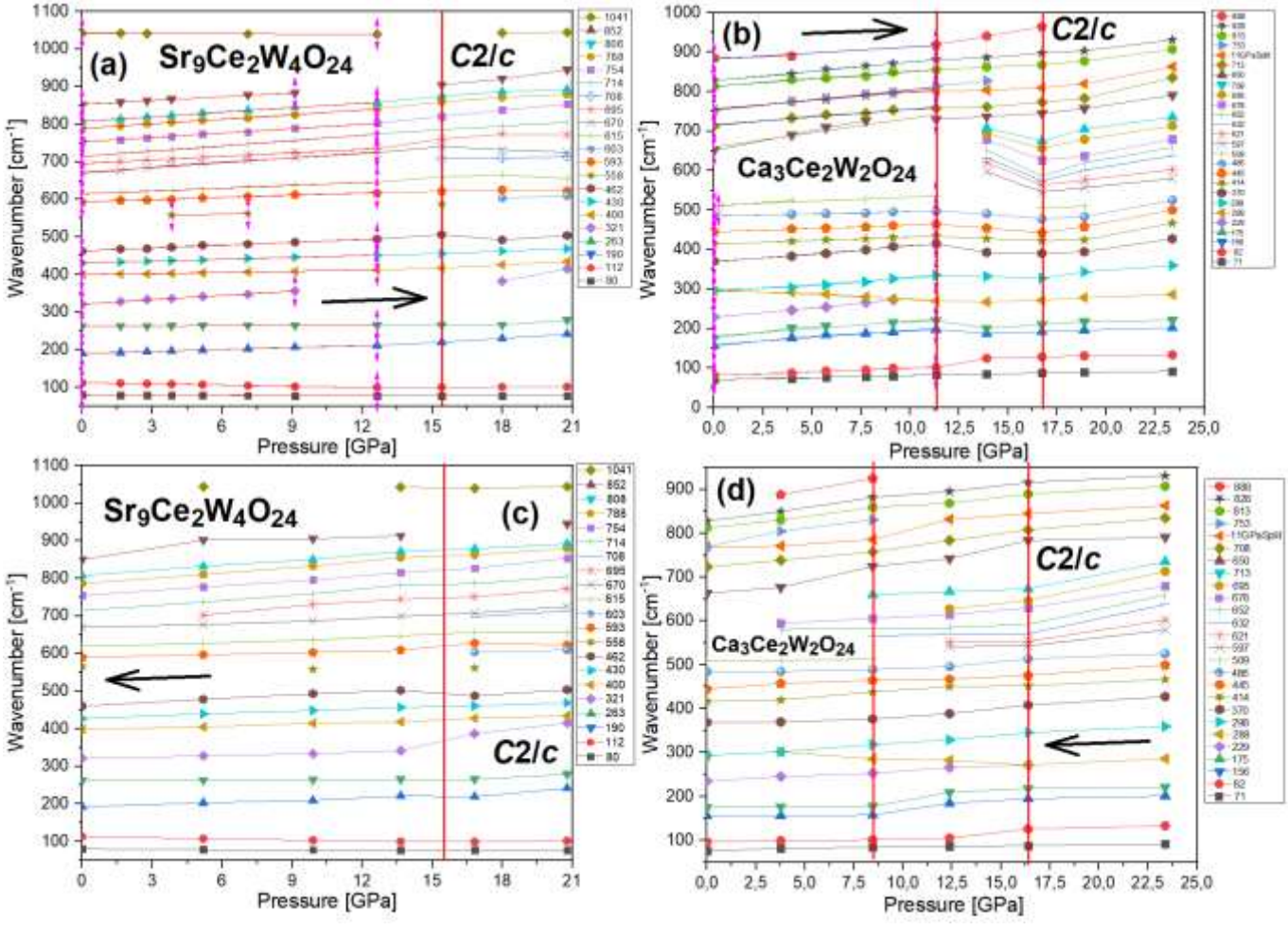

Figure 30 Raman peak position vs. pressure relations for modes featured in previous *Figure 29* regarding acquired derivatives. Presented similarly, compression is shown on the top, while decompression dependencies are on the bottom. SCWO to the left, CCWO to the right. Inserted right and left arrows guide the eye. Red vertical lines also cut the pressure range into sections where theoretically-reported second-order phase transition starts. Pink anchors mark the areas of linear fits. Error bars are too small to be visually noticed.

Table 17 Room temperature wavenumbers vs. pressure coefficients of Raman lines presented previously in *Figure 30* compression cycles for both SCWO and CCWO perovskite derivatives before any noticeable changes occurred.

$Sr_9Ce_2W_4O_{24}$ (up to 15 GPa)			**$Ca_3Ce_2W_2O_{12}$** (up to 11 GPa)		
ω_0 [cm^{-1}]	$d\omega/dP$ [cm^{-1}/GPa]	R^2	ω_0 [cm^{-1}]	$d\omega/dP$ [cm^{-1}/GPa]	R^2
80	– 0.25 ± 0.01	0.97	71	1.09 ± 0.08	0.98
112	– 1.06 ± 0.04	0.98	82	1.85 ± 0.12	0.98
			156	3.61 ± 0.37	0.95
190	1.70 ± 0.05	0.99	175	3.78 ± 0.58	0.91
			229	4.81 ± 0.15	0.99
263	0.19 ± 0.03	0.82	288	– 2.29 ± 0.31	0.91
321	3.79 ± 0.11	0.99	298	3.35 ± 0.38	0.94
			370	4.02 ± 0.19	0.99
400	1.01 ± 0.05	0.98	414	1.75 ± 0.06	0.99
430	1.67 ± 0.04	0.99	445	1.68 ± 0.05	0.99
462	2.53 ± 0.09	0.99	486	1.03 ± 0.06	0.98
558*	1.47	1*	509	2.07 ± 0.41	0.89
593	1.95 ± 0.10	0.98			
615	2.51 ± 0.08	0.99			
670	4.31 ± 0.18	0.98	650	7.27 ± 1.37	0.90
695	3.12 ± 0.05	0.99			
714	4.70 ± 0.09	0.99	713	3.91 ± 0.33	0.97
			713 SPLIT	4.33 ± 0.36	0.97
754	3.88 ± 0.07	0.99	753	5.13 ± 0.22	0.99
788	4.07 ± 0.09	0.99	813	3.70 ± 0.23	0.98
808	4.00 ± 0.07	0.99	828	4.70 ± 0.13	0.99
852	3.37 ± 0.11	0.99	888	3.09 ± 0.71	0.95
1041*	– 0.18 ± 0.07	0.55*			

'* - Peaks having doubtful factors (2-point or low R-squared)

At low temperatures, tungstate derivatives seem to be stable. Nothing out of the ordinary transpires in *Figure 31*. No new peaks or position swings – just slow-but-gradual, linear ω(T) progress, although in mixed directions, as seen in *Table 18*. The blue/red shifts are so minuscule that one can practically say that after confronting Raman setup, set with apparent error bars for the modes, they are particularly standing in place.

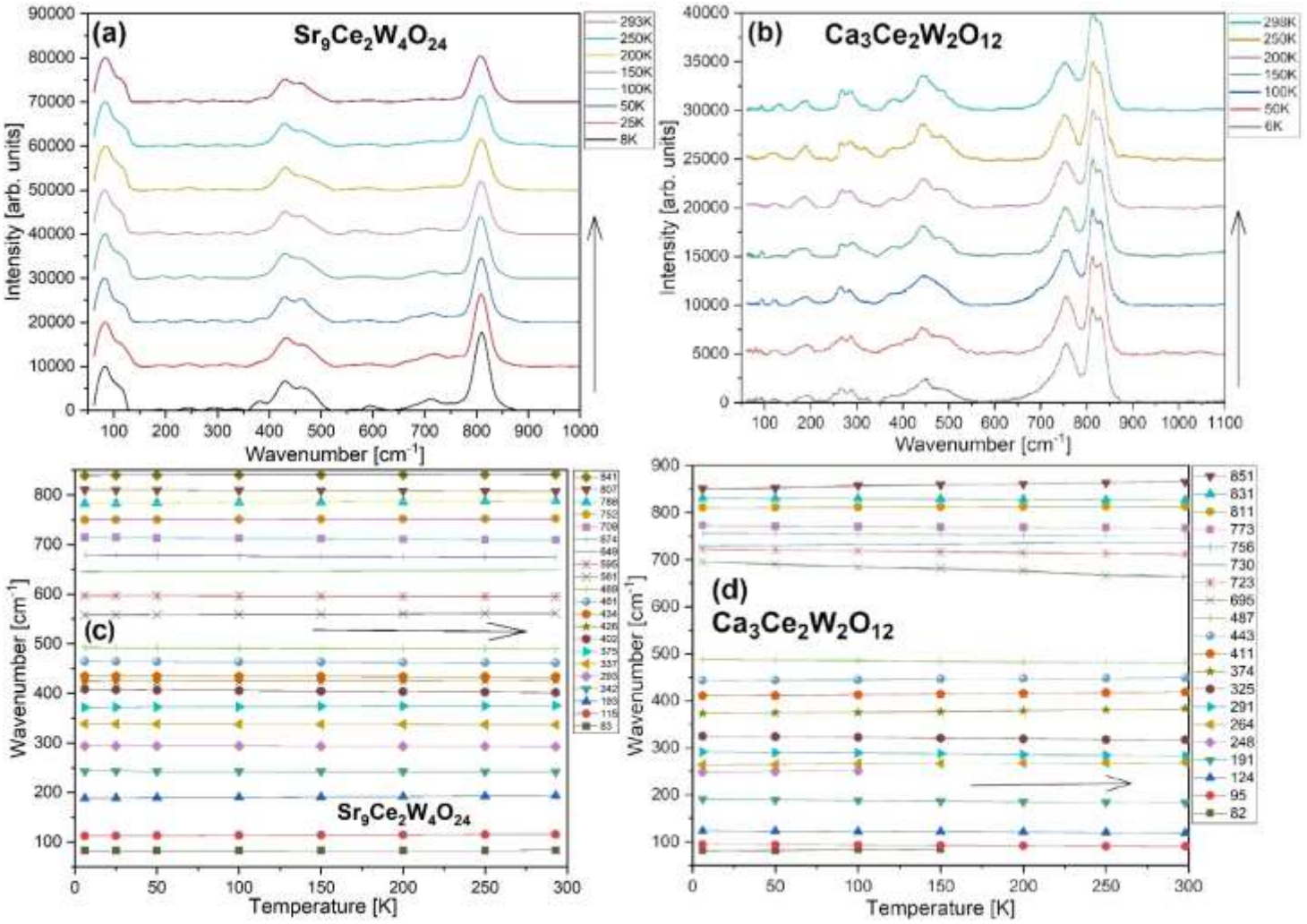

Figure 31 Low-temperature Raman spectra of perovskite derivatives presented in the function of heating from cryogenic to RT while their peak position vs. temperature dependencies are shown below. SCWO quaternary perovskite data is presented to the left, while CCWO ilmenite is to the right. Arrows guide the eye. Error bars are too small to be legible.

Table 18 Linear fit parameters obtained for temperature-dependent data presented in *Figure 31* for both SCWO & CCWO perovskite derivatives after cooling at ambient pressure.

$Sr_9Ce_2W_4O_{24}$			**$Ca_3Ce_2W_2O_{12}$**		
ω_0 [cm^{-1}]	$d\omega/dT$ [cm^{-1}/K]	R^2	ω_0 [cm^{-1}]	$d\omega/dT$ [cm^{-1}/K]	R^2
83	0.0031 ± 0.0002	0.98	82	0.020 ± 0.006	0.83
115	0.0113 ± 0.0005	0.98	95	– 0.015 ± 0.001	0.98
			124	– 0.014 ± 0.002	0.94
193	0.0174 ± 0.0005	0.99	191	– 0.025 ± 0.002	0.98
242	– 0.0041 ± 0.0001	0.99	248	0.029 ± 0.003	0.99
293	– 0.0027 ± 0.0006	0.70	291	– 0.028 ± 0.002	0.98
337	– 0.0047 ± 0.0001	0.99			
375	0.0121 ± 0.0005	0.98	374	0.032 ± 0.003	0.95
402	– 0.0218 ± 0.0007	0.99	411	0.029 ± 0.001	0.99
426	0.0064 ± 0.0001	0.99			
434	– 0.0041 ± 0.0001	0.99	443	0.022 ± 0.002	0.97
461	– 0.0099 ± 0.0004	0.98	487	– 0.021 ± 0.002	0.96
489	– 0.0100 ± 0.0008	0.95			
561	0.0120 ± 0.0003	0.99			

595	– 0.0066 ± 0.0002	0.99			
649	0.0116 ± 0.0003	0.99			
674	– 0.0156 ± 0.0004	0.99	695	– 0.108 ± 0.008	0.97
709	– 0.0189 ± 0.0002	0.99	723	– 0.038 ± 0.002	0.98
			730	0.025 ± 0.001	0.98
752	0.0090 ± 0.0005	0.98	756	– 0.019 ± 0.001	0.97
788	0.0172 ± 0.0005	0.99			
807	– 0.0100 ± 0.0003	0.99	811	0.008 ± 0.001	0.92
			831	– 0.013 ± 0.001	0.97
841	0.0067 ± 0.0002	0.99			
			851	0.051 ± 0.005	0.95

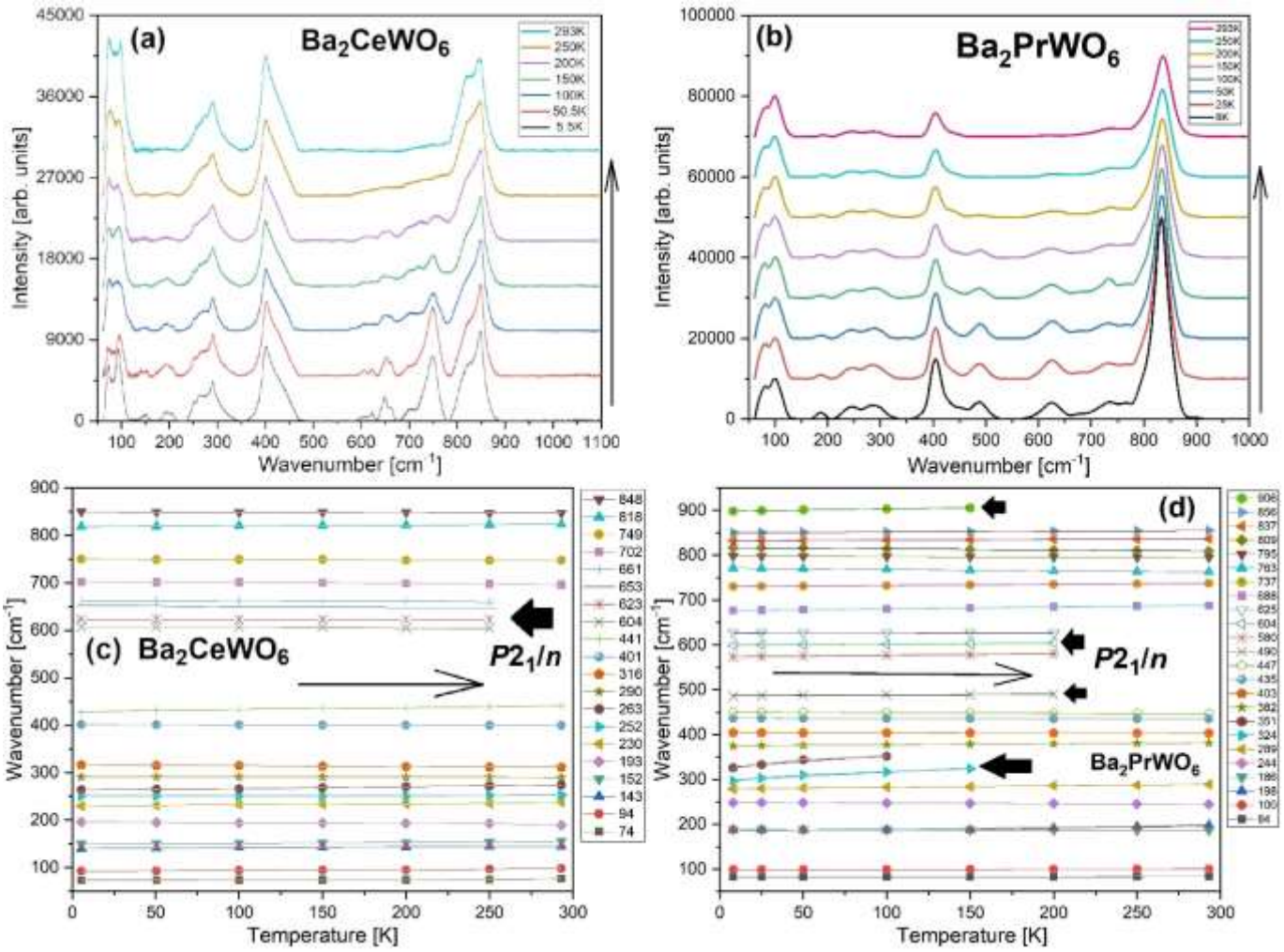

Figure 32 Low-temperature Raman spectra of barium double perovskites presented in the function of heating from cryogenic to RT, while their peak position vs temperature dependencies are shown at the bottom. BCW data is presented to the left, while BPW is to the right. Arrows guide the eye and pinpoint eventual changes related to the second-order phase transition. Error bars are too small to be visually noticed.

Again, the situation changes to the opposite in the case of barium DPs – they seem to undergo some sort of transition just below 200K. As shown in *Figure 32*, new ones appear near the set of typical peaks and sharpen down to He-level temperatures. Mostly between 550-650 cm^{-1} but in BPW, there are slightly more of them (just above 1000 and around 300 cm^{-1}) - all of them are marked as red in *Table 19* to distinguish them from the others. They appear probably because the material hosts largely unmatched RE/W B-site 'pairs', resulting in many oxygen defects and RE

vacancies distorting the overall structures (angle tilt) during temperature shrinkage.[323–325,355] At that point, one could argue that this change could be decomposition, but that would not be reversible in heating. A more likely scenario is a stretched, continuous (second-order) phase transition, as suggested by Howard et al.[71,72] or many others in the literature, given the prominent dissonance between *R*-3 & *I*2/*m* SG assessment.[356–360] As it turns out, both structures could coexist with each other at RT (*R*-3 often transits to *I*2/*m* at ~50÷125°C, but some exceptions may apply). Usually, XRD would not be enough to assess the proper form of the powders at that point if one does not possess an ordered, more sophisticated single crystal or access to NPD.[361] The exact number of Raman active modes between each group also would not answer their elevated count after cooling. However, if those modes were just not accounted for (not visible) due to weak intensity or reforming RE-O bonds/strengthening defects (*Figure A11*), this would indicate a slow, gradual transition to a lower symmetry SG. Progressing angle tilt often causes a monoclinic SG, like $P2_1/n$, to emerge from any tilted cubic structure.[356,360,362] This still, however, would require some confirmation using techniques like LT XRD, but any temperature dependence could help. HT XRD could tell us even more about angular dependencies concerning a wider range of temperatures if no transitions transpire – discussed later in *section 3.5*. Considering that only a few modes tend to change at LT – some just slightly faster than others, especially at the lowest 5K÷25K - most barely move and should be considered stationary - just like in SCWO & CCWO case. Their ω(T) coefficients are often so small that the given error bars could be roughly rounded up to zero, given the current resolution of the equipment. So, presented subtle blue/red shifts are just crude, statistical approximations that should be approached or rather judged carefully with some skepticism.

All aforementioned phase transitions and changes in this chapter were briefly summarized in graphs presented in supplementary *Figure A14*. One can view Howard's DFT-calculated DP transitions and counter them against experimental results.[71,72]

Table 19 Linear fit parameters obtained for temperature-dependent data presented in *Figure 32* for both investigated barium double perovskites after cooling at ambient pressure. New LT peaks are marked as **red** and linearized in the whole range of existence.

Ba_2CeWO_6			**Ba_2PrWO_6**		
ω_0 [cm^{-1}]	$d\omega/dT$ [cm^{-1}/K]	R^2	ω_0 [cm^{-1}]	$d\omega/dT$ [cm^{-1}/K]	R^2
74	0.009 ± 0.002	0.69	84	0.0044 ± 0.0002	0.99
94	0.018 ± 0.002	0.96	100	0.0041 ± 0.0001	0.99
143	0.016 ± 0.002	0.94			
152	0.017 ± 0.002	0.91	186	-0.0058 ± 0.0003	0.98
193	– 0.019 ± 0.004	0.77	198 Split	0.076 ± 0.003	0.99
203	0.023 ± 0.002	0.95			
252	0.006 ± 0.001	0.78	244	– 0.0149 ± 0.0003	0.99
263	0.035 ± 0.002	0.98			
290	– 0.0035 ± 0.0009	0.71	289	0.034 ± 0.002	0.98
316	– 0.0179 ± 0.0007	0.99	324	0.183 ± 0.019	0.96
			351	0.273 ± 0.052	0.90
			382	0.023 ± 0.001	0.98
401	– 0.0051 ± 0.0008	0.87	403	– 0.0041 ± 0.0002	0.98

441	0.043 ± 0.003	0.96	435	– 0.0054 ± 0.0001	0.99
			447	– 0.0118 ± 0.0003	0.99
			490	0.020 ± 0.003	0.88
			580	0.035 ± 0.001	0.99
604	– 0.014 ± 0.002	0.84	604	0.024 ± 0.002	0.96
623	– 0.0018 ± 0.0006	0.62	625	– 0.006 ± 0.001	0.78
653	– 0.020 ± 0.003	0.86			
661	– 0.019 ± 0.005	0.73	688	0.040 ± 0.001	0.98
702	– 0.020 ± 0.002	0.92	737	0.0241 ± 0.0003	0.99
749	– 0.009 ± 0.002	0.83	763	– 0.0305 ± 0.0004	0.99
			795	– 0.0107 ± 0.0004	0.99
818	0.016 ± 0.009	0.98	809	– 0.0107 ± 0.0004	0.99
848	– 0.0095 ± 0.0009	0.94	837	0.0260 ± 0.0006	0.99
			856	0.0180 ± 0.0003	0.99
			906	0.049 ± 0.003	0.98

3.2 XAS spectra at cryogenic temperatures

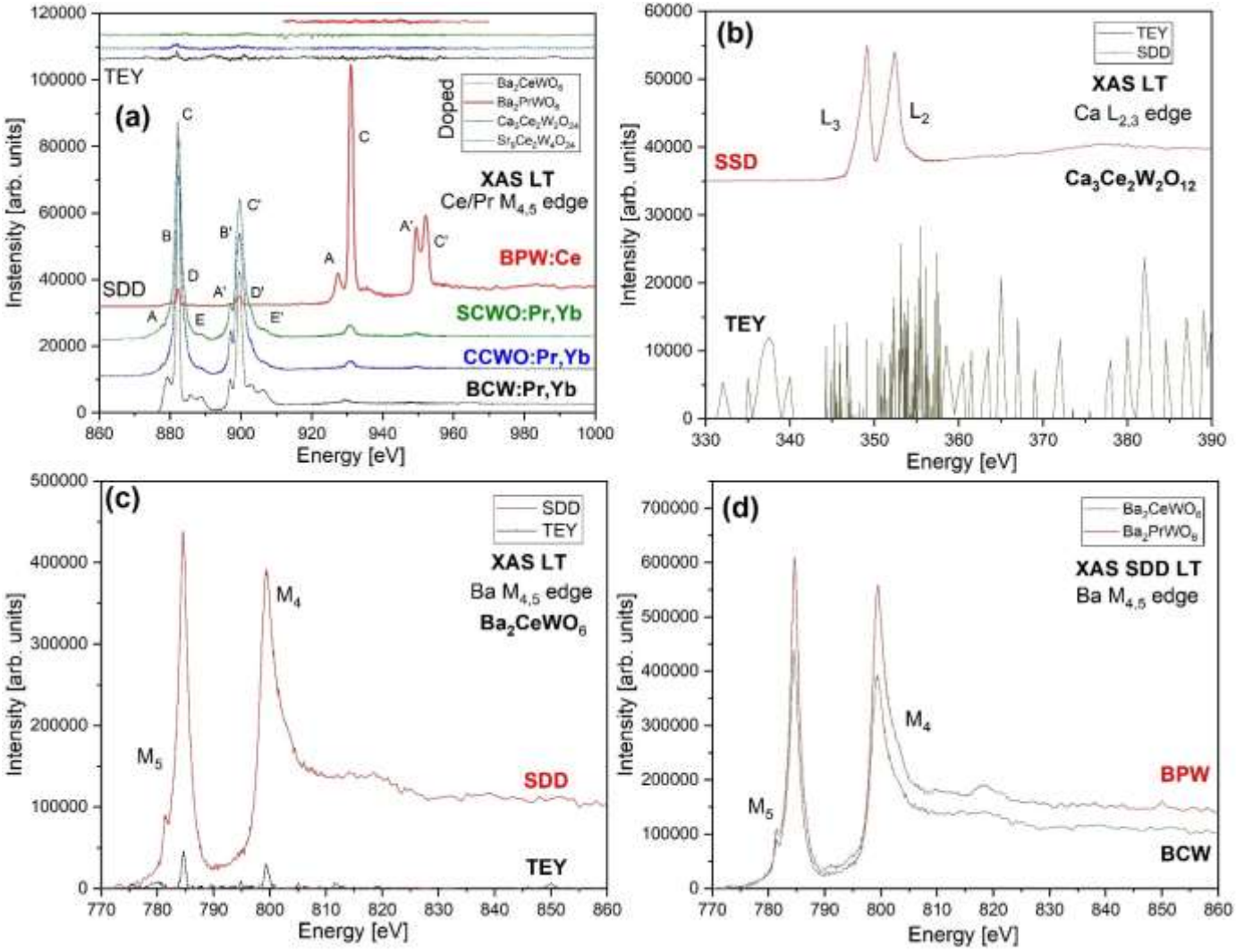

Figure 33 Low-Temperature XAS spectra yielded in dual acquisition mode showcasing prominent quality degradation of registered signals due to a significant drop in conductivity/rising insulating properties at various absorption edges: (a) Ce/Pr $M_{4,5}$ for all doped materials, as well as undoped (b) Ca $L_{2,3}$ edge CCWO, (c) Ba $M_{4,5}$ shells in BCW compared to (d) BPW using the only useful SSD mode.

Low-temperature X-ray absorption studies were done at some point, given access to other synchrotron facilities available on site. Knowing (from Raman spectra) that some of our materials (hosting barium) could have changed below 200K in cryogenic conditions, it is necessary to check using other techniques (like XAS) whether or not any of these claims were true. Here, the charge of given ions (mainly concerning RE/W) could also change during unit cell evolution (shrinkage/tilt) or SG transitions (to lower symmetry),[363–365] especially concerning future PL energy transfer experiments (in *chapter 4*). So some of the most prominent results adhering to that prospect were collected and shown in *Figure 33*.

The spectra were not outstanding at first glance. SDD acquisition mode only gave some noticeable signals but solely in terms of constituents. Still, they were much weaker and quite noisy than their RT counterparts. RE^{3+} dopants were barely visible, and their complex features were not very distinguishable (especially considering low 1÷5% concentrations of Pr). One could fit a lot (of possible peak sets) into those small, noisy spaces, and the error bars would be so high that a scientist could easily find any suitable match in the region of interest – compared to RT results. Befitting those conclusions - nothing majorly could be said about dopants, but two things stood out of the ordinary at LT. Firstly, the TEY acquisition mode barely registered anything at all. This method is a leading technique of signal registration, closely related to the sample's contact and conductivity. It is superior in all means to SDD if the conductivity of the sample is just right. Given all the adjustments: visual confirmation about the physical contact, appearance via camera, no problem with the status of the synchrotron beamline (feed), & the pins holding all the pellets to their molybdenum holders (in 4 separate cases) were good; the only conclusion that could accommodate for such a sudden drop of intensity would be a drastic decrease of conductivity towards insulating values (so that the detector could not receive any low-energy electrons showered off the pellets' surfaces (down the Mo drain).[366,367] That prompted several problematic issues concerning upcoming cryogenic PL & EPR experiments for all RE paramagnetic dopants and constituents that could be influenced (potentially frozen e^- carriers or magnetic transitions) during that time.[368–370] What is interesting is that conductivity changes are related to both Ba samples' phase transition phenomena and the whole batch of derivatives (CCWO & SCWO too). The issue might stem from previously mentioned 200÷150K (*section 3.1*) changes and some entrapping vacancies or W (mainly exotic & unstable 5+ ion changing quickly to 6+). SCWO & CCWO RE ions are seemingly unaffected, so tungsten might be the actual band gap manipulation culprit; however, it is uninvestigable since all its prominent shell edges lay outside the beamline's experimental range. *Section 2.3* XPS reports on slightly elevated stoichiometric O count, just like in *Table 10*, so that phenomenon might also be partially related to O_i/V_o presence (however severely limited). Expanding on that last issue, some spontaneous chemical reactions (resulting in stoichiometry changes or partial decomposition) might also take place at that time but only for both double perovskites (BPW more than BCW) due to much higher O_i content - these changes would be irreversible.

Barium samples seem to possess grossly elevated Ce^{3+} and Pr^{3+} content at LT, sacrificing much of their 4+ ions, but Sr and Ca derivatives do not. Since XAS edges do not look exactly the same as XPS, a need to compare through an analogy of M_5 A-E & M_4 A'-E' peaks vs. 3d shell $d_{5/2}$ v_o-v''' + $d_{3/2}$ u_o-u''' sets is necessary – original RT XAS was presented in *section's 2.3 Figure 19* while reference spectra are placed in appendix *Figure A10* if needed. Since the tungsten mentioned above could not be measured efficiently as an eventual donor of electrons at LT, to capture some perspective on apparent changes, the only way to counter that issue would be

indirect LT PL $W^{6+}O_4$ octahedra measurements - more about it later, in *section 4*. With the assistance of DFT band projections, one could confront models with actual reflectance spectra and discuss the W ionic charge state influence with actual matrix evolution. A lasting impression, for now, would be that some e^- donor, like $W^{4+/5+}$, could influence RE ions to change and upset the internal B-site balance by such mechanism: $2RE^{4+} + W^{4+} \rightarrow 2RE^{3+} + W^{6+}$ or $RE^{4+} + W^{5+} \rightarrow RE^{3+} + W^{6+}$. That charge transfer would surely influence any phenomena regarding energy transfer and overall stoichiometry of Ba_2REWO_6 to something resembling $Ba_{2+x}RE^{3+}\square W^{6+}O^*_{6+x}$ species (possibly similar to tilted $Ba_3Pr_2W_2O_{12}$ species hosting 9+ balance at LT. If O_i would be introduced into the matrix, that would further complicate the transition/recovery. A hint of possible application as a PL temperature sensor was made at that point; however, as a one-way-ticket if photobleaching (RE^{4+}) effect would take place.[371,372]

3.3 Low-temperature EPR studies

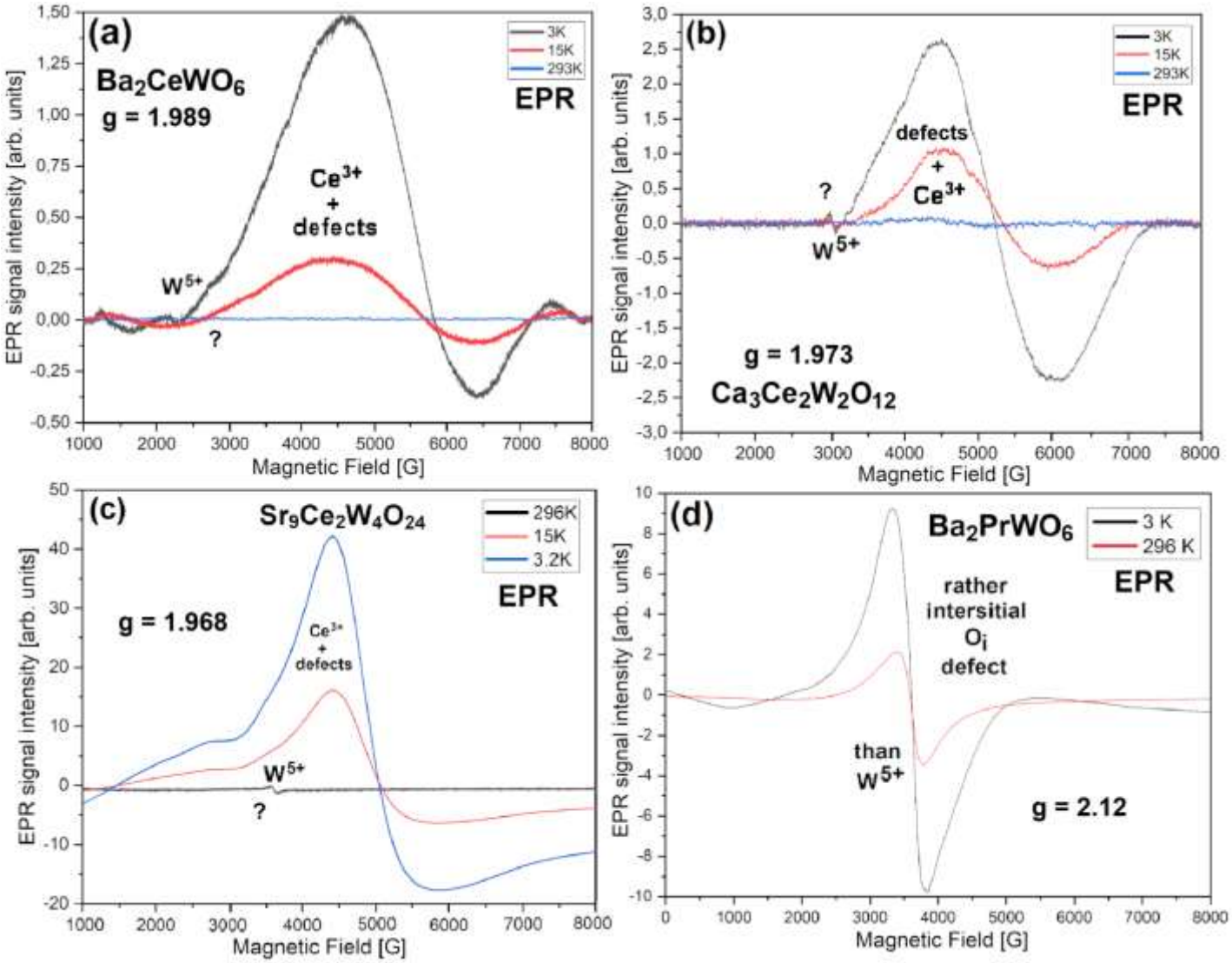

Figure 34 Cryogenically cooled EPR spectra collected for all investigated, undoped tungstate powders placed in perpendicular magnetic fields before any experiments or further modifications.

EPR spectroscopy was performed to assess the true form of ions in discovered, undoped materials knowing that most of RE reveal their paramagnetic nature abruptly at helium-level

temperatures while other ions like d-block W should be visible from the get-go. This technique would also allow the detection of other, specific magnetically active sites (O_i defects) or differentiate between subspecies sensitive to **perpendicular** & horizontal magnetic fields.[373,374] Since our scientific group has only access to the setup with the **former** orientation of the magnetic field, a careful approach to see and compare the changes in W, Ce, or Pr magnetically active content before and after the eventual phase transition (below 150K) in barium double perovskites. To compare them with the other two tungstate derivatives concerning W^{5+}, Ce^{3+} & Pr^{4+} ions. Complementary verification of (dropping) conductivity through microwaves would also be an asset.[375,376]

As can be observed in *Figure 34,* all spectra are crude and robust except the last one (d) regarding BPW. They all have an unfortunate effect associated with powders that possess defective, anisotropic structures hosting chaotically scattered paramagnetic domains highly diluted across the matrices. That makes subtle multisites not distinguishable to the naked eye.[328,377] Moreover, the signal from Ce^{3+} in the first three graphs (a - BCW, b – CCWO, and c - SCWO) envelopes features of something else on its back (lower Gauss range). Given acquired g-factors, which are slightly below 2 (1.989, 1.973, 1.968, respectively), the electro-donor species could be associated only qualitatively via their positions (maximum value of curves' derivative) versus what the literature truly says without procuring any prolific details. A quite similar type of signal was achieved for the precursor, $BaWO_4$:Ce. [328,378–380] As Ce^{3+} species seem to fit quite well into the Gaussian range (~4.8 kG bracket) showcasing "below 20K" activation mechanisms with $x<2$ g-factors, these lumps present at the slopes in the lower magnetic fields seem definitely different in origin. - there might be something else there. Possible defects or exotic W^{5+}. The problem with the last one is its low content & highly unstable nature. Furthermore, as a d-block ion, it should be visible already at RT if not influenced by any external charge-transfer sources at LT. It does not possess such an activation mechanism as RE ions & should be visible from the start with the g-factor lowered to $1.6 \div 1.7$.[381,382] The range of this eaten-up signal (~3.4 kG), however, fits that dogma. It is just too weak and misshaped to be sure of its origin. Yes, it is contained as a minor phase, but should not be so weak and disfigured. The answer possibly lies within the BPW spectrum. There, the signal is much clearer, well-defined at RT, and with the given g-factor (above 2 ~ 2.12), it would debunk its presence as interstitial oxygen (O_i).[383–385] That would n fit the scenario of g-factors at previous spectra. This, however, might be just an outcome of both species coinciding with each other in one matrix resulting in these final g-factor's values.[386,387] What is more troubling is the absence of $Pr^{4+,}$ which should be there at LT (visible just like Ce^{3+} given its e^- configuration), around 1.9 kG (g_z) joined by O_i at 3.5 ($g_{x,y}$) as seen in REO_{2-x} references [388–391] in the supplementary *Figure A15*. [388,392,393] According to XPS & XAS, this ion is abundant in the matrix at RT. The spectrum (d) should look at least similar to the other 3 (a,b,c). Yet still, nothing. That could vouch for either change of Pr^{4+} to Pr^{3+} at LT via photoionization,[394–396] or antiferromagnetic phase transition encountered previously at similar Ba_2PrRuO_6 family of compounds featuring $T_{Neél}$ in between 90-117K.[397] That would render Pr^{4+} & W^{5+} ions completely undetectable at 20-3K.

Later (*chapter 4*), this EPR investigation, alongside XAS & PL, will lay firm fundaments to support time-resolved, charge-transfer phenomena (between RE🡐🡒W) research shedding some light on gradual O_i evolution in barium DPs during RT highly-energetic illumination. The nature of possible photoionization at LT would be approved in between 90 & 150K where possible $T_{Neél}$ & Raman phase transition lie.[398–401]

3.4 DSC & TG stability research

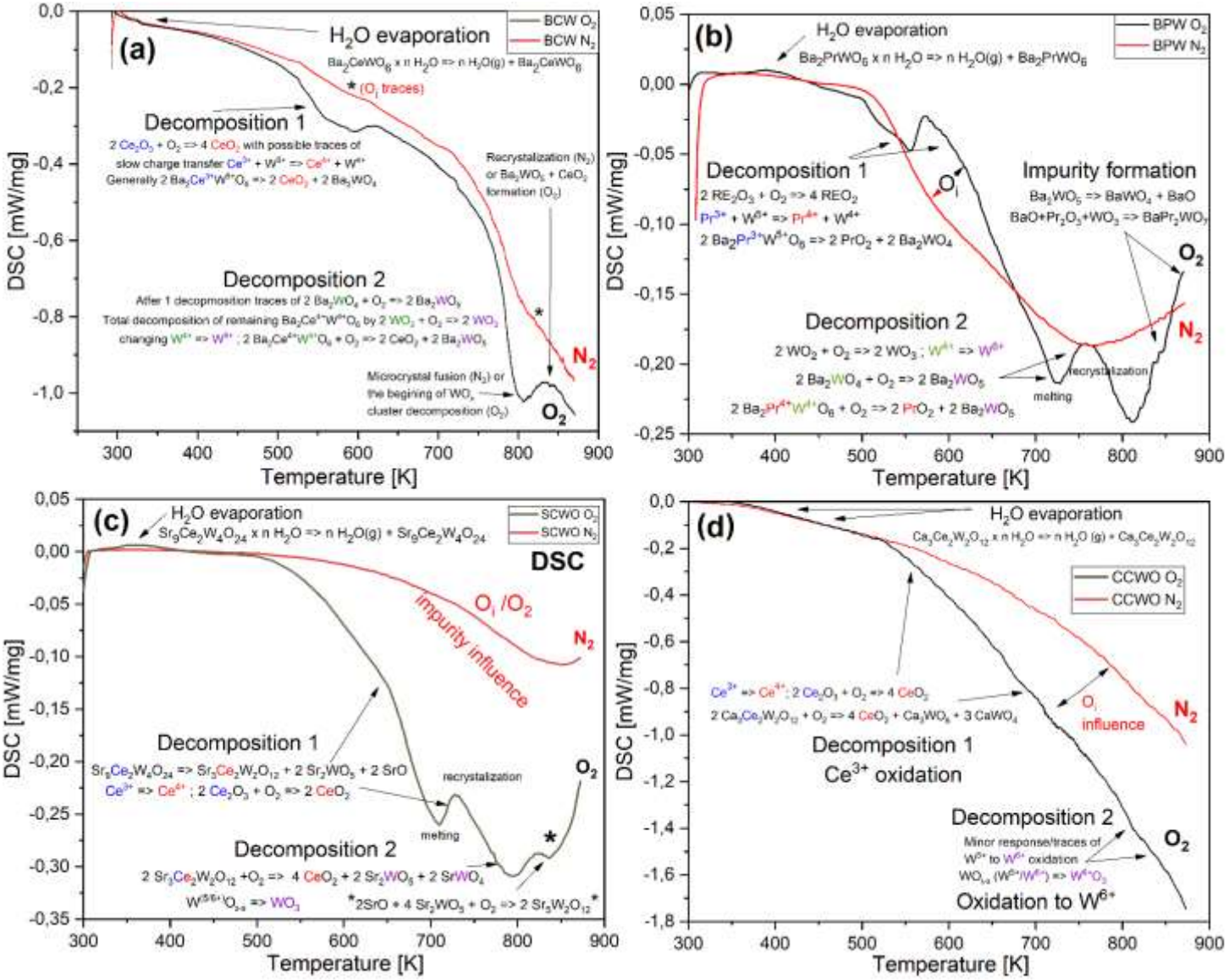

Figure 35 Differential Calorimetry Scans of all investigated, undoped materials in referral, inert N_2 (red) and air (black) atmospheres showcasing the regions of stability and decomposition done in the perspective of future usage at ambient conditions: for both (a) Ba_2CeWO_6, (b) Ba_2PrWO_6 double perovskites, together with (c) $Sr_9Ce_2W_4O_{24}$, (d) $Ca_3Ce_2W_2O_{12}$ tungstate derivatives.

Differential Scanning Calorimetry (DSC) and Thermogravimetry (TG) were included as pre-emptive reconnaissance methods to investigate the first signs of materials' instability since perovskites, as a whole mineral group, have a lot of unstable variants – at least when exposed to some specific stimuli in the long run, like heat or strong, monochromatic light in the air. Confronting this data with the literature,[402–404] some estimates could be made regarding chemical reactions and decay (oxidation) to specific subspecies supported shortly thereafter by HT XRD and Raman spectroscopy studies. That way, some genuine phase transitions could be noticed in protected inert conditions unrelated to decomposition. If not, the patterns and spectra will still reference those changes seen in the air.[405,406] Also, in the areas of more noticeable changes (air), the techniques mentioned above could efficiently probe the structures in a more detailed, small-step manner without losing any time and resources.

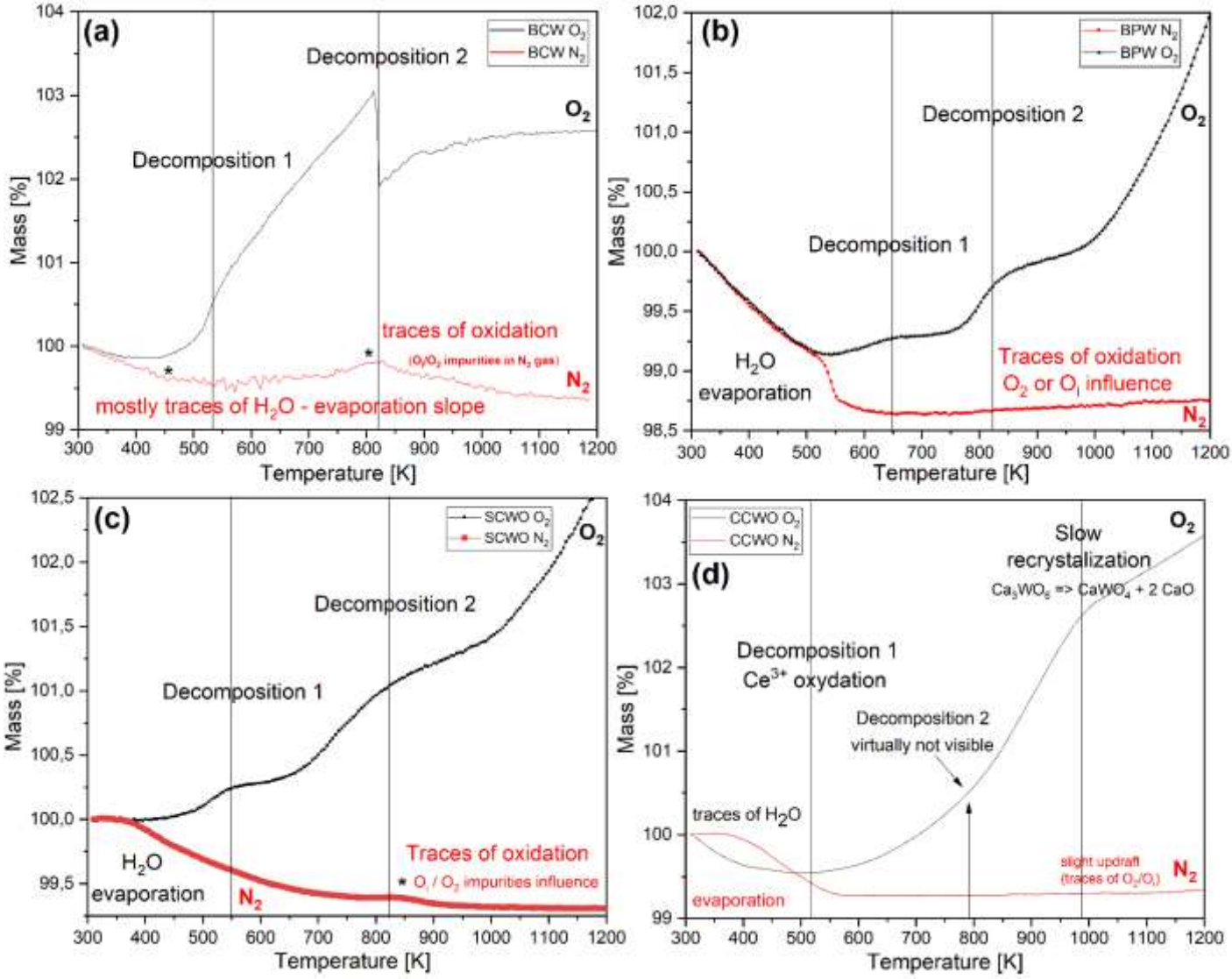

Figure 36 Thermogravimetry diagrams of all investigated, undoped materials in referral, inert N_2 (red) and air (black) atmospheres showcasing the regions of stability and decomposition done in the perspective of future usage at ambient conditions: for both (a) Ba_2CeWO_6, (b) Ba_2PrWO_6 double perovskites, together with (c) $Sr_9Ce_2W_4O_{24}$, (d) $Ca_3Ce_2W_2O_{12}$ tungstate derivatives.

Before divulging specifics about apparent changes deduced from foreseeable features in all graphs presented in that chapter, air-related **(black)** curves show a more complex nature than N_2-related (red) ones. Although much could be told in comparison between each one of them, one could impute that they should be completely flat (if no decay, decomposition, or phase transition occurs); however, despite countless efforts, some influence from ingrained impurities, like O_i, could not be avoided for samples submerged in N_2.[407,408] (Intercalated water could be by preheating all materials in the first, inert cycle but this effect is counted more as a genuine, storing feature than a problem). This bends all lines towards each other, creating an exo-energetic effect but with much weaker, less prevalent consequences. Let it be a baseline since O_i could not be expelled from the materials efficiently (they are oxide, after all) without affecting their matrix as a whole (by incoherent reduction, -OH creation, or expansion of intercalated H_2O content). It will still behave like air to some extent but with a limited (trace) supply and higher activation energy.[387,409,410]

Following DSC measurements in *Figure 35* with complementary TG measurements *in Figure 36,* one can distinguish some common features not only between all materials (double perovskites lines progress similarly just like Sr and Ca derivatives between each other) but also air curves show prominent lumps and dents related to the same type of changes in closely-related temperature frames. N_2 is less rich & prevalent, but it is to be expected. It is no surprise since all of them contain mostly the same ions, just arranged differently – they should be as sensitive and react the same way as presented in the insets. However, the actual question is whether or not they (materials & their curves) relate to the same processes for sure – that is why they should be collectively analyzed not only with literature but alongside some crystallographic (HT XRD) or spectroscopic (HT Raman) techniques to be completely sure. Those measurements were done later on the basis of this data to focus on the main features like "Decomposition 1 or 2" meaning that in the next chapter, they will confirm given reactions with higher precision by a tighter step-by-step method. General processes commence as follows:

First, the evaporation of the water stored in not pre-heated samples is a typical process. Even in a desiccator, the moisturization could not be entirely stopped – it just slowed down to some decent degree. In TG, evaporation is shown as an initial drop of weight while approaching the boiling point of water at ambient pressure. In DSC, the curve should either show an endothermic (+ value) uprise or balance itself out discretely due to some opposite competing processes (as observed here).[411,412] There, the curves are temporarily flat or show less steep descent until oxidation (more pronounced by O_2 from the **air**) or more subtle by the influence of O_i (confined within the material in limited amount while **N_2** is surrounding the material) overtakes the balance as a dominating exothermic (-) process above ~400/500K.

The aforementioned processes look more-or-less like the reactions presented below (or in the insets of *Figure 35*) and will not show much on XRD or Raman spectra if only some traces of water are left. Few patterns might just slightly improve in intensity by lowering the general amorphization caused by water.

Equation 1: (n ~ 6)
(a) BCW: $Ba_2CeWO_6 \times n\ H_2O \rightarrow n\ H_2O\ (g) + Ba_2CeWO_6$
(b) BPW: $Ba_2PrWO_6 \times n\ H_2O \rightarrow n\ H_2O\ (g) + Ba_2PrWO_6$
(c) SCWO: $Sr_9Ce_2W_4O_{24} \times n\ H_2O \rightarrow n\ H_2O\ (g) + Sr_9Ce_2W_4O_{24}$
(d) CCWO: $Ca_3Ce_2W_2O_{12} \times n\ H_2O \rightarrow n\ H_2O\ (g) + Ca_3Ce_2W_2O_{12}$

The 'n' number is often associated with the ligand number depending on the coordination and strength of the crystallographic field surrounding the main structure. Steric hindrance and the main ions' size or rather charge state dictate it to be 2, 4, 6, or 8. Regarding water dipoles, it is often six as each hydrogen bonding has the angular freedom to bend towards oxygen at each neighboring *xyz* (+/-) axis. Therefore, water encapsulates such structures in a neat bubble.[413–415]

The first significant decomposition process is related to $RE^{3+} \rightarrow RE^{4+}$ oxidation. Mainly Ce or Pr, which starts slightly faster for Ce but is more abrupt for Pr. The first definitive signs in decay processes could be distinguished above 475K, but at 550K, the culmination point peaks.[416–420] This is also the terminus (endpoint) of stability and usage in the air, as later, one will end up with a totally different blend of products at their disposal. The overall reactions dictated by the literature progress at this stage as follows:

Equation 2:
(a) $Ce^{3+} \rightarrow Ce^{4+}$; $2\ Ce_2O_3 + O_2$ (if $O_i + O_{2-x}$) $\rightarrow 4\ CeO_{2(-x)}$;
$14\ Ce_2O_3 + 3\ O_2 \rightarrow 4\ Ce_7O_{12}$ (CeO_{2-x}); $Ce_7O_{12} + O_2$ ($O_i + O_{2-x}$ if present) $\rightarrow 7\ CeO_{2(-x)}$
(b) $Pr^{3+} \rightarrow Pr^{4+}$; $2Pr_2O_3 + O_2 \rightarrow 4\ PrO_2$;
$3\ Pr_2O_3 + O_2 \rightarrow Pr_6O_{11}$ (PrO_{2-x}); $2\ Pr_6O_{11} + O_2$ ($O_i + O_{2-x}$ if present) $\leftrightarrow 12\ PrO_{2(-x)}$

However, These sets are not customized to actual products, as seen in the insets. More about them in HT XRD/Raman *3.5 chapter* below. For now, let us elaborate on the actual mixed valence state of REO_{2-x} oxides present in the equations above. They are all justified due to the availability of various B-site ions previously reported by XAS/XPS. Pure PrO_2 is neither stable nor achievable in its purest form (only temporary) – it reverts to & is referred to as PrO_{2-x} form (Pr_7O_{12}, Pr_5O_9, Pr_6O_{11}, $Pr_{11}O_{20}$).[196] This last fact might cause a lot of disorder, abrupt breakage, and insert more O_i into the matrix creating V_o, like in BPW.

More pronounced DSC curve features reported (by XPS) $(Ce,Pr)^{3/4+}/W^{5/4+}$ disproportions by smaller peak area for the former RE 'pair', which brings us to the following (later) 'Decomposition 2' process associated with intense W^{4+} oxidation to the W^{6+} state. Any remaining residual W^{5+} does the same but slowly and subtly.[421–424] The process actually starts above 725-750K but reaches its culmination point at +800K:

Equation 3
$W^{4/5+} \rightarrow W^{6+}$; $2\ WO_2 + O_2 \rightarrow 2\ WO_3$; $2\ W_{18}O_{49}$ ($W^{(5/6+)}O_{3-x}$) $+ 5\ O_2 \rightarrow 36\ W^{6+}O_3$

The reaction does not stop there. More subtle, slowly progressing exothermic processes could be traced as curves progress vertically up or down (melting or recrystallization since only horizontal flat lines symbolize discrete & brief temperature stop/reaction balance).[402–404] Processes gradually penetrate the material deeper and faster with each minute in the air (in N_2 negligible influence of O_i) while main products dismantle further to salts (tungstates) or rather, more importantly, (alkaline) oxides and carbides (that last group concerns W with graphite/residual carbonates). The last group is only temporarily stable, solely above 1000K (as showcased more prominently by TG & post-processing XRD since DSC could reach that high due to apparatus limit).[421,425,426] Later, the former alkaline oxides will diminish (on the surface) and react with each other stuff, like moisture or CO_2 from the atmosphere. Traces of this phenomenon will be visible after milling the pellets and seeing their insides –all minor XRD phases are shown in *section 2.2*. It also seems that AO oxides try to react with REO_{2-x} giving something in the shape of $BaREO_{3-x}$.

In the range of ambient environmental stability (below any signs of decomposition stage 1), an average heat capacity (C_p) can be calculated against proper references (like sapphire) from data gathered in *Figure 37*. This extensive physical propriety is crucial in designing materials used in civil engineering, like sensors and solar panels. Working in different temperatures, energy is needed: to control their energy usage, storage, and expansion; to avoid damage and eventual resource loss, so their estimation would be definitely useful.[427,428] As shown in *Table 20*, their value strictly depends on the mass and expands with growing stoichiometry. By comparing them to other double perovskites, at least barium compounds fit gently into declared ranges.[401,429,430] Derivatives do not have much reference to compare with other than close-call garnets vs. ilmenites – matches are good too.[431]

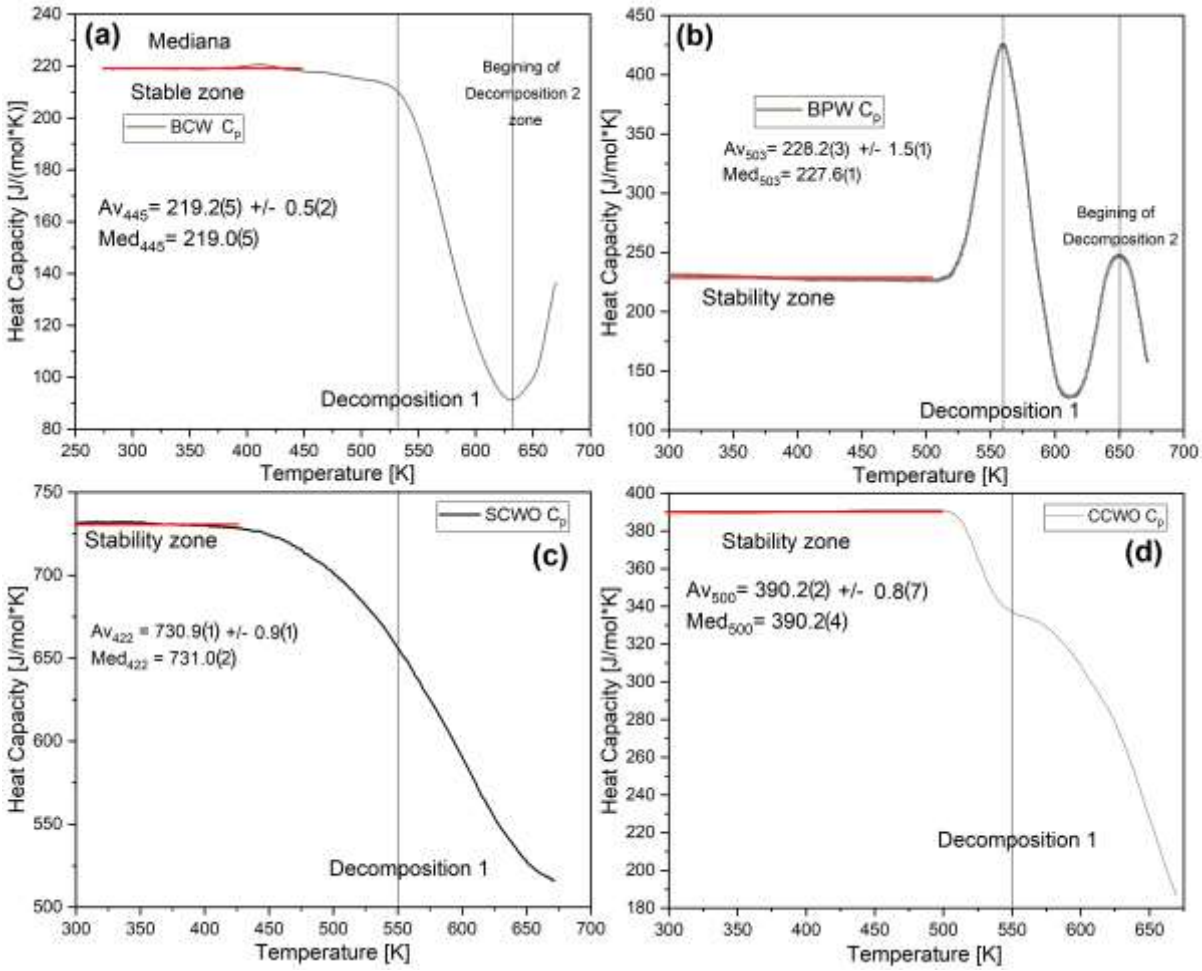

Figure 37 Molar heat capacity measured in the air for all investigated compounds in the function of heating against a sapphire reference. The mean values given in the text refer to stable zones marked by red lines.

Table 20 Standardized experimental molar C_p values calculated for all 4 investigated compounds against sapphire reference in the air during previous DSC measurements in *Figure 37*.

Material	Average [J×mol^{-1}×K^{-1}]	Average deviation ± [J×mol^{-1}×K^{-1}]	Median [J×mol^{-1}×K^{-1}]	Maximum stable temperature of calculations [K]
Ba_2CeWO_6	219.2(5)	0.5(2)	219.0(5)	445
Ba_2PrWO_6	228.2(3)	1.5(1)	227.6(1)	503
$Sr_9Ce_2W_4O_{24}$	730.9(1)	0.9(1)	731.0(2)	422
$Ca_3Ce_2W_2O_{12}$	390.2(2)	0.8(7)	390.2(4)	500

3.5 High-temperature decomposition via XRD & Raman

High temperatures (investigated via XRD & Raman spectra) are equally important as LT from a technical standpoint, knowing that solar panels could work both in space and on the roof of the house at high noon. Especially since HT can be explored in the broader temperature range (mainly using XRD, which was not possible at LT), some axial and angular dependencies could be studied having a better perspective in mind. As foreshadowed in the previous chapter by DSC and TG, all our substances seemed unstable (DPs apparently more than the other two derivatives). The remaining task was to check to what exact materials they are decomposing to and are those changes also occurring in the protective N_2 atmosphere (are they negligible enough to withstand the influence of residually stored O_i)? If yes, can we use them in an oxygen-deprived environment, given that no HT phase transition transpires?[65,142,146,387] One shall see.

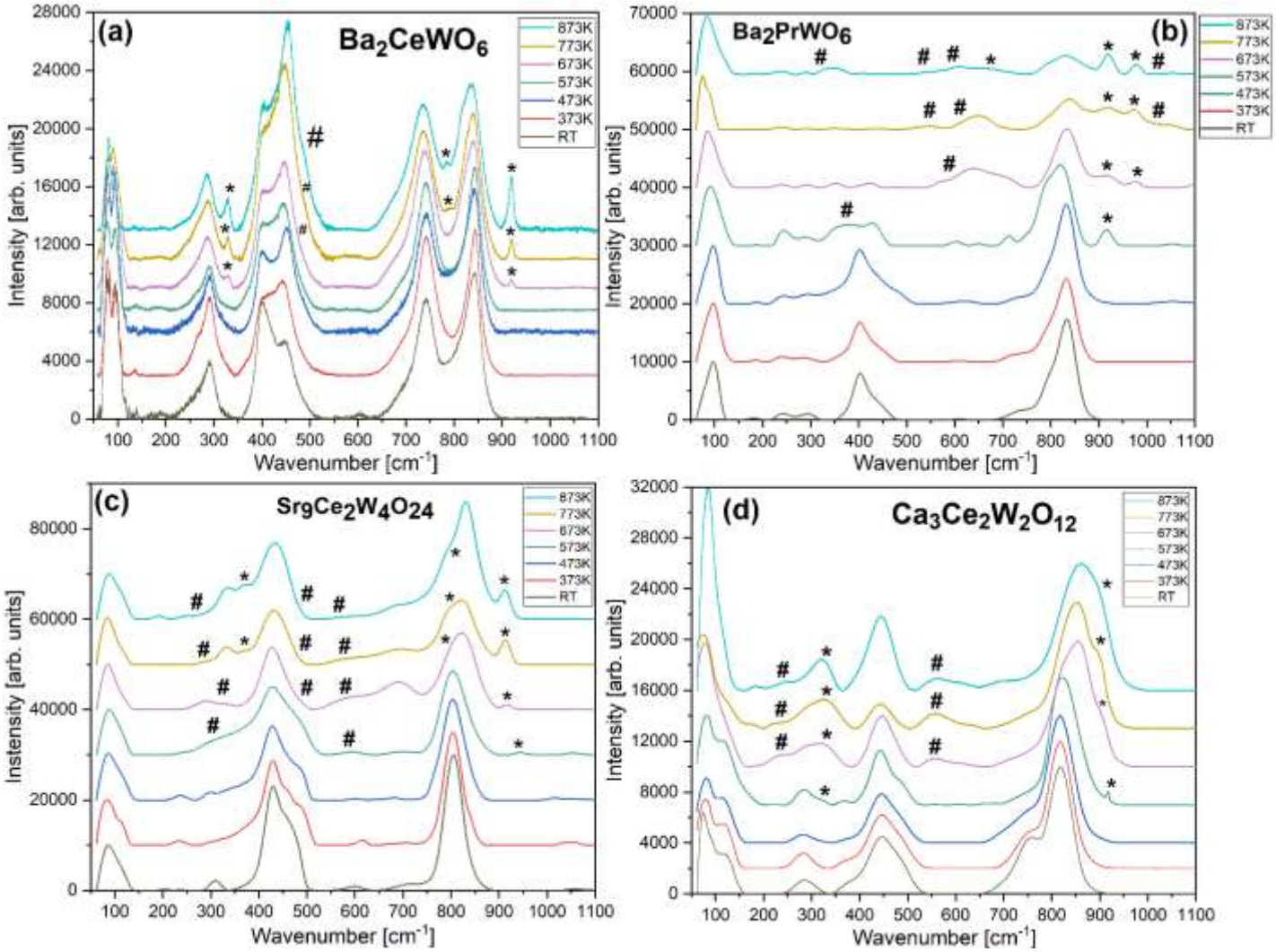

Figure 38 Raman spectra of all studied materials collected in the function of heating from room temperature up to 873 K in the air (without any protective, inert N_2 atmosphere) show noticeable features of decomposition mostly above 573 K. Asterisks mark modes originating from forming tungstates (A_xWO_4). Hashtags signify a group of various defective REO_{2-x} oxides detaching from the original matrix.

Raman HT spectra depicted in *Figure 38,* without N_2 protective atmosphere (air), show many features emerging at temperatures above 573K – they correspond to 1st stage of decomposition related to Ce^{3+} (*Figures 35 & 36*). Browsing the literature,[319,320,322–326,417,431,432] they could be easily associated with mixed valency REO_{2-x} oxides (#hashtags) and later, A_xWO_{3+x} tungstate species (*asterisks) marking gradual changes towards 2nd stage of decay.[2,15,22,23,26,28,203,433] Gradual, visual degradation of the samples could also be traced by the naked eye via prominent discoloration from originally reported colors (*Figure 13*) – from green or brown to i,e, yellowish or greyish powders as shown in *Figure A16*. In N_2, this change was not present – at least not macroscopically, as depicted in *Figure A17*. Since Raman detected something resembling the REO_{2-x} phase sweated off BPW and SCWO surface, that might happen in some highly-limited amount (O_i influence).

This is, however, not enough to pass the final verdict about the usage & actual phases. If there is no natural first or second-order transition in N_2 but pure decomposition, HT powder XRD diffraction patterns in *Figure 39* would be crucial to assess that situation. They were done to confirm that in the air, materials decay to more (barium DPs *Figure 39a,b*) or less (Ca and Sr derivatives *Figure 39c,d*) prevalent phases occur, taking into account all weakening & shifting peaks with additional, new features appearing spontaneously here and there (arrows guide the eye). Amorphization is also a big issue concerning all flattening patterns in the CCWO.

Peaks' FWHMs increase gradually with the temperature to the point where nothing is visible - chemical changes might still occur but are not distinguishable from the noise & glassy structure.[434,435] Another derivative, SCWO quaternary perovskite, seems to undergo only some subtle changes – the least of them all. One could also see some broadening peaks swinging or disappearing here and there (vouching for slow, gradual decay to tungstates & oxides) put in big close-ups in appendix *Figure A18*. It seems that expanded O & W^{6+} content (featured in XPS *section 2.3*) benefits the stability of these structures in general. Measurements acquired later, at RT, from decomposed matrices at specific temperatures assess the status of samples in much greater detail regarding possible chemical mechanisms of decay - see *Figure 40* for reference. Together with already gathered data about minor phases in *section 2.2* & DSC with TG measurements presented in *section 3.4,* one can deduce (to some extent) all the plausible reactions that occur at HT in the investigated materials. Beneath is the list of all currently-recorded materials & impurities:

- Ba_2CeWO_6: BaO (~1000K),[436] $CeO_{2(-x)}$ i.e. Ce_7O_{12},[437] $BaWO_4$, Ba_2WO_5, Ba_2WO_4;[2,313]
- Ba_2PrWO_6: Pr_2O_3 (PrO_{2-x}),[167] $BaPr_2WO_7$,[190] $BaWO_4$, Ba_2WO_5, Ba_2WO_4;
- $Sr_9Ce_2W_4O_{24}$: $Sr_3Ce_2W_2O_{12}$,[438] $CeO_{2(-x)}$, $SrWO_4$,[439] Sr_2WO_5,[440] $Sr_5W_2O_{12}$;[441,442]
- $Ca_3Ce_2W_2O_{12}$: CaO (~1000K),[442,443] $CeO_{2(-x)}$, Ca_3WO_6,[444] $CaWO_4$;[445,446]

Collectively, the XRD database suggests that such decomposition products occur in various ratios using an unprotected atmosphere at HT. That leads us to establish some crude stoichiometric reactions of decay (from *Figure 35*) leading at specific intervals of temperature:

At decomposition series 1 (Cerium ~550K):[416,417,419,420,425]

- BCW: $2\ Ba_2Ce^{3+}W^{5+}O_6 \rightarrow 2\ CeO_2 + 2\ Ba_2WO_4$
- BPW: $2\ Ba_2Pr^{3+}W^{5+}O_6 \rightarrow 2\ PrO_2 + 2\ Ba_2WO_4$
- SCWO: $Sr_9Ce_2W_4O_{24} \rightarrow Sr_3Ce_2W_2O_{12} + 2\ Sr_2WO_5 + 2\ SrO$
- CCWO: $2\ Ca_3Ce_2W_2O_{12} + O_2 \rightarrow 4\ CeO_2 + Ca_3WO_6 + 3\ CaWO_4$

At decomposition series 2 (Tungsten ~800K):[421–424]

- BCW: $2\ Ba_2Ce^{4+}W^{4+}O_6 + O_2 \rightarrow 2\ CeO_2 + 2\ Ba_2WO_5$; $2\ Ba_2WO_4 + O_2 \rightarrow 2\ Ba_2WO_5$
- BPW: $2\ Ba_2Pr^{4+}W^{4+}O_6 + O_2 \rightarrow 2\ PrO_2 + 2\ Ba_2WO_5$; $2\ Ba_2WO_4 + O_2 \rightarrow 2\ Ba_2WO_5$
- SCWO: $2\ Sr_3Ce_2W_2O_{12} + O_2 \rightarrow 4\ CeO_2 + 2\ Sr_2WO_5 + 2\ SrWO_4$

Brief reactions that take place later (continue after +900K - 2nd stage of decay) or their intermediate products are just contemporary (mainly referring to alkaline impurities disappearing after cooling - probably reacting with REO_{2-x}, CO_2, or moisture if exposed to air)*:[442,447–449]

- BCW: $Ba_2WO_5 \rightarrow BaWO_4 + BaO^*$; $BaO + CeO_{2-x} \rightarrow BaCeO_{3-x}$
- BPW: $Ba_2WO_5 \rightarrow BaWO_4 + BaO^*$; $BaO + Pr_2O_3 + WO_3 \rightarrow BaPr_2WO_7$
- SCWO: $2\ SrO^* + 4\ Sr_2WO_5 + O_2 \rightarrow 2\ Sr_5W_2O_{12}$
- CCWO: $Ca_3WO_6 \rightarrow CaWO_4 + 2\ CaO^*$; $CaO + CeO_{2-x} \rightarrow CaCeO_{3-x}$

Now, seeing some evidence about regional stability and all of the processes mentioned above taking place in the air, one can calculate axial and structural parameters (up to roughly ~550K), which would be necessary for future applications and modeling. Ba_2CeWO_6, Ba_2PrWO_6, $Sr_9Ce_2W_4O_{24}$ & $Ca_3Ce_2W_2O_{12}$ data are presented consecutively in *Figures 41, 42, 43, and 44* however, all their linear fits are gathered in *Table 21*.

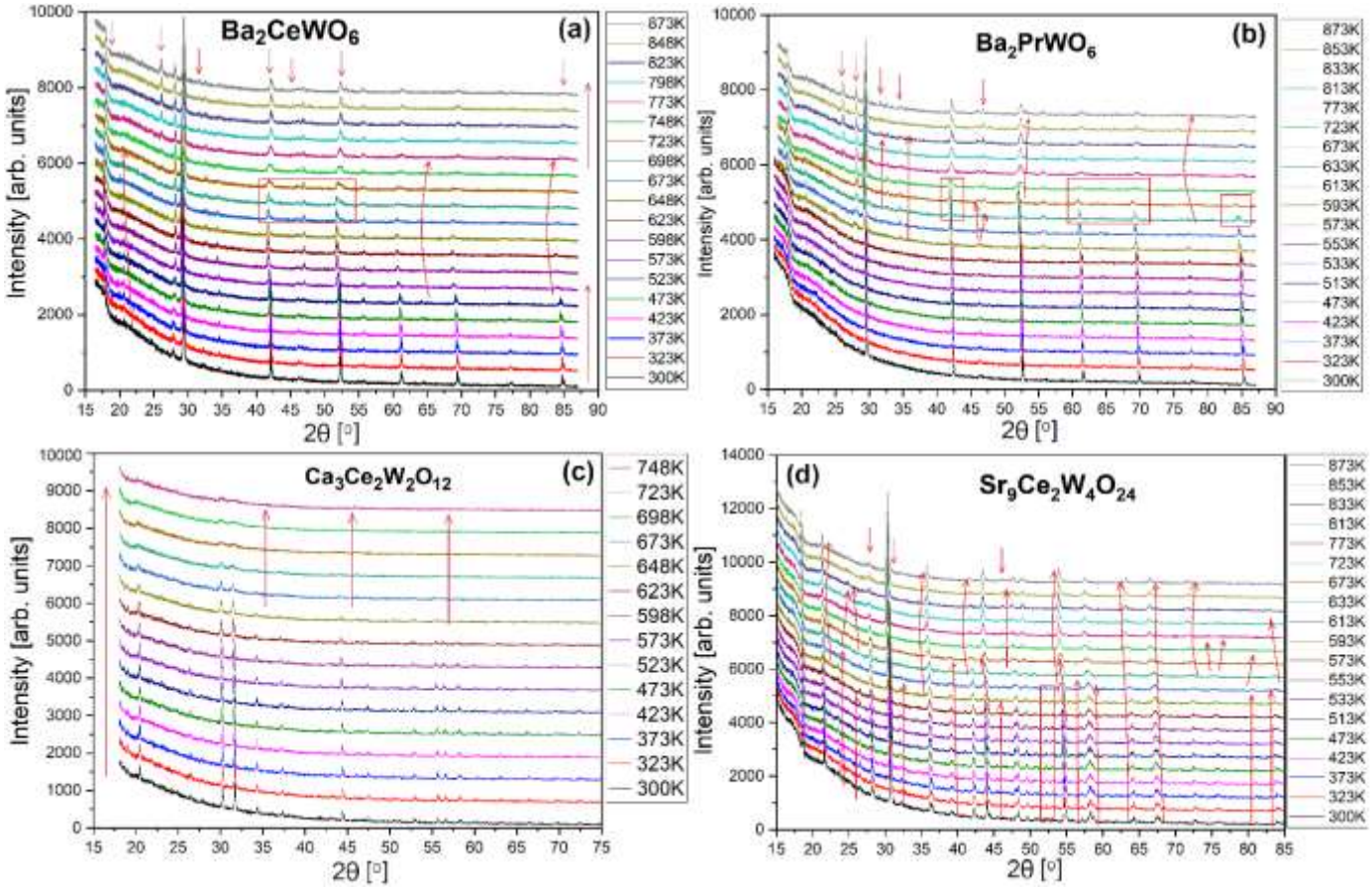

Figure 39 High-temperature powder XRD diffractograms presented the function of heating for all 4 investigated RE-tungstates. Each pair (double perovskites and derivatives) share a similar degree of decay after submerging in hot air - to emphasize those rates, red arrows were implemented to guide the eye regarding a few key features. In (a) BCW and (b) BPW, they are more abrupt, but in (c) CCWO & (d) SCWO more subtle & required assistance in the form of close-ups available in supplementary *Figure A18*.

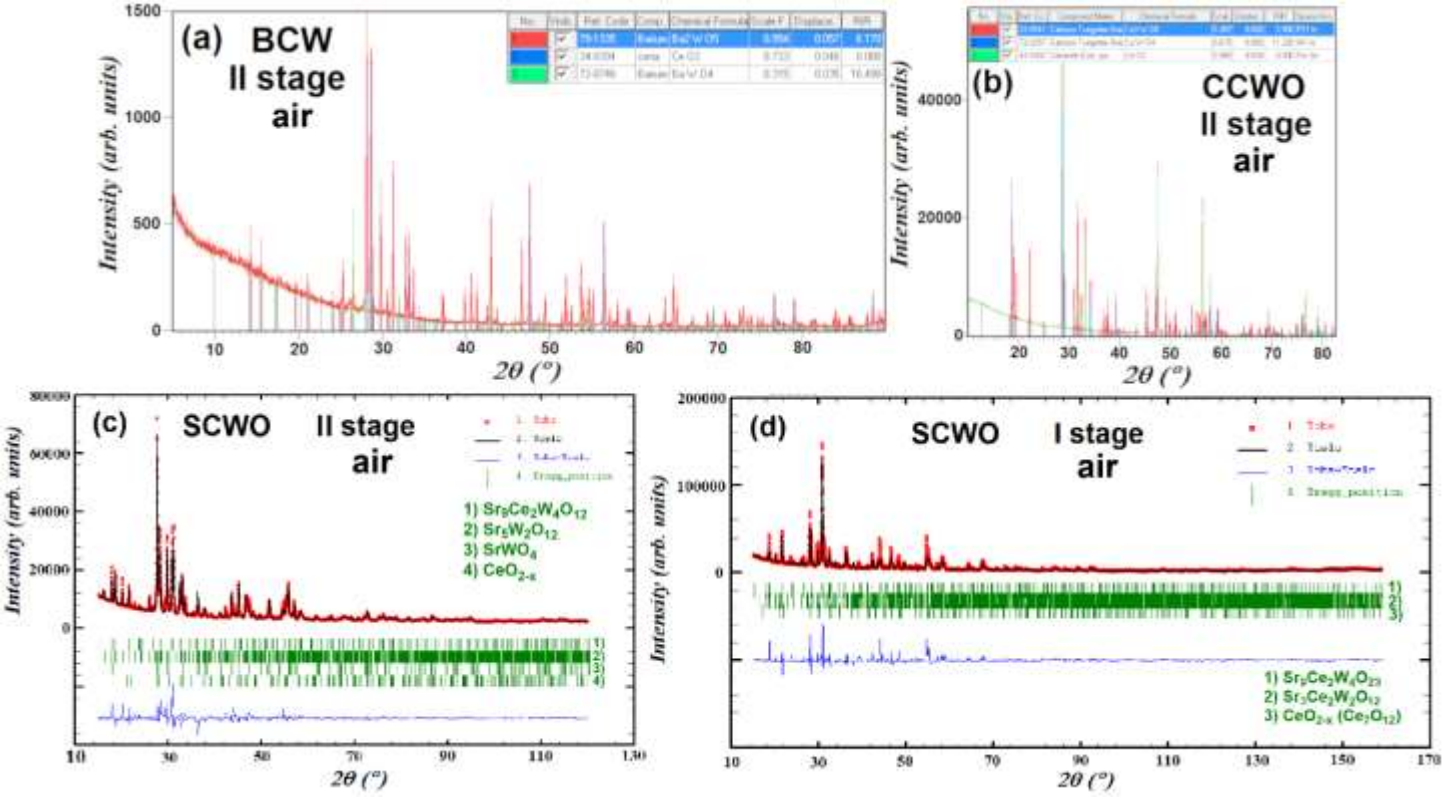

Figure 40 Powder XRD patterns after heating in the air (solid state synthesis without protective environment) at 2nd stage of decomposition temperatures for (a) BCW, (b) CCWO, and (c) SCWO while 1st stage (for the last-mentioned compound) is presented in figure (d). Fitting was performed using the HighScore databank.

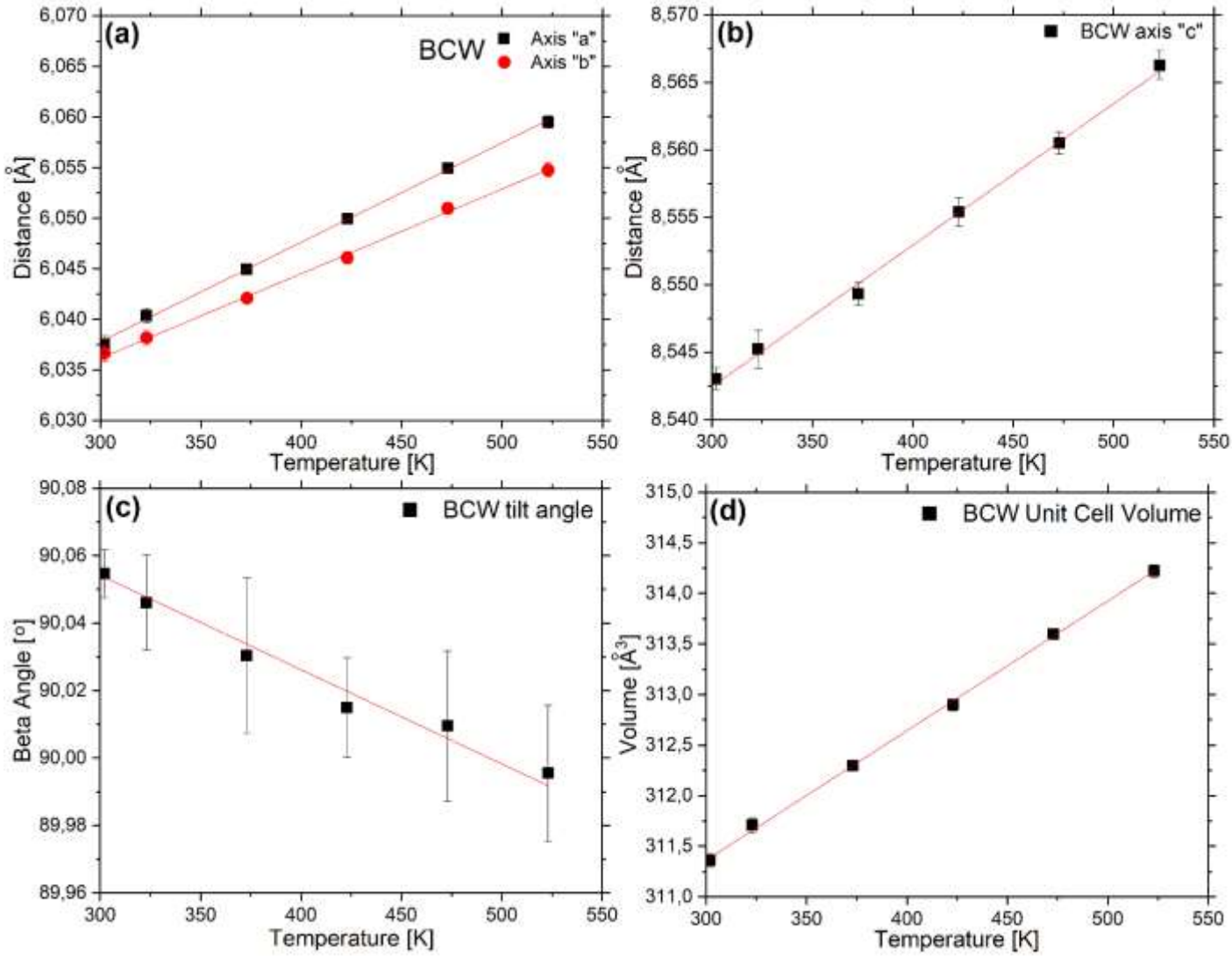

Figure 41 Various unit-cell structural dependencies determined through HT powder XRD measurements for the novel Ba_2CeWO_6 double perovskite. The crystallographic structure was investigated while heating in the air before any possible signs of decomposition were noticed. Figure (a) covers expansion along similar "a" and "b" axes, while (b) presents changes for a slightly longer "c" dimension. Graph (c) showcases a particular case of angular tilting being straightened towards a perfect, right angle, while in (d), a progressive, volumetric expansion can be seen. Red lines are linear fits, after which mean values were derived and stored in *Table 21*.

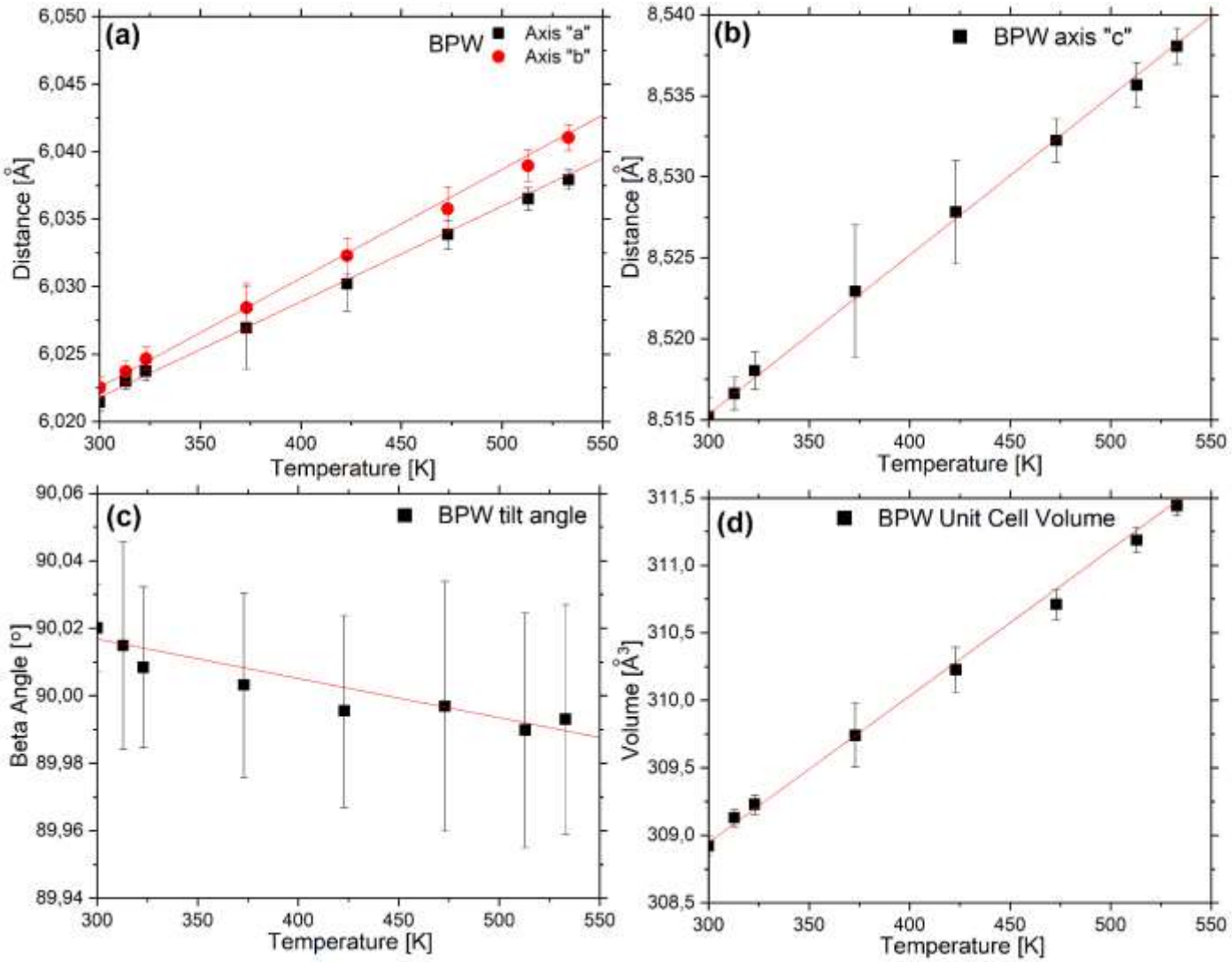

Figure 42 Various unit-cell structural dependencies determined through HT powder XRD measurements for the novel Ba_2PrWO_6 double perovskite. The crystallographic structure was investigated while heating in the air before any possible signs of decomposition were noticed. Figure (a) covers expansion along similar "a" and "b" axes, while (b) presents changes for a slightly longer "c" dimension. Graph (c) depicts a particular case of angular tilting being straightened towards a perfect, right angle, while in (d), a progressive, volumetric expansion can be seen. Red lines are linear fits, after which mean values were derived and stored in *Table 21*.

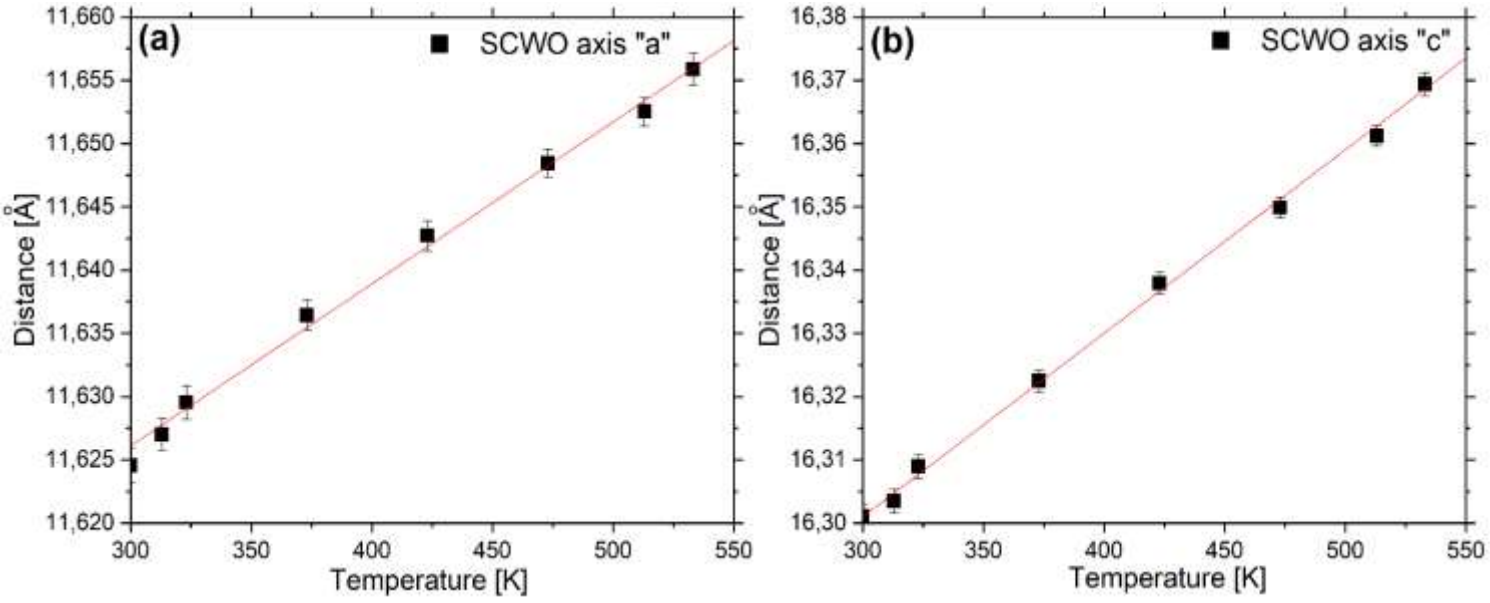

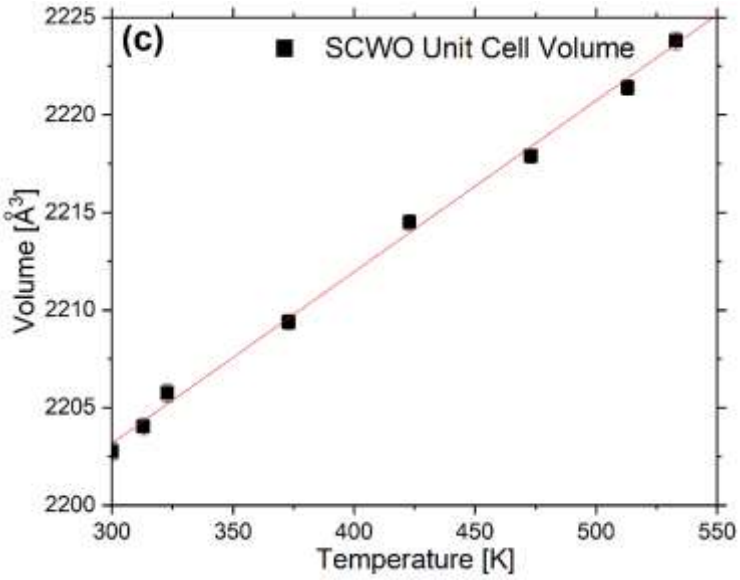

Figure 43 Various unit-cell structural dependencies determined through HT powder XRD measurements for the novel $Sr_9Ce_2W_4O_{24}$ quaternary perovskite. The crystallographic structure was investigated while heating in the air before any possible signs of decomposition were noticed. Figure (a) covers expansion along the "a=b" axis while (b) presents changes for a slightly longer "c" dimension. Graph (c) shows the same unit cell's progressive, volumetric expansion. Red lines are linear fits, after which mean values were derived and stored in *Table 21*.

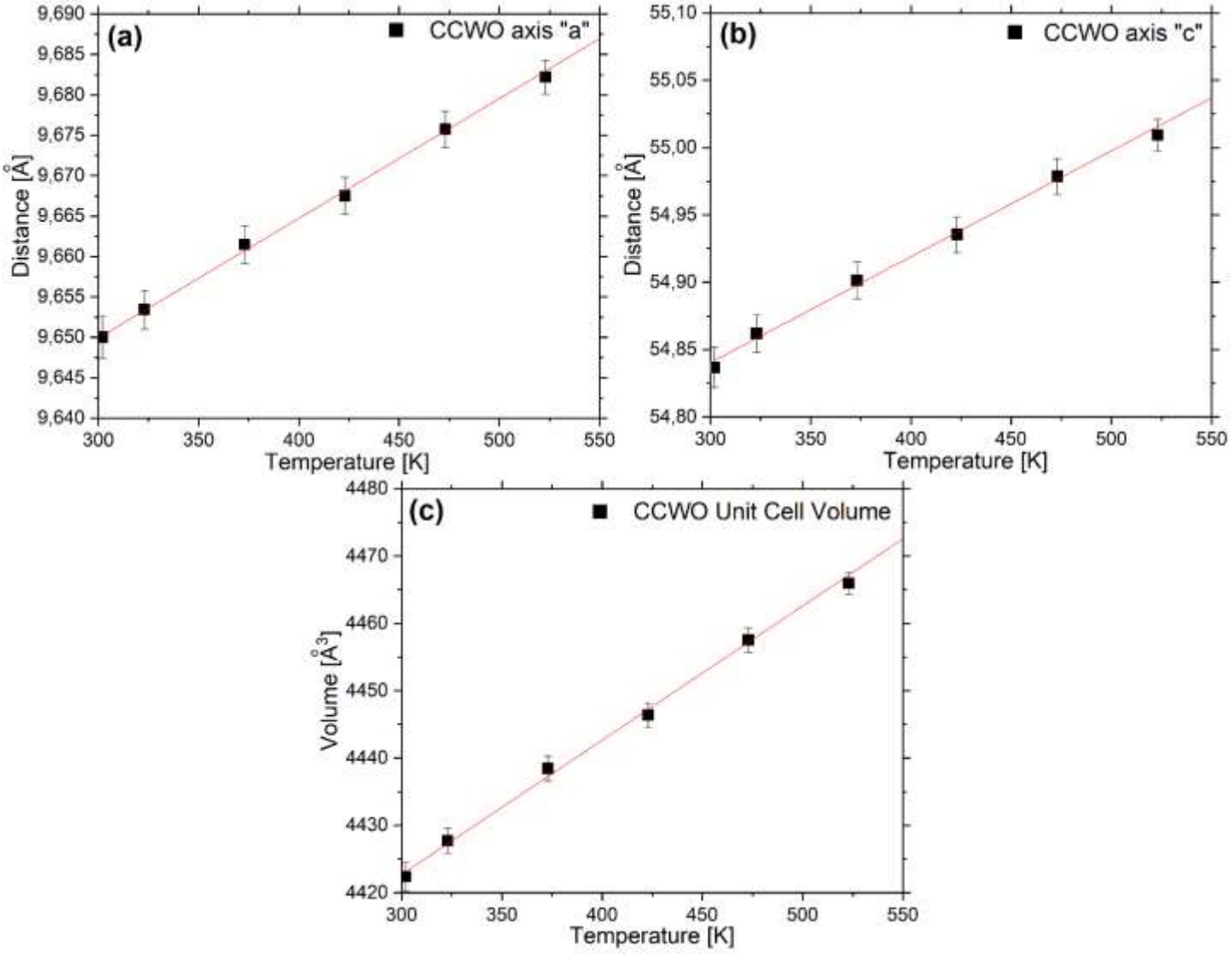

Figure 44 Various unit-cell structural dependencies determined through HT powder XRD measurements for the novel $Ca_3Ce_2W_2O_{12}$ ilmenite. The crystallographic structure was investigated while heating in the air before any possible signs of decomposition were noticed. Figure (a) covers expansion along the "a=b" axis while (b) presents changes for a much longer "c" dimension. Graph (c) presents the same unit cell's progressive, volumetric expansion. Red lines are linear fits, after which mean values were derived and stored in *Table 21*.

Table 21 Crystallographic expansion coefficients deducted from powder XRD data presented above in function heating while submerged in the air for all investigated materials just before their decomposition commenced (roughly above 500÷550K).

Sample	Axis direction *[Å/K]* ($\times10^{-5}$)			Angle *[deg/K]* ($\times10^{-4}$)	Volume *[Å³/K]* ($\times10^{-2}$)
	a	b	c		
BCW	9.83(0)±0.14(0)	8.36(9)±0.18(5)	10.48(7)±0.28(6)	-2.79(8)±0.17(7)	1.28(2)±0.01(9)
BPW	7.08(0)±0.17(2)	8.06(5)±0.16(3)	9.83(3)±0.23(2)	-1.16(7)±0.10(5)	1.08(6)±0.02(7)
SCWO	12.81(7)±0.35(0)	---	29.01(7)±0.48(7)	---	8.78(3)±0.19(7)
CCWO	14.19(6) ±0.29(9)	---	78.63(1)±2.17(7)	---	19.94(1)±0.47(2)

As for barium DP's, the expansion coefficients seem quite unremarkable,[449–452] but the presence of the progressive angle tilt somehow creates a solid base for a lowering symmetry phase transition at some temperature points – in our case, probably monoclinic noticed earlier at LT below 200K (see *section 3.1*).[453,454] This also does not neglect any possibility of other transitions at HT if only these compounds were stable enough (even concerning inert conditions). Derivatives, especially CCWO, have substantially large coefficients but also possess giant unit cells.[450,455] This fact, in comparison with abundant defects, vacancies, and partially-substituted A^{2+}/RE-sites, might also lead to some interesting properties via mending, rebonding, and lack of internal lattice-relaxation issues when exposed to stimuli in the opposite direction (like decomposition after compression or irreversibility while cooling from HT),[456–458] however without any progressive tilt (angular dependency) the only thing which could change the unit cell (as LT-HT measurements seemed uneventful) is the packing order while axial expansion/regression transpires – those would however be only related to transitions within the same Laue group.[459]

4. Optical studies with and without RE dopants

4.1 Luminescence - excitation and emission spectra

Lastly, PL studies regarding possible future solar panels and sensory device applications. All this detailed research up to now set a firm base towards divulging possible phenomena that could be encountered in this most promising field of study. It has proven worthwhile since there is still a chance for those materials to benefit the industry despite them turning out to be weak, unstable phosphors of volatile/alternating structural nature. Some of them are thoroughly divulged upon, the others briefly speculated. The hypothesis suggests that with more sophisticated techniques, one could confirm a few of the most questionable properties but with more available time & resources reaching outside standard Ph.D. capabilities. Even though a lot must be done addressing all of the registered phenomena thoroughly, the chosen scope of literature and the given initial R&D approach must suffice for now.

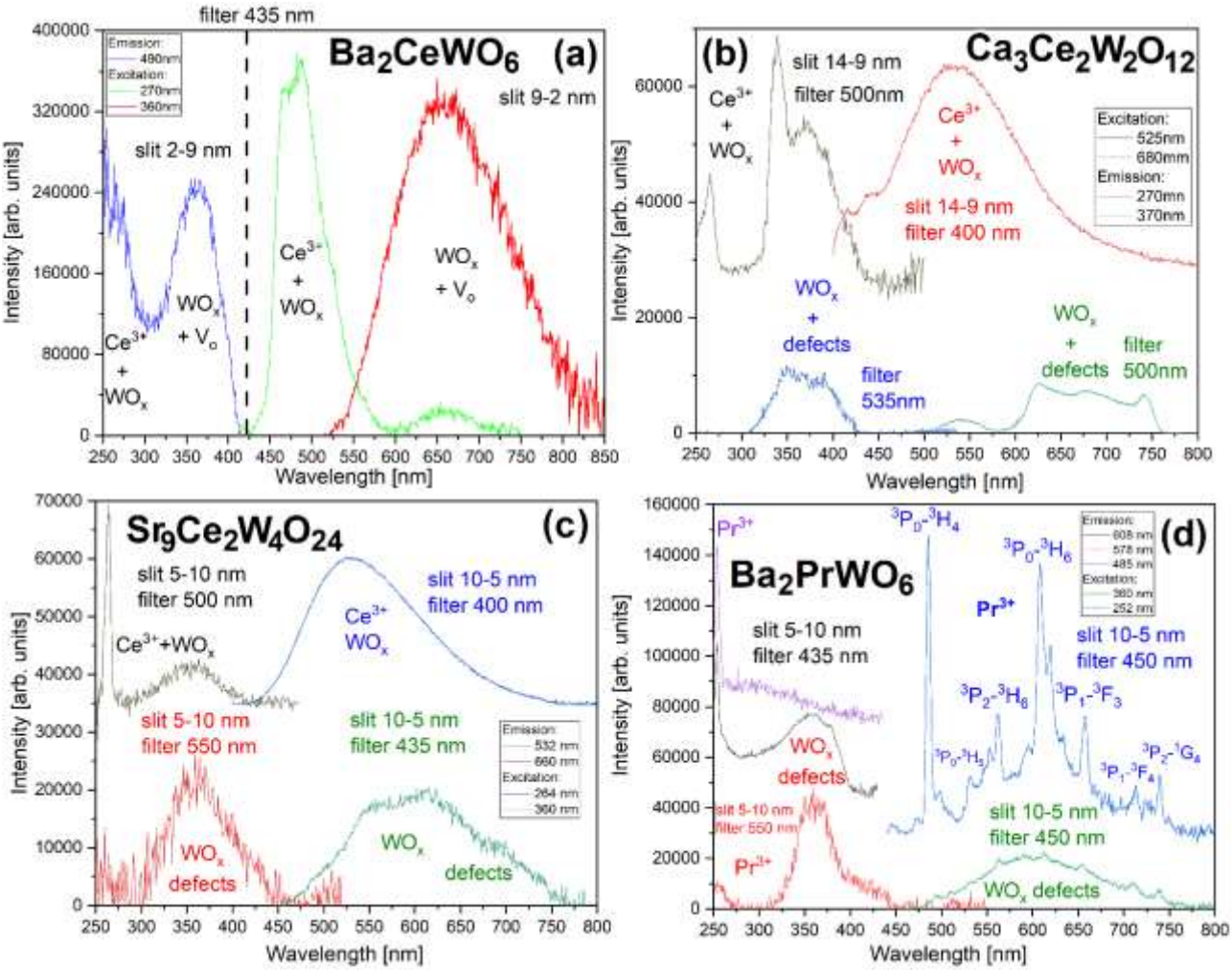

Figure 45 Excitation and emission spectra taken at ambient conditions using Xe lamp for all 4 investigated RE-tungstate materials: (a) BCW, (b) CCWO, and (c) SCWO cerates alongside with (d) BPW praseodymate. Adjusted monochromator's entrance and exit slits reflect the maintained, relative resolution of registered bands.

The excitation and emission spectra of tungstates (WO_x), visible above in *Figure 45*, are actually quite typical for many materials from this widespread family.[2,5,8,202,460–465] Wide blueish-violet absorption band at around 360-380 nm emits further at an even broader, greenish-yellow 500-600 nm range. Sometimes V_o/O_i complexes introduce deep red components in low energy above +630 nm. This is even a typical, defect-related behavior encountered in our previous scintillator – bands positioning could change slightly, though with respect to SG & crystal field's strength (as seen in SCWO & CCWO).[466–468] Since tungsten is a common component in every matrix of our novel materials, their appearance is anticipated & much appreciated, given that they could enhance future energy transfers considering the cooperation with RE ions. Speaking of which, RE ions like Ce^{3+} (*Figure 45abc*) often contribute to PL by enhancing the total intensity & broadening the range of excitation into UV.[469–472] The only issue might come forth from a sharpish (not in the case of BCW) excitation band at around 270 – 250 nm. In many oxides, it is referred to as a charge-transfer band that, if hit directly or above, could trigger an e^- transfer between RE-W and nearest O defects (not exactly being at 2- state).[468,473–479]. Pr^{3+} in *Figure 45d* has a very similar peak, closer to UV ~252 nm & behaves similarly, at least relatively, considering its multiple, lower electronic states creating much more sharp lines localized on the bulgy WO_x emission.[470,480,481] (Ce, in comparison, has more pronounced non-radiative relaxation between higher and lower ^5D states entangled with W 5d/4f states and emits poorly towards ^2F levels).[482] More about that phenomenon later, but for now, it is worth noting that considering the general performance of these materials, it will be essential to work around those NUV bands (slightly above at ~228÷232 nm, as it turned out) since longer excitation

wavelengths, typical for such RE ions (such as 325 nm for Ce^{3+} or 430-460 nm for Pr^{3+}), did not perform as well in terms of acquiring any actual response from the samples as can be seen in supplementary *Figure A19*. Transitions registered above and beyond that NUV threshold were the only detailed & strong ones to hold any significance despite having smaller absorption cross-sections. They will also be crucial regarding planned down conversion with dopants (BCW, CCWO, SCWO: (sensitizers) Pr^{3+}→ (mediators) WO_x→ (activators) Yb^{3+}; BPW: (Ce^{3+}→Pr^{3+}) hν donors → (mediators) WO_x → Yb^{3+} hν acceptors) – working with the constituents (BCW, CCWO, SCWO – Ce; BPW - Pr) and fighting against PL quenching issues (while changing their total mass % concentrations to optimize the set) as depicted in *Figure 46*. For true amounts of PL-active (3+) dopants, please refer to *Table 11* & *Figure 25* in *section 2.3.* All basic PL components were determined from all the convoluted spectra & verified through the literature.[483–488] Each specific contribution is visible via colorful insets below. To avoid possible confusion and to make the graphs more legible in terms of upcoming PL qualitative analysis, all *Figure 46* transitions marked as RE (Ce – purple, Pr - blue)$^{3+}$/WO_x (orange) and V_o+O_i defects (red) were summarized in comprehensive energy schemes shown in *Figure 47.*

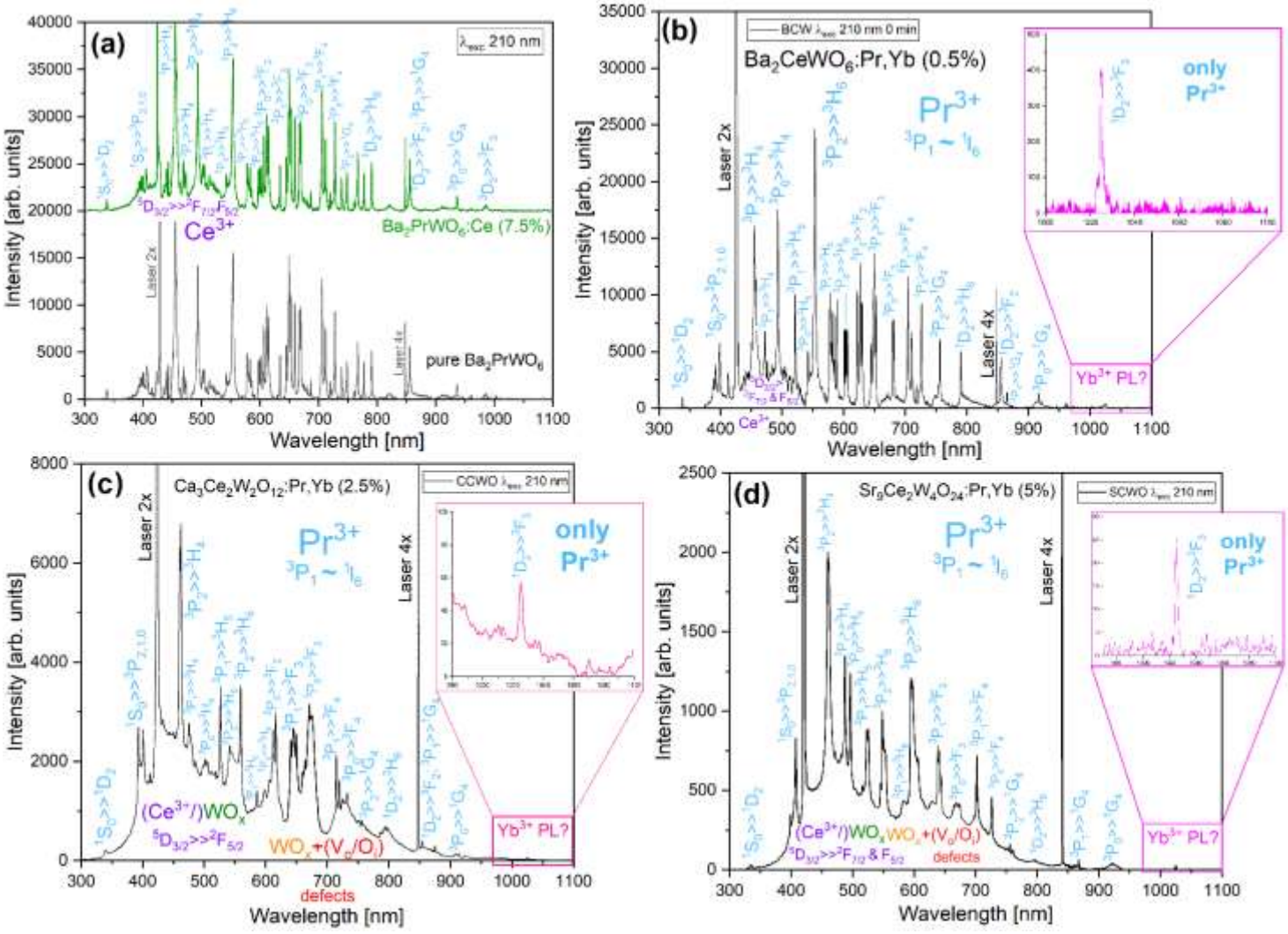

Figure 46 Fully described photoluminescence spectra of all RE^{3+} doped tungstates excited with 210 nm laser light under ambient conditions: (a) pure BPW double perovskite compared to BPW matrix hosting 7.5% of Ce, and the rest (b) BCW, (c) CCWO & (d) SCWO containing 0.5, 2.5 and 5% (Pr, Yb) respectively.

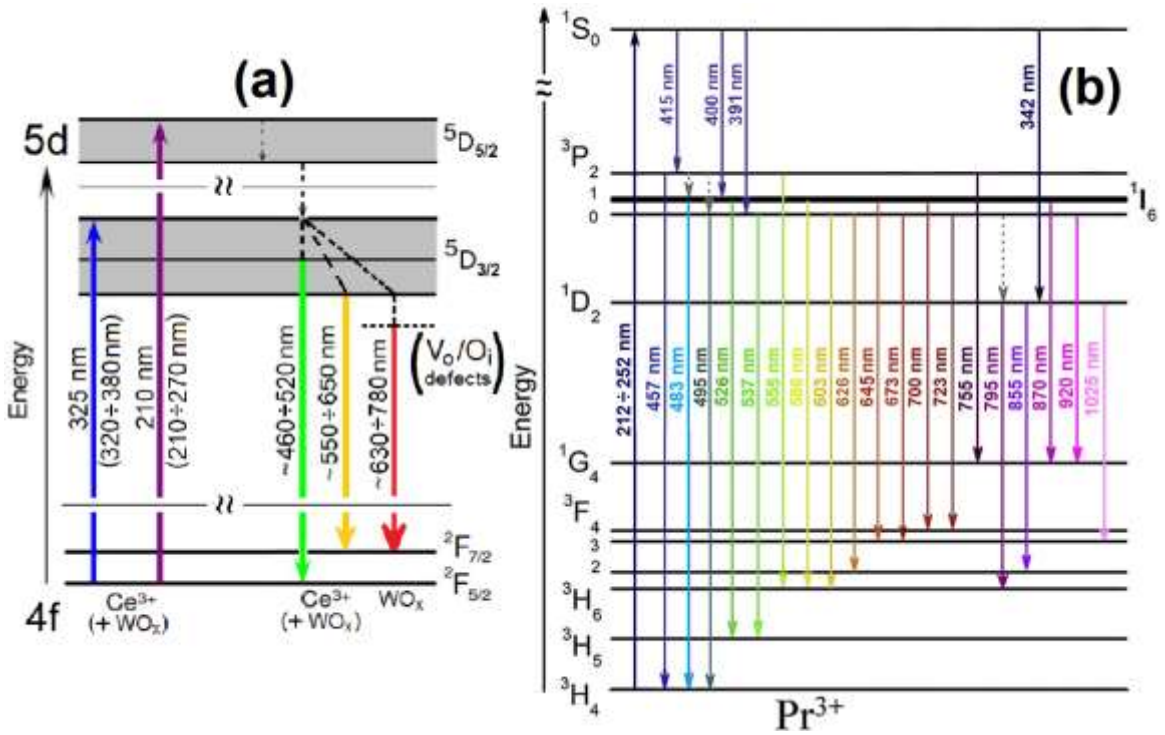

Figure 47 Energetical schemes of observable: (a) Ce^{3+}/WO_x and (b) Pr^{3+} emission bands.

As Ce^{3+} emission is unremarkable, it would not be much elaborated upon; however, an interesting fact is that one can excite easily with weaker (not essentially narrow) near-violet light, but, Pr^{3+} requires more potent (intense) UV light to have any response at all. That last (preferably 215 or 232 nm) source brings us to the bottom of the $^1S_0$ level in Pr-related compounds where e^- most likely relax to lower ^3P states. The mechanism of relaxation is probably fully radiative since all $^1S_0 \rightarrow {}^3P_{2,1,0}$ bands are visible just before double (2×) laser lines in all Pr-doped materials held in Figure 46, but they are quite weak – especially $^1S_0 \rightarrow {}^1D_2$ which is not always or barely visible around 342 nm.[16,489] Most energy is presumably used further in a cascade of deexcitation processes towards much lower levels. Here, worth noting is $^1S_0 \rightarrow {}^3P_2(\ldots){}^3P_0 \rightarrow {}^3H_4$ passage resembling quantum cutting in NUV-blue region close to 400-450 nm. Also, closely overlapping $^1I_6$ and $^3P_1$ states - differentiating between one another would be quite a daunting task, so a broader $^3P_1$ mark was used instead as an abbreviation. Together with the $^3P_0$ state, they would theoretically be the sensitizing key of Yb (activator) by quantum-cutting red emission lines towards $^3H_6 \div {}^3F_4$ levels.

Furthermore, the most problematic aspect was encountered here - the appearance/composition of the area shown in graphs as their pinkish insets. The last, almost vacant region where Yb^{3+} should have been, given theoretically planned energy transfer (*Figure 2*) and aforementioned quantum cutting (but instead of blue should be the red region).[294,297,298,306,307,490,491] As it turned out in *Figure 48abc*, only direct excitation shows anything at all and, what is worse, only weak peaks at helium-level temperatures where they should be quite radiant.[492–494] Although an interesting stark-splitting effect was spotted and several dependencies were observed: one, unexpected (6>4) being confirmed by two different pulsed laser wavelengths – visible under 917 but not during 978 nm excitation as seen in *Figure 48d* followed up by selection rules supported by weak kT effects; and the second – BCW time-resolved uprising of slowly strengthening weak Yb peaks.[492,493,495–497] This ion did not act as a theoretically planned hν activator. The actual culprit was surprisingly not only weak effectiveness and unfortunate coloring of the samples (derivatives) but also a time-resolved $Yb^{2+\rightarrow 3+}$ evolution (barium double perovskites) as seen in *Figure 49*. The first hint about the latter phenomena is suggested in the next chapter, where a direct, internal RE↔W charge transfer appears to be dumping electrons from RE to W during subtle NIR illumination, but, as it will turn out later on, another chemically oxidizing agent, localized in the interstitial gaps of the crystallographic plane, might be responsible for such oxidizing, PL-enhancing behavior. Inversely, it might also be accountable for the reduction of Yb during the synthesis by feeding its electrons through shallowly placed bands while being submerged in Ar:H_2 medium [303–305,498,499]

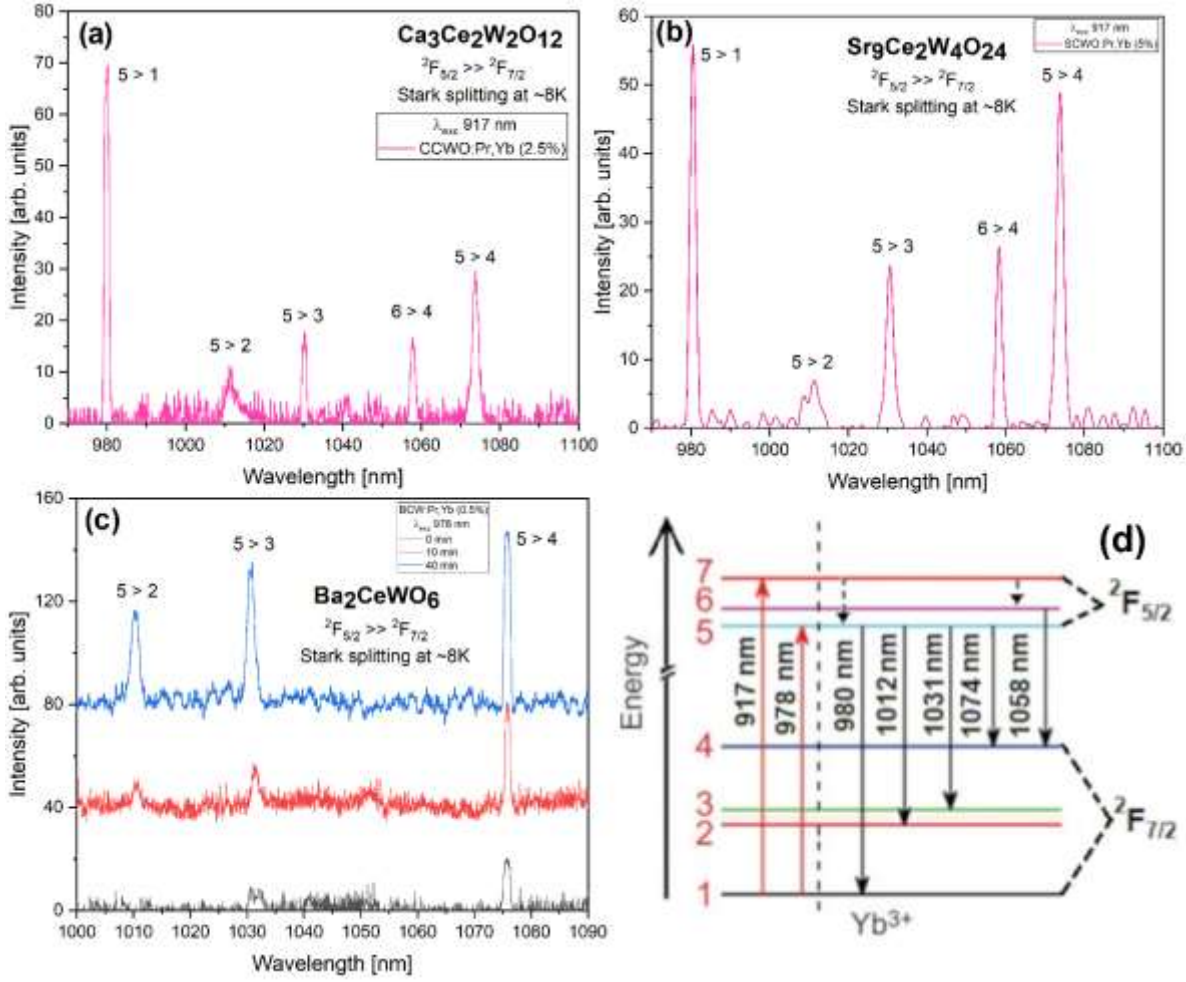

Figure 48 Weak but stable Yb^{3+} emission registered solely under characteristic NIR light excitations for tungstate derivatives at LT: (a) CCWO, and (b) SCWO featuring prominent Stark splitting under 917 nm wavelength. Unexpectedly strengthening time-dependent emission of BCW double perovskite is shown in figure (c) using a slightly weaker 978 nm excitation. Time refers here to the relative period of 210 nm Pr^{3+} wavelength exposition measured from the start of the experimental cycle. To emphasize exclusive Yb^{3+} PL bands, an energetical scheme of observable transitions was constructed in figure (d).

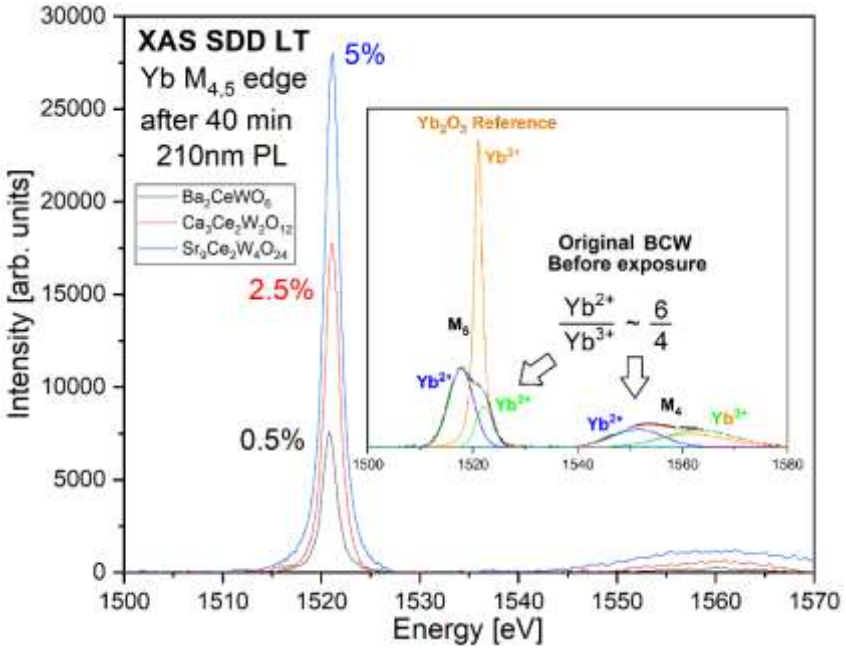

Figure 49 XAS Yb LT M-edge spectra presenting prominent changes in charge states after 40 min of exposure to UV λ_{exc} = 210 nm light in comparison to the original composition & Yb_2O_3 reference registered at RT (as inset from *Figure 25b* shows).

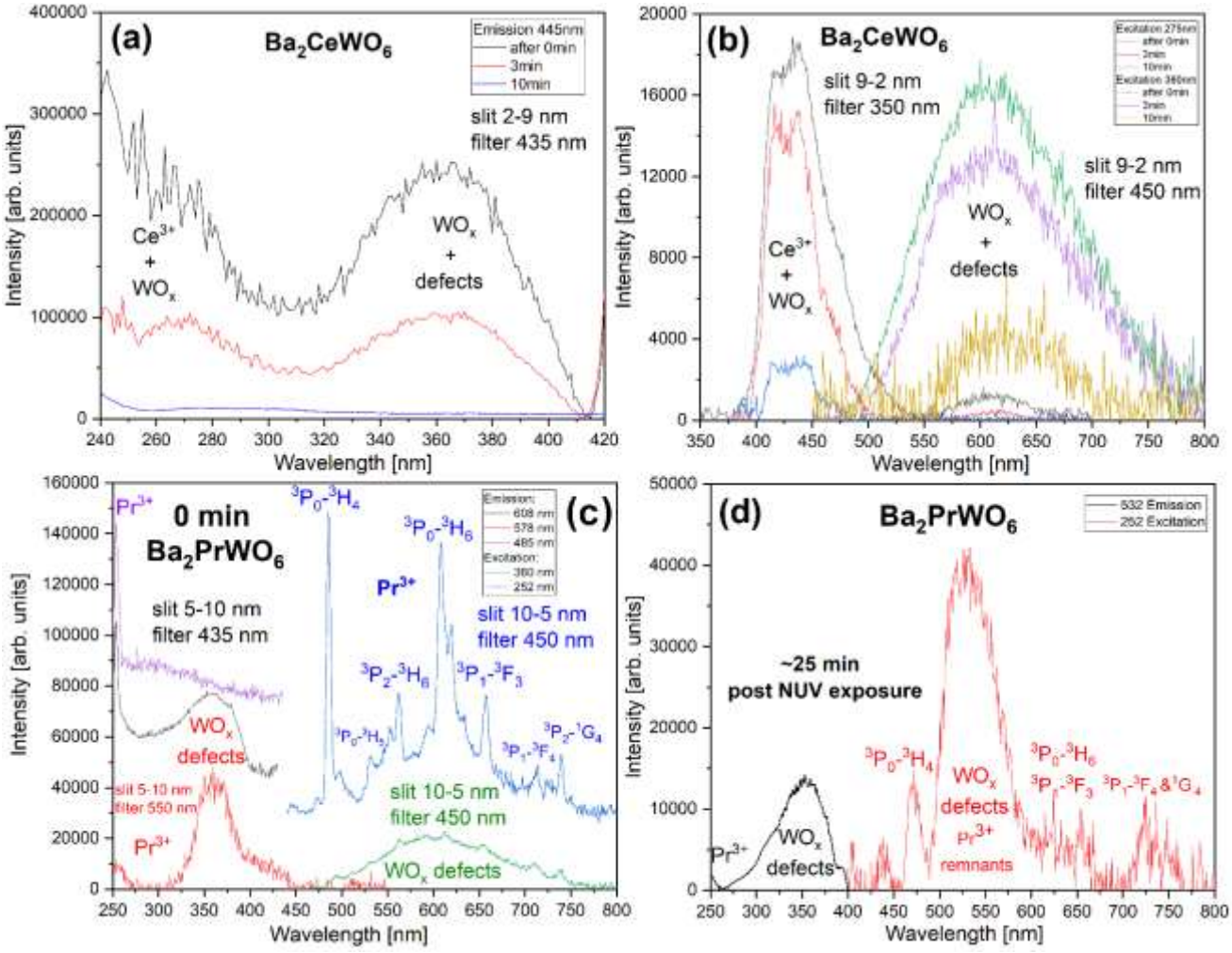

Figure 50 Time-resolved evolution of excitation end emission spectra in barium double perovskites prone to charge-transfer/photobleaching effect: simplistic (a) excitation and (b) emission bands of BCW are presented on the top while more complex BPW on the bottom (c). Post-NUV exposure data was presented on separate figure (d) to avoid illegibility final.

4.2 Charge transfer & photobleaching phenomena

Ytterbium bands in *Figure 48* were not actually the first signs to pinpoint us in the direction of charge-transfer phenomena – they were just luckily encountered cases of strengthening PL in contrast to previously recorded excitation/emission spectra in *Figure 50* while searching the area for stronger, repeatable signals. Only by considering such bizarre behavior were the measurements once again repeated, and some key features were quickly distinguished during weak, time-resolved illumination with the Xe lamp. It was first considered an equipment error while investigating specific excitation/emission bands. However, this assumption was quickly discarded since moving from place to place/exchanging the sample (placing a new portion) had similar outcomes. As PLE & PL spectra in *Figure 50* indicate, in both barium RE tungstates, all well-distinguished bands dropped with time – some faster (less detailed BCW in *Figure 50a,b*) than the other (BPW - *Figure 50c,d*) and did not recover if left in the dark. That was strange, considering that acquired derivatives (SCWO & CCWO) did not show such tendencies and remained the same, as seen in *Figure 45*. The next logical step was to check what happened to the PL-active ions since the sample visually did not change. As X-rays and EPR spectra of exposed

DPs samples shown in *Figure 51*, something regarding B-site ions indeed did change. When compared to the original (not exposed to light), signal-rich XPS and XAS spectra in *Figures 19 & 20* from previous *chapter 2.3*, it becomes evident that previously balanced matrices hosting a mix of RE^{3+}/RE^{4+} cations were drained entirely out of electrons changing into PL-inactive (Ce and Pr)$^{4+}$ species while W^{5+} ions were flooded by them turning completely into W^{4+}. EPR seems to follow such claims when compared analogically to unexposed samples in *Figure 34*, *chapter 3.3*. In BCW, the Ce^{3+} signal completely disappeared at LT, and, given the activation mechanism of RE ions, that could only prove its conversion to Ce^{4+}. Pr^{3+}'s case is slightly more complicated since it is visible only in horizontal fields. Pr^{4+} would be visible under given perpendicular fields only if the signal was not jammed by antiferromagnetic phase transition below ~90÷110K. RE bands are already broad & weak thanks to polycrystalline, anisotropic domains, and defects, but at least some evidence could be told what is actually happening in BPW at RT – after bathing in reducing 1:1 Ar/H_2 conditions, both Pr^{4+} and O_i would disappear but, RE are not visible at that temperature point so these sharp signals are definitely related to encapsulated O species. As mentioned, oxygen could be partially involved in the charge transfer/oxidization procedure. Here, after NUV irradiation, interstitial oxygen or dangling O^- species disappear (just like ozone) and presumably integrate with the lattice. This process makes the matrix enriched in oxygen – typical for antiferromagnets - where new O^{2-} ions are presumably also created by devouring electrons from Pr^{3+}, making the matrix further PL inactive. Thus, the aforementioned drop in excitation and emission spectra. There is most likely some competition between O and W ions since the most unstable W^{5+} (being already in the minority) disappears almost instantly.

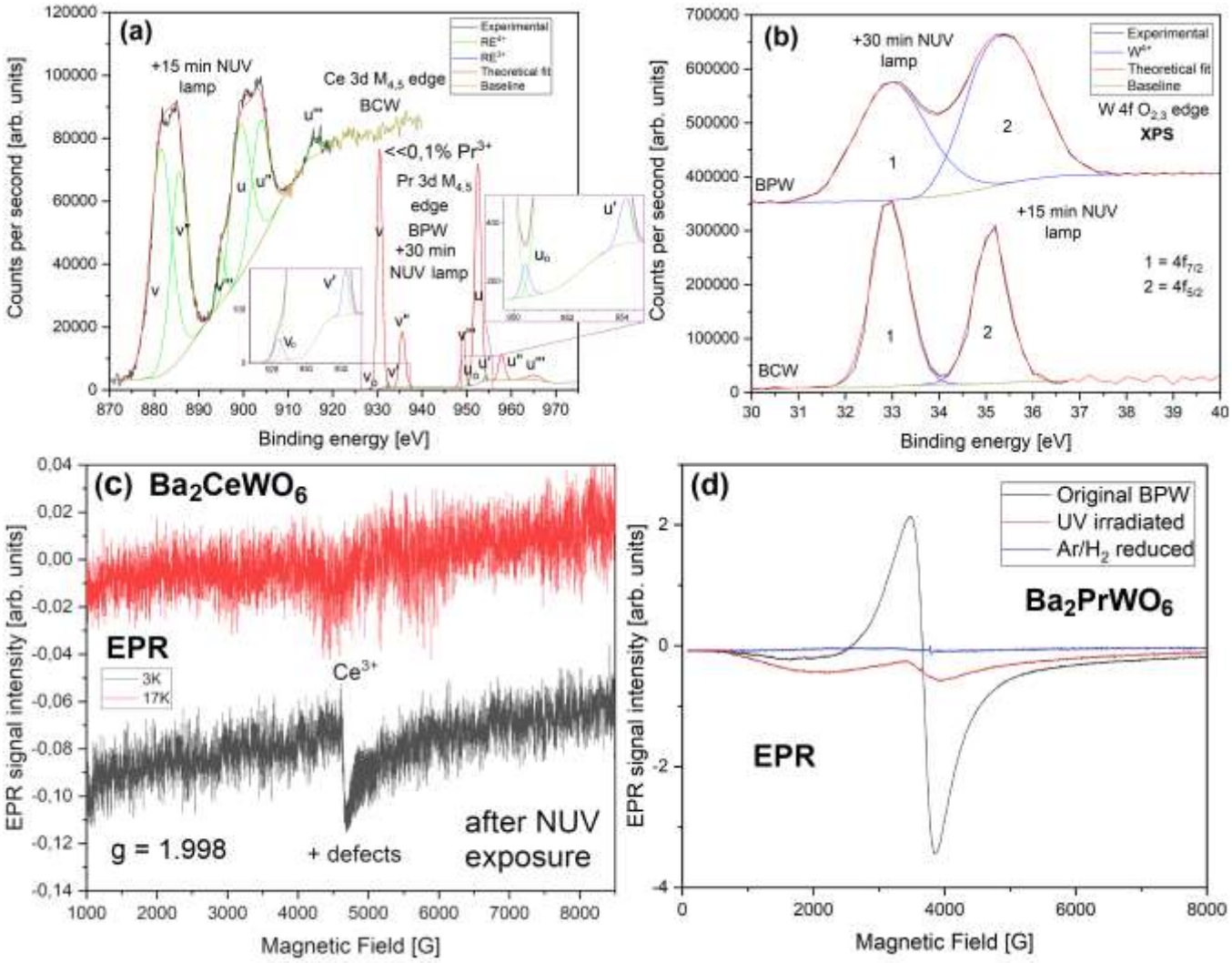

Figure 51 XPS ambient spectra of both, undoped tungstate double perovskites (Ba_2CeWO_6 & Ba_2PrWO_6) investigating changes in ionic states of crucial B-site ions after brief (15 & 30 min respectively) NUV exposure: (a) Ce/Pr 3d spin-orbit multiplets, and (b) W 4f dublet shells. EPR was done in consecutive order regarding the same issue for (c) BCW at LT & (d) BPW but at RT.

Further discussion revolving around changing PL requires some clarification regarding the actual chain of events and the causality of facts that transpired during this work. Since the data presented here are ordered arbitrarily, to truly understand the final outcome, one must piece together scattered evidence from:

- RT PL spectra at weak, Xe lamp excitation in any gas atmosphere (done first & already presented above in this and previous *section 4.1*),
- HP PL experiments in inert PTM (Ar) using lasers (described below),
- LT PL in vacuum-pumped or inert (He) conditions using lasers (described further below),
- RT PL spectra at strong laser excitations in the air (elaborated in the next *section 4.3*).

Starting with HP PL, there should be no surprise why such in-situ investigations presented in the appendix *Figure A20* came up short with not many remarkable results and were dropped not long after considering the aforementioned fast PL quenching.[161,500–502] While measuring Raman spectra with simultaneous access to 325 nm excitation wavelength (stimulating broad WO_x+V_o bands in undoped samples), the changes that transpired during compression (in air-deprived, Ar PTM) were quite subtle, noisy, and rapidly diminished to almost 0 intensity. The emission in more stable derivatives persisted until the investigable range's top pressure limit/chosen GPa aim. While approaching the region of possible phase transition (*Figure A20*a,b SCWO ~15 GPa, and *Figure A20*c,d CCWO ~9GPa), both sets of data swing slightly in positions changing the progression trend from weak blue to red-shift and vice-versa when going back. CCWO's PL even increased slightly until 12 GPa, which is the presumed endpoint of the eventual change to *C*2/*c* or *C*2/*m* SG.[71,72] At least both changes are reversible and to a similar degree considering the noted hysteresis on Raman spectra. In *Figure A20*e,f the BCW double perovskite is presented as a contrasting issue. No phase transition was observed, but the same problem, consistent with results acquired in *Figure 50*a,b takes place. Not only the PL is quickly diminished during compression but, it is also irreversible. Moreover, it is indefinitely quenched when exposed to radiation at the same place for an extended period of time (while maintaining a certain level of pressure). That proves that the charge-transfer process is at least partially responsible and takes place mainly during light stimulation. Not much can be experimentally said & done to estimate how HP influences such a phenomenon (it definitely does, as can be seen in literature)[503–507] but, for sure, it seems hopeless to look into energy-transfer and band-gap-related phenomena if no actual response from the sample is received. Neither full range of PL interest could be registered and analyzed before photobleaching commences, so the only natural way to progress further is to drop HP & investigate the region at lower temperatures where the emission should naturally increase.[508–513]

While exposing undoped cerates at LT (in a function of heating while being vacuum-pumped in helium-filled cryostat), nothing unusual happened in the formerly presented region of spectral interest (WO_x), as seen in *Figure 52*. If there was any PL, it was weak, broad, and bared the same 2-component (RE+WO_x, and WO_x+defects) characteristics as those seen before in *Figure A20*. Only results for the two most extreme temperatures were shown for derivatives regarding their borderline cases in *Figure 52*a,b (solely related to intensity changes). PL spectra expectedly gain strength when approaching cold helium temperatures. Especially BCW exposition had an

interesting outcome, so it was expanded upon in *Figure 52*c to d. At the lowest temperatures, PL was relatively stable (at least time-wise compared to RT quenching). Presumably, the electron charge carriers were frozen (as lack of any features at LT XAS TEY measurements shown in *Figure 33*)[514–516] or the phase transition had some stabilizing effect on PL-active ions (RE^{3+}/W^{6+}) - probably by manipulating fixated states of the electronic structure.[363,517–520] Considering that outcome, those cryogenic conditions could scientifically enable a more detailed approach to efficiently investigate other bands while using more befitting, intense, but pulsed illumination (on OPO). For sure, the duality and the constant presence of registered signals together with their significant improvement/enhancement when joined with Ce^{3+} (now not only dopant but constituent) signifies that they are at least partially tied/codependent, as stated in our previous work where it was still a dopant.[2,521] This general behavior will benefit the amount of gained intensity and serve as a reference background while stimulating more complex matrices containing other RE (Pr,Yb) dopants for any signs of efficient down-conversion.

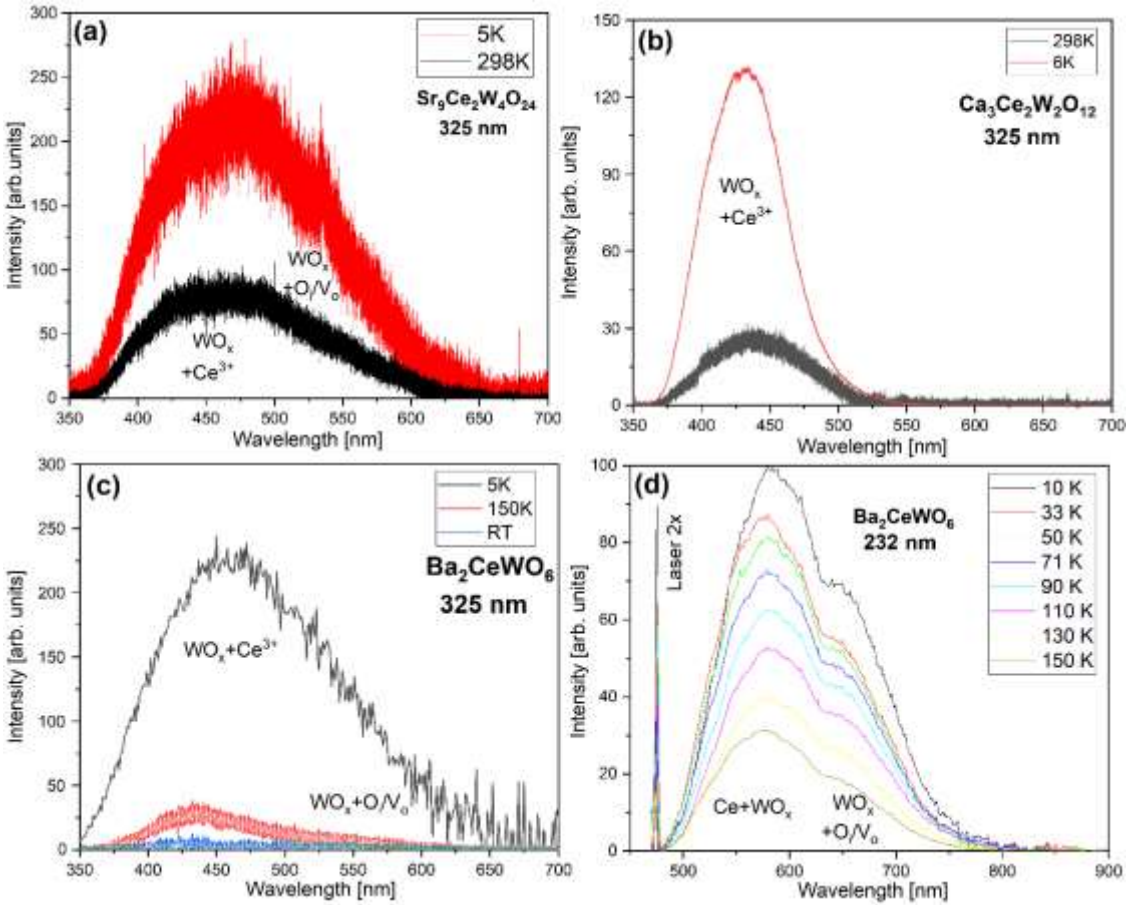

Figure 52 LT PL spectra of undoped cerium tungstates in the heating function present only weak WO_x emission bands influenced by various structural defects or Ce^{3+} (double component/shoulder feature). Figures (a) & (b) present both SCWO & CCWO derivatives, respectively, with (c) BCW double perovskite measured under NUV 325 nm laser light while being investigated in situ by Raman spectrometer in the most extreme temperatures. Figure (d) shows the same last compound under more effective 232 nm excitation with more detailed, intermittent steps.

In Pr-doped samples, the situation indeed became more complicated. While derivatives' PL decays smoothly, as *Figure 53*a,b shows during heating from helium-level temperatures up to ambient conditions, barium double perovskites in *Figure 53*c,d possess two types of behavioral patterns that differentiate above and below possible phase transition region (150-100K) – one

addresses the recoverable PL below 90K (as presented in supplementary *Figure A21*a), and the other, unrecoverable above 150K (*Figure A21b*). The first situation, however, has a limited number of cycles (3) that could be reapplied while moving back and forth between each borderline temperature – *Figure A21*c. That means that whatever is responsible for LT Pr^{3+}/W^{6+} transformation and recovery during illumination is not persistent, limited to a certain degree, or at least its fueling sources (traps) are irrecoverably depleted. There are most probably two phenomena working almost simultaneously at the same conditions: a broad low-symmetry SG transition (presumably to $P2_1/n$ SG around 150K) which was already reported in the literature considering several DPs;[183,356,360,362] And, presumably, the indirectly-observed magnetic transition set tightly somewhere in between 120-90K. The latter sometimes could significantly impact overall optical properties at a varying degree. By this, I am not only simply referring to trivial changes in certain B-site states (charge-transfer and freezing e- carrier effects that manipulate SGs, local Brulloin zone, and effectively the whole band gaps structures)[237,365,368,478,514–516,522] but also imply the existence of more subtle phenomena like metal-insulator (Mott-Hubbard-like) antiferromagnetic transition changing the whole electromagnetic arrangement within the samples which would be, in particular, BPW.[397,398,400,401,514]. That would surely add much commotion (additional factors) amongst already data-rich experiments between all the 150-100K related phenomena, but at least it would confirm the change to be second-order in origin. There, the general temperature quenching stops and the blue region of emission loses its intensity abruptly in contrast to the red spectral zone. Prominent erratic swings in regional PL intensity also appear. PL barely recovers when cooled down from 150K back to ~10K, as depicted in supplementary *Figure A21b*.

Contrary to the 90K dependence in *Figure A21a,* it looks almost the same as before - weak, noisy, maybe closer to 130K. That provides clear evidence that all previously-described PL problems are directly connected to the ionization through a specific CTB illumination. Certainly, apparent conditions (like current temperature kT effect) also apply - at least to some extent, given emerging SG/electromagnetic transitions interfering with the width of the local band gap. Unfortunately, complex, structural fluctuations (i.e., mostly from stimulating the aforementioned CTB between RE & W) have yet another factor to be acquainted with - a time-resolved charge-transfer component. [370,371,479,514,517,523–527] That last phenomenon indeed progresses parallelly within the sample. Sometimes at such a rate that its contribution is difficult to assess quantitatively. Since ionization happens so fast at LT (within 1 or 2 seconds before some discrete equilibrium is established as observed by the microscope-aided eye), the PL spectra presented in *Figure 53* can only refer to the state where that last phenomenon progressed thoroughly and already reached its own balance at certain conditions.

The issue further evolves while using different media/gases in which the substances are submerged. That is why most PL experiments performed in the air on Barium DPs were cut off above 150K (in contrast to derivatives or other LT measurements where samples were closed in controlled. evacuated, He-filled cryostats). Air's (crucial yet destructive) influence via oxidation and local overheating of O_i creating additional V_o complexes in polycrystalline lattice further complicated already complex interpretation – the number of stimuli needed to be reduced in other to analyze what was actually happening. On the other hand, the air's impact later added an interesting twist to overall observable PL effects. More about this in the next *chapter 4.3*. For now, it is important to be aware that there is some clear evidence of 2 simultaneous processes influencing PL. One is time-dependent, directly related to CTB stimuli (affecting not only RE↔W but also O_i/O^- presence). The other, temperature-activated or rather dependant transition through some sort of barrier from shallow RE (Pr^{3+}) states up to CB and ionizing RE^{3+} ions from shallowly placed traps (presumably oxygen related).[370,384,387,475,478,479,528–531]

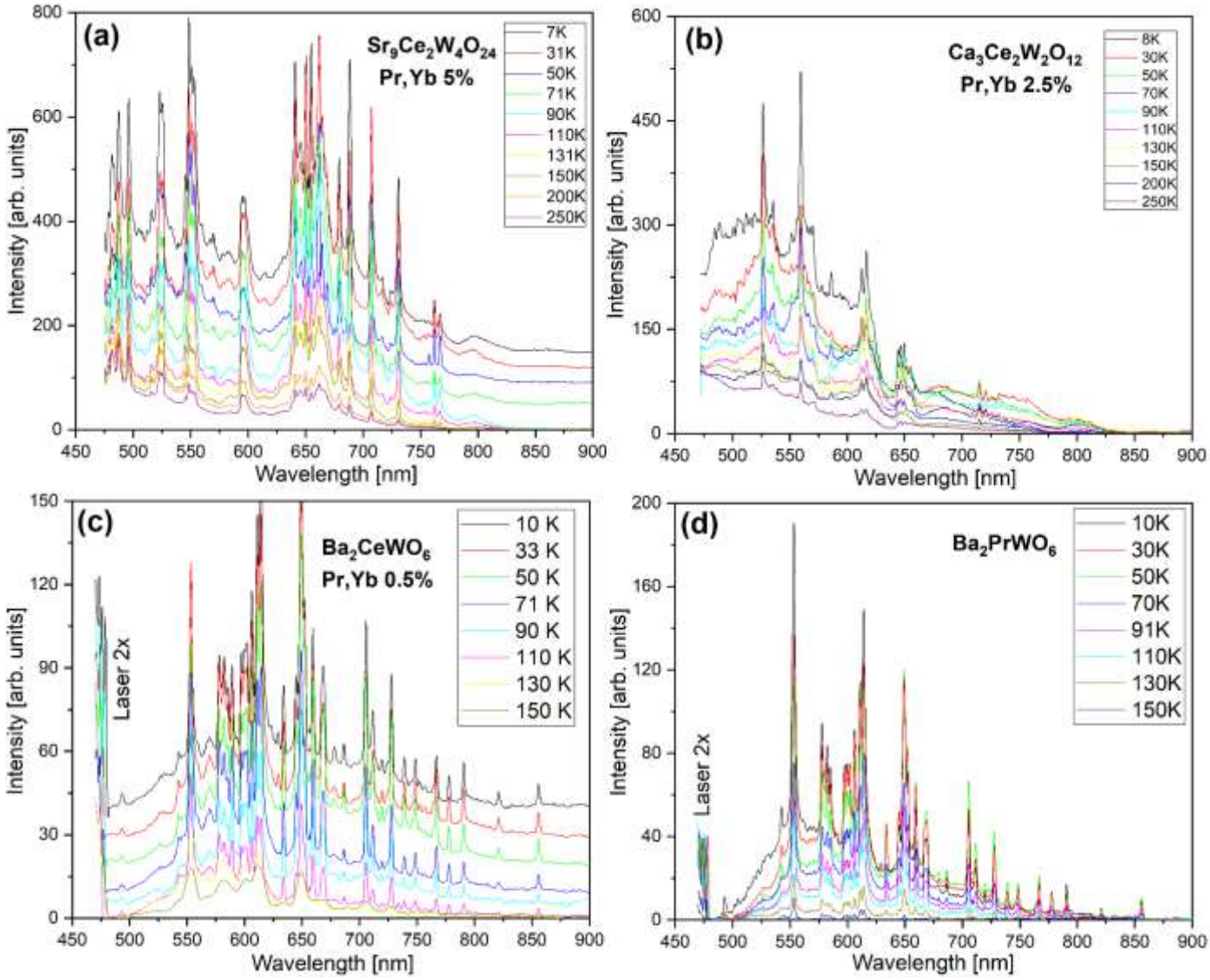

Figure 53 Low-temperature PL dependency of all $(Pr,Yb)^{3+}$ doped materials: derivatives (a) SCWO, (b) CCWO, and double perovskite (c) BCW compared to (d) pure Pr archetype BPW. Data was collected in the function of heating towards RT with λ_{exc} = 232 nm from the optical parametric oscillator.

From the last-mentioned process and its thermally-quenched LT PL dependencies depicted in *Figure 53,* unique activation energies (E_a) could be obtained. They could be useful to interpret what is actually happening with the electrons – ionization through some sort of thin barrier from shallowly placed RE^{3+} states or traps by exciting them up to the CB. They could be roughly calculated from empiric equations such as Arrhenius law[532] and its modifications depicted in *Equation 4* below:

Equation 4:
$$\frac{I(T)}{Io} = \frac{1}{1+Cexp(-\frac{Ea}{kT})}$$

Such an equation implies balanced, stable materials in their chemical (nonreactive) equilibrium state during illumination. Everything we excite with light from the ground to the excited states should return, whether as radiative or non-radiative (temperature-dependent) recombination. Both during and after turning off the light, we should have a constant concentration of the admixture, independent of the temperature. So, given the law and assumptions derived from it in the appendix (*Equations A1*), they also imply that if there are more energy levels (i.e., from the impurity), the whole process must concern solely the same ion. Considering our materials' apparent interactions with the conduction band, that is not it.

The other scenario and set of equations are based on the case of one dopant in the only available charge state ionized to another with no traps present in the way. The equation ends in a quadratic state

incorporating concentration values, even in the most straightforward cases (as shown in supplementary *Equations A2*). r(T) very rarely depends exponentially on temperature; it is usually a dependence to the power of X (X usually = 2), but it is again not the case since when the light is turned off, all electrons return to the impurity, i.e., concentration $N=N_0$.

The third case is related to ionization from the excited states, including traps (V_o, O_i, W^{5+}, RE ion shallow states), so justifiably, our case. Still, many assumptions and simplifications must be made, but at least there are as many traps as imbalanced RE^{3+}/W^{5+} & RE^{4+}/W^{4+} ratios state. Amongst them, interstitial oxygen is placed. The EPR O^- signal is extinguished after UV illumination at room temperature, but surely not completely. The traps are presumably deep and not thermally ionized at RT since the pairs would be processed on their own towards one of the presented forms. If we assume that all the traps are M_0 and they are not ionized by light, then the formula derived from all the presented in supplement *Equations A3* would finalize themselves in the form of *Equation 5*:

Equation 5
$$N(T) = N(0)\left|1 - \beta\, exp\left(-{}^{E}/_{kT}\right)t_0\right|$$

Where N(T) is the concentration of a specific ionized dopant in certain conditions. N(0) is the whole concentration of specific ionized dopant available at the start/beginning of the experiment at the most extreme temperature in our case. β is the probability of ionization (in our case, high). k – Boltzmann constant [meV/K]. T – Temperature [K]. t_0 – the time of reaching charge transfer equilibrium within a specific temperature (in our case, much shorter - 3÷5 seconds - than the measurement lasting approximately 1 minute); and finally E – the desired activation/barrier energy in meV obtained after logarithmic linearization from the slope of *Equation 6:*

Equation 6
$$\frac{Ea}{k} \times \frac{1}{T} - A = ln\left\{\frac{N(0)}{[N(T)-N(0)]}\right\}$$
$$a \times x + B = y$$

'A' is a linear constant B containing $\ln(-\beta\times t_0)$, and N_0 and N_T could be vaguely substituted with the normalized intensity of I_0 at T_{min} and I_T at specific temperatures. However, since each step contains two (rapid time-resolved and longer temperature-resolved factors) processes, the $N_0=I_0$ equilibrium must be derived from the previously acquired step, so I_0 will now be marked as I_{T-1}. That holds true if the repeatability of PL is maintained. Given the results (3 repeatable cycles below 90K) in supplementary *Figure A21,* this could stand true to some degree, and calculations done in *Figure 54* could be made.

Original yet small, all acquired values were compared to BPW as reference (a) being approximately 7.9 meV. Other 5%, 2.5% & 0.5% Pr (and Yb) doped (b) SCWO, (c) CCWO cerium-tungstate derivatives with (d) BCW double perovskite follow a particular pattern suggesting the deeper the E_a (barrier by ±5 eV) with lowering radius of A^{2+} ion: 19.0 (Ca), 15.9 (Sr) & 10.2 (Ba) meV respectively. The results seem rather consistent despite all the above approximations and simplifications (standard deviation is not bigger than 6÷10%). For pure BCW, in supplementary *Figure A22,* E_a is ~ 7.3 meV. This value is slightly smaller than for BPW but still within the error bar range. The answer for this might lie in measuring undoped cerate crystals hosting fewer defects.[533] Of course, independent confirmation from outside sources is still required since the results could differ from batch to batch, given the pronounced instability of RE ions.

The (E_a=)kT thermal effects and the expected placement of the shallow Pr $^1S_0$ states could be deduced from those slopes and these values. Not just for BPW but all Pr-doped materials alike. Evidently, they signify the thermal ionization energy ($a = E_a/k = T$ [K]) to eject electrons from the $^1S_0$ state to CB.[489,491,534] Judging by LT experiments, those CTB ionized electrons can be retrapped on Pr states but also could fall on other traps, of which there could be many (meaning O_i/O^- or W^{5+} states reported previously by XPS & EPR in *sections 2.3 & 3.3*). If we heat the samples slightly from low temperatures, we will ionize the shallow traps or breach the barrier of the shallow RE levels. The

more heating-cooling-heating PL cycles we carry out (especially DPs in *Figure A21*), the more Pr^{3+} ions would be depleted. Some compounds seem more stable than the others and resist that process more, as seen in this and the previous section. Ca & Sr derivatives triumph in that matter much more than Ba cerates and praseodymates – that stems from the depth of ionization temperature values derived from the 'a' slope coefficient in *Figure 54,* indicating at which conditions those barriers could be naturally crossed. These temperatures equal 92, 184, 220 & 117K for BPW and Pr-doped SCWO, CCWO, and BPW, respectively. At room temperature, kT energy would equal roughly 25 meV, so we would have only deep traps working and a significantly high probability of self-ionization (by any given stimuli). As a result, we should have reloaded all electrons from Pr^{3+} and irreversibly changed the whole material composition. However, it is not precisely the case as can be seen on the next page - only after prolonged exposure Ba DPs do it, again, proving the existence of varyingly-deep traps stabilizing them at certain conditions until they get exposed. This phenomenon could be useful for dosimetry purposes[535–540] but not in down-conversion.

One more remark. No wonder only ~30% of the grains emit so differently when shallowly placed Pr sublevels deviate subtly by several meV from the CB. Most of them are probably ionized. If more traps are localized near the bottom of the conduction band, this could severely impact the efficiency of the PL. [541–545] With significant structural fluctuations taking place in the sample, simple thermal changes could change the whole PL intensity or diminish bands altogether by manipulating the E_g. Such a small photoelectric work function would also easily stimulate $RE^{3+/.4+}$ charge transfer to or from the W or O_i/O^- taking a nonradiative route of energy dissipation.[372,524–526,533]

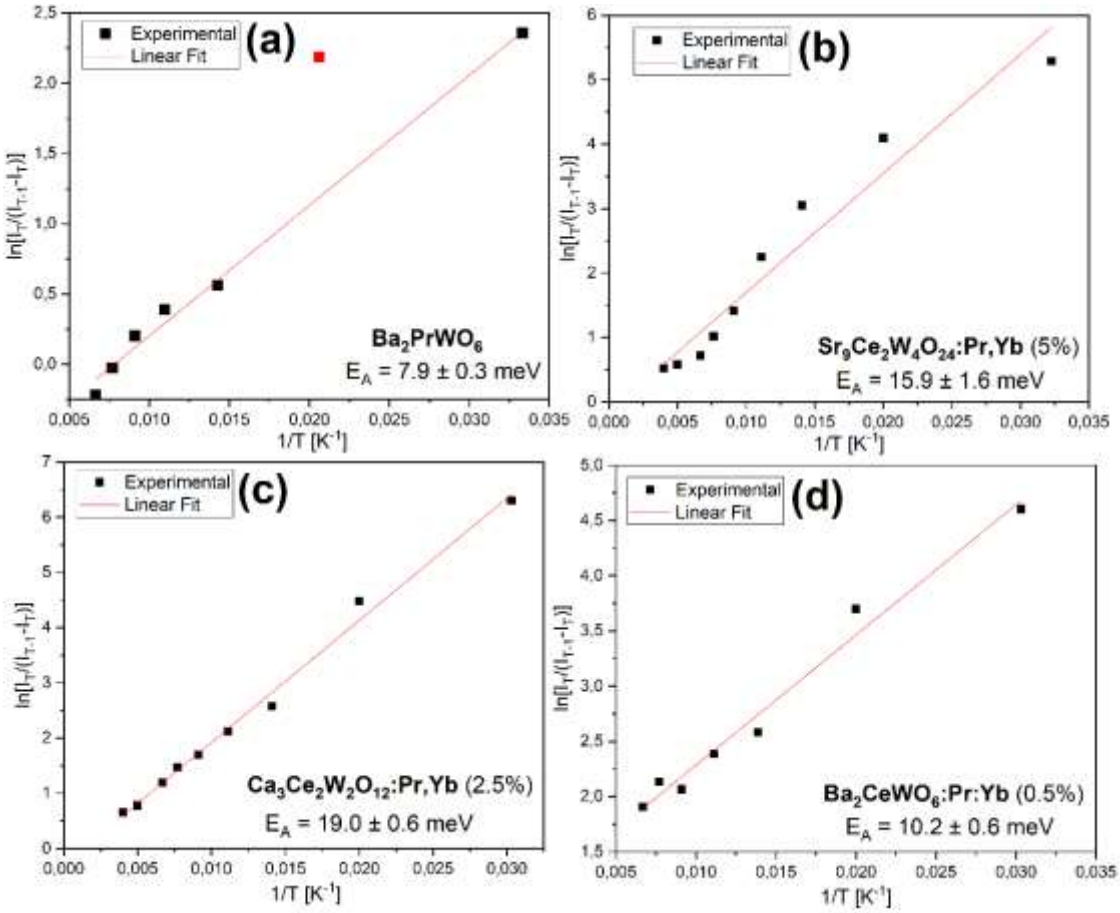

Figure 54 Activation energy estimates done for all investigated compounds based on the modified Arrhenius equation and measurements at LT temperatures in a pumped, helium-filled cryostat. Undoped barium tunsgate DP reference - BPW is presented in figure (a), while other Pr,Yb-doped tungstates having similar E_a values are shown in graphs (c) & (d) regarding 5% SCWO & 2.5% CCWO derivatives. Graph (d) hosts data about 0.5% doped BCW double perovskite.

4.3 Oxygen evolution & lack of the energy transfer

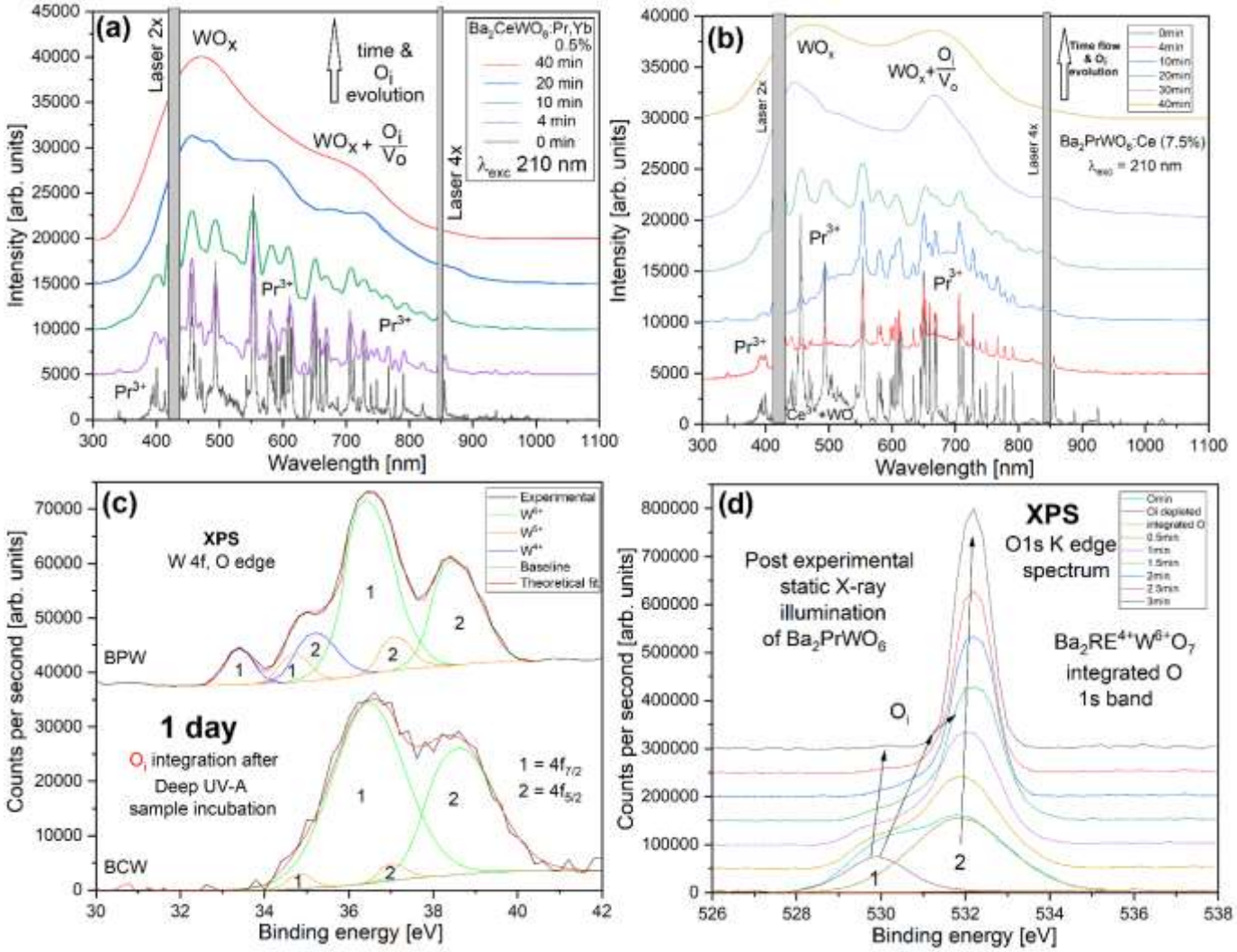

Figure 55 Time-resolved PL evolution of both doped barium double perovskites (a) BCW:Pr,Yb (0.5%), and (b) BPW:Ce (7.5%) in RT while exposed to intense λ_{exc}= 210 nm radiation in the air showcasing progressive transformation from sharp, Pr-specific to broad $BaWO_4$:Ce/Pr-like bands. Those changes originate from (c) prominent W oxidation featured on XPS supported instead by (d) O_i integration than RE-supplied charge transfer.

For a good reason, barium double perovskites' photoluminescence was investigated at LT only up to 150K. Not only was it already weak, but a strange phenomenon occurred while heating towards RT – all Pr^{3+} lines rapidly declined, broadened, and turned into two broad bands, completely not resembling anything from the initial spectra. The same phenomenon occurred when fresh samples were exposed to air for a few minutes at RT, as seen in *Figure 55*a,b. During HT measurements (up to 573K), those changes progressed even faster while being very weak (similar to HP results shown in *Figure A20*) during in-situ Raman investigation using a 325 nm laser. Above (till 873K), only WO_x bands were visible, if any at all, so the first assumption was probably just oxidation due to nonradiative processes such as rapid overheating or straightforward absorption. Samples' unfortunate coloring contributes to that factor, but that would not explain why those changes would also progress (though much, much slower) in oxygen-deprived conditions. An XPS check was made on a small amount of recovered material and, as it turned out, in *Figure 55*c composition of tungsten B-site ions has completely changed.

Given the exact nature of registered changes, W was initially to blame since the final form of the PL resembles the bands registered for $BaWO_4$ scintillators (possibly another instance of RE↔W charge transfer),[2,202,521,546] but while checking oxygen's O1s spectrum a time-resolved rapid evolution of its content was discovered.

So, not only was the material oxidizing from the air while exposed to radiation spot on or above the energy of the CTB band,[370,475,478,479,528,529] but also internally kept O_i/O^- species were involved in the whole procedure.[384,387,530,531] Moreover, complementary XPS RE edges provided analogical evidence about the state of all given RE ions and another barium compound being treated the same way, as seen in supplementary *Figure A23*. This, unfortunately, meant that the materials were not just unstable (like many other known perovskites),[547–549] but also compromised most of the initially made measurements due to exposition - they were more unstable than expected. Only those firstly-collected edges were valid. Each other shell needed to be measured on a different sample portion or rather 'spot' to avoid changing the initial composition of the material. That problematic outcome needed some deep tuning of the measuring equipment and much patience with frequent sample exchange to have proper, reliable conclusions; however, it was dealt with the utmost care, and all further presented spectra (i.e., in *section 2.3*) were attuned to that matter accordingly.

Initially, the proposed mechanism for mixed valency and all charge-transfer-related phenomena indeed involved both RE↔W interactions (as seen in the previous *chapter 4.2*). But now, O_i influence could not be entirely disregarded in general. Some circumstances, though, facilitate one of these two paths of matrix evolution when exposed to certain external stimuli. *Figure 56* proposes such conditions given all collected evidence until now – from the whole work considering both X-ray absorption and photoelectron edges with emission and excitation spectra. It is more evident that weak sources of light and pumped or inert atmospheres process O bands negligibly slow, but RE-related luminescence still changes based on photobleached Xe lamp spectra provided in *Figure 50*. That suggests that one could presumably stimulate the structure (and probably also the band gap width) only in a subtle way suggested by the inserted blue bracket. Nevertheless, when exposed to stronger radiation like UV or deeper (purple area), not fully reduced O^{2-} species (so O_i or dangling O^-) oxidize everything in the vicinity - to not emitting RE^{4+} species while slowly progressing through 5/6+ tungstates to familiar species like insulating $BaWO_4$ scintillators (which emit primarily at HP when its E_g is lowered through compression and double phase transitions to a monoclinic phase via metastable fergusonite).

The process would seem irreversible (at least in the air or at HT), given the chemism and excessive oxygen supply. Both compounds (BCW & BPW) would heat up, rebond and uncouple their various BB'sites to REO_{2-x} + $BaWO_4$ species. Prominent HT color bleaching (to yellow) and several orangish grains acquired after exposure (*Figure A16*) would support that scenario with similar XRD patterns as those stated in *Figure 39* or *40* in *chapter 3.5*. However, since in air-deprived conditions, the original color of the samples seems to be maintained (at least under the microscope while PL properties still change), a plausible outcome of $Ba_2(Ce/Pr)^{4+}W^{6+}O_7$ system would also be achievable since the XRD diffractograms stay relatively the same. Just as Ivanov and Carmine suggested in their analogical work with lead-based $Mn^{2+}W^{6+}$ DPs,[356,398,550] or many other scientists referring to similar monoclinic ($P2_1/n$) $BaRE_2WO_7$ or ($C2/c$) $BaCr_2O_7$ structure archetypes (which appear structurally sound to our $BaPr_2WO_7$ impurity from the chemical standpoint).[191–193,430,551] In other cases introducing more oxygen, especially after a long exposure time, would upset the B-site charge balance with non-stoichiometric values and decouple the structure to cerates and tungstates as stated before if not create something resembling $Ca_3Ce_2W_2O_{12}$ ilmenite or $Sr_9Ce_2W_4O_{24}$ quaternary perovskite since these compounds are popular side products.[97,98,114,401] These derivatives have more O, are more stable and are not prone to such prominent changes as barium DPs – reasonably because of the presence of fully

oxidized W^{6+}, which is more stable & would expand the band gap exponentially given the odds presented in available scientific literature.

Reconstructing these bonds (to the previous, mixed ion, less stable state) and oxidation to RE^{4+}/W^{6+} species is a contradictory process. It would need subtle heating in highly reductive atmospheres proportionally mixed with artificially added inert media.[552] An attempt was made to recover them, but the outcome was doubtful. The final batches had a completely different color (dark blue) than the initial ones (BCW – dark greyish blue, BPW – greyish green) and were problematic to analyze. They were wet (a lot of OH formed, not only on the surface), what required middle-range temperature treatment in pure inert gases (between 800-600°C just like in suggested W^{5+} acquiring methods in WO_{3-x}) to make them relatively dry - EPR indeed did not register any moisture.[173–176] Solely Ce^{3+} with paramagnetic defects in BCW since Pr^{3+} in perpendicular fields is not detectable – Pr^{4+} was not seen in LT, probably due to antiferromagnetic phase transition at LT >90K or complete transition to Pr^{3+}, so the water was gone. However, XRD & Raman spectra showcased a mix of particularly everything in appendix *Figure A24*. There, many substances like highly distorted REO_{2-x} oxides (hosting mainly RE^{3+}); AWO_{3+x} tungstates and their derivatives - most prominent, e.g., $BaWO_4$; W/WC, WO_2, and WO_3 oxides emerge joined together with main double perovskite phases. Optimizing the recovery process on such a batch was deemed futile, considering the lack of sufficient purism, but a point has been made. Reducing, breaking & correctly reassembling all $RE^{3/4+}$ bonds together with abundant defects (stemming from different -O- bridges like -OH & =O) to their prior RE/W charge-balanced states seems just unnecessarily time-consuming considering overall poor effects; however, not entirely impossible.

The conclusion is that only signs of anything recyclable would be present in the blue region of *Figure 56*. Especially if introduced to PL stimuli of reasonable strength at LT (for sure below 90K) in pumped atmospheres without any traces of air. In that regime, everything seemed repeatable and consistent regarding measurements – at least to some extent, as given by the number of cycles introduced in supplementary *Figure A21*. This temperature region of presumed recovery (and stability) could be somehow connected not only to the coexistence of coupled, wider band-gap $(Ce/Pr)^{3+}$ / W^{6+} ions but also to change towards lower symmetry SG (presumably to monoclinic $P2_1/n$ joined exclusively by antiferromagnetic transition just in BPW).[71,72,397–400] This makes those materials bad and unstable phosphors with limited recovery capabilities. There are just too many conventional obstacles and competing phenomena happening simultaneously for them to serve as efficient downconverters. No wonder any of the theoretically predicted mechanisms in *Figure 57* will not work.[3,306,490,491] Surely, they are interesting to investigate (i.e., UV→blue light quantum cutting) but do not possess any conventional means. They might have some potential in dosimetry or as a one-way, low-temperature radiation sensor; however, that last statement is yet to be verified by other extensive measurements concerning repeatability.[553–555]

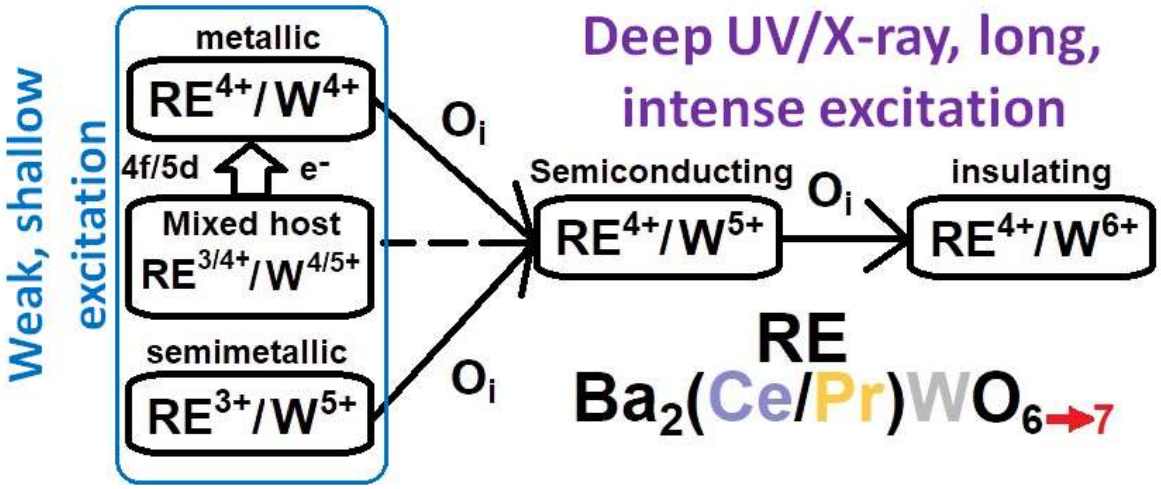

Figure 56 Exclusive mechanism proposal of aforementioned 4f/5d RE÷W charge transfer phenomena including a mixed path involving O_i interference followed by different strengths of Ba DPs illumination.

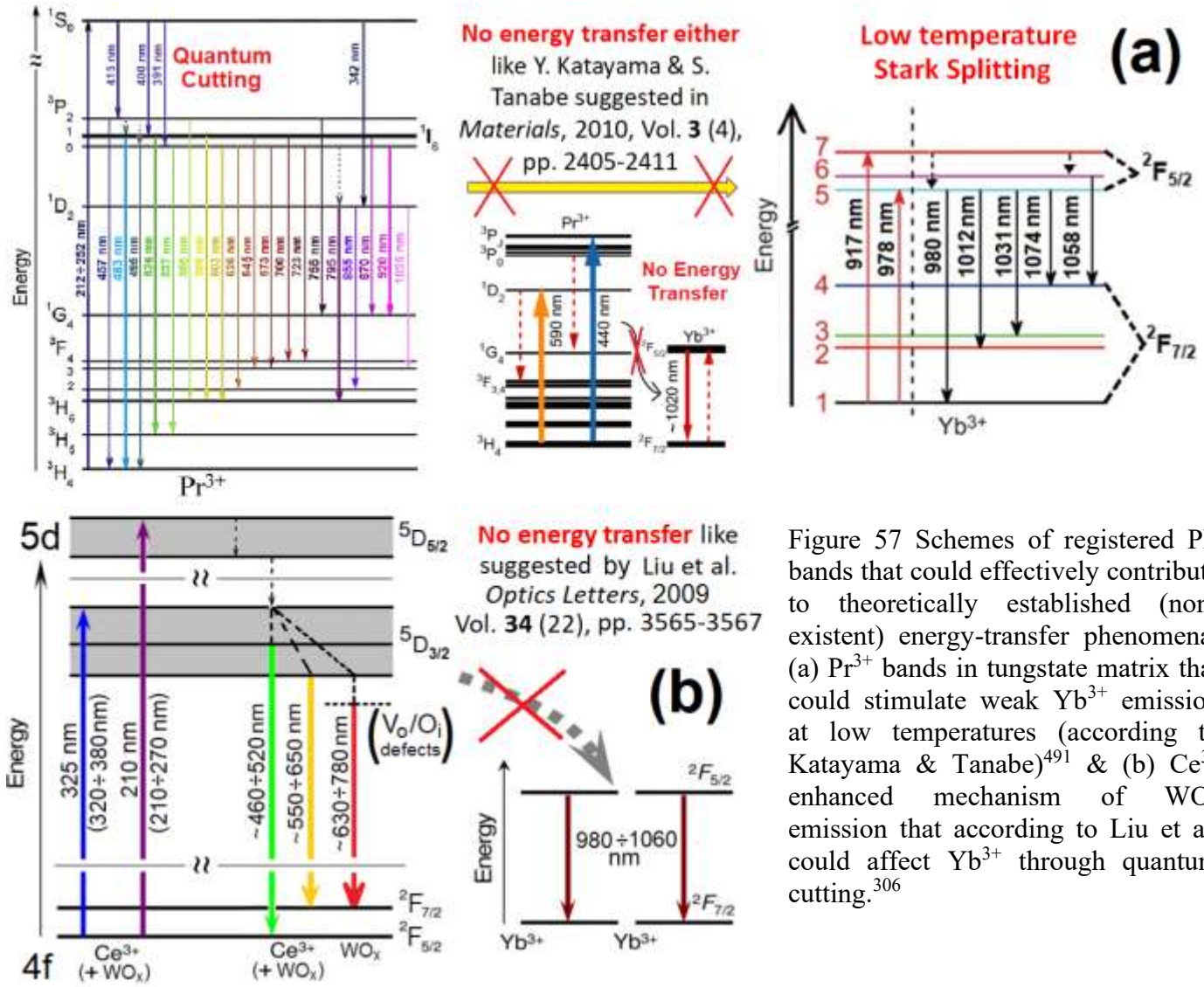

Figure 57 Schemes of registered PL bands that could effectively contribute to theoretically established (non-existent) energy-transfer phenomena: (a) Pr^{3+} bands in tungstate matrix that could stimulate weak Yb^{3+} emission at low temperatures (according to Katayama & Tanabe)[491] & (b) Ce^{3+} enhanced mechanism of WO_x emission that according to Liu et al. could affect Yb^{3+} through quantum cutting.[306]

4.4 Band gap estimations & absorption edges

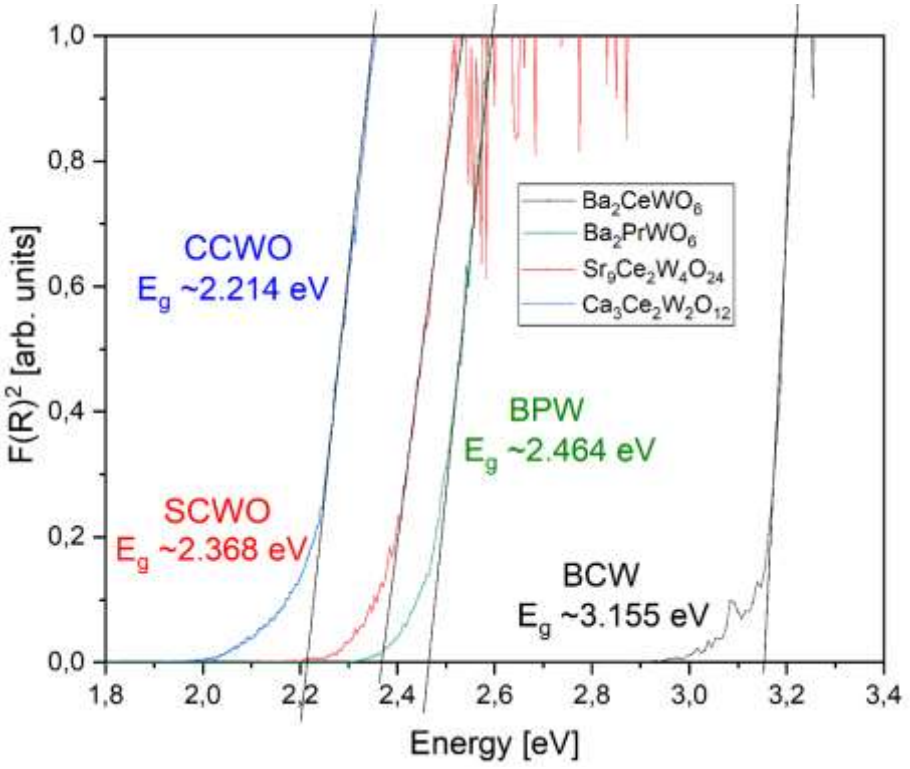

Figure 58 Kubelka-Munk equation incorporated into experimental reflectance spectra collected for all undoped samples at ambient conditions to provide practical insight about possible band gaps.

Experimental band gap (E_g) estimations were done by performing RT reflectance measurements on powders placed inside an integrating sphere in the widest possible range. Their results were processed through Kubelka-Munk equations[556,557] for direct band gaps and are shown in *Figure 58* regarding all discovered undoped tungstates. As one can see, they progress quite smoothly regarding the shrinking of ionic radii. The gap will downsize substantially if one substitutes B-site, Ce central ion with Pr (while maintaining the charge state ratio). The same goes for alkali A^{2+} ions when Cerium is maintained inside – E_g closes going down Ba→Sr→Ca chain. These tendencies are to be expected, but other band gap 'manipulation factors' must be considered, like changes in temperature, stoichiometry, SG, or B-site charge ratios with partial site occupancy.[517,558] Testament to this fact could be E_a values calculated for the doped materials in *Figure 54* where, beneath the CB, shallowly placed $^1S_0$ Pr state utilized mainly for the ionization process are ordered inversely (Ca→Sr→Ba) to declared tendency – the E_a value (by around +5 meV) rises as the E_g decreases (by +100 meV or more).

A more problematic issue is that those (experimentally & theoretically established) gaps are too small (by at least 2×) to be realistic even if they match & progress as expected when compared - *Figure 58* vs. *59*. While their width matches the values mentioned in common literature for such systems, they are rather improbable given that we observe all this luminescence described thoroughly in the previous *4.1-4.2 sections*. Since the lowest PL excitation lines are around 4.92 eV for all Pr-containing samples (i.e., $^1S_0$ ~252 nm in BPW *Figure 45d*) and they are neither broadened nor Fano-shaped,[559–562] it means that these states are not in the conduction band but in the gap. The ground Pr^{3+} states are also in the gap (otherwise, there would be no overcharging), so E_g must be greater than the aforementioned 4.92 eV. We do not know where the ground state ($^3H_4$) exactly lies (relative to the valence band,) but we can infer that it lies 4.92+0.0077 eV below the bottom of the conduction band. Also, seeing bands from $^1S_0$ states gives the impression of gaps ranging to 5.5 eV or higher (not three or below), placing all compounds deep into the insulating range.[398,550,563,564] Cerium hosts doped with Pr would also remotely adhere to that scenario by precedence. Not all samples gave out prominent PL, though – roughly 25-30% of grains emitted at all in the VIS range if doped with Pr. There are several hypotheses to answer that issue - one being based on theoretical Wannier/Tight-binding equations given available CIF files and discovered coexisting BB'-site cations balanced in (*section 2.3*) reported (4/4+ & 3/5+) charge state ratios.[565,566] It would be most convenient to start with this concept and progress on using it as a base for further discussion. The divagations will be primarily based on barium double perovskites since they possess elementary, small unit cells without notable vacancies or partial substitution, making calculations reasonably processable. As seen in *Figure 59*ab, normal band gap estimations for $RE(Ce,Pr)^{4/3+}/W^{4+}$ systems place Fermi level (E_F) shallowly buried inside the conduction bands. These systems are metallic and would not emit at all (without any spontaneous defects or vacancies). That is why probably most of the samples' grains do not give any response. Exposed to typical excitation wavelengths (as seen in *Figure A19*), they would be prone to fast, gap-closing charge transfer phenomena (which seems to take place while comparing *Figures 19* and *20* with *Figure 51ab*).[363,366,369,371,523,529] However, when W starts to slowly oxidize through spontaneous charge transfer (initially to W^{5+}), i.e., during synthesis or illumination (weak CBT band stimulation), the E_F level would move out just slightly below the conduction band, making the whole matrix semi-metallic.[474–479] That brings us to the previous discussion about E_a estimates. If such a small band gap with subtly placed sublevels is introduced to the system together with major structural fluctuations, simple thermal kT stimuli (between 90÷120K) could easily eject electrons from shallower states ionizing the RE dopants and constituents.[372,524–526,533] Subtle electron work function (in the range of 8-11 meV) would influence $RE^{3+/.4+}$ states, moving the charge carriers to nearby, i.e., W^{5+} traps and further complicating the electronic structure. That phenomenon could take a non-radiative turn, taking the energy's portion and proceeding further through a semi-metallic band gap towards the bottom of

the conduction band via nearby O_i sublevels. That cascade could also propagate through widespread vacancies all the way down to the valence band, hampering deeply desired chance for (sharp) radiative emission and, consequently, effective energy transfer.[475,529,533,542,544,545]

Contrary to non-emitters (~70% of grains), the influence of CTB in these (presumably) semi-metallic multisite oxide structures could easily explain the small amount of initially discovered, not-quenched grains resisting nonradiative processes by exploiting brief RE↔W or O sub-band evolution moments. Changing RE charge states with W ions or O devouring excited electrons would (by chance) inadvertently & irreversibly expand the E_g by not a small amount - mainly due to O^{2-} injection from interjected O_i/O^- if not supplied from the air that binds with W (but, more about that mechanism in a moment).[530,531,567–569] Different radiative responses could develop via crystallographic lattice evolution - uncontrolled expansion of local defects could separate many interjected states in the fluctuating E_g by creating an artificial ladder. Additional PL lines could emerge, split, or resurface from underneath the CB. At the same time, the gap is being modulated (especially inflated in shared or half-occupied atomic sites like in reported derivatives). [498,503,518,519,527,558] All inclusions and erratic interatomic interaction between various ions (especially Pr^{3+}↔W^{5+}/O_i, O^-) in the lattice would unintentionally manipulate the crystal field universally changing clear, theoretically-established E_g into a more complex construct – rich in many sub-conductive (RE^{4+},W^{6+},O_i), intermediate (RE^{3+},W^{5+}) and over-valence (W^{6+},O^-,O^{2-}) states which would make all simply-modeled tight-binding estimations & PL-related spectra not trivial to interpret jointly. The final outcome of this evolution mechanism would be a semi-conducting or even insulating system.[398,550,563,570–572] Then, E_g values at Γ, while still greatly underestimated, would at least match those received from previously done reflectance measurements. A visual description of the *I*2/*m* Brillouin's high point symmetry zone can be seen in the appendix *Figure A25a*.

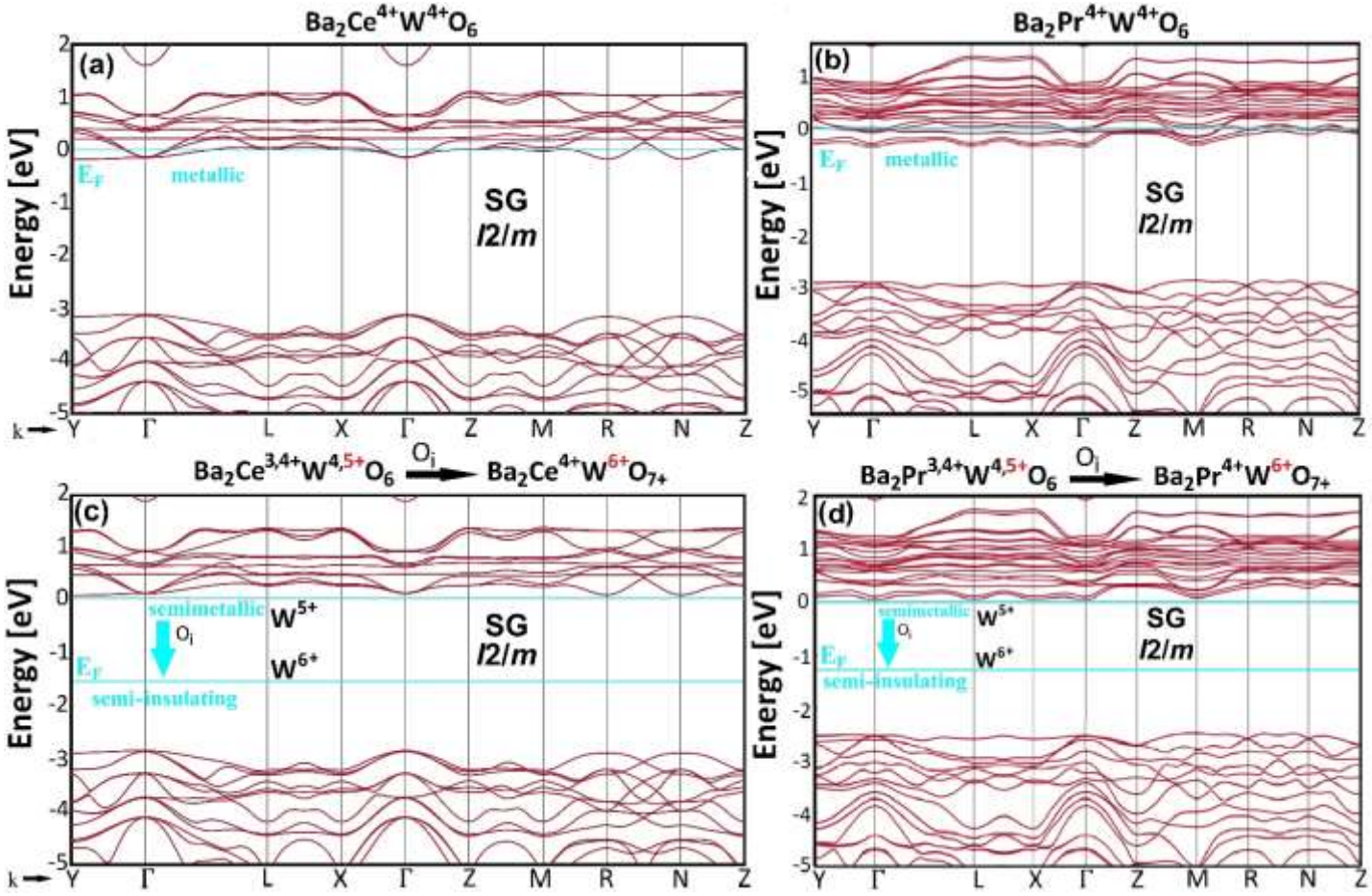

Figure 59 Theoretical band gap estimates provided by VASP software using Wannier/Tight-binding equations for both barium double perovskites (BCW & BPW) hosting primarily-selected, simplistic *I*2/*m* unit cells with: (a,b) only pure $(RE/W)^{4+}$ ion couples, and (c,d) those being imbalanced by W^{5+} ions further influenced by the O_i presence towards W^{6+}.

The O_i interference or O^- from internal V_o complexes is the most plausible scenario. Those species mediate in the E_g spreading process from ground 2p up to near-CB Pr states by involuntarily oxidizing the sample's ions (ionizing not intentionally applying various stimuli/changing conditions), i.e., tungsten to the 6+ state and moving the E_F level as shown in *Figure 59*c,d. That could exponentially distance conduction from the valence band (VB) towards the deeper UV region.[527,530,531,568,569] Usually, interstitial forms of O like O-O dimers in a neutral state break upon capturing a traveling electron (thus quenching PL). When bond-breaking relaxation occurs (to dangling O^- or fully integrated O^{2-}), the antibonding defect level lowers itself from the conduction band (CB) towards valence states.[531,569] The implication suggests that those O species act as temporary electron traps for the E_F close to the CB; thus, the excessive amount of interstitial atoms could positively shift the threshold of E_g towards values, as presented above in Wannier-shaped diagrams. Here, under weaker light illumination or negative stress stimuli (stretching), the Fermi level could lower itself toward the edge of the VB where O-O dimers could feed upon capturing free hole carriers with neglectable energy barriers (a theoretically recoverable process), but that might not be the case (as tested, the process is rather irreversible considering most grains are non-PL-active / semi-metallic in origin).[531,568,569] Shallowly place RE states might be responsible, especially considering the presence of RE^{3+} charge states even if in minuscule amount after exposure – when O-O bands would move back up (looping) after feasting upon the holes crossing Pr states would drain them up quickly.[569] This phenomenon can be temporarily preserved, given that it originates from defective REO_{2-x} substrates (mainly referring to Pr). PL from them is also visible in our doped materials & is partially recoverable for a short while in progressing through a few cycles - *Figure 50*. However, one must maintain inert, protective atmospheres in LT (stored without an additional income of outside O to be sure of what one is dealing with). So probably RE partially hijacked this mechanism at the very start, given their shallow-placed states exist nearby with a reasonably small gap till they are also 'fed up' with oxygen-processes holes [363,479,531,568,573,574] - competing CB to VB processes of O^-, O^{2-}, RE^{3+},$W^{4,5+}$←e^-,h^+→ O-O, O^-, RE^{4+},W^{6+} would suggest some discrete balance without and distinct priority since all these forms coexist with each other; however, less detectable O^-/O_i forms seem to dominate the process at the end. This last statement would explain what happens during the HT synthesis (disproportionation between 3+/4+ species, 2+/3+ in Yb due to kT influence, and O_i/O^- coexistence). However, eventually everything would be forced to oxidize and turn into RE^{4+}/W^{6+} states by changing the stoichiometry towards $Ba_2RE^{4+}W^{6+}O_7$ systems and adding $+1O^{2-}$ to the O_6 subscript (like in air - *Figure 55*) during strong laser excitation.[550] In this scenario, the E_g could grow even bigger and more insulating than predicted. E_F placed in the middle of such vast E_g would stop all these aforementioned phenomena - at last, some long-term current-voltage stability would be maintained between RE/W B-site ions. The whole process would resemble HT annealing, given that all the additional oxygen would integrate itself with the crystallographical lattice (O^{2-}) and forge/retrofit some sort of effective band gap in temperature-induced multi-oxide systems.[527,530] That total outcome was initially unexpected and would require excessive band gap engineering.[527,530] Divulging upon this subject could create a new, stand-alone topic for a separate dissertation and will not be expanded upon here. This field seems to be a rather hopeless expansion at that point while tackling basic BB'-site instability issues (this is a fundamental study for newly discovered materials), and energy transfer will always be affected by it [370,371,479,528,573] considering the chosen concentrations of remaining, scattered emitters (Ce and Pr)$^{3+}$ will always diminish with respect to the planned amount of receivers (Yb^{2+}→Yb^{3+} - refer to *Figure 25* for details) but, at least PL quenching could be partially taken care of here given the limited supply of oxidizing agents during vacuum-pumped or N_2/Ar/He-filled synthesis/experiments.

The other issue to address probable large E_g (stationary, not only based on acute broadening) could be the presence of intrusions and the influence from the nonuniform distribution of RE dopants or, rather, their 3+ ions within all the investigated matrices given randomly scattered PL-active grains and

possible minor phases visible on XRD diffraction patterns (summarized briefly in *Table 6*). Since we are investigating (novel) powders, not crystals, having RE ions as their constituents scattered in different charge ratios throughout doped matrices is a widespread problem - researchers usually encounter such issues during first stages of synthesis and either try to develop a perfect purity/RE distribution ratio by improving diffusion rates, prolong the sintering time/cycles or switch to highly-ordered crystals if possible.[567,575,576] In our case, the syntheses needed to stop at some point, considering every cycle introduced slightly more oxygen defects to the isolated system and too high diffusion rates facilitated segregation of AWO_4 systems from REO_2 oxides (as *section 1.2* states), thus resignation from Pechini method and backtracking to SSR. The percentage of the luminous grains could showcase such struggles, but their constant spatial and behavioral repeatability (at least visually for the measurements performed under the microscope) would suggest some effort towards mitigating those problems. Those grains seem not to be just some random entities (physically unidentified phases) scattered around. They are too abundant (easy to find ~ 30 volumetric %) and consistent in their performance to be undetected.

That brings us to the last, most plausible solution of the alternating E_g problem, the other, most probable *R*-3 phase. As discussed at the beginning of paragraph 2.2, both barium RE tungstates could possess one of the two indistinguishable SG - just basing on the powder XRD and Raman spectroscopy was insufficient (- access to NPD would be required). By order of elimination using spectral techniques in non-ambient conditions, the trial concluded that we most likely deal with *I*2/*m* (*C*2/*m*) SG system, and the discussion proceeded with that conclusion further on. However, the '1-0' disqualification procedure might not be a valid approach. Both materials could hang in a discrete balance within a specific temperature given that the alternate *R*-3 phase is the less stable (as the literature suggests, it persists at around 353K or even more).[29,71,72,357,359,360] That theoretically assumed coexistence might be the actual culprit for not distinguishing any of those two primary components of the batch. That rhombohedral phase (presumably being in these conditions in the minority given the low number of emitting grains) might be responsible for band gap differences given the changes in the Brillouin zone (depicted in *Figure A25*b) with respectable RE/W BB'-site ions. Adequately, similarly-tailored Tight-binding projections of E_g were made and presented in supplementary *Figure A26*. They apparently still disprove our suspicions by at least half the value, although slightly bigger than in *I*2/*m* (especially in the case of BPW, whose gap still rose by ~0,5 eV). Even if the calculations underestimate the gap (they usually do), the differences are just too big to be neglected and left without any answers. Sometimes E_g width progresses in monoclinic > rhombohedral ≥ cubic SG order while other (p, T) conditions are maintained but not as much.[518,519,577–580] The reason for such PL must lie elsewhere, presumably in disproportionate RE^{3+}/W^{6+} intrusions. At LT (below 150K), both barium tungstate systems also undergo a phase transition to most probably monoclinic $P2_1/n$ SG,[359,361] which usually widens the band gaps even more,[517,576–578] but BPW additionally goes through antiferromagnetic transformation slightly below 120K (stretching down to 90K) which might contribute to the effect in many unpredictable ways – probably would make it an antiferromagnetic insulator after ultimately moving the charge to Pr^{3+}/W^{6+} states.[399,581]

All aforementioned structural fluctuations play a pivotal role in meddling with E_g and PL-related phenomena: mixed or changing ionic radii after stimulating Pr↔W, O sublevels by CTB, mobility-related defects, vacancies from redistributed oxygen, shared octahedral or half-occupied dodecahedral sites were reported here as well as in other less complicated structures having similar issues. This alone could explain all phenomena mentioned above, E_g evolution and potential 'fluidity' or rather instability of excitation and charge-related states.[524–526]

Conclusions

- Not all four newly-discovered compounds did turn into desired double perovskites due to apparent tilting from shrinking of A^{2+} polyhedral sites as the worsening Goldschmidt factor predicted. Spacious barium accommodated truly desired perovskite matrices, although slightly tilted from the perfect cuboid cell. Strontium created an intermediate structure called quaternary perovskite riddled with many defects - partially occupied $A^{2+}/RE^{3/4+}$ sites and half-empty vacancies. Calcium made densely-packed ilmenite, which in comparison to Sr, expanded two-fold while maintaining partially-substituted sites but did not possess any noticeable A-site vacancies.
- Barium cerium tungstate (BCW = Ba_2CeWO_6) and barium praseodymium tungstate (BPW = Ba_2PrWO_6) turned out to be compact but slightly-tilted, cuboid *I*2/*m* SG, although (through powder XRD) the alternative *R*-3 SG can not be entirely discarded. The same issue concerns huge unit-cell of calcium cerium tungstate (CCWO = $Ca_3Ce_2W_2O_{12}$), which is probably centrosymmetric *R*-3*c* than (noncentrosymmetric) *R*3*c* – neutron powder diffraction studies are required at reputable nuclear reactor sites to be sure of that matter. The least-concerning compound (regarding SG assignment) is strontium cerium tungstate (SCWO = $Sr_9Ce_2W_4O_{24}$) which, although belonging to a hotly-debated group of minerals, has a pretty accurate fit – a tetragonal $I4_1/a$ SG without any close-call alternatives. (The other, much worse, is *Fm*-3*m*)
- All compounds present themselves with some internal B-site cation duality balance making them more stable (Sr & Ca derivatives) or not (Ba double perovskites). Derivatives such as SCWO and CCWO seem to last longer at ambient conditions, given that no external NUV or deeper-energetic stimuli are applied, probably because of their $Ce^{4/3+}$ vs. $W^{5/6+}$ 9+ charge balance. Their W^{6+}-based SGs seem unfazed since the ions' highest oxidation state does not have an alternative to go any higher. In SCWO & BPW, the general B(RE/W)-site ratios seem to be upset and do not fit as well as in their BCW & CCWO counterparts. Barium compounds seem to behave differently. Not only do they bestow internal 8+ B-site balance – $RE^{3/4+}$ ions are artificially 'paired' most likely with $W^{5/4+}$ counterparts (not closely but distanced, presumably scattered - balanced in the whole volume of the sample). Their response to the external radiation is also different – (at first) weak photosensitive stimuli seem to change them towards other non-radiative species like RE^{4+}/W^{4+} phase irreversibly. This might be because of their shallower ionization levels (E_a ~7-11 meV) compared to cerate derivatives, which reach 15-20 meV. That correlation would definitely reflect in some of their kT thermal properties vs. PL dependencies at LT.
- This situation is, however, brief. If exposed longer to more intense illumination (highly energetic +250 nm source or through overheating), this transformation proceeds much further. Both barium compounds react irreversibly with interstitial oxygen (O_i) stored in nearby vacancies (V_o) or complexes and oxidize by attaching 1 (dangling O^-) more oxygen (O^{2-}) to the stated initially stoichiometric formulae. This phenomenon, alongside some shallowly present 4f/5d RE charge-transfer states, could contribute to overall photobleaching phenomena transforming all constituents & dopants from RE^{3+} species to photo-inactive RE^{4+} ions rendering these already-weak phosphors as bad emitters.
- At high temperatures, when overheated (intentionally) in the air-filled furnace or by a laser, a similar process (to this stated in the previous bullet point) would be responsible for the same oxidation effect. It concerns, however, throughout decomposition of the structures into separate products like RE oxides (substrates) and AWO_4 tungstates. When overheated above a specific limit, as stated by DSC & TG, specific $RE^{(3+)}$ or $W^{(4/5+)}$ species will oxidize, changing the band gap barrier by utilizing the materials' current structure in the ambient environment. This was confirmed while comparing the behavior against a sealed or protective inert gas environment media. In those gases, the process was still present, however severely limited. Unintentional O_i/O^- storage might be the culprit behind all of this. It is difficult, if not impossible, to monitor & control the content of all O species even during the synthesis since oxygen substrates are also the actual donors. However, some signs of unit cells'

amorphization or (octahedral) tilting are quite prominent. That statement alone might create a firm basis for all material's time-resolved sensitivity to photoionization.

- Polymorphism investigation in high pressure concluded that CCWO and SCWO derivatives could encounter some type of (theoretically-supported)[71,72] reversible phase transition above 11 and 15 GPa, respectively. Most likely to *C*2/*c* SG of lower, monoclinic symmetry (possible for both CCWO & SCWO) than *C*2/*m* (exclusive solely for SCWO). However, this statement needs to be verified by HP XRD since the change was observed only on the Raman spectrometer. It all seems to bear second-order transition characteristics - stretched out, continuous yet subtle phonon energy fluctuations, although with noticeable yet slight hysteresis during decompression (first order?). Barium double perovskites, contrary, stay the same up to 20 GPa.
- DFT calculations provided by *Howard et al.* also support low-temperature research by reporting another set of second-order phase transitions - this time related to barium DPs. In them, the *I*2/*m* phase probably shrinks and tilts more towards the monoclinic $P2_1/n$ SG. However, this could also be a reversible transition from coexisting *R*-3 ÷ *I*2/*m* phases towards a more RT-stable (latter = *I*2/*m*) option.[71,72] On the other hand, that last presumption would not support spectral group theory calculations with an additional number of Raman-active modes slowly appearing just below 200K (↔100K). Just as before, further investigation through LT powder XRD or NPD would be required since this might be just some sort of decomposition (not likely since irreversible) or rather $RE^{4+} \leftrightarrow RE^{3+}$ & $W^{4/5+} \leftrightarrow W^{6+}$ disproportion including O_i ionization as further XAS & EPR measurements will show.
- Low-temperature XAS was done to check whether or not changing conditions & probable phase transitions (for BPW & BCW) will influence the ionic, B-site structures of our materials during the unit cell's shrinkage. The charge-transfer phenomenon would surely upset the discrete balance of B-site ions, influencing future down-converters' PL & energy-transfer properties. Low-eV radiation (during PL experiments) does not seem to influence barium RE-tungstates' unpredictable behavior. LT phase transition that transpires in them seems to have something more lurking beneath their purely structural nature. In LT, the SDD acquisition mode of XAS shows signals from derivatives (SCWO & CCWO) with similar ratios regarding Pr dopants, although relatively weak and noisy. The error bars are huge enough to set all values in common grounds to RT with no proper conclusions derived. However, things are different regarding barium samples & their constituents. RE^{4+} seems to change entirely to RE^{3+} - that is probably the reason why EPR does not see any Pr^{4+}. Moreover, TEY results show nothing at all (or only a few residual peaks from previously main features), promptly hinting at a massive drop in the conductivity of pellets towards more insulating values – as confirmed later by EPR's microwaves. Such behavior would imply temporal freezing of the carriers below a specific temperature (presumably supported by obstructed e^- propagation through abundant-in-V_o/defects matrix - mainly in derivatives) or charge transfer from W to RE in such a way that it would expand the band gap - that last scenario seems reasonable for barium samples). The last process would expand the bandgap (i.e., lone $W^{4/5+} + O_i \rightarrow W^{6+}$ or $2\ RE^{4+} + W^{4+} \rightarrow 2\ RE^{3+} + W^{6+}$; $RE^{4+} + W^{5+} \rightarrow 2\ RE^{3+} + W^{6+}$) & probably change stoichiometry for both barium DPs due to prominent tilt from changing ionic radii. O_i/O^- is probably involved too, but not much since EPR does see considerable amounts of it in BCW. The interference might be a result of changing magnetic properties.
- While the postulated conductivity changes for all the materials, the phase transition seems to proceed reversibly & only within BCW & BPW - somewhere below 150K (according to Raman spectra, the point is not sharp). There is also a hint about another antiferromagnetic change – a phase that would appear around 120-90K solely for BPW, which clearly has more O_i content than the other materials and does not possess any Pr^{4+} & W^{5+} ions on LT EPR (20÷3K). Below (typical, second-order) transition temperature, PL Pr^{3+} peaks also seem to recover quite nicely during (3) heating-cooling-heating cycles in the cryostat, so radiative processes there seem to be at least partially recoverable.

- All gradual changes in PL seem to be induced by time-resolved exposure to high-energy radiation or phase transitions mentioned above (structural or magnetic still awaiting further confirmation by more elaborate techniques). Both changes could carry a bit different stoichiometric outcome – simple cryogenic cooling seems to spare RE^{3+} ions but sacrifices all RE^{4+} & most importantly, $W^{4/5+}$ species towards W^{6+}. The assumed outcome would influence the structure by changing ionic radii or B-site balance, introducing a total 8➔9+ charge disproportion compensated by reintegrated $O_i \rightarrow O^{2-}$. Barium samples would be affected by the creation of $Ba_{2+x}RE^{3+}\square W^{6+}O^*_{6+Oi}$ complexes where '□' is a 'defect' or rather a vacancy. Sever outcome would presumably be $Ba_3RE^{3+}{}_2W^{6+}{}_2O_{12}$, similar to $Ca_3Ce_2W_2O_{12}$. Both (BPW & BCW) LT transitions, however, seem to be reversible (as proven by Raman spectra), so the $Ba_{2+x}Ce^{3+}\square W^{6+}O^*_{6+Oi}$ structure would be a more adequate approximation considering that $Ba_3RE^{3+}{}_2W^{6+}{}_2O_{12}$ would completely (irreversibly) change the internal packing order. The band gap modeling, absorption, and widespread RT & LT PL measurements commenced shortly after since radiative mechanisms of shallowly placed $RE^{3/4+}$ charge-transfer states (under the 5d conduction band) were at risk. Their response would be pivotal in the energy transfer phenomena we dearly searched for based on introduced RE^{3+} ions.
- Compounds naturally containing W^{6+} indeed fit experimentally estimated values of absorption spectra & theoretically established tight-binding E_g - SCWO & CCWO are presumably semiconducting. However, band gap modeling in VASP software showed that BCW & BPW should be semi-metallic with ions such as $W^{4/5+}$ (respectively E_F shallowly buried or just below the CB). That mainly explains no PL from ~70% of the grains. Both materials transform during intense illumination (NUV or deeper) due to charge transfer, defects, or O_i photoionization. Time-resolved acquisition with a weaker Xe lamp gives room to observe a slow, progressive evolution (allowing only for a short, brief exchange of 1 e^- from RE^{3+} to W^{5+}), making PL spectra completely flat. Later stages of the experiment, involving potent laser power, instant feature integration of O_i/O^- into the matrix (Ba_2REWO_{6+1}), promptly changing the $W^{4/5+}$ mix towards $W^{5/6+}$ and eventually, W^{6+} expanding the band gap & lowering the Fermi level from almost the bottom of the conduction (semi-metallic) to nearly half the way towards the valence band making them; as a result, deeply-insulating. All aforementioned discussion refers to theoretical values at Γ fitting and the chemical mechanism depicted in *Figure 56*. RE would also be fully oxidized at the end (to 4+ species), creating $Ba_2RE^{4+}W^{6+}O_7$ by that point – they seem to respond first to the stimuli towards W, but its sole oxidation (to 6+ charge, whether from RE or O^- electrons) is what actually steers the band gap and whole observable PL effects.
- Based on modified Arrhenius law (*Equation 6*), activation energies (E_a) of all Pr-doped compounds and pure barium DP matrices were calculated. Thanks to that procedure, the depth of shallowly placed RE sublevels (8-19 meV) and their common interactions with the conduction band could be addressed (E_a rises with Ba➔Sr➔Ca substitution contrary to the E_g). Of course, that does not change the fact that both tight-binding band gap approximations made in VASP software and reflectance measurements grossly underestimated the width of the E_g - by at least ½ of its value. Given the emission seen from Pr, the band gap is undoubtedly bigger, and part of it corresponds to radiative transitions from $^1S_0$ states placed somewhere close by the CB (E_a values would correspond to that). Since the influence of possibly coexisting alternate (*R*-3) SG was rejected (considering it to be an intrusion having a more significant E_g), there could be only two other sets of solutions to answer this 'bigger-than-usual' band gap dilemma. First are independent inclusions since most (~70%) non-emitting grains presumably have almost-closed, direct band gaps. The other is a nonuniform distribution of dopants/RE ions. Both cases could explain such an erratic response. The origin and effects of the first scenario are quite obvious. Structural fluctuations in non-trivial LT/HT conditions would influence the second outcome during low/high laser-powered experiments. The electronic structure of DPs could be manipulated during synthesis by just slight changes in delicate p(T)/media conditions influencing final B-site ratios. The interchanging RE/W charge states with varying ionic radii (especially towards W^{6+}), artificially injected O^{2-} from O_i/O^- intrusions mangled within the lattice, and structural or possible LT antiferromagnetic

transitions (the last one very typical for oxides) would also unpredictably modulate the band gap by blurring its width with many intermittent levels – that unintentional meddling with the band gap seems like engineering, but in our case, it could cause electrons to weakly emit or slide non-radiatively back to their valence bands what is not appreciated.

- All the main Pr $^1S_0$ and ^3P bands (from dopants & constituents) with their weaker Ce+WO_x contribution at the base of the PL were accounted for. There was only one particular ion missing. The Yb^{3+} emission was searched to find any signs of energy transfer phenomena. However, unfortunately, only direct illumination (typical for NIR Yb excitation) gave some weak to almost no response despite interesting Pr emission in the form of quantum cutting just beneath the blue region (- we were expecting red). Yb^{3+} response was later measured at LT, hosting an interesting Stark splitting effect – some of the Yb lines that emerged might be useful for future applications. However, one, denoted as 6>4 transition, required special attention regarding selection rules since its odd appearance depends on 917, 978 nm laser illumination.
- Without any direct energy transfer/UV excitation from Pr^{3+} sensitizers or WO_x mediators, the whole energy transfer ordeal seems rather futile. Derivatives were slightly better in exposing Yb, though, maybe because they are more stable than barium DPs regarding PL. As it turned out later on XAS, a part of Yb^{3+} was reduced during the synthesis - the expected/applied dopant concentration dropped towards Yb^{2+} probably while applying Ar:H_2 atmosphere during SSR or due to reversed charge-transfer phenomena (a charge transfer side-effect victim). O_i interference could also meddle in that matter; however, in terms of Yb, it helps by oxidizing their ions fully back to the 3+ state. O_i/RE interference seems not selective and mainly worsens the PL effects by changing Ce/Pr^{3+} to 4+. In the case of Yb, the 3+ charge is the highest PL-active oxidation state, so the whole system benefits from this process.
- Materials (primarily referring to Ba DPs since derivatives are slightly more stable) are weak phosphors and are only useful (PL-wise) when RE^{3+} ions exist within a limited time frame of coherent-light exposure –at least from HT, RT, down to 150K where changes are rapid and irreversible. That is probably due to the proximity of several states & thermal kT effect dictated by E_a - 10-15 meV gaps of states placed maybe not coincidentally between 115-170K where transitions mentioned above occur). Below 90K, there is a chance to recover them but not entirely - to the same value as before but up to approximately three times). The general implication is that they could be, unfortunately, used only as a one-time, irreversible sensor, best without any air around & when cooled down under respectable and coherent NUV excitation light.
- As it can be necessary for any other purpose, it is worth stating that, during charge transfer (RE-W/O_i RT/HT evolution involving NUV lasers), most RE modes broaden, red-shift, and diminish, giving place to much stronger $W^{6+}O_4$ bands - typical for Ca/Sr/$BaWO_4$ scintillators. That means the (irreversible but surely noticeable) changes disrupt the balance of differently charged RE/W ions. A brief moment of exposure (around 20-40 min in RT, NUV light shrinking to mere seconds in LT, deep X-rays) could be a trigger signal of changing B-site ratios outside their delicate equilibria, swiftly diminishing white light from RE→WO_x energy transfer. Any external, highly energetic stimuli in RT or HT could be easily distinguished if exposed to UV by rapidly growing yellowish-green emission. In LT, the cold-white light would partially decay – just like under the weak Xe lamp.
- Judging by LT experiments on Pr-doped samples, ionized electrons can be retrapped on Pr^{3+}. They can also land on deeper electron traps, which could be many (like O_i/O^-, W^{5+} reported by XPS & EPR). Slightly heated-up samples at low temperatures can ionize the shallow traps close to praseodymium levels and jump to the conduction band. Some electrons may recombine, and others may go toward other shallow traps. However, at RT room temperature, kT would be ~25 meV, so only deep traps would remain with increased ionization probability towards emission. As a result, after prolonged exposure, we should have reloaded all electrons from Pr^{3+} towards the deeper potential well. This phenomenon could be useful in dosimetry, especially if forged into more efficient crystals.

Bibliography

(1) Nishinaga, T. *Handbook of Crystal Growth: Bulk Crystal Growth: Second Edition*; Elsevier Inc., 2014; Vol. 2. https://doi.org/10.1016/C2013-0-09791-5.

(2) Wlodarczyk, D.; Bulyk, L. I.; Berkowski, M.; Glowacki, M.; Kosyl, K. M.; Kaczmarek, S. M.; Kowalski, Z.; Wittlin, A.; Przybylinska, H.; Zhydachevskyy, Y.; Suchocki, A. High-Pressure Low Temperature Optical Studies of BaWO4:Ce,Na Crystals. *Inorg Chem* **2019**, *58* (9), 5617–5629. https://doi.org/10.1021/acs.inorgchem.8b03606.

(3) Pinatti, I. M.; Pereira, P. F. S.; de Assis, M.; Longo, E.; Rosa, I. L. V. Rare Earth Doped Silver Tungstate for Photoluminescent Applications. *J Alloys Compd* **2019**, *771*, 433–447. https://doi.org/10.1016/j.jallcom.2018.08.302.

(4) Groenink, J. A.; Blasse, G. Some New Observations on the Luminescence of PbMoO4 and PbWO4. *J Solid State Chem* **1980**, *32* (1), 9–20. https://doi.org/10.1016/0022-4596(80)90263-7.

(5) Grasser, R.; Scharmann, A.; Strack, K. R. On the Intrinsic Nature of the Blue Luminescence in CaWO4. *J Lumin* **1982**, *27* (3), 263–272. https://doi.org/10.1016/0022-2313(82)90004-7.

(6) Baccaro, S.; Borgia, B.; Cecilia, A.; Dafinei, I.; Diemoz, M.; Fabeni, P.; Nikl, M.; Martini, M.; Montecchi, M.; Pazzi, G.; Spinolo, G.; Vedda, A. Investigation of Lead Tungstate (PbWO4) Crystal Properties. *Nucl Phys B Proc Suppl* **1998**, *61* (3), 66–70. https://doi.org/10.1016/S0920-5632(97)00540-9.

(7) Korzhik, M. V.; Pavlenko, V. B.; Timoschenko, T. N.; Katchanov, V. A.; Singovskii, A. V.; Annenkov, A. N.; Ligun, V. A.; Solskii, I. M.; Peigneux, J. P. Spectroscopy and Origin of Radiation Centers and Scintillation in PbWO4 Single Crystals. *Physica Status Solidi A Appl Res* **1996**, *154* (2), 779–788. https://doi.org/10.1002/pssa.2211540231.

(8) Sokolenko, E. V.; Zhukovskii, V. M.; Buyanova, E. S.; Krasnobaev, Y. A. Luminescent Properties of Oxygen-Disordered Scheelite-Structure Tungstates: Steady-State Luminescence. *Inorganic materials* **1998**, *34* (5), 611–615.

(9) Shi, C.; Wei, Y.; Yang, X.; Zhou, D.; Guo, C.; Liao, J.; Tang, H. Spectral Properties and Thermoluminescence of $PbWO_4$ Crystals Annealed in Different Atmospheres. *Chem Phys Lett* **2000**, *328* (1–2), 1–4. https://doi.org/10.1016/S0009-2614(00)00897-6.

(10) Chen, Y.; Shi, C.; Hu, G. Influence of Sb Doping on the Luminescent Properties of $PbWO_4$ Single Crystals. *J Appl Phys* **2000**, *87* (3), 1503–1506. https://doi.org/10.1063/1.372041.

(11) Qi, Z.; Shi, C.; Zhou, D.; Tang, H.; Liu, T.; Hu, T. The Green Emission and Local Structure of the Scintillator $PbWO_4$. *Physica B Condens Matter* **2001**, *307* (1–4), 45–50. https://doi.org/10.1016/S0921-4526(01)00973-5.

(12) Sinelnikov, B. M.; Sokolenko, E. V.; Zvekova E.G. Effect of Nonstoichiometry on the 420-Nm Luminescence of Calcium Tungstate. *Inorganic materials* **1996**, *32* (9), 999–1001.

(13) Campos, A. B.; Simões, A. Z.; Longo, E.; Varela, J. A.; Longo, V. M.; de Figueiredo, A. T.; De Vicente, F. S.; Hernandes, A. C. Mechanisms behind Blue, Green, and Red Photoluminescence Emissions in $CaWO_4$ and $CaMoO_4$ Powders. *Appl Phys Lett* **2007**, *91* (5), 051923. https://doi.org/10.1063/1.2766856.

(14) Longo, V. M.; Figueiredo, A. T. de; Campos, A. B.; Espinosa, J. W. M.; Hernandes, A. C.; Taft, C. A.; Sambrano, J. R.; Varela, J. A.; Longo, E. Different Origins of Green-Light Photoluminescence Emission in Structurally Ordered and Disordered Powders of Calcium Molybdate. *J Phys Chem A* **2008**, *112* (38), 8920–8928. https://doi.org/10.1021/jp801587w.

(15) Lacomba-Perales, R.; Errandonea, D.; Segura, A.; Ruiz-Fuertes, J.; Rodríguez-Hernández, P.; Radescu, S.; López-Solano, J.; Mujica, A.; Muñoz, A. A Combined High-Pressure Experimental and Theoretical Study of the Electronic Band-Structure of Scheelite-Type AWO_4 (A = Ca, Sr, Ba, Pb) Compounds. *J Appl Phys* **2011**, *110* (4), 043703. https://doi.org/10.1063/1.3622322.

(16) Dorenbos, P.; Rogers, E. G. Vacuum Referred Binding Energies of the Lanthanides in Transition Metal Oxide Compounds. *ECS Journal of Solid State Science and Technology* **2014**, *3* (8), R150–R158. https://doi.org/10.1149/2.0061408jss.

(17) Sleight, A. W. Accurate Cell Dimensions for ABO_4 Molybdates and Tungstates. *Acta Crystallogr B* **1972**, *28* (10), 2899–2902. https://doi.org/10.1107/S0567740872007186.

(18) Gürmen, E.; Daniels, E.; King, J. S. Crystal Structure Refinement of $SrMoO_4$, $SrWO_4$, $CaMoO_4$, and $BaWO_4$ by Neutron Diffraction. *J Chem Phys* **1971**, *55* (3), 1093–1097. https://doi.org/10.1063/1.1676191.

(19) Itoh, M.; Fujita, M. Optical Properties of Scheelite and Raspite $PbWO_4$ Crystals. *Phys Rev B* **2000**, *62* (19), 12825–12830. https://doi.org/10.1103/PhysRevB.62.12825.

(20) Martini, M.; Meinardi, F.; Spinolo, G.; Vedda, A.; Nikl, M.; Usuki, Y. Shallow Traps in $PbWO_4$ Studied by Wavelength-Resolved Thermally Stimulated Luminescence. *Phys Rev B* **1999**, *60* (7), 4653–4658. https://doi.org/10.1103/PhysRevB.60.4653.

(21) Mürk, V.; Nikl, M.; Mihoková, E.; Nitsch, K. A Study of Electron Excitations in $CaWO_4$ and $PbWO_4$ Single Crystals. *Journal of Physics: Condensed Matter* **1997**, *9* (1), 249–256. https://doi.org/10.1088/0953-8984/9/1/026.

(22) Errandonea, D.; Pellicer-Porres, J.; Manjón, F. J.; Segura, A.; Ferrer-Roca, Ch.; Kumar, R. S.; Tschauner, O.; López-Solano, J.; Rodríguez-Hernández, P.; Radescu, S.; Mujica, A.; Muñoz, A.; Aquilanti, G. Determination of the High-Pressure Crystal Structure of $BaWO_4$ and $PbWO_4$. *Phys Rev B* **2006**, *73* (22), 224103. https://doi.org/10.1103/PhysRevB.73.224103.

(23) Manjon, F. J.; Errandonea, D.; Garro, N.; Pellicer-Porres, J.; López-Solano, J.; Rodríguez-Hernández, P.; Radescu, S.; Mujica, A.; Muñoz, A.; Manjón, F. J.; Errandonea, D.; Garro, N.; Pellicer-Porres, J.; Rodríguez-Hernández, P.; Radescu, S.; López-Solano, J.; Mujica, A.; Muñoz, A. Lattice Dynamics Study of Scheelite Tungstates under High Pressure $BaWO_4$. *Phys Rev B* **2006**, *74* (14), 144111. https://doi.org/10.1103/PhysRevB.74.144111.

(24) Grzechnik, A.; Crichton, W. A.; Marshall, W. G.; Friese, K. High-Pressure x-Ray and Neutron Powder Diffraction Study of $PbWO_4$ and $BaWO_4$ Scheelites. *Journal of Physics: Condensed Matter* **2006**, *18* (11), 3017–3029. https://doi.org/10.1088/0953-8984/18/11/008.

(25) Panchal, V.; Garg, N.; Chauhan, A. K.; Sangeeta; Sharma, S. M. High Pressure Phase Transitions in $BaWO_4$. *Solid State Commun* **2004**, *130* (3–4), 203–208. https://doi.org/10.1016/J.SSC.2004.01.043.

(26) Jayaraman, A.; Batlogg, B.; VanUitert, L. G. High-Pressure Raman Study of Alkaline-Earth Tungstates and a New Pressure-Induced Phase Transition in $BaWO_4$. *Phys Rev B* **1983**, *28* (8), 4774–4777. https://doi.org/10.1103/PhysRevB.28.4774.

(27) Lacomba-Perales, R.; Martinez-García, D.; Errandonea, D.; Le Godec, Y.; Philippe, J.; Le Marchand, G.; Chervin, J. C.; Polian, A.; Múñoz, A.; López-Solano, J. Experimental and Theoretical Investigation of the Stability of the Monoclinic $BaWO_4$-II Phase at High Pressure and High Temperature. *Phys Rev B* **2010**, *81* (14), 144117. https://doi.org/10.1103/PhysRevB.81.144117.

(28) Gomis, O.; Sans, J. A.; Lacomba-Perales, R.; Errandonea, D.; Meng, Y.; Chervin, J. C.; Polian, A. Complex High-Pressure Polymorphism of Barium Tungstate. *Phys Rev B* **2012**, *86* (5), 054121. https://doi.org/10.1103/PhysRevB.86.054121.

(29) Tan, D.; Xiao, W.; Zhou, W.; Chen, M.; Zhou, W.; Li, X.; Li, Y.; Liu, J. High Pressure X-Ray Diffraction Study on $BaWO_4$-II. *High Press Res* **2012**, *32* (2), 262–269. https://doi.org/10.1080/08957959.2012.658789.

(30) Tan, D.-Y.; Xiao, W.-S.; Zhou, W.-G.; Song, M.-S.; Xiong, X.-L.; Chen, M. Raman Investigation of $BaWO_4$-II Phase under Hydrostatic Pressures up to 14.8 GPa. *Chinese Physics Letters* **2009**, *26* (4), 046301. https://doi.org/10.1088/0256-307X/26/4/046301.

(31) Kawada, I.; Kato, K.; Fujita, T.; IUCr. $BaWO_4$-II (a High-Pressure Form). *Acta Crystallogr B* **1974**, *30* (8), 2069–2071. https://doi.org/10.1107/S0567740874006431.

(32) Zhao, Z.; Liang, X.; Zhang, T.; Hu, K.; Li, S.; Zhang, Y. Effects of Cerium Doping on Dielectric Properties and Defect Mechanism of Barium Strontium Titanate Glass-Ceramics. *J Eur Ceram Soc* **2020**, *40* (3), 712–719. https://doi.org/10.1016/j.jeurceramsoc.2019.10.023.

(33) Edgar, A.; Bartle, M.; Varoy, C.; Raymond, S.; Williams, G. Structure and Scintillation Properties of Cerium-Doped Barium Chloride Ceramics: Effects of Cation and Anion Substitution. *IEEE Trans Nucl Sci* **2010**, *57* (3), 1218–1222. https://doi.org/10.1109/TNS.2010.2046181.

(34) Dhananjaya, N.; Nagabhushana, H.; Nagabhushana, B. M.; Rudraswamy, B.; Shivakumara, C.; Narahari, K.; Chakradhar, R. P. S. Enhanced Photoluminescence of Gd2O3:Eu3+ Nanophosphors with Alkali (M = Li+, Na+, K+) Metal Ion Co-Doping. *Spectrochim Acta A Mol Biomol Spectrosc* **2012**, *86*, 8–14. https://doi.org/10.1016/j.saa.2011.05.072.

(35) Mandal, S.; Pati, R. Codoping in a Single Molecular Junction from First Principles. *Phys Rev B Condens Matter Mater Phys* **2011**, *83* (19), 195420. https://doi.org/10.1103/PhysRevB.83.195420.

(36) Głuchowski, P.; Nikonkov, R.; Tomala, R.; Stręk, W.; Shulha, T.; Serdechnova, M.; Zarkov, A.; Murauskas, T.; Pakalaniškis, A.; Skaudžius, R.; Kareiva, A.; Kholkin, A.; Bushinsky, M.; Latushka, S.; Karpinsky, D. Impact of Alkali Ions Codoping on Magnetic Properties of La0.9a0.1mn0.9co0.1o3 (a: Li, k, Na) Powders and Ceramics. *Applied Sciences* **2020**, *10* (24), 8786–8798. https://doi.org/10.3390/app10248786.

(37) Vasala, S.; Karppinen, M. A2B'B"O6 Perovskites: A Review. *Progress in Solid State Chemistry*. Pergamon May 1, 2015, pp 1–36. https://doi.org/10.1016/j.progsolidstchem.2014.08.001.

(38) A Stand out Family. *Nature Materials*. Nature Publishing Group September 24, 2021, p 1303. https://doi.org/10.1038/s41563-021-01127-8.

(39) Chakhmouradian, A. R.; Mitchell, R. H. Compositional Variation of Perovskite-Group Minerals from the Khibina Complex, Kola Peninsula, Russia. *Can Mineral* **1998**, *36* (4), 953–969.

(40) Johnsson, M.; Lemmens, P. Perovskites and Thin Films - Crystallography and Chemistry. *Journal of Physics Condensed Matter* **2008**, *20* (26), 264001. https://doi.org/10.1088/0953-8984/20/26/264001.

(41) Mitchell, R. H.; Welch, M. D.; Chakhmouradian, A. R. Nomenclature of the Perovskite Supergroup: A Hierarchical System of Classification Based on Crystal Structure and Composition. *Mineral Mag* **2017**, *81* (3), 411–461. https://doi.org/10.1180/minmag.2016.080.156.

(42) Passi, M.; Pal, B. A Review on CaTiO3 Photocatalyst: Activity Enhancement Methods and Photocatalytic Applications. *Powder Technology*. Elsevier August 1, 2021, pp 274–304. https://doi.org/10.1016/j.powtec.2021.04.056.

(43) Moreira, M. L.; Paris, E. C.; do Nascimento, G. S.; Longo, V. M.; Sambrano, J. R.; Mastelaro, V. R.; Bernardi, M. I. B.; Andrés, J.; Varela, J. A.; Longo, E. Structural and Optical Properties of CaTiO3 Perovskite-Based Materials Obtained by Microwave-Assisted Hydrothermal Synthesis: An Experimental and Theoretical Insight. *Acta Mater* **2009**, *57* (17), 5174–5185. https://doi.org/10.1016/j.actamat.2009.07.019.

(44) Megaw, H. D. Crystal Structure of Barium Titanate [9]. *Nature*. Nature Publishing Group 1945, pp 484–485. https://doi.org/10.1038/155484b0.

(45) Bhalla, A. S.; Guo, R.; Roy, R. The Perovskite Structure - A Review of Its Role in Ceramic Science and Technology. *Materials Research Innovations* **2000**, *4* (1), 3–26. https://doi.org/10.1007/s100190000062.

(46) Hao, J.; Li, W.; Zhai, J.; Chen, H. Progress in High-Strain Perovskite Piezoelectric Ceramics. *Materials Science and Engineering R: Reports*. Elsevier January 1, 2019, pp 1–57. https://doi.org/10.1016/j.mser.2018.08.001.

(47) Shi, C.; Ma, J. J.; Jiang, J. Y.; Hua, M. M.; Xu, Q.; Yu, H.; Zhang, Y.; Ye, H. Y. Large Piezoelectric Response in Hybrid Rare-Earth Double Perovskite Relaxor Ferroelectrics. *J Am Chem Soc* **2020**, *142* (21), 9634–9641. https://doi.org/10.1021/jacs.0c00480.

(48) Hossain, A.; Bandyopadhyay, P.; Roy, S. An Overview of Double Perovskites A2B'B"O6 with Small Ions at A Site: Synthesis, Structure and Magnetic Properties. *J Alloys Compd* **2018**, *740*, 414–427. https://doi.org/10.1016/j.jallcom.2017.12.282.

(49) Chakraborty, K. R.; Das, A.; Krishna, P. S. R.; Yusuf, S. M.; Patwe, S. J.; Achary, S. N.; Tyagi, A. K. A Low Temperature Magnetization and Neutron Diffraction Study of Ca2NiWO6. *J Alloys Compd* **2008**, *457* (1–2), 15–18. https://doi.org/10.1016/j.jallcom.2007.02.141.

(50) Azad, A. K.; Ivanov, S. A.; Eriksson, S. G.; Eriksen, J.; Rundlöf, H.; Mathieu, R.; Svedlindh, P. Nuclear and Magnetic Structure of Ca2MnWO6: A Neutron Powder Diffraction Study. *Mater Res Bull* **2001**, *36* (13–14), 2485–2496. https://doi.org/10.1016/S0025-5408(01)00708-5.

(51) Bijelić, J.; Tatar, D.; Hajra, S.; Sahu, M.; Kim, S. J.; Jagličić, Z.; Djerdj, I. Nanocrystalline Antiferromagnetic High-κ Dielectric Sr2NiMO6 (M = Te, W) with Double Perovskite Structure Type. *Molecules* **2020**, *25* (17), 3996–4012. https://doi.org/10.3390/molecules25173996.

(52) Goodenough, J. B.; Longo, M. General Remarks. In *Part A*; Hellwege, K.-H., Hellwege, A. M., Eds.; Springer-Verlag: Berlin Heidelberg, 2005; Vol. 4A, pp 126–129. https://doi.org/10.1007/10201420_36.

(53) Solovyev, I. V. Electronic Structure and Stability of the Ferrimagnetic Ordering in Double Perovskites. *Phys Rev B Condens Matter Mater Phys* **2002**, *65* (14), 1–17. https://doi.org/10.1103/PhysRevB.65.144446.

(54) Pickett, W. E.; Singh, D. J. Electronic Structure and Half-Metallic Transport in t System. *Phys Rev B Condens Matter Mater Phys* **1996**, *53* (3), 1146–1160. https://doi.org/10.1103/PhysRevB.53.1146.

(55) Cava, R. J.; Batlogg, B.; Krajewski, J. J.; Farrow, R.; Rupp, L. W.; White, A. E.; Short, K.; Peck, W. F.; Kometani, T. Superconductivity near 30 K without Copper: The Ba0.6K 0.4BiO3 Perovskite. *Nature* **1988**, *332* (6167), 814–816. https://doi.org/10.1038/332814a0.

(56) Li, M.; Pietrowski, M. J.; de Souza, R. A.; Zhang, H.; Reaney, I. M.; Cook, S. N.; Kilner, J. A.; Sinclair, D. C. A Family of Oxide Ion Conductors Based on the Ferroelectric Perovskite Na0.5Bi0.5TiO3. *Nat Mater* **2014**, *13* (1), 31–35. https://doi.org/10.1038/nmat3782.

(57) Bednorz, J. G.; M̈ller, K. A. Perovskite-Type OxidesThe New Approach to High-Tc Superconductivity. *Rev Mod Phys* **1988**, *60* (3), 585–600. https://doi.org/10.1103/RevModPhys.60.585.

(58) Chen, D. Y.; Chien, F. Z.; Ling, D. C.; Tseng, J. L.; Sheen, S. R.; Wang, M. J.; Wu, M. K. Superconductivity in Ru-Based Double Perovskite - The Possible Existence of a New Superconducting Pairing State. *Physica C: Superconductivity and its Applications* **1997**, *282–287* (1), 73–76. https://doi.org/10.1016/S0921-4534(97)00214-1.

(59) Tanaka, H.; Misono, M. Advances in Designing Perovskite Catalysts. *Curr Opin Solid State Mater Sci* **2001**, *5* (5), 381–387. https://doi.org/10.1016/S1359-0286(01)00035-3.

(60) Yin, W. J.; Weng, B.; Ge, J.; Sun, Q.; Li, Z.; Yan, Y. Oxide Perovskites, Double Perovskites and Derivatives for Electrocatalysis, Photocatalysis, and Photovoltaics. *Energy and Environmental Science*. The Royal Society of Chemistry February 13, 2019, pp 442–462. https://doi.org/10.1039/c8ee01574k.

(61) Schwertmann, L.; Wark, M.; Marschall, R. Sol–Gel Synthesis of Defect-Pyrochlore Structured CsTaWO6 and the Tribochemical Influences on Photocatalytic Activity. *RSC Adv* **2013**, *3* (41), 18908–18915. https://doi.org/10.1039/C3RA42768D.

(62) Zheng, K.; Świerczek, K. Evaluation of W-Containing Sr1 -XBaxFe0.75W0.25O3-δ (x = 0, 0.5, 1) Anode Materials for Solid Oxide Fuel Cells. *Solid State Ion* **2016**, *288*, 124–129. https://doi.org/10.1016/j.ssi.2015.11.022.

(63) Huang, Y. H.; Dass, R. I.; King, Z. L.; Goodenough, J. B. Double Perovskites as Anode Meterials for Solid-Oxide Fuel Cells. *Science (1979)* **2006**, *312* (5771), 254–257. https://doi.org/10.1126/science.1125877.

(64) Afroze, S.; Karim, A. H.; Cheok, Q.; Eriksson, S.; Azad, A. K. Latest Development of Double Perovskite Electrode Materials for Solid Oxide Fuel Cells: A Review. *Frontiers in Energy* **2019**, *13* (4), 770–797. https://doi.org/10.1007/s11708-019-0651-x.

(65) Green, M. A.; Ho-Baillie, A.; Snaith, H. J. The Emergence of Perovskite Solar Cells. *Nature Photonics*. Nature Publishing Group June 27, 2014, pp 506–514. https://doi.org/10.1038/nphoton.2014.134.

(66) Zhang, Z.; Zhang, Y.; Guo, X.; Wang, D.; Lao, Y.; Qu, B.; Xiao, L.; Chen, Z. Realizing High-Efficiency and Stable Perovskite Solar Cells via Double-Perovskite Nanocrystal Passivation. *ACS Appl Energy Mater* **2022**, *5* (1), 1169–1174. https://doi.org/10.1021/acsaem.1c03544.

(67) Yang, X.; Wang, W.; Ran, R.; Zhou, W.; Shao, Z. Recent Advances in Cs2AgBiBr6-Based Halide Double Perovskites as Lead-Free and Inorganic Light Absorbers for Perovskite Solar Cells. *Energy and Fuels* **2020**, *34* (9), 10513–10528. https://doi.org/10.1021/acs.energyfuels.0c02236.

(68) Kobayashi, K. I.; Kimura, T.; Sawada, H.; Terakura, K.; Tokura, Y. Room-Temperature Magnetoresistance in an Oxide Material with an Ordered Double-Perovskite Structure. *Nature* **1998**, *395* (6703), 677–680. https://doi.org/10.1038/27167.

(69) Glazer, A. M. The Classification of Tilted Octahedra in Perovskites. *Acta Crystallogr B* **1972**, *28* (11), 3384–3392. https://doi.org/10.1107/s0567740872007976.

(70) Woodward, P. M. Octahedral Tilting in Perovskites. II. Structure Stabilizing Forces. *Acta Crystallogr B* **1997**, *53* (1), 44–66. https://doi.org/10.1107/S0108768196012050.

(71) Howard, C. J.; Kennedy, B. J.; Woodward, P. M. Ordered Double Perovskites - A Group-Theoretical Analysis. *Acta Crystallogr B* **2003**, *59* (4), 463–471. https://doi.org/10.1107/S0108768103010073.

(72) Howard, C. J.; Stokes, H. T. Structures and Phase Transitions in Perovskites - A Group-Theoretical Approach. *Acta Crystallogr A* **2005**, *61* (1), 93–111. https://doi.org/10.1107/S0108767304024493.

(73) Goldschmidt, V. M. Die Gesetze Der Krystallochemie. *Naturwissenschaften* **1926**, *14* (21), 477–485. https://doi.org/10.1007/BF01507527.

(74) Bartel, C. J.; Sutton, C.; Goldsmith, B. R.; Ouyang, R.; Musgrave, C. B.; Ghiringhelli, L. M.; Scheffler, M. New Tolerance Factor to Predict the Stability of Perovskite Oxides and Halides. *Sci Adv* **2019**, *5* (2), ID eaavo693. https://doi.org/https://doi.org/10.1126/sciadv.aav0693.

(75) Ijdo, D. J. W.; Fu, W. T.; Akerboom, S. Crystal Structure of Ba9La2W4O24 and Sr9Gd2W4O24: A New B-Site Vacancy Ordered 4×4×4 Cubic Perovskite. *J Solid State Chem* **2016**, *238*, 236–240. https://doi.org/10.1016/j.jssc.2016.03.039.

(76) Jeitschko, W.; Mons, H. A.; Rodewald, U. C.; Möller, M. H. The Crystal Structure of the Potential Ferroelectric Calcium Rhenate(VI, VII) Ca11Re4O24 and Its Relation to the Structure of Sr11Os4O24. *Zeitschrift fur Naturforschung - Section B Journal of Chemical Sciences* **1998**, *53* (1), 31–36. https://doi.org/10.1515/ZNB-1998-0108.

(77) Han, Y. jie; Wang, S.; Liu, H.; Shi, L.; Zhang, W. xin; Cai, L. ke; Mao, Z. yong; Wang, D. jian; Mu, Z. fei; Zhang, Z. wei; Zhao, Y. Mn4+ Doped Tetratungstate Sr9Gd2W4O24 Far-Red Phosphor: Synthesis, Luminescence Properties, and Potential Applications in Indoor Plant Cultivation. *J Lumin* **2020**, *220*, 117027. https://doi.org/10.1016/j.jlumin.2020.117027.

(78) Zeng, Q.; He, P.; Pang, M.; Liang, H.; Gong, M.; Su, Q. Sr9R2-XEuxW4O24 (R=Gd and Y) Red Phosphor for near-UV and Blue InGaN-Based White LEDs. *Solid State Commun* **2009**, *149* (21–22), 880–883. https://doi.org/10.1016/j.ssc.2009.02.056.

(79) Xie, Z.; Liu, X.; Zhao, W. Tunable Photoluminescence and Energy Transfer of Novel Phosphor Sr9La2W4O24:Sm3+, Eu3+ for near-UV White LEDs. *Journal of Materials Science: Materials in Electronics* **2020**, *31* (9), 7114–7122. https://doi.org/10.1007/s10854-020-03282-1.

(80) Nag, A.; Ray, S. Magnetoresistance Stories of Double Perovskites. *Pramana - Journal of Physics* **2015**, *84* (6), 967–975. https://doi.org/10.1007/s12043-015-0995-7.

(81) Reaney, I. M.; Colla, E. L.; Setter, N. Dielectric and Structural Characteristics of Ba- and Sr-Based Complex Perovskites as a Function of Tolerance Factor. *Jpn J Appl Phys* **1994**, *33* (7R), 3984–3390. https://doi.org/10.1143/JJAP.33.3984.

(82) Akbas, M. A.; Davies, P. K. Ordering-Induced Microstructures and Microwave Dielectric Properties of the Ba(Mg1/3Nb2/3)O3-BaZrO3 System. *Journal of the American Ceramic Society* **1998**, *81* (3), 670–676. https://doi.org/10.1111/j.1151-2916.1998.tb02388.x.

(83) Ali Akbas, M.; Davies, P. K. Structure and Dielectric Properties of the Ba(Mg1/3Nb2/3)O3-La(Mg2/3Nb1/3)O3 System. *Communications of the American Ceramic Society* **1998**, *81* (8), 2205–2208.

(84) Sleight, A. W.; Gillson, J. L.; Bierstedt, P. E. High-Temperature Superconductivity in the BaPb1-XBixO3 Systems. *Solid State Commun* **1975**, *17* (1), 27–28. https://doi.org/10.1016/0038-1098(75)90327-0.

(85) Baxter, E. F.; Caddick, M. J.; Ague, J. J. Garnet: Common Mineral, Uncommonly Useful. *Elements* **2013**, *9* (6), 415–419. https://doi.org/10.2113/gselements.9.6.415.

(86) Cesare, B.; Nestola, F.; Johnson, T.; Mugnaioli, E.; Della Ventura, G.; Peruzzo, L.; Bartoli, O.; Viti, C.; Erickson, T. Garnet, the Archetypal Cubic Mineral, Grows Tetragonal. *Sci Rep* **2019**, *9* (1), 1–13. https://doi.org/10.1038/s41598-019-51214-9.

(87) Gambhire, A. B.; Lande, M. K.; Rathod, S. B.; Arbad, B. R.; Vidhate, K. N.; Gholap, R. S.; Patil, K. R. Synthesis and Characterization of FeTiO3 Ceramics. *Arabian Journal of Chemistry* **2016**, *9*, S429–S432. https://doi.org/10.1016/j.arabjc.2011.05.012.

(88) Sibum, H.; Güther, V.; Roidl, O.; Habashi, F.; Wolf, H. U. Titanium, Titanium Alloys, and Titanium Compounds. In *Ullmann's Encyclopedia of Industrial Chemistry*; John Wiley & Sons, Ltd, 2000; pp 40–54, 103–119. https://doi.org/10.1002/14356007.a27_095.

(89) Emsley, J. *Nature´s Building: An A-Z Guide to the Elements*, 1st ed.; Oxford University Press: Oxford, UK, 2003.

(90) William, G. *Observations and Experiments Regarding Menaccanite [i.e., Ilmenite], a Magnetic Sand Found in Cornwall*, 1st ed.; Chemische Annalen für die Freunde der Naturlehre, Arzneygelahrtheit, 1791; Vol. 1.

(91) Surkov, Y.; Shkuratov, Y.; Kaydash, V.; Korokhin, V.; Videen, G. Lunar Ilmenite Content as Assessed by Improved Chandrayaan-1 M3 Data. *Icarus* **2020**, *341*, 113661. https://doi.org/10.1016/j.icarus.2020.113661.

(92) Sasaki, K.; Nakashima, K.; Kanisawa, S. Pyrophanite and High Mn Ilmenite Discovered in the Cretaceous Tono Pluton, NE Japan. *Neues Jahrbuch fur Mineralogie, Monatshefte* **2003**, *7*, 302–320. https://doi.org/10.1127/0028-3649/2003/2003-0302.

(93) Habashi, F. *Historical Introduction to Refractory Metals*, 7th ed.; Taylor & Francis Group, 2001; Vol. 22. https://doi.org/10.1080/08827509808962488.

(94) Kogel, J. E.; Trivedi, N. C.; Barker, J. M.; Krukowski, S. T. *Industrial Minerals & Rocks : Commodities, Markets, and Uses.*, 7th ed.; Society for Mining, Metallurgy, and Exploration, 2006; Vol. 1.

(95) Völz, H. G.; Kischkewitz, J.; Woditsch, P.; Westerhaus, A.; Griebler, W.-D.; De Liedekerke, M.; Buxbaum, G.; Printzen, H.; Mansmann, M.; Räde, D.; Trenczek, G.; Wilhelm, V.; Schwarz, S.; Wienand, H.; Adel, J.; Adrian, G.; Brandt, K.; Cork, W. B.; Winkeler, H.; Mayer, W.; Schneider, K.; Leitner, L.; Kathrein, H.; Schwab, E.; Jakusch, H.; Ohlinger, M.; Veitch, R.; Etzrodt, G.; Pfaff, G.; Franz, K.-D.; Emmert, R.; Nitta, K.; Besold, R.; Gaedcke, H. Pigments, Inorganic. In *Ullmann's Encyclopedia of Industrial Chemistry*; John Wiley & Sons, Ltd: Weinheim, 2006; pp 101–130. https://doi.org/10.1002/14356007.a20_243.pub2.

(96) Nguyen, T. H.; Lee, M. S. A Review on the Recovery of Titanium Dioxide from Ilmenite Ores by Direct Leaching Technologies. *Mineral Processing and Extractive Metallurgy Review* **2019**, *40* (4), 231–247. https://doi.org/10.1080/08827508.2018.1502668.

(97) Zhai, J.; Chen, P.; Sun, W.; Chen, W.; Wan, S. A Review of Mineral Processing of Ilmenite by Flotation. *Miner Eng* **2020**, *157*, 106558. https://doi.org/10.1016/j.mineng.2020.106558.

(98) Samal, S.; Mukherjee, P. S.; Mukherjee, T. K. Thermal Plasma Processing of Ilmenite: A Review. In *Transactions of the Institutions of Mining and Metallurgy, Section C: Mineral Processing and Extractive Metallurgy*; Taylor & Francis, 2010; Vol. 119, pp 116–123. https://doi.org/10.1179/174328509X481891.

(99) Ibrahim, S. A.; Yunus, N. F.; Ariffin, K. S.; Sheikh Abdul Hamid, S. A. R.; Ismail, S.; Jabit, N. The Removal of Fe from the Reduced Ilmenite via Aeration Leaching; Assessing the Effect of Operating Parameters. *Physicochemical Problems of Mineral Processing* **2021**, *57* (6), 186–199. https://doi.org/10.37190/ppmp/143285.

(100) Tarasevich, Y. Y.; Panchenko, T. V. Investigation into the Influence of the Degree of Cation Ordering on the Magnetic Properties of 1:1 Double Perovskites in the Framework of the Heisenberg Model. *Physics of the Solid State* **2007**, *49* (7), 1283–1286. https://doi.org/10.1134/S1063783407070153.

(101) Shimada, T.; Nakamura, J.; Motohashi, T.; Yamauchi, H.; Karppinen, M. Kinetics and Thermodynamics of the Degree of Order of the B Cations in Double-Perovskite Sr2FeMoO6. *Chemistry of Materials* **2003**, *15* (23), 4494–4497. https://doi.org/10.1021/cm030409y.

(102) King, G.; Woodward, P. M. Cation Ordering in Perovskites. *J Mater Chem* **2010**, *20* (28), 5785–5796. https://doi.org/10.1039/b926757c.

(103) Rosenstein, R. D.; Schor, R. Superlattice Madelung Energy of Idealized Ordered Cubic Perovskites. *The Journal of Chemical Physics*. American Institute of PhysicsAIP July 20, 1963, p 1789. https://doi.org/10.1063/1.1776962.

(104) Saltzman, M. N.; Schor, R. Madelung Energy of Perovskite Structures. II. The Tetragonal Case. *J Chem Phys* **1965**, *42* (10), 3698–3700. https://doi.org/10.1063/1.1695782.

(105) Katz, L.; Ward, R. Structure Relations in Mixed Metal Oxides. *Inorg Chem* **1964**, *3* (2), 205–211. https://doi.org/10.1021/ic50012a013.

(106) Choy, J. H.; Park, J. H.; Hong, S. T.; Kim, D. K. Competition of Covalency between CrIII-O and Tav-O Bonds in the Perovskites Ca2CrTaO6 and Sr2CrTaO6. *J Solid State Chem* **1994**, *111* (2), 370–379. https://doi.org/10.1006/jssc.1994.1241.

(107) Cussen, E. J.; Battle, P. D. The Influence of Structural Disorder on the Magnetic Properties of Sr2Fe1-XGaxTaO6 (0≤x≤1). *J Mater Chem* **2003**, *13* (5), 1210–1214. https://doi.org/10.1039/b211286h.

(108) Galasso, F.; Darby, W. Ordering of the Octahedrally Coördinated Cation Position in the Perovskite Structure. *Journal of Physical Chemistry* **1962**, *66* (1), 131–132. https://doi.org/10.1021/j100807a028.

(109) Cox, D. E.; Sleight, A. W. Crystal Structure of Ba2Bi3+Bi5+O6. *Solid State Commun* **1976**, *19* (10), 969–973. https://doi.org/10.1016/0038-1098(76)90632-3.

(110) Cox, D. E.; Sleight, A. W. Mixed-Valent Ba2Bi3+Bi5+O6 : Structure and Properties vs Temperature. *Acta Crystallogr B* **1979**, *35* (1), 1–10. https://doi.org/10.1107/s0567740879002417.

(111) Lufaso, M. W.; Woodward, P. M. Jahn-Teller Distortions, Cation Ordering and Octahedral Tilting in Perovskites. *Acta Crystallogr B* **2004**, *60* (1), 10–20. https://doi.org/10.1107/S0108768103026661.

(112) Lufaso, M. W.; Barnes, P. W.; Woodward, P. M. Structure Prediction of Ordered and Disordered Multiple Octahedral Cation Perovskites Using SPuDS. *Acta Crystallogr B* **2006**, *62* (3), 397–410. https://doi.org/10.1107/S010876810600262X.

(113) Lobo, R. P. S. M.; Gervais, F. Bismuth Disproportionation in BaBiO3 Studied by Infrared and Visible Reflectance Spectra. *Phys Rev B* **1995**, *52* (18), 13294–13299. https://doi.org/10.1103/PhysRevB.52.13294.

(114) Brusset, H.; Gillier-Pandraud, M. H.; Rajaonera, P. Sur Des Niobates, Antimoniates et Tantalates Ternaires et Quaternaires de Structure Perovskite. *Mater Res Bull* **1975**, *10* (3), 209–216. https://doi.org/10.1016/0025-5408(75)90158-0.

(115) Sakai, C.; Doi, Y.; Hinatsu, Y. Crystal Structures and Magnetic Properties of Double Perovskite Compounds Ca2LnRuO6 (Ln = Y, La-Lu). In *Journal of Alloys and Compounds*; Elsevier, 2006; Vol. 408–412, pp 608–612. https://doi.org/10.1016/j.jallcom.2004.12.068.

(116) Sakai, C.; Doi, Y.; Hinatsu, Y.; Ohoyama, K. Magnetic Properties and Neutron Diffraction Study of Double Perovskites Ca2LnRuO6 (Ln = Y, La-Lu). *Journal of Physics Condensed Matter* **2005**, *17* (46), 7383–7394. https://doi.org/10.1088/0953-8984/17/46/022.

(117) Anderson, M. T.; Greenwood, K. B.; Taylor, G. A.; Poeppelmeier, K. R. B-Cation Arrangements in Double Perovskites. *Progress in Solid State Chemistry*. Pergamon January 1, 1993, pp 197–233. https://doi.org/10.1016/0079-6786(93)90004-B.

(118) Gomis, O.; Sans, J. A.; Lacomba-Perales, R.; Errandonea, D.; Meng, Y.; Chervin, J. C.; Polian, A. Complex High-Pressure Polymorphism of Barium Tungstate. *Phys Rev B Condens Matter Mater Phys* **2012**, *86* (5), 054121. https://doi.org/10.1103/PhysRevB.86.054121.

(119) Faizan, M.; Xie, J.; Murtaza, G.; Echeverría-Arrondo, C.; Alshahrani, T.; Bhamu, K. C.; Laref, A.; Mora-Seró, I.; Haidar Khan, S. A First-Principles Study of the Stability, Electronic Structure, and Optical Properties of Halide Double Perovskite Rb2Sn1−xTexI6for Solar Cell Applications. *Physical Chemistry Chemical Physics* **2021**, *23* (8), 4646–4657. https://doi.org/10.1039/d0cp05827k.

(120) Han, D.; Zhang, T.; Huang, M.; Sun, D.; Du, M. H.; Chen, S. Predicting the Thermodynamic Stability of Double-Perovskite Halides from Density Functional Theory. *APL Mater* **2018**, *6* (8), 084902. https://doi.org/10.1063/1.5027414.

(121) Li, A.; Liu, Q.; Chu, W.; Liang, W.; Prezhdo, O. V. Why Hybrid Tin-Based Perovskites Simultaneously Improve the Structural Stability and Charge Carriers' Lifetime: Ab Initio Quantum Dynamics. *ACS Appl Mater Interfaces* **2021**, *13* (14), 16567–16575. https://doi.org/10.1021/acsami.1c03145.

(122) Farzin, Y. A.; Babaei, A.; Ataie, A. Low-Temperature Synthesis of Sr2FeMoO6 Double Perovskite; Structure, Morphology, and Magnetic Properties. *Ceram Int* **2020**, *46* (10), 16867–16878. https://doi.org/10.1016/j.ceramint.2020.03.264.

(123) Tang, Y.; Gomez, L.; Van Der Laan, M.; Timmerman, D.; Sebastian, V.; Huang, C. C.; Gregorkiewicz, T.; Schall, P. Room Temperature Synthesis and Characterization of Novel Lead-Free Double Perovskite Nanocrystals with a Stable and Broadband Emission. *J Mater Chem C Mater* **2021**, *9* (1), 158–163. https://doi.org/10.1039/d0tc04394j.

(124) Holman, K. L.; Huang, Q.; Klimczuk, T.; Trzebiatowski, K.; Bos, J. W. G.; Morosan, E.; Lynn, J. W.; Cava, R. J. Synthesis and Properties of the Double Perovskites La2NiVO6, La2CoVO6, and La2CoTiO6. *J Solid State Chem* **2007**, *180* (1), 75–83. https://doi.org/10.1016/j.jssc.2006.09.013.

(125) Zhou, Q.; Kennedy, B. J. High Temperature Structure of BaBiO3 - A Synchrotron X-Ray Powder Diffraction Study. *Solid State Commun* **2004**, *132* (6), 389–392. https://doi.org/10.1016/j.ssc.2004.08.002.

(126) Aimi, A.; Mori, D.; Hiraki, K. I.; Takahashi, T.; Shan, Y. J.; Shirako, Y.; Zhou, J.; Inaguma, Y. High-Pressure Synthesis of A-Site Ordered Double Perovskite CaMnTi 2O6 and Ferroelectricity Driven by Coupling of A-Site Ordering and the Second-Order Jahn-Teller Effect. *Chemistry of Materials* **2014**, *26* (8), 2601–2608. https://doi.org/10.1021/cm500016z.

(127) Feng, H. L.; Deng, Z.; Segre, C. U.; Croft, M.; Lapidus, S. H.; Frank, C. E.; Shi, Y.; Jin, C.; Walker, D.; Greenblatt, M. High-Pressure Synthesis of Double Perovskite Ba2NiIrO6: In Search of a Ferromagnetic Insulator. *Inorg Chem* **2021**, *60* (2), 1241–1247. https://doi.org/10.1021/acs.inorgchem.0c03402.

(128) Yuan, Y.; Feng, H. L.; Ghimire, M. P.; Matsushita, Y.; Tsujimoto, Y.; He, J.; Tanaka, M.; Katsuya, Y.; Yamaura, K. High-Pressure Synthesis, Crystal Structures, and Magnetic Properties of 5d Double-Perovskite Oxides Ca2MgOsO6 and Sr2MgOsO6. *Inorg Chem* **2015**, *54* (7), 3422–3431. https://doi.org/10.1021/ic503086a.

(129) Buryy, O.; Vasylechko, L.; Sydorchuk, V.; Lakhnik, A.; Suhak, Y.; Wlodarczyk, D.; Hurskyj, S.; Yakhnevych, U.; Zhydachevskyy, Y.; Sugak, D.; Suchocki, A.; Fritze, H. Crystal Structure, Raman Spectra and Electrical Conductivity of LiNb1 – XTaxO3Nanopowders Obtained with High-Energy Ball Milling. *Journal of Nano- and Electronic Physics* **2021**, *13* (2), 02038. https://doi.org/10.21272/JNEP.13(2).02038.

(130) Krahne, R.; Arciniegas, M. P. Triple-Decker Layered Perovskite Materials. *Nature*. Nature Publishing Group September 15, 2021, pp 333–334. https://doi.org/10.1038/d41586-021-02433-6.

(131) Tartakovskii, A. Excitons in 2D Heterostructures. *Nature Reviews Physics*. Nature Publishing Group December 11, 2020, pp 8–9. https://doi.org/10.1038/s42254-019-0136-1.

(132) Wang, Z.; Lin, Q.; Chmiel, F. P.; Sakai, N.; Herz, L. M.; Snaith, H. J. Efficient Ambient-Air-Stable Solar Cells with 2D-3D Heterostructured Butylammonium-Caesium-Formamidinium Lead Halide Perovskites. *Nat Energy* **2017**, *2* (9), 1–10. https://doi.org/10.1038/nenergy.2017.135.

(133) Roy, C. R.; Pan, D.; Wang, Y.; Hautzinger, M. P.; Zhao, Y.; Wright, J. C.; Zhu, Z.; Jin, S. Anion Exchange of Ruddlesden-Popper Lead Halide Perovskites Produces Stable Lateral Heterostructures. *J Am Chem Soc* **2021**, *143* (13), 5212–5221. https://doi.org/10.1021/jacs.1c01573.

(134) Aubrey, M. L.; Saldivar Valdes, A.; Filip, M. R.; Connor, B. A.; Lindquist, K. P.; Neaton, J. B.; Karunadasa, H. I. Directed Assembly of Layered Perovskite Heterostructures as Single Crystals. *Nature* **2021**, *597* (7876), 355–359. https://doi.org/10.1038/s41586-021-03810-x.

(135) Wang, Y.; Tsiumra, V.; Peng, Q.; Liang, H.; Zhydachevskyy, Y.; Chaika, M.; Dluzewski, P.; Przybylińska, H.; Suchocki, A. Hole Trapping Process and Highly Sensitive Ratiometric Thermometry over a Wide Temperature Range in Pr3+-Doped Na2La2Ti3O10 Layered Perovskite Microcrystals. *Journal of Physical Chemistry A* **2019**, *123* (18), 4021–4033. https://doi.org/10.1021/acs.jpca.9b01759.

(136) Wang, Y.; Peng, Q.; Liang, H.; Brik, M. G.; Suchocki, A. 3P0 → 1D2 Non-Radiative Relaxation Control via IVCT State in Pr3+-Doped Na2Ln2Ti3O10 (Ln=La, Gd) Micro-Crystals with Triple-Layered Perovskite Structure. *J Lumin* **2019**, *213*, 510–518. https://doi.org/10.1016/j.jlumin.2019.04.048.

(137) Arai, M.; Matsuda, N.; Tamatani, M. Luminescence Properties of Pr3+ in Monoclinic Gadolinium Sesquioxide. *J Alloys Compd* **1993**, *192* (1–2), 45–47. https://doi.org/10.1016/0925-8388(93)90181-L.

(138) Aumüller, G. C.; Köstler, W.; Grabmaier, B. C.; Frey, R. Luminescence Properties of Pr3+ in Cubic Rare Earth Oxides. *Journal of Physics and Chemistry of Solids* **1994**, *55* (8), 767–772. https://doi.org/10.1016/0022-3697(94)90029-9.

(139) Gonalakrishnan, J.; Bhat, V. A2ln2ti3o10(A = K Or Rb; Ln = La Or Rare Earth): A New Series of Layered Perovskites Exhibiting Ion Exchange. *Inorganic Chemistry*. American Chemical Society December 1, 1987, pp 4299–4301. https://doi.org/10.1021/ic00273a001.

(140) Ruddlesden, S. N.; Popper, P. New Compounds of the K2NIF4 Type. *Acta Crystallogr* **1957**, *10* (8), 538–539. https://doi.org/10.1107/s0365110x57001929.

(141) Fu, P.; Liu, Y.; Yu, S.; Yin, H.; Yang, B.; Ahmad, S.; Guo, X.; Li, C. Dion-Jacobson and Ruddlesden-Popper Double-Phase 2D Perovskites for Solar Cells. *Nano Energy* **2021**, *88*, 106249. https://doi.org/10.1016/j.nanoen.2021.106249.

(142) Kim, H. S.; Seo, J. Y.; Park, N. G. Material and Device Stability in Perovskite Solar Cells. *ChemSusChem*. John Wiley & Sons, Ltd September 22, 2016, pp 2528–2540. https://doi.org/10.1002/cssc.201600915.

(143) Gao, F.; Zhao, Y.; Zhang, X.; You, J. Recent Progresses on Defect Passivation toward Efficient Perovskite Solar Cells. *Advanced Energy Materials*. John Wiley & Sons, Ltd April 1, 2020, p 1902650. https://doi.org/10.1002/aenm.201902650.

(144) Bai, Y.; Xiao, S.; Hu, C.; Zhang, T.; Meng, X.; Lin, H.; Yang, Y.; Yang, S. Dimensional Engineering of a Graded 3D–2D Halide Perovskite Interface Enables Ultrahigh Voc Enhanced Stability in the p-i-n Photovoltaics. *Adv Energy Mater* **2017**, *7* (20), 1701038. https://doi.org/10.1002/aenm.201701038.

(145) Grancini, G.; Nazeeruddin, M. K. Dimensional Tailoring of Hybrid Perovskites for Photovoltaics. *Nature Reviews Materials*. Nature Publishing Group November 28, 2019, pp 4–22. https://doi.org/10.1038/s41578-018-0065-0.

(146) Zhang, F.; Zhu, K. Additive Engineering for Efficient and Stable Perovskite Solar Cells. *Advanced Energy Materials*. John Wiley & Sons, Ltd April 1, 2020, p 1902579. https://doi.org/10.1002/aenm.201902579.

(147) Li, X.; Hoffman, J. M.; Kanatzidis, M. G. The 2D Halide Perovskite Rulebook: How the Spacer Influences Everything from the Structure to Optoelectronic Device Efficiency. *Chemical Reviews*. American Chemical Society February 24, 2021, pp 2230–2291. https://doi.org/10.1021/acs.chemrev.0c01006.

(148) Rodríguez-Carvajal, J. Recent Advances in Magnetic Structure Determination by Neutron Powder Diffraction. *Physica B: Physics of Condensed Matter* **1993**, *192* (1–2), 55–69. https://doi.org/10.1016/0921-4526(93)90108-I.

(149) Syassen, K. Ruby under Pressure. *High Press Res* **2008**, *28* (2), 75–126. https://doi.org/10.1080/08957950802235640.

(150) Mao, H. K.; Xu, J.; Bell, P. M. Calibration of the Ruby Pressure Gauge to 800 Kbar under Quasi-Hydrostatic Conditions. *J Geophys Res Solid Earth* **1986**, *91* (B5), 4673–4676. https://doi.org/10.1029/JB091IB05P04673.

(151) Dimesso, L. Pechini Processes: An Alternate Approach of the Sol–Gel Method, Preparation, Properties, and Applications. In *Handbook of Sol-Gel Science and Technology*; Klein, L., Aparicio, M., Jitianu, A., Eds.; Springer International Publishing, 2016; pp 1–22. https://doi.org/10.1007/978-3-319-19454-7_123-1.

(152) Feng, S. H.; Li, G. H. Hydrothermal and Solvothermal Syntheses. In *Modern Inorganic Synthetic Chemistry: Second Edition*; Elsevier, 2017; pp 73–104. https://doi.org/10.1016/B978-0-444-63591-4.00004-5.

(153) Cao, R.; Xu, H.; Peng, D.; Gou, Q.; Zhou, S.; Liu, P.; Yu, X. Synthesis and Luminescence Properties of $BaWO_4$:Sm^{3+}, Mo^{6+}/K^+ Red Phosphor. *Journal of Materials Science: Materials in Electronics* **2015**, *26* (9), 6776–6780. https://doi.org/10.1007/s10854-015-3288-5.

(154) Sczancoski, J. C.; Cavalcante, L. S.; Joya, M. R.; Espinosa, J. W. M.; Pizani, P. S.; Varela, J. A.; Longo, E. Synthesis, Growth Process and Photoluminescence Properties of SrWO4 Powders. *J Colloid Interface Sci* **2009**, *330* (1), 227–236. https://doi.org/10.1016/j.jcis.2008.10.034.

(155) Shcherbakov, A. I. Theory of Dissolution of Binary Alloys and the Tamman Rule. *Protection of Metals* **2005**, *41* (1), 30–35. https://doi.org/10.1007/s11124-005-0004-5.

(156) Yamagaki, T.; Watanabe, T. Hydrogen Radical Removal Causes Complex Overlapping Isotope Patterns of Aromatic Carboxylic Acids in Negative-Ion Matrix-Assisted Laser Desorption/Ionization Mass Spectrometry. *Mass Spectrometry* **2012**, *1* (1), A0005. https://doi.org/10.5702/massspectrometry.a0005.

(157) Yamagaki, T.; Watanabe, T.; Tanaka, M.; Sugahara, K. Laser-Induced Hydrogen Radical Removal in UV MALDI-MS Allows for the Differentiation of Flavonoid Monoglycoside Isomers. *J Am Soc Mass Spectrom* **2014**, *25* (1), 88–94. https://doi.org/10.1007/s13361-013-0764-0.

(158) Galwey, A. K. Solid State Reaction Kinetics, Mechanisms and Catalysis: A Retrospective Rational Review. *Reaction Kinetics, Mechanisms and Catalysis*. Springer September 14, 2015, pp 1–29. https://doi.org/10.1007/s11144-014-0770-7.

(159) GIESS, E. A. Equations and Tables for Analyzing Solid-state Reaction Kinetics. *Journal of the American Ceramic Society* **1963**, *46* (8), 374–376. https://doi.org/10.1111/j.1151-2916.1963.tb11754.x.

(160) Schmalzried, H. *Monographs in Modern Chemistry: Solid State Reactions*, 5th ed.; ETDEWEB: Germany, 1981; Vol. 12.

(161) Wang, Y.; Suchocki, A.; Włodarczyk, D.; Brik, M. G.; Barzowska, J.; Shekhovtsov, A. N.; Belikov, K. N.; Paszkowicz, W.; Li, L.; Zhou, X. Effect of Temperature and High Pressure on Luminescence Properties of Mn3+ Ions in Ca3Ga2Ge3O12 Single Crystals. *Journal of Physical Chemistry C* **2021**, *125* (9), 5146–5157. https://doi.org/10.1021/acs.jpcc.0c09845.

(162) Liu, B.; Song, K. X. Vibrational Spectroscopy and Microwave Dielectric Properties of Two Novel Ca3Ln2W2O12 (Ln = La, Sm) Tungstate Ceramics. *Mater Res Bull* **2021**, *133*. https://doi.org/10.1016/j.materresbull.2020.111022.

(163) Li, K.; van Deun, R. Enhancing the Energy Transfer from Mn4+ to Yb3+ via a Nd3+ Bridge Role in Ca3La2W2O12:Mn4+,Nd3+,Yb3+ Phosphors for Spectral Conversion of c-Si Solar Cells. *Dyes and Pigments* **2019**, *162*, 990–997. https://doi.org/10.1016/J.DYEPIG.2018.11.030.

(164) Hirrle, R.; Kemmler-Sack, S. Energietransfer Im System Ca3La2W2O12: Mn, Nd,Yb. *Zeitschrift fur Naturforschung - Section A Journal of Physical Sciences* **1988**, *43* (1), 81–84. https://doi.org/10.1515/zna-1988-0112.

(165) Li, K.; van Deun, R. Enhancing the Energy Transfer from Mn4+ to Yb3+ via a Nd3+ Bridge Role in Ca3La2W2O12:Mn4+,Nd3+,Yb3+ Phosphors for Spectral Conversion of c-Si Solar Cells. *Dyes and Pigments* **2019**, *162*, 990–997. https://doi.org/10.1016/j.dyepig.2018.11.030.

(166) Autenrieth, H. D.; Kemmler-Sack, S. Lumineszenz von Ca3La2W2O12: Mn Und Ca3La2Te2O12: Mn. *Mater Chem Phys* **1985**, *12* (5), 437–442. https://doi.org/10.1016/0254-0584(85)90069-0.

(167) Gazulla, M. F.; Ventura, M. J.; Andreu, C.; Gilabert, J.; Orduña, M.; Rodrigo, M. Praseodymium Oxides. Complete Characterization by Determining Oxygen Content. *Microchemical Journal* **2019**, *148*, 291–298. https://doi.org/10.1016/J.MICROC.2019.05.013.

(168) Ferro, S. Physicochemical and Electrical Properties of Praseodymium Oxides. *International Journal of Electrochemistry* **2011**, *2011* (ID 561204), 1–7. https://doi.org/10.4061/2011/561204.

(169) Popa, M.; Kakihana, M. Praseodymium Oxide Formation by Thermal Decomposition of a Praseodymium Complex. *Solid State Ion* **2001**, *141–142*, 265–272. https://doi.org/10.1016/S0167-2738(01)00754-8.

(170) Sharma, R.; Hinode, H.; Eyring, L. A Study of the Decomposition of Praseodymium Hydroxy Carbonate and Praseodymium Carbonate Hydrate. *J Solid State Chem* **1991**, *92* (2), 401–419. https://doi.org/10.1016/0022-4596(91)90348-L.

(171) Hussein, G. A. M. Formation of Praseodymium Oxide from the Thermal Decomposition of Hydrated Praseodymium Acetate and Oxalate. *J Anal Appl Pyrolysis* **1994**, *29* (1), 89–102. https://doi.org/10.1016/0165-2370(93)00782-I.

(172) Netz, A.; Chu, W. F.; Thangadurai, V.; Huggins, R. A.; Weppner, W. Investigations of Praseodymium Oxide Electrodes in Lithium Concentration Cells. *Ionics 1999 5:5* **1999**, *5* (5), 426–433. https://doi.org/10.1007/BF02376009.

(173) Chala, T. F.; Wu, C. M.; Chou, M. H.; Gebeyehu, M. B.; Cheng, K. B. Highly Efficient near Infrared Photothermal Conversion Properties of Reduced Tungsten Oxide/Polyurethane Nanocomposites. *Nanomaterials* **2017**, *7* (7), 191. https://doi.org/10.3390/nano7070191.

(174) Takeda, H.; Adachi, K. Near Infrared Absorption of Tungsten Oxide Nanoparticle Dispersions. *Journal of the American Ceramic Society* **2007**, *90* (12), 4059–4061. https://doi.org/10.1111/j.1551-2916.2007.02065.x.

(175) Mu, J.; Meng, X.; Chen, L.; Lu, Z.; Mou, Q.; Li, X.; Wang, S.; Yue, H. Highly Stable and Biocompatible W18O49@PEG-PCL Hybrid Nanospheres Combining CT Imaging and Cancer Photothermal Therapy. *RSC Adv* **2017**, *7* (18), 10692–10699. https://doi.org/10.1039/c6ra28161c.

(176) Zhou, Y.; Zhang, Y.; Li, R.; Cai, M.; Sun, X. One-Step in Situ Synthesis and Characterization of W18O 49@carbon Coaxial Nanocables. *J Mater Res* **2009**, *24* (5), 1833–1841. https://doi.org/10.1557/jmr.2009.0214.

(177) Cotton, F. A.; Rice, C. E. Tungsten Pentachloride. *Acta Crystallogr B* **1978**, *34* (9), 2833–2834. https://doi.org/10.1107/s0567740878009322.

(178) McCann, E. L.; Brown, T. M.; Djordjevic, C.; Morris, R. E. Tungsten(V) Chloride (Tungsten Pentachloride). In *Inorganic Syntheses*; John Wiley & Sons, Ltd, 2007; Vol. 13, pp 150–154. https://doi.org/10.1002/9780470132449.ch29.

(179) Holzwarth, U.; Gibson, N. The Scherrer Equation versus the "Debye-Scherrer Equation." *Nature Nanotechnology*. Nature Publishing Group August 28, 2011, p 534. https://doi.org/10.1038/nnano.2011.145.

(180) Langford, J. I.; Wilson, A. J. C. Scherrer after Sixty Years: A Survey and Some New Results in the Determination of Crystallite Size. *J Appl Crystallogr* **1978**, *11* (2), 102–113. https://doi.org/10.1107/s0021889878012844.

(181) Lufaso, M. W.; MacQuart, R. B.; Lee, Y.; Vogt, T.; Zur Loye, H. C. Pressure-Induced Phase Transition and Octahedral Tilt System Change of Ba2BiSbO6. *J Solid State Chem* **2006**, *179* (3), 917–922. https://doi.org/10.1016/j.jssc.2005.12.024.

(182) Zhou, Q.; Kennedy, B. J.; Avdeev, M.; Giachini, L.; Kimpton, J. A. Structural Studies of the Phases in Ba2LaIrO6-New Light on an Old Problem. *J Solid State Chem* **2009**, *182* (11), 3195–3200. https://doi.org/10.1016/j.jssc.2009.08.026.

(183) Wlodarczyk, D.; Amilusik, M.; Kosyl, K. M.; Chrunik, M.; Lawniczak-Jablonska, K.; Strankowski, M.; Zajac, M.; Tsiumra, V.; Grochot, A.; Reszka, A.; Suchocki, A.; Giela, T.; Iwanowski, P.; Bockowski, M.; Przybylinska, H. Synthesis Attempt and Structural Studies of Novel A2CeWO6 Double Perovskites (A2+ = Ba, Ca) in and Outside of Ambient Conditions. *ACS Omega* **2022**, *7* (22), 18382–18408. https://doi.org/10.1021/acsomega.2c00669.

(184) Lenz, A.; Müller-Buschbaum, H. Eine Anmerkung Über Geordnete Perowskite Mit Bi5+: Ba2BiMO6 (M ≡ Y, Dy). *Journal of The Less-Common Metals*. Elsevier June 1, 1990, pp L15–L17. https://doi.org/10.1016/0022-5088(90)90331-D.

(185) Fu, W. T.; Au, Y. S.; Akerboom, S.; IJdo, D. J. W. Crystal Structures and Chemistry of Double Perovskites Ba2M(II)M'(VI)O6 (M=Ca, Sr, M'=Te, W, U). *J Solid State Chem* **2008**, *181* (9), 2523–2529. https://doi.org/10.1016/j.jssc.2008.06.024.

(186) IJdo, D. J. W.; Helmholdt, R. B. Ba2Ce3/4SbO6, a Rietveld Refinement of Neutron Powder Diffraction Data. *Acta Crystallogr C* **1993**, *49* (4), 652–654. https://doi.org/10.1107/s0108270192010850.

(187) Hong, S. T. Novel Perovskite-Related Barium Tungstate Ba11W4O23. *J Solid State Chem* **2007**, *180* (11), 3039–3048. https://doi.org/10.1016/j.jssc.2007.08.027.

(188) Garrido Barrios, L. del C. Predicción de Las Propiedades Estructurales, Cohesivas y Electrónicas En Sistemas Tipo Perovskitas A2BB'O6 Utilizando Machine Learning (ML) y La Teoría Funcional de Densidad (DFT), Universidad del Magdalena, Santa Marta, 2021. http://repositorio.unimagdalena.edu.co/handle/123456789/5985 (accessed 2022-11-08).

(189) Shannon, R. D. Revised Effective Ionic Radii and Systematic Studies of Interatomic Distances in Halides and Chalcogenides. *Acta Crystallographica Section A* **1976**, *32* (5), 751–767. https://doi.org/10.1107/S0567739476001551.

(190) Zhou, X.; Zhou, H.; Wu, Q.; Luan, X.; Hu, S.; Deng, J.; Li, S.; Wang, K.; Chen, X. Novel Series of MLa2WO7(M = Sr, Ba) Microwave Dielectric Ceramic Systems with Monoclinic Structures. *Journal of Materials Science: Materials in Electronics* **2020**, *31* (13), 10819–10824. https://doi.org/10.1007/s10854-020-03633-y.

(191) Zhou, X.; Zhou, H.; Wu, Q.; Luan, X.; Hu, S.; Deng, J.; Li, S.; Wang, K.; Chen, X. Novel Series of MLa2WO7(M = Sr, Ba) Microwave Dielectric Ceramic Systems with Monoclinic Structures. *Journal of Materials Science: Materials in Electronics* **2020**, *31* (13), 10819–10824. https://doi.org/10.1007/s10854-020-03633-y.

(192) Choi, S.; Park, B. Y.; Jung, H. K.; Moon, Y. M. BaLa2WO7:Eu3+ as a Novel Red-Emitting Phosphor for UV LEDs. *Journal of the Korean Physical Society* **2010**, *57* (1), 169–172. https://doi.org/10.3938/jkps.57.169.

(193) Hussain, S. K.; Yu, J. S. Sol-Gel Synthesis of Eu3+/Bi3+ Ions Co-Doped BaLa2WO7 Phosphors for Red-LEDs under NUV Excitation and FEDs Applications. *J Lumin* **2017**, *183*, 39–47. https://doi.org/10.1016/j.jlumin.2016.11.003.

(194) Ma, W.; Mashimo, T.; Tamura, S.; Tokuda, M.; Yoda, S.; Tsushida, M.; Koinuma, M.; Kubota, A.; Isobe, H.; Yoshiasa, A. Cerium Oxide (CeO2-x) Nanoparticles with High Ce3+ Proportion Synthesized by Pulsed Plasma in Liquid. *Ceram Int* **2020**, *46* (17), 26502–26510. https://doi.org/10.1016/j.ceramint.2020.07.093.

(195) Klochkov, V. K.; Malyukin, Y. V.; Grygorova, G. V.; Sedyh, O. O.; Kavok, N. S.; Seminko, V. V.; Semynozhenko, V. P. Oxidation-Reduction Processes in CeO2-x Nanocrystals under UV Irradiation. *J Photochem Photobiol A Chem* **2018**, *364*, 282–287. https://doi.org/10.1016/j.jphotochem.2018.06.025.

(196) Schweda, E.; Bevan, D. J. M.; Eyring, L. On the PrnO2n-2 Series of Oxides and the Structure of Pr24O44: An Investigation by High-Resolution Electron Microscopy. *J Solid State Chem* **1991**, *90* (1), 109–125. https://doi.org/10.1016/0022-4596(91)90178-K.

(197) Tuenge, R. T.; Eyring, L. On the Structure of the Intermediate Phases in the Praseodymium Oxide System. *J Solid State Chem* **1979**, *29* (2), 165–179. https://doi.org/10.1016/0022-4596(79)90221-4.

(198) Wolf, H. C. R.; Hoppe, R. Eine Notiz Zum A-Typ Der Lanthanoidoxide: Über Pr2O3. *ZAAC - Journal of Inorganic and General Chemistry* **1985**, *529* (10), 61–64. https://doi.org/10.1002/zaac.19855291009.

(199) Ferro, S. Physicochemical and Electrical Properties of Praseodymium Oxides. *International Journal of Electrochemistry* **2011**, *2011*, ID-561204. https://doi.org/10.4061/2011/561204.

(200) Chiang, Y. M.; Lavik, E. B.; Kosacki, I.; Tuller, H. L.; Ying, J. Y. Defect and Transport Properties of Nanocrystalline CeO2-x. *Appl Phys Lett* **1996**, *69* (2), 185–187. https://doi.org/10.1063/1.117366.

(201) Della Mea, G. B.; Matte, L. P.; Thill, A. S.; Lobato, F. O.; Benvenutti, E. V; Arenas, L. T.; Jürgensen, A.; Hergenröder, R.; Poletto, F.; Bernardi, F. Tuning the Oxygen Vacancy Population of Cerium Oxide (CeO2−x , 0<x<0.5) Nanoparticles. *Appl Surf Sci* **2017**, *422*, 1102–1112. https://doi.org/10.1016/j.apsusc.2017.06.101.

(202) Tyagi, M.; Sangeeta; Sabharwal, S. C. Luminescence Properties of BaWO4 Single Crystal. *J Lumin* **2008**, *128* (9), 1528–1532. https://doi.org/10.1016/j.jlumin.2008.02.006.

(203) Oliveira, M. C.; Gracia, L.; Nogueira, I. C.; Do Carmo Gurgel, M. F.; Mercury, J. M. R.; Longo, E.; Andrés, J. Synthesis and Morphological Transformation of BaWO4 Crystals: Experimental and Theoretical Insights. *Ceram Int* **2016**, *42* (9), 10913–10921. https://doi.org/10.1016/j.ceramint.2016.03.225.

(204) Smirnov, S. A.; Evdokimov, A. A.; Kovba, L. M. New Data on Phase Relationships in Tungstate Systems. *Dokl. Chem.* **1987**, *292* (1), 99–102.

(205) Bramnik, K. G.; Miehe, G.; Ehrenberg, H.; Fuess, H.; Abakumov, A. M.; Shpanchenko, R. V.; Pomjakushin, V. Y.; Balagurov, A. M. Preparation, Structure, and Magnetic Studies of a New Sr11Re4O24 Double Oxide. *J Solid State Chem* **2000**, *149* (1), 49–55. https://doi.org/10.1006/jssc.1999.8493.

(206) Zeng, Q.; He, P.; Zhang, X.; Liang, H.; Gong, M.; Su, Q. M9Gd2W4O24:Eu3+ (M2+ = Ca2+ and Sr2+) Red Phosphors for NUV and Blue InGaN-Based WLEDs. *Chem Lett* **2009**, *38* (12), 1172–1173. https://doi.org/10.1246/cl.2009.1172.

(207) Cloß, K. K.; Kemmler-Sack, S. Lumineszenz Des Selten Erd-Aktivierten Polymorphen Perowskits Sr2Sr14Gd1/2□1/4WO6(= Sr8SrGd2□W4O24). *J Solid State Chem* **1983**, *48* (2), 295–299. https://doi.org/10.1016/0022-4596(83)90084-1.

(208) Kemmler-Sack, S.; Ehmann, A. Über Geordnete Perowskite Mit Kationenfehlstellen. IX. Verbindungen Vom Typ Sr2Sr1/4B 1/2III□1/4WO6≙Sr8SrB 2III□W4O24 (BIII ? La, Pr, Nd, Sm – Tm, Y). *ZAAC - Journal of Inorganic and General Chemistry* **1981**, *479* (8), 184–190. https://doi.org/10.1002/zaac.19814790823.

(209) Qin, C.; Huang, Y.; Seo, H. J. The Thermal Stability and Structural Site-Distribution of Eu3+ Ions in the Red-Emitting Phosphors Ca9Eu2W4O24 and Sr9Eu2W4O24. *J Alloys Compd* **2012**, *534*, 86–92. https://doi.org/10.1016/j.jallcom.2012.04.034.

(210) Wakeshima, M.; Hinatsu, Y. Crystal Structure and Magnetic Ordering of Novel Perovskite-Related Barium Osmate Ba11Os4O24. *Solid State Commun* **2005**, *136* (9–10), 499–503. https://doi.org/10.1016/j.ssc.2005.09.025.

(211) Kubo, A.; Akaogi, M. Post-Garnet Transitions in the System Mg4Si4O12-Mg3Al2Si3O12 up to 28 GPa: Phase Relations of Garnet, Ilmenite and Perovskite. *Physics of the Earth and Planetary Interiors* **2000**, *121* (1–2), 85–102. https://doi.org/10.1016/S0031-9201(00)00162-X.

(212) Villars, P.; Cenzual, K.; Daams, J.; Gladyshevskii, R.; Shcherban, O.; Dubenskyy, V.; Melnichenko-Koblyuk, N.; Pavlyuk, O.; Savysyuk, I.; Stoyko, S.; Sysa, L. Structure Types. Part 5: Space Groups (173) P63- (166) R-3m Pr0.7Bi0.3O1.5. In *Landolt-Börnstein - Group III Condensed Matter - Crystal Structures of Inorganic Compounds*; Villars, P., Cenzual, K., Eds.; Landolt-Börnstein - Group III Condensed Matter; Springer Berlin Heidelberg: Berlin, Heidelberg, 2007; Vol. 43. https://doi.org/10.1007/978-3-540-46933-9.

(213) Engelhard, M. H.; Droubay, T. C.; Du, Y. X-Ray Photoelectron Spectroscopy Applications. In *Encyclopedia of Spectroscopy and Spectrometry*; Lindon, J. C., Tranter, G. E., Koppenaal, D. W., Eds.; Academic Press, 2016; pp 716–724. https://doi.org/10.1016/B978-0-12-409547-2.12102-X.

(214) Hunsperger, R. G. Basic Principles of Light Emission in Semiconductors. In *Integrated Optics: Theory and Technology*; Springer: Berlin, 2002; pp 193–210. https://doi.org/10.1007/978-3-540-38843-2_11.

(215) Blasse, G. Influence of Crystal Structure on Luminescence. *Mater Res Bull* **1968**, *3* (10), 807–815. https://doi.org/10.1016/0025-5408(68)90097-4.

(216) Bivour, M.; Temmler, J.; Steinkemper, H.; Hermle, M. Molybdenum and Tungsten Oxide: High Work Function Wide Band Gap Contact Materials for Hole Selective Contacts of Silicon Solar Cells. *Solar Energy Materials and Solar Cells* **2015**, *142*, 34–41. https://doi.org/10.1016/j.solmat.2015.05.031.

(217) Hendi, A. H. Y.; Al-Kuhaili, M. F.; Durrani, S. M. A.; Faiz, M. M.; Ul-Hamid, A.; Qurashi, A.; Khan, I. Modulation of the Band Gap of Tungsten Oxide Thin Films through Mixing with Cadmium Telluride towards Photovoltaic Applications. *Mater Res Bull* **2017**, *87*, 148–154. https://doi.org/10.1016/j.materresbull.2016.11.032.

(218) Romeo, M.; Bak, K.; El Fallah, J.; Le Normand, F.; Hilaire, L. XPS Study of the Reduction of Cerium Dioxide. *Surface and Interface Analysis* **1993**, *20* (6), 508–512. https://doi.org/10.1002/sia.740200604.

(219) Nachimuthu, R. K.; Jeffery, R. D.; Martyniuk, M.; Woodward, R. C.; Metaxas, P. J.; Dell, J. M.; Faraone, L. Investigation of Cerium-Substituted Europium Iron Garnets Deposited by Biased Target Ion Beam Deposition. *IEEE Trans Magn* **2014**, *50* (12), 1–7. https://doi.org/10.1109/TMAG.2014.2331016.

(220) Konysheva, E. Y.; Kuznetsov, M. V. Fluctuation of Surface Composition and Chemical States at the Hetero-Interface in Composites Comprised of a Phase with Perovskite Structure and a Phase Related to the Ruddlesden-Popper Family of Compounds. *RSC Adv* **2013**, *3* (33), 14114–14122. https://doi.org/10.1039/c3ra41355a.

(221) Guzik, A.; Talik, E.; Pajączkowska, A.; Turczyński, S.; Kusz, J. Magnetic Properties of Manganese Doped PrAlO3 Monocrystalline Fibres. *Materials Science- Poland* **2014**, *32* (4), 633–640. https://doi.org/10.2478/s13536-014-0240-y.

(222) Aragón, F. H.; Gonzalez, I.; Coaquira, J. A. H.; Hidalgo, P.; Brito, H. F.; Ardisson, J. D.; Macedo, W. A. A.; Morais, P. C. Structural and Surface Study of Praseodymium-Doped SnO2 Nanoparticles Prepared by the Polymeric Precursor Method. *Journal of Physical Chemistry C* **2015**, *119* (16), 8711–8717. https://doi.org/10.1021/acs.jpcc.5b00761.

(223) Kamecki, B.; Miruszewski, T.; Karczewski, J. Structural and Electrical Transport Properties of Pr-Doped SrTi 0.93 Co 0.07 O 3-δ a Novel SOEC Fuel Electrode Materials. *J Electroceram* **2019**, *42* (1–2), 31–40. https://doi.org/10.1007/s10832-018-0143-0.

(224) Vazirov, R. A.; Sokovnin, S. Y.; Ilves, V. G.; Bazhukova, I. N.; Pizurova, N.; Kuznetsov, M. V. Physicochemical Characterization and Antioxidant Properties of Cerium Oxide Nanoparticles. In *Journal of Physics: Conference Series*; IOP Publishing, 2018; Vol. 1115, p 032094. https://doi.org/10.1088/1742-6596/1115/3/032094.

(225) He, X.; Liu, X.; Li, R.; Yang, B.; Yu, K.; Zeng, M.; Yu, R. Effects of Local Structure of Ce3+ Ions on Luminescent Properties of Y3Al5O12:Ce Nanoparticles. *Sci Rep* **2016**, *6* (1), 1–11. https://doi.org/10.1038/srep22238.

(226) Gupta, A.; Das, S.; Neal, C. J.; Seal, S. Controlling the Surface Chemistry of Cerium Oxide Nanoparticles for Biological Applications. *J Mater Chem B* **2016**, *4* (19), 3195–3202. https://doi.org/10.1039/c6tb00396f.

(227) Mysliveček, J.; Matolín, V.; Matolínová, I. Heteroepitaxy of Cerium Oxide Thin Films on Cu(111). *Materials*. MDPI AG 2015, pp 6346–6359. https://doi.org/10.3390/ma8095307.

(228) Stojadinović, S.; Ćirić, A. Ce3+/Eu2+ Doped Al2O3 Coatings Formed by Plasma Electrolytic Oxidation of Aluminum: Photoluminescence Enhancement by Ce3+→Eu2+ Energy Transfer. *Coatings* **2019**, *9* (12), 819. https://doi.org/10.3390/coatings9120819.

(229) Naganuma, T.; Traversa, E. Stability of the Ce 3+ Valence State in Cerium Oxide Nanoparticle Layers. *Nanoscale* **2012**, *4* (16), 4950–4953. https://doi.org/10.1039/c2nr30406f.

(230) Connor, P. A.; Yue, X.; Savaniu, C. D.; Price, R.; Triantafyllou, G.; Cassidy, M.; Kerherve, G.; Payne, D. J.; Maher, R. C.; Cohen, L. F.; Tomov, R. I.; Glowacki, B. A.; Kumar, R. V.; Irvine, J. T. S. Tailoring SOFC Electrode Microstructures for Improved Performance. *Advanced Energy Materials*. John Wiley & Sons, Ltd August 1, 2018, p 1800120. https://doi.org/10.1002/aenm.201800120.

(231) Tsui, C. K. J.; Leung, K. M.; Tay, Y. Y.; Liao, C.; Ho, C. K.; Yau, H. T.; Salim, T.; Li, C. Y. V.; Chan, K. Y. Highly Durable Pt-Ru-Doped Ce0.9Zr0.1O2as an Effective Dual Catalyst for Low-Temperature Simultaneous Propane and Carbon Monoxide Oxidation. *Journal of Physical Chemistry C* **2022**, *126* (22), 9334–9351. https://doi.org/10.1021/acs.jpcc.2c01012.

(232) Maslakov, K. I.; Teterin, Y. A.; Popel, A. J.; Teterin, A. Y.; Ivanov, K. E.; Kalmykov, S. N.; Petrov, V. G.; Petrov, P. K.; Farnan, I. XPS Study of Ion Irradiated and Unirradiated CeO2 Bulk and Thin Film Samples. *Appl Surf Sci* **2018**, *448*, 154–162. https://doi.org/10.1016/j.apsusc.2018.04.077.

(233) Vazirov, R. A.; Sokovnin, S. Y.; Ilves, V. G.; Bazhukova, I. N.; Pizurova, N.; Kuznetsov, M. V. Physicochemical Characterization and Antioxidant Properties of Cerium Oxide Nanoparticles. In *Journal of Physics: Conference Series*; IOP Publishing, 2018; Vol. 1115, p ID-032094. https://doi.org/10.1088/1742-6596/1115/3/032094.

(234) Paparazzo, E. Use and Mis-Use of x-Ray Photoemission Spectroscopy Ce3d Spectra of Ce2O3 and CeO2. *Journal of Physics: Condensed Matter* **2018**, *30* (34), ID-343003. https://doi.org/10.1088/1361-648X/AAD248.

(235) Howald, L.; Stilp, E.; De Réotier, P. D.; Yaouanc, A.; Raymond, S.; Piamonteze, C.; Lapertot, G.; Baines, C.; Keller, H. Evidence for Coexistence of Bulk Superconductivity and Itinerant Antiferromagnetism in the Heavy Fermion System CeCo(In1-x Cdx)5. *Sci Rep* **2015**, *5* (1), 1–15. https://doi.org/10.1038/srep12528.

(236) Skála, T.; Tsud, N.; Orti, M. Á. N.; Mente, T. O.; Locatelli, A.; Prince, K. C.; Matolín, V. In Situ Growth of Epitaxial Cerium Tungstate (100) Thin Films. *Physical Chemistry Chemical Physics* **2011**, *13* (15), 7083–7089. https://doi.org/10.1039/c0cp03012k.

(237) Vasili, H. B.; Casals, B.; Cichelero, R.; Macià, F.; Geshev, J.; Gargiani, P.; Valvidares, M.; Herrero-Martin, J.; Pellegrin, E.; Fontcuberta, J.; Herranz, G. Direct Observation of Multivalent States and 4f→3d Charge Transfer in Ce-Doped Yttrium Iron Garnet Thin Films. *Phys Rev B* **2017**, *96* (1), ID-014433. https://doi.org/10.1103/PhysRevB.96.014433.

(238) Wilkens, H.; Schuckmann, O.; Oelke, R.; Gevers, S.; Schaefer, A.; Bäumer, M.; Zoellner, M. H.; Schroeder, T.; Wollschläger, J. Stabilization of the Ceria ι-Phase (Ce7O12) Surface on Si(111). *Appl Phys Lett* **2013**, *102* (11), ID-111602. https://doi.org/10.1063/1.4795867.

(239) Bêche, E.; Charvin, P.; Perarnau, D.; Abanades, S.; Flamant, G. Ce 3d XPS Investigation of Cerium Oxides and Mixed Cerium Oxide (Ce XTiyOz). In *Surface and Interface Analysis*; John Wiley & Sons, Ltd, 2008; Vol. 40, pp 264–267. https://doi.org/10.1002/sia.2686.

(240) Lan, L.; Ding, C.; He, P.; Su, H.; Huang, B.; Xu, J.; Zhang, S.; Peng, J. The Mechanism of the Photostability Enhancement of Thin-Film Transistors Based on Solution-Processed Oxide Semiconductors Doped with Tetravalent Lanthanides. *Nanomaterials* **2022**, *12* (21), 3902–3914. https://doi.org/10.3390/nano12213902.

(241) Escalera-López, D.; Griffin, R.; Isaacs, M.; Wilson, K.; Palmer, R. E.; Rees, N. V. MoS2 and WS2 Nanocone Arrays: Impact of Surface Topography on the Hydrogen Evolution Electrocatalytic Activity and Mass Transport. *Appl Mater Today* **2018**, *11*, 70–81. https://doi.org/10.1016/j.apmt.2018.01.006.

(242) Guo, C.; Yin, S.; Dong, Q.; Sato, T. The near Infrared Absorption Properties of W18O49. *RSC Adv* **2012**, *2* (12), 5041–5043. https://doi.org/10.1039/c2ra01366e.

(243) You, L.; Liu, B.; Liu, T.; Fan, B.; Cai, Y.; Guo, L.; Sun, Y. Organic Solar Cells Based on WO2.72 Nanowire Anode Buffer Layer with Enhanced Power Conversion Efficiency and Ambient Stability. *ACS Appl Mater Interfaces* **2017**, *9* (14), 12629–12636. https://doi.org/10.1021/acsami.6b15762.

(244) Sundberg, M. Structure and "Oxidation Behavior" of W24O70, a New Member of the {103} CS Series of Tungsten Oxides. *J Solid State Chem* **1980**, *35* (1), 120–127. https://doi.org/10.1016/0022-4596(80)90472-7.

(245) Zhang, M.; Sun, H.; Guo, Y.; Wang, D.; Sun, D.; Su, Q.; Ding, S.; Du, G.; Xu, B. Synthesis of Oxygen Vacancies Implanted Ultrathin WO3-x Nanorods/Reduced Graphene Oxide Anode with Outstanding Li-Ion Storage. *J Mater Sci* **2021**, *56* (12), 7573–7586. https://doi.org/10.1007/s10853-020-05747-4.

(246) Crist, B. V. XPS in Industry—Problems with Binding Energies in Journals and Binding Energy Databases. *Journal of Electron Spectroscopy and Related Phenomena*. Elsevier February 1, 2019, pp 75–87. https://doi.org/10.1016/j.elspec.2018.02.005.

(247) Balcar, H.; Bastl, Z. Ring Opening Metathesis Polymerization of Norbornene by WCl6: Formation of WCl5 and WCl4 and Their Catalytic Activity. *Collect Czechoslov Chem Commun* **1996**, *61* (9), 1353–1359. https://doi.org/10.1135/cccc19961353.

(248) Díaz-Reyes, J.; Castillo-Ojeda, R.; Galván-Arellano, M.; Zaca-Moran, O. Characterization of WO3 Thin Films Grown on Silicon by HFMOD. *Advances in Condensed Matter Physics* **2013**, *2013*, ID-591787. https://doi.org/10.1155/2013/591787.

(249) Sale, F. R. Heat Capacities of the Tungsten Oxides WO3, W20O58, W18O49 and WO2. *Thermochim Acta* **1979**, *30* (1–2), 163–171. https://doi.org/10.1016/0040-6031(79)85051-0.

(250) Shen, Z.; Zhao, Z.; Wen, J.; Qian, J.; Peng, Z.; Fu, X. Role of Oxygen Vacancies in the Electrical Properties of WO3- x Nano/Microrods with Identical Morphology. *J Nanomater* **2018**, *2018*, ID-7802589. https://doi.org/10.1155/2018/7802589.

(251) Katrib, A.; Hemming, F.; Hilaire, L.; Wehrer, P.; Maire, G. XPS Studies of Supported Tungsten Carbide(s). *J Electron Spectros Relat Phenomena* **1994**, *68* (C), 589–595. https://doi.org/10.1016/0368-2048(94)02162-7.

(252) Forsberg, P.; Gustavsson, F.; Renman, V.; Hieke, A.; Jacobson, S. Performance of DLC Coatings in Heated Commercial Engine Oils. *Wear* **2013**, *304* (1–2), 211–222. https://doi.org/10.1016/j.wear.2013.04.036.

(253) Carpen, L. G.; Acsente, T.; Sătulu, V.; Matei, E.; Vizireanu, S.; Biță, B. I.; Dinescu, G. Hybrid Nanostructures Obtained by Transport and Condensation of Tungsten Oxide Vapours onto Cnw Templates. *Nanomaterials* **2021**, *11* (4), 835–854. https://doi.org/10.3390/nano11040835.

(254) Chattaraj, A.; Balal, M.; Yadav, A. K.; Barman, S. R.; Sinha, A. K.; Jha, S. N.; Joulie, S.; Serin, V.; Claverie, A.; Kumar, V.; Kanjilal, A. Unravelling Oxygen Driven α to β Phase Transformation in Tungsten. *Sci Rep* **2020**, *10* (1), 1–10. https://doi.org/10.1038/s41598-020-71650-2.

(255) Wu, L. Q.; Li, Y. C.; Li, S. Q.; Li, Z. Z.; Tang, G. D.; Qi, W. H.; Xue, L. C.; Ge, X. S.; Ding, L. L. Method for Estimating Ionicities of Oxides Using O1s Photoelectron Spectra. *AIP Adv* **2015**, *5* (9), ID-097210. https://doi.org/10.1063/1.4931996.

(256) Frati, F.; Hunault, M. O. J. Y.; De Groot, F. M. F. Oxygen K-Edge X-Ray Absorption Spectra. *Chemical Reviews*. American Chemical Society May 13, 2020, pp 4056–4110. https://doi.org/10.1021/acs.chemrev.9b00439.

(257) Suntivich, J.; Hong, W. T.; Lee, Y. L.; Rondinelli, J. M.; Yang, W.; Goodenough, J. B.; Dabrowski, B.; Freeland, J. W.; Shao-Horn, Y. Estimating Hybridization of Transition Metal and Oxygen States in Perovskites from o k -Edge X-Ray Absorption Spectroscopy. *Journal of Physical Chemistry C* **2014**, *118* (4), 1856–1863. https://doi.org/10.1021/jp410644j.

(258) De Groot, F. M. F.; Grioni, M.; Fuggle, J. C.; Ghijsen, J.; Sawatzky, G. A.; Petersen, H. Oxygen 1s X-Ray-Absorption Edges of Transition-Metal Oxides. *Phys Rev B* **1989**, *40* (8), 5715–5723. https://doi.org/10.1103/PhysRevB.40.5715.

(259) De Groot, F. High-Resolution X-Ray Emission and X-Ray Absorption Spectroscopy. *Chemical Reviews*. American Chemical Society June 2001, pp 1779–1808. https://doi.org/10.1021/cr9900681.

(260) Myers, C. E.; Bergmann, K. D.; Sun, C. Y.; Boekelheide, N.; Knoll, A. H.; Gilbert, P. U. P. A. Exceptional Preservation of Organic Matrix and Shell Microstructure in a Late Cretaceous Pinna Fossil Revealed by Photoemission Electron Spectromicroscopy. *Geology* **2018**, *46* (8), 711–714. https://doi.org/10.1130/G45271.1.

(261) Myers, C. E.; Bergmann, K. D.; Sun, C. Y.; Boekelheide, N.; Knoll, A. H.; Gilbert, P. U. P. A. Exceptional Preservation of Organic Matrix and Shell Microstructure in a Late Cretaceous Pinna Fossil Revealed by Photoemission Electron Spectromicroscopy. *Geology* **2018**, *46* (8), 711–714. https://doi.org/10.1130/G45271.1.

(262) Lee, S. K.; Eng, P. J.; Mao, H. kwang. Probing of Pressure-Induced Bonding Transitions in Crystalline and Amorphous Earth Materials: Insights from X-Ray Raman Scattering at High Pressure. *Spectroscopic Methods in Mineralogy and Materials Sciences* **2014**, *78* (1), 139–174. https://doi.org/10.2138/rmg.2014.78.4.

(263) Soni, S.; Vats, V. S.; Kumar, S.; Dalela, B.; Mishra, M.; Meena, R. S.; Gupta, G.; Alvi, P. A.; Dalela, S. Structural, Optical and Magnetic Properties of Fe-Doped CeO2 Samples Probed Using X-Ray Photoelectron Spectroscopy. *Journal of Materials Science: Materials in Electronics* **2018**, *29* (12), 10141–10153. https://doi.org/10.1007/s10854-018-9060-x.

(264) Qian, K.; Du, L.; Zhu, X.; Liang, S.; Chen, S.; Kobayashi, H.; Yan, X.; Xu, M.; Dai, Y.; Li, R. Directional Oxygen Activation by Oxygen-Vacancy-Rich WO2 Nanorods for Superb Hydrogen Evolution via Formaldehyde Reforming. *J Mater Chem A Mater* **2019**, *7* (24), 14592–14601. https://doi.org/10.1039/c9ta03051d.

(265) Ma, R.; Jahurul Islam, M.; Amaranatha Reddy, D.; Kim, T. K. Transformation of CeO2 into a Mixed Phase CeO2/Ce2O3 Nanohybrid by Liquid Phase Pulsed Laser Ablation for Enhanced Photocatalytic Activity through Z-Scheme Pattern. *Ceram Int* **2016**, *42* (16), 18495–18502. https://doi.org/10.1016/j.ceramint.2016.08.186.

(266) Khajeh Aminian, M.; Hakimi, M. Surface Modification by Loading Alkaline Hydroxides to Enhance the Photoactivity of WO3. *Catal Sci Technol* **2014**, *4* (3), 657–664. https://doi.org/10.1039/c3cy00781b.

(267) Smith, M.; Scudiero, L.; Espinal, J.; McEwen, J. S.; Garcia-Perez, M. Improving the Deconvolution and Interpretation of XPS Spectra from Chars by Ab Initio Calculations. *Carbon N Y* **2016**, *110*, 155–171. https://doi.org/10.1016/j.carbon.2016.09.012.

(268) Pawlak, D. A.; Ito, M.; Oku, M.; Shimamura, K.; Fukuda, T. Interpretation of XPS O (1s) in Mixed Oxides Proved on Mixed Perovskite Crystals. *Journal of Physical Chemistry B* **2002**, *106* (2), 504–507. https://doi.org/10.1021/jp012040a.

(269) Akamatsu, H.; Fujita, K.; Kuge, T.; sen Gupta, A.; Togo, A.; Lei, S.; Xue, F.; Stone, G.; Rondinelli, J. M.; Chen, L. Q.; Tanaka, I.; Gopalan, V.; Tanaka, K. Inversion Symmetry Breaking by Oxygen Octahedral Rotations in the Ruddlesden-Popper NaRTiO4 Family. *Phys Rev Lett* **2014**, *112* (18), ID-187602. https://doi.org/10.1103/PhysRevLett.112.187602.

(270) Cesar, A.; Gel'mukhanov, F.; Luo, Y.; Ågren, H.; Skytt, P.; Glans, P.; Guo, J.; Gunnelin, K.; Nordgren, J. Resonant X-Ray Scattering beyond the Born-Oppenheimer Approximation: Symmetry Breaking in the Oxygen Resonant x-Ray Emission Spectrum of Carbon Dioxide. *Journal of Chemical Physics* **1997**, *106* (9), 3439–3456. https://doi.org/10.1063/1.474111.

(271) Egami, T.; Toby, B. H.; Dmowski, W.; Billinge, S.; Davies, P. K.; Jorgensen, J. D.; Subramanian, M. A.; Sleight, A. W. Symmetry Breaking Oxygen Displacements in Superconducting Oxides. *Physica C: Superconductivity and its applications* **1989**, *162–164* (PART 1), 93–94. https://doi.org/10.1016/0921-4534(89)90933-7.

(272) Zhou, G.; Wang, P.; Hu, B.; Shen, X.; Liu, C.; Tao, W.; Huang, P.; Liu, L. Spin-Related Symmetry Breaking Induced by Half-Disordered Hybridization in BixEr2-XRu2O7 Pyrochlores for Acidic Oxygen Evolution. *Nat Commun* **2022**, *13* (1), 1–10. https://doi.org/10.1038/s41467-022-31874-4.

(273) Ko, J. Y. P.; Yiu, Y. M.; Liang, H.; Sham, T. K. X-Ray Absorption and Luminescence Studies of Ba2 Ca (BO 3)2: Ce3+ / Na+ Phosphors. *Journal of Chemical Physics* **2010**, *132* (23), ID-234701. https://doi.org/10.1063/1.3437612.

(274) Sharma, A.; Varshney, M.; Chae, K. H.; Won, S. O. Electronic Structure and Luminescence Assets in White-Light Emitting Ca2V2O7, Sr2V2O7 and Ba2V2O7 Pyro-Vanadates: X-Ray Absorption Spectroscopy Investigations. *RSC Adv* **2018**, *8* (46), 26423–26431. https://doi.org/10.1039/c8ra03347a.

(275) Craciun, V.; Singh, R. K. Characteristics of the Surface Layer of Barium Strontium Titanate Thin Films Deposited by Laser Ablation. *Appl Phys Lett* **2000**, *76* (14), 1932–1934. https://doi.org/10.1063/1.126216.

(276) Hao, Y.; Deng, J.; Zhou, L.; Sun, X.; Zhong, J. Depth-Reduction Induced Low Onset Potential of Hematite Photoanodes for Solar Water Oxidation. *RSC Adv* **2015**, *5* (39), 31086–31090. https://doi.org/10.1039/c5ra04204f.

(277) Johns, W. D.; Gier, S. X- Ray Photoelectron Spectroscopic Study of Layer Charge Magnitude in Micas and Illite-Smectite Clays. *Clay Miner* **2001**, *36* (3), 355–367. https://doi.org/10.1180/000985501750539454.

(278) Verhoeven, J. A. T.; van Doveren, H. XPS Studies on Ba, BaO and the Oxidation of Ba. *Applications of surface science* **1980**, *5* (4), 361–373. https://doi.org/10.1016/0378-5963(80)90101-4.

(279) Maia, L. J. Q.; Mastelaro, V. R.; Schneider, J. F.; Parent, P.; Laffon, C. Structural Studies in the BaO-B2O3-TiO2 System by XAS and 11B-NMR. *J Solid State Chem* **2005**, *178* (5), 1452–1463. https://doi.org/10.1016/j.jssc.2005.02.014.

(280) Hatch, R. C.; Choi, M.; Posadas, A. B.; Demkov, A. A. Comparison of Acid- and Non-Acid-Based Surface Preparations of Nb-Doped SrTiO 3 (001). *Journal of Vacuum Science & Technology B, Nanotechnology and Microelectronics: Materials, Processing, Measurement, and Phenomena* **2015**, *33* (6), 061204. https://doi.org/10.1116/1.4931616.

(281) Hatch, R. C.; Fredrickson, K. D.; Choi, M.; Lin, C.; Seo, H.; Posadas, A. B.; Demkov, A. A. Surface Electronic Structure for Various Surface Preparations of Nb-Doped SrTiO3 (001). *J Appl Phys* **2013**, *114* (10), ID-103710. https://doi.org/10.1063/1.4821095.

(282) Bachelet, R.; Sánchez, F.; Palomares, F. J.; Ocal, C.; Fontcuberta, J. Atomically Flat SrO-Terminated SrTiO3 (001) Substrate. *Appl Phys Lett* **2009**, *95* (14), ID-141915. https://doi.org/10.1063/1.3240869.

(283) Liu, X.; Cao, Y.; Pal, B.; Middey, S.; Kareev, M.; Choi, Y.; Shafer, P.; Haskel, D.; Arenholz, E.; Chakhalian, J. Synthesis and Electronic Properties of Ruddlesden-Popper Strontium Iridate Epitaxial

Thin Films Stabilized by Control of Growth Kinetics. *Phys Rev Mater* **2017**, *1* (7), ID-075004. https://doi.org/10.1103/PhysRevMaterials.1.075004.

(284) Fernández-Rodríguez, L.; Gorni, G.; Mather, G. C.; Savvin, S.; Cuello, G. J.; Durán, A.; Pascual, M. J. X-Ray Absorption Spectroscopy and Neutron-Diffraction Study of Persistent Luminescent Sr2MgSi2O7 Glass-Ceramics. *Acta Mater* **2021**, *215*, ID-117080. https://doi.org/10.1016/j.actamat.2021.117080.

(285) Akamatsu, H.; Fujita, K.; Kuge, T.; sen Gupta, A.; Togo, A.; Lei, S.; Xue, F.; Stone, G.; Rondinelli, J. M.; Chen, L. Q.; Tanaka, I.; Gopalan, V.; Tanaka, K. Inversion Symmetry Breaking by Oxygen Octahedral Rotations in the Ruddlesden-Popper NaRTiO4 Family. *Phys Rev Lett* **2014**, *112* (18), ID-187602. https://doi.org/10.1103/PhysRevLett.112.187602.

(286) Kühl, F.-C.; Müller, M.; Schellhorn, M.; Mann, K.; Wieneke, S.; Eusterhues, K. Near-Edge x-Ray Absorption Fine Structure Spectroscopy at Atmospheric Pressure with a Table-Top Laser-Induced Soft x-Ray Source. *Journal of Vacuum Science & Technology A: Vacuum, Surfaces, and Films* **2016**, *34* (4), 041302. https://doi.org/10.1116/1.4950599.

(287) Politi, Y.; Metzler, R. A.; Abrecht, M.; Gilbert, B.; Wilt, F. H.; Sagi, I.; Addadi, L.; Weiner, S.; Gilbert, P. Transformation Mechanism of Amorphous Calcium Carbonate into Calcite in the Sea Urchin Larval Spicule. *Proc Natl Acad Sci U S A* **2008**, *105* (45), 17362–17366. https://doi.org/10.1073/pnas.0806604105.

(288) Miedema, P. S.; Ikeno, H.; De Groot, F. M. F. First Principles Multiplet Calculations of the Calcium L2, 3 x-Ray Absorption Spectra of CaO and CaF2. *Journal of Physics Condensed Matter* **2011**, *23* (14), ID-145501. https://doi.org/10.1088/0953-8984/23/14/145501.

(289) Singh, J. P.; Lim, W. C.; Won, S. O.; Kim, S. O.; Chae, K. H. Synthesis and Local Electronic Structure of Calcite Nanoparticles. *J Nanosci Nanotechnol* **2016**, *16* (11), 11429–11433. https://doi.org/10.1166/jnn.2016.13523.

(290) Krüger, P.; Natoli, C. R. Theory of Ca L2,3-Edge XAS Using a Novel Multichannel Multiple-Scattering Method. *J Synchrotron Radiat* **2005**, *12* (1), 80–84. https://doi.org/10.1107/S0909049504027888.

(291) Naftel, S. J.; Sham, T. K.; Yiu, Y. M.; Yates, B. W. Calcium L-Edge XANES Study of Some Calcium Compounds. *J Synchrotron Radiat* **2001**, *8* (2), 255–257. https://doi.org/10.1107/S0909049500019555.

(292) Sharma, R.; Hinode, H.; Eyring, L. A Study of the Decomposition of Praseodymium Hydroxy Carbonate and Praseodymium Carbonate Hydrate. *J Solid State Chem* **1991**, *92* (2), 401–419. https://doi.org/10.1016/0022-4596(91)90348-L.

(293) Hu, Y.; Li, Z.; Pan, W. Sandwich-like Transparent Ceramic Demonstrates Ultraviolet and Visible Broadband Downconversion Luminescence. *RSC Adv* **2018**, *8* (24), 13200–13204. https://doi.org/10.1039/c8ra02195c.

(294) Man, S. Q.; Zhang, H. L.; Liu, Y. L.; Meng, J. X.; Pun, E. Y. B.; Chung, P. S. Energy Transfer in Pr3+/Yb3+ Codoped Tellurite Glasses. *Opt Mater (Amst)* **2007**, *30* (2), 334–337. https://doi.org/10.1016/j.optmat.2006.11.045.

(295) Shi, R.; Huang, Y.; Tao, Y.; Dorenbos, P.; Ni, H.; Liang, H. Luminescence and Energy Transfer between Ce3+ and Pr3+ in BaY2Si3O10 under VUV-Vis and X-Ray Excitation. *Inorg Chem* **2018**, *57* (14), 8414–8421. https://doi.org/10.1021/acs.inorgchem.8b01084.

(296) Shi, R.; Huang, Y.; Tao, Y.; Dorenbos, P.; Ni, H.; Liang, H. Luminescence and Energy Transfer between Ce3+ and Pr3+ in BaY2Si3O10 under VUV-Vis and X-Ray Excitation. *Inorg Chem* **2018**, *57* (14), 8414–8421. https://doi.org/10.1021/acs.inorgchem.8b01084.

(297) Xiang, G.; Zhang, J.; Hao, Z.; Zhang, X.; Pan, G.; Luo, Y.; Lü, S.; Zhao, H. The Energy Transfer Mechanism in Pr3+ and Yb3+ Codoped β-NaLuF4 Nanocrystals. *Physical Chemistry Chemical Physics* **2014**, *16* (20), 9289–9293. https://doi.org/10.1039/c4cp01184h.

(298) Voroshilov, I. V.; Lebedev, V. A.; Gavrilenko, A. N.; Ignatiev, B. V.; Isaev, V. A.; Shestakov, A. V. Study of Yb3+-Yb3+ and Yb3+-Ce3+ Energy Transfer in Yb,Ce:CaGd4Si3O13 (Yb,Ce:CGS) Crystals. *Journal of Physics Condensed Matter* **2000**, *12* (12), 211–215. https://doi.org/10.1088/0953-8984/12/12/101.

(299) Nachimuthu, R. K.; Jeffery, R. D.; Martyniuk, M.; Woodward, R. C.; Metaxas, P. J.; Dell, J. M.; Faraone, L. Investigation of Cerium-Substituted Europium Iron Garnets Deposited by Biased Target Ion Beam Deposition. *IEEE Trans Magn* **2014**, *50* (12), 1–7. https://doi.org/10.1109/TMAG.2014.2331016.

(300) Syryanyy, Y.; Zając, M.; Guziewicz, E.; Wozniak, W.; Melikhov, Y.; Chernyshova, M.; Ratajczak, R.; Demchenko, I. N. Polarized Dependence of Soft X-Ray Absorption near Edge Structure of ZnO Films Implanted by Yb. *Mater Sci Semicond Process* **2022**, *144*, ID-106609. https://doi.org/10.1016/j.mssp.2022.106609.

(301) Suga, S. Recent Development in Soft X-Ray Spectroscopy of Correlated Materials: High Resolution Absorption and Bulk-Sensitive Photoemission. In *Surface Review and Letters*; World Scientific Publishing Co. Pte. Ltd., 2002; Vol. 9, pp 1221–1228. https://doi.org/10.1142/S0218625X02001707.

(302) Zhang, Z.; Ten Kate, O. M.; Delsing, A. C. A.; Stevens, M. J. H.; Zhao, J.; Notten, P. H. L.; Dorenbos, P.; Hintzen, H. T. Photoluminescence Properties of Yb 2+ in CaAlSiN 3 as a Novel Red-Emitting Phosphor for White LEDs. *J Mater Chem* **2012**, *22* (45), 23871–23876. https://doi.org/10.1039/c2jm35170f.

(303) Lv, Y.; Wang, L.; Zhuang, Y.; Zhou, T. L.; Xie, R. J. Discovery of the Yb2+-Yb3+ Couple as Red-to-NIR Persistent Luminescence Emitters in Yb-Activated (Ba1-XSrx)AlSi5O2N7 Phosphors. *J Mater Chem C Mater* **2017**, *5* (28), 7095–7101. https://doi.org/10.1039/c7tc01600j.

(304) Ma, Z.; Tian, S.; Wu, H.; Zhang, J.; Li, H. Self-Reduction of Yb3+ to Yb2+ and Red Persistent Luminescence of Na2CaGe2O6:Yb2+ Phosphor. *Ceram Int* **2018**, *44* (12), 14582–14586. https://doi.org/10.1016/j.ceramint.2018.05.078.

(305) Raipurkar, J. R.; Atram, R. G.; Muthal, P. L.; Dhopte, S. M.; Moharil, S. V. Luminescence of Yb2+ in RbCaCl3. *J Lumin* **2013**, *134*, 456–458. https://doi.org/10.1016/j.jlumin.2012.08.001.

(306) Liu, X.; Qiao, Y.; Dong, G.; Ye, S.; Zhu, B.; Lakshminarayana, G.; Chen, D.; Qiu, J. Cooperative Downconversion in Yb3+–RE3+ (RE=Tm or Pr) Codoped Lanthanum Borogermanate Glasses. *Opt Lett* **2008**, *33* (23), 2858. https://doi.org/10.1364/ol.33.002858.

(307) Zhao, J.; Guo, C.; Li, T. Near-Infrared Down-Conversion and Energy Transfer Mechanism of Ce3+ -Yb3+ Co-Doped Ba2Y(BO3)2Cl Phosphors. *ECS Journal of Solid State Science and Technology* **2016**, *5* (1), R3055–R3058. https://doi.org/10.1149/2.0071601jss.

(308) Andrews, R. L.; Heyns, A. M.; Woodward, P. M. Raman Studies of A2MWO6 Tungstate Double Perovskites. *Dalton Transactions* **2015**, *44* (23), 10700–10707. https://doi.org/10.1039/c4dt03789h.

(309) Wang, J.; Wang, M.; You, J.; Lu, L.; Wan, S.; Wu, Y.; Zheng, S. Fine Structures and Their Impacts on the Characteristic Raman Spectra of Molten Binary Alkali Tungstates. *Journal of Raman Spectroscopy* **2021**, *52* (8), 1452–1461. https://doi.org/10.1002/jrs.6173.

(310) Hardcastle, F. D.; Wachs, I. E. Determination of the Molecular Structures of Tungstates by Raman Spectroscopy. *Journal of Raman Spectroscopy* **1995**, *26* (6), 397–405. https://doi.org/10.1002/jrs.1250260603.

(311) Borowiec, M. T.; Szymczak, H.; Zaleski, M.; Kaczor, P.; Adamowicz, L.; Strzeszewski, J.; Watterich, A.; Kovacs, L. Raman and IR Spectroscopy Investigations of Double Tungstates. In *International Conference on Solid State Crystals '98: Single Crystal Growth, Characterization, and Applications*; SPIE, 1999; Vol. 3724, p 288. https://doi.org/10.1117/12.343008.

(312) Prosandeev, S. A.; Waghmare, U.; Levin, I.; Maslar, J. First-Order Raman Spectra of AB1/2'B1/2''O3 Double Perovskites. *Phys Rev B Condens Matter Mater Phys* **2005**, *71* (21), ID-214307. https://doi.org/10.1103/PhysRevB.71.214307.

(313) Alsabah, Y. A.; Alsalhi, M. S.; Mustafa, E. M.; Elbadawi, A. A.; Devanesan, S.; Siddig, M. A. Synthesis, Phase Transition, and Optical Studies of Ba2−xSrxZnWO6 (X = 1.00, 1.25, 1.50, 1.75, 2.00) Tungsten Double Perovskite Oxides. *Crystals (Basel)* **2020**, *10* (4), 316. https://doi.org/10.3390/cryst10040299.

(314) Alsabah, Y. A.; Elbadawi, A. A.; Mustafa, E. M.; Siddig, M. A. The Effect of Replacement of Zn2+ Cation with Ni2+ Cation on the Structural Properties of Ba2Zn1–XNixWO6 Double Perovskite Oxides (X = 0, 0.25, 0.50, 0.75, 1). *Journal of Materials Science and Chemical Engineering* **2016**, *04* (02), 61–70. https://doi.org/10.4236/msce.2016.42007.

(315) Rahimi-Nasrabadi, M.; Pourmortazavi, S. M.; Khalilian-Shalamzari, M. Facile Chemical Synthesis and Structure Characterization of Copper Molybdate Nanoparticles. *J Mol Struct* **2015**, *1083* (2), 229–235. https://doi.org/10.1016/j.molstruc.2014.12.017.

(316) Rahimi-Nasrabadi, M.; Pourmortazavi, S. M.; Khalilian-Shalamzari, M. Facile Chemical Synthesis and Structure Characterization of Copper Molybdate Nanoparticles. *J Mol Struct* **2015**, *1083* (2), 229–235. https://doi.org/10.1016/j.molstruc.2014.12.017.

(317) da Cruz Severn, E.; Abaide, E. R.; Anchieta, C. G.; Foletto, V. S.; Weber, C. T.; Garlet, T. B.; Collazzo, G. C.; Mazutti, M. A.; Gündel, A.; Kuhn, R. C.; Foletto, E. L. Preparation of Zinc Tungstate (ZnWO4) Particles by Solvo-Hydrothermal Technique and Their Application as Support for Inulinase Immobilization. *Materials Research* **2016**, *19* (4), 781–785. https://doi.org/10.1590/1980-5373-MR-2015-0100.

(318) Medidi, S.; Markapurapu, S.; Kotupalli, M. R.; Chinnam, R. K. R.; Susarla, V. M.; Gandham, H. B.; Sanasi, P. D.; Medidi, S.; Markapurapu, S.; Kotupalli, M. R.; Chinnam, R. K. R.; Susarla, V. M.; Gandham, H. B.; Sanasi, P. D. Visible Light Photocatalytic Degradation of Methylene Blue and

Malachite Green Dyes with CuWO4-GO Nano Composite. *Modern Research in Catalysis* **2018**, *7* (2), 17–34. https://doi.org/10.4236/MRC.2018.72002.

(319) Mohamed Saadon, N. A. F.; Ali, N. M.; Ibrahim, N.; Mohamed, Z. Structural, Optical and Dielectric Properties of Sr2Ni1−xMgxWO6(X= 0.00, 0.02, 0.04, and 0.06) Double Perovskite. *J Mater Chem C Mater* **2021**, *9* (38), 13439–13446. https://doi.org/10.1039/d1tc02149d.

(320) Zamiri, R.; Ahangar, H. A.; Kaushal, A.; Zakaria, A.; Zamiri, G.; Tobaldi, D.; Ferreira, J. M. F. Dielectrical Properties of CeO2 Nanoparticles at Different Temperatures. *PLoS One* **2015**, *10* (4), ID-e0122989. https://doi.org/10.1371/journal.pone.0122989.

(321) Jayakumar, G.; Albert Irudayaraj, A.; Dhayal Raj, A. A Comprehensive Investigation on the Properties of Nanostructured Cerium Oxide. *Opt Quantum Electron* **2019**, *51* (9), 1–15. https://doi.org/10.1007/s11082-019-2029-z.

(322) Wang, M.; Shen, M.; Jin, X.; Tian, J.; Li, M.; Zhou, Y.; Zhang, L.; Li, Y.; Shi, J. Oxygen Vacancy Generation and Stabilization in CeO2- x by Cu Introduction with Improved CO2 Photocatalytic Reduction Activity. *ACS Catal* **2019**, *9* (5), 4573–4581. https://doi.org/10.1021/acscatal.8b03975.

(323) Nikolenko, A.; Strelchuk, V.; Gnatyuk, O.; Kraszkiewicz, P.; Boiko, V.; Kovalska, E.; Mista, W.; Klimkiewicz, R.; Karbivskii, V.; Dovbeshko, G. In Situ Raman Study of Laser-Induced Stabilization of Reduced Nanoceria (CeO2−x) Supported on Graphene. *Journal of Raman Spectroscopy* **2019**, *50* (4), 490–498. https://doi.org/10.1002/jrs.5542.

(324) Schilling, C.; Hofmann, A.; Hess, C.; Ganduglia-Pirovano, M. V. Raman Spectra of Polycrystalline CeO2: A Density Functional Theory Study. *Journal of Physical Chemistry C* **2017**, *121* (38), 20834–20849. https://doi.org/10.1021/acs.jpcc.7b06643.

(325) Aškrabiač, S.; Dohčeviač-Mitroviač, Z.; Kremenoviač, A.; Lazareviač, N.; Kahlenberg, V.; Popoviač, Z. V. Oxygen Vacancy-Induced Microstructural Changes of Annealed CeO 2-x Nanocrystals. *Journal of Raman Spectroscopy* **2012**, *43* (1), 76–81. https://doi.org/10.1002/jrs.2987.

(326) Lawrence, N. J.; Brewer, J. R.; Wang, L.; Wu, T. S.; Wells-Kingsbury, J.; Ihrig, M. M.; Wang, G.; Soo, Y. L.; Mei, W. N.; Cheung, C. L. Defect Engineering in Cubic Cerium Oxide Nanostructures for Catalytic Oxidation. *Nano Lett* **2011**, *11* (7), 2666–2671. https://doi.org/10.1021/nl200722z.

(327) Shi, Q.; Long, H. M.; Chun, T. J.; Gao, Z. F. Catalytic Combustion of Chlorobenzene with Vox/Ceo2 Catalystsïš Influence of Catalyst Synthesis Method. *International Journal of Chemical Reactor Engineering* **2019**, *17* (12), 1–12. https://doi.org/10.1515/ijcre-2019-0084.

(328) Bodziony, T.; Kaczmarek, S. M. Theoretical Investigation of the Epr G-Factor for the Axial Symmetry Ce3+ Center in the Bawo4 Single Crystal. *Crystals (Basel)* **2021**, *11* (7), 811. https://doi.org/10.3390/cryst11070804.

(329) Vočadlo, N. L.; Price, G. D. The Grüneisen Parameter - Computer Calculations via Lattice Dynamics. *Physics of the Earth and Planetary Interiors* **1994**, *82* (3–4), 261–270. https://doi.org/10.1016/0031-9201(94)90076-0.

(330) Vočadlo, L.; Poirer, J. P.; Price, G. D. Gruneisen Parameters and Isothermal Equations of State. *American Mineralogist* **2000**, *85* (2), 390–395. https://doi.org/10.2138/am-2000-2-319.

(331) Wang, L.; Rybacki, E.; Bonnelye, A.; Bohnhoff, M.; Dresen, G. Experimental Investigation on Static and Dynamic Bulk Moduli of Dry and Fluid-Saturated Porous Sandstones. *Rock Mech Rock Eng* **2021**, *54* (1), 129–148. https://doi.org/10.1007/s00603-020-02248-3.

(332) Donaldson, E. C.; Alam, W.; Begum, N. Rock Mechanics of Fracturing. In *Hydraulic Fracturing Explained*; Gulf Publishing Company, 2013; pp 47–76. https://doi.org/10.1016/b978-1-933762-40-1.50012-x.

(333) Bolmatov, D.; Zhernenkov, M.; Zav'yalov, D.; Tkachev, S. N.; Cunsolo, A.; Cai, Y. Q. The Frenkel Line: A Direct Experimental Evidence for the New Thermodynamic Boundary. *Sci Rep* **2015**, *5* (1), ID-15850. https://doi.org/10.1038/srep15850.

(334) Henderson, M.; Wertheim, M. S. Phase Diagram and PV Isotherms of Argon. *J Chem Phys* **1969**, *51* (12), 5420–5429. https://doi.org/10.1063/1.1671965.

(335) Shimizu, H.; Hori, S.; Kume, T.; Sasaki, S. Optical Microscopy and Raman Scattering of a Single Crystalline Argon Hydrate at High Pressures. *Chem Phys Lett* **2003**, *368* (1–2), 132–138. https://doi.org/10.1016/S0009-2614(02)01809-2.

(336) Watson, G. H.; Daniels, W. B. Raman Scattering from Solid Argon at High Pressure. *Phys Rev B* **1988**, *37* (5), 2669–2673. https://doi.org/10.1103/PhysRevB.37.2669.

(337) Klotz, S.; Chervin, J. C.; Munsch, P.; Le Marchand, G. Hydrostatic Limits of 11 Pressure Transmitting Media. *J Phys D Appl Phys* **2009**, *42* (7), ID-075413. https://doi.org/10.1088/0022-3727/42/7/075413.

(338) Celeste, A.; Borondics, F.; Capitani, F. Hydrostaticity of Pressure-Transmitting Media for High Pressure Infrared Spectroscopy. *High Press Res* **2019**, *39* (4), 608–618. https://doi.org/10.1080/08957959.2019.1666844.

(339) Goncharov, A. F. Raman Spectroscopy at High Pressures. *Int J Spectrosc* **2012**, *2012*, 1–16. https://doi.org/10.1155/2012/617528.

(340) Akahama, Y.; Kawamura, H. High-Pressure Raman Spectroscopy of Diamond Anvils to 250 GPa: Method for Pressure Determination in the Multimegabar Pressure Range. *J Appl Phys* **2004**, *96* (7), 3748–3751. https://doi.org/10.1063/1.1778482.

(341) Xiao, W.; Tan, D.; Xiong, X.; Liu, J.; Xu, J. Large Volume Collapse Observed in the Phase Transition in Cubic PbCrO 3 Perovskite. *Proc Natl Acad Sci U S A* **2010**, *107* (32), 14026–14029. https://doi.org/10.1073/pnas.1005307107.

(342) Gateshki, M.; Igartua, J. M. Crystal Structures and Phase Transitions of the Double-Perovskite Oxides Sr2CaWO6 and Sr2MgWO6. *Journal of Physics Condensed Matter* **2004**, *16* (37), 6639–6649. https://doi.org/10.1088/0953-8984/16/37/001.

(343) Aoba, T.; Tiittanen, T.; Suematsu, H.; Karppinen, M. Pressure-Induced Phase Transitions of Hexagonal Perovskite-like Oxides. *J Solid State Chem* **2016**, *233*, 492–496. https://doi.org/10.1016/j.jssc.2015.11.028.

(344) Mall, A. K.; Garg, N.; Verma, A. K.; Errandonea, D.; Chitnis, A. V.; Srihari, V.; Gupta, R. Discovery of High-Pressure Post-Perovskite Phase in HoCrO3. *Journal of Physics and Chemistry of Solids* **2023**, *172*, 111078. https://doi.org/10.1016/j.jpcs.2022.111078.

(345) Morana, M.; Malavasi, L. Pressure Effects on Lead-Free Metal Halide Perovskites: A Route to Design Optimized Materials for Photovoltaics. *Solar RRL*. John Wiley & Sons, Ltd November 1, 2021, p 2100550. https://doi.org/10.1002/solr.202100550.

(346) Bhadram, V. S.; Joseph, B.; Delmonte, D.; Gilioli, E.; Baptiste, B.; Le Godec, Y.; Lobo, R. P. S. M.; Gauzzi, A. Pressure-Induced Structural Phase Transition and Suppression of Jahn-Teller Distortion in the Quadruple Perovskite Structure. *Phys Rev Mater* **2021**, *5* (10), 104411. https://doi.org/10.1103/PhysRevMaterials.5.104411.

(347) Jaffe, A.; Lin, Y.; Mao, W. L.; Karunadasa, H. I. Pressure-Induced Metallization of the Halide Perovskite (CH3NH3)PbI3. *J Am Chem Soc* **2017**, *139* (12), 4330–4333. https://doi.org/10.1021/jacs.7b01162.

(348) Brunetti, B.; Cavallo, C.; Ciccioli, A.; Gigli, G.; Latini, A. On the Thermal and Thermodynamic (In)Stability of Methylammonium Lead Halide Perovskites. *Sci Rep* **2016**, *6* (1), ID-31896. https://doi.org/10.1038/srep31896.

(349) Wang, Y.; Hrubiak, R.; Turczyński, S.; Pawlak, D. A.; Malinowski, M.; Włodarczyk, D.; Kosyl, K. M.; Paszkowicz, W.; Przybylińska, H.; Wittlin, A.; Kaminska, A.; Zhydachevskyy, Y.; Brik, M. G.; Li, L.; Ma, C. G.; Suchocki, A. Spectroscopic Properties and Martensitic Phase Transition of Y4Al2O9:Ce Single Crystals under High Pressure. *Acta Mater* **2019**, *165*, 346–361. https://doi.org/10.1016/j.actamat.2018.11.057.

(350) Belik, A. A.; Yi, W. High-Pressure Synthesis, Crystal Chemistry and Physics of Perovskites with Small Cations at the A Site. *Journal of Physics Condensed Matter*. IOP Publishing April 1, 2014, p 163201. https://doi.org/10.1088/0953-8984/26/16/163201.

(351) Cheng, J. G.; Alonso, J. A.; Suard, E.; Zhou, J. S.; Goodenough, J. B. A New Perovskite Polytype in the High-Pressure Sequence of BaIrO 3. *J Am Chem Soc* **2009**, *131* (21), 7461–7469. https://doi.org/10.1021/ja901829e.

(352) Cheng, J. G.; Alonso, J. A.; Suard, E.; Zhou, J. S.; Goodenough, J. B. A New Perovskite Polytype in the High-Pressure Sequence of BaIrO 3. *J Am Chem Soc* **2009**, *131* (21), 7461–7469. https://doi.org/10.1021/ja901829e.

(353) Chen, J.; Tsujimoto, Y.; Belik, A. A.; Yamaura, K.; Matsushita, Y. Crystal Structure of the Cubic Double-Perovskite Sr 2 Cr 0.84 Ni 0.09 Os 1.07 O 6. *Acta Crystallogr E Crystallogr Commun* **2022**, *78* (11), 1135–1137. https://doi.org/10.1107/s205698902201012x.

(354) Kronbo, C. H.; Menescardi, F.; Ceresoli, D.; Bremholm, M. High Pressure Structure Studies of Three SrGeO3 Polymorphs – Amorphization under Pressure. *J Alloys Compd* **2021**, *855*, 157419. https://doi.org/10.1016/j.jallcom.2020.157419.

(355) Lawrence, N. J.; Brewer, J. R.; Wang, L.; Wu, T. S.; Wells-Kingsbury, J.; Ihrig, M. M.; Wang, G.; Soo, Y. L.; Mei, W. N.; Cheung, C. L. Defect Engineering in Cubic Cerium Oxide Nanostructures for Catalytic Oxidation. *Nano Lett* **2011**, *11* (7), 2666–2671. https://doi.org/10.1021/nl200722z.

(356) Ivanov, S. A.; Nordblad, P.; Mathieu, R.; Tellgren, R.; Ritter, C. Structural and Magnetic Properties of the Ordered Perovskite Pb 2CoTeO6. *Dalton Transactions* **2010**, *39* (46), 11136–11148. https://doi.org/10.1039/c0dt00558d.

(357) Faik, A.; Igartua, J. M.; Gateshki, M.; Cuello, G. J. Crystal Structures and Phase Transitions of Sr2CrSbO6. *J Solid State Chem* **2009**, *182* (7), 1717–1725. https://doi.org/10.1016/j.jssc.2009.04.014.

(358) Zhou, Q.; Blanchard, P.; Kennedy, B. J.; Reynolds, E.; Zhang, Z.; Miiller, W.; Aitken, J. B.; Avdeev, M.; Jang, L. Y.; Kimpton, J. A. Synthesis, Structural and Magnetic Studies of the Double

Perovskites Ba 2Ce M O 6 (M = Ta, Nb). *Chemistry of Materials* **2012**, *24* (15), 2978–2986. https://doi.org/10.1021/cm301278a.

(359) Eriksson, A. K.; Eriksson, S. G.; Ivanov, S. A.; Knee, C. S.; Rundlöf, H. Phase Transitions of the Magnetoelectric A2NiMoO6 (A = Ba, Sr) and Ca2NiWO6 by Neutron Diffraction. In *Ferroelectrics*; Taylor & Francis Group, 2006; Vol. 339, pp 235–243. https://doi.org/10.1080/00150190600740317.

(360) Zaraq, A.; Orayech, B.; Faik, A.; Igartua, J. M.; Jouanneaux, A.; El Bouari, A. High Temperature Induced Phase Transitions in SrCaCoTeO6 and SrCaNiTeO6 Ordered Double Perovskites. *Polyhedron* **2016**, *110* (110), 119–124. https://doi.org/10.1016/j.poly.2016.02.041.

(361) Kisi, E. H.; Howard, C. J. *Applications of Neutron Powder Diffraction*, 1st ed.; Oxford University Press: New York, 2009; Vol. 9780198515. https://doi.org/10.1093/acprof:oso/9780198515944.001.0001.

(362) Gateshki, M.; Igartua, J. M. Crystal Structures and Phase Transitions of the Double Perovskite Oxides SrLaCuRuO6 and SrLaNiRuO6. *Mater Res Bull* **2003**, *38* (14), 1893–1900. https://doi.org/10.1016/j.materresbull.2003.09.001.

(363) Tokoro, H.; Namai, A.; Yoshikiyo, M.; Fujiwara, R.; Chiba, K.; Ohkoshi, S. I. Theoretical Prediction of a Charge-Transfer Phase Transition. *Sci Rep* **2018**, *8* (1), 1–11. https://doi.org/10.1038/s41598-017-18213-0.

(364) Zhu, H.; Yang, C.; Li, Q.; Ren, Y.; Neuefeind, J. C.; Gu, L.; Liu, H.; Fan, L.; Chen, J.; Deng, J.; Wang, N.; Hong, J.; Xing, X. Charge Transfer Drives Anomalous Phase Transition in Ceria. *Nat Commun* **2018**, *9* (1), 1–8. https://doi.org/10.1038/s41467-018-07526-x.

(365) Chorazy, S.; Podgajny, R.; Nogaś, W.; Nitek, W.; Kozieł, M.; Rams, M.; Juszyńska-Gałązka, E.; Nakabayashi, K.; Kapusta, C.; Nakabayashi, K.; Fujimoto, T.; Ohkoshi, S. I.; Sieklucka, B. Charge Transfer Phase Transition with Reversed Thermal Hysteresis Loop in the Mixed-Valence Fe9[W(CN)8]6·xMeOH Cluster. *Chemical Communications* **2014**, *50* (26), 3484–3487. https://doi.org/10.1039/c3cc48029a.

(366) Mahfoud, T.; Molnár, G.; Bonhommeau, S.; Cobo, S.; Salmon, L.; Demont, P.; Tokoro, H.; Ohkoshi, S. I.; Boukheddaden, K.; Bousseksou, A. Electric-Field-Induced Charge-Transfer Phase Transition: A Promising Approach toward Electrically Switchable Devices. *J Am Chem Soc* **2009**, *131* (41), 15049–15054. https://doi.org/10.1021/ja9055855.

(367) Torrance, J. B. An Overview of Organic Charge-Transfer Solids: Insulators, Metals, and the Neutral-Ionic Transition. *Molecular Crystals and Liquid Crystals* **1985**, *126* (1), 55–67. https://doi.org/10.1080/15421408508084154.

(368) Chorazy, S.; Stanek, J. J.; Nogaś, W.; Majcher, A. M.; Rams, M.; Kozieł, M.; Juszyńska-Gałazka, E.; Nakabayashi, K.; Ohkoshi, S. I.; Sieklucka, B.; Podgajny, R. Tuning of Charge Transfer Assisted Phase Transition and Slow Magnetic Relaxation Functionalities in {Fe9-XCox[W(CN)8]6} (x = 0-9) Molecular Solid Solution. *J Am Chem Soc* **2016**, *138* (5), 1635–1646. https://doi.org/10.1021/jacs.5b11924.

(369) Krockenberger, Y.; Irie, H.; Matsumoto, O.; Yamagami, K.; Mitsuhashi, M.; Tsukada, A.; Naito, M.; Yamamoto, H. Emerging Superconductivity Hidden beneath Charge-Transfer Insulators. *Sci Rep* **2013**, *3* (1), 1–6. https://doi.org/10.1038/srep02235.

(370) GoleŽ, D.; Boehnke, L.; Eckstein, M.; Werner, P. Dynamics of Photodoped Charge Transfer Insulators. *Phys Rev B* **2019**, *100* (4), ID-041111. https://doi.org/10.1103/PhysRevB.100.041111.

(371) Orgel, L. E. Charge-Transfer Spectra and Some Related Phenomena. *Quarterly Reviews, Chemical Society* **1954**, *8* (4), 422–450. https://doi.org/10.1039/qr9540800422.

(372) Diaspro, A.; Chirico, G.; Usai, C.; Ramoino, P.; Dobrucki, J. Photobleaching. In *Handbook of Biological Confocal Microscopy: Third Edition*; Springer US, 2006; pp 690–702. https://doi.org/10.1007/978-0-387-45524-2_39.

(373) Pan, Y.; Nilges, M. J. Electron Paramagnetic Resonance Spectroscopy: Basic Principles, Experimental Techniques and Applications to Earth and Planetary Sciences. In *Spectroscopic Methods in Mineralogy and Materials Sciences*; GeoScienceWorld, 2014; Vol. 78, pp 655–690. https://doi.org/10.2138/rmg.2014.78.16.

(374) Watkins, G. D. EPR of Defects in Semiconductors: Past, Present, Future. *Physics of the Solid State* **1999**, *41* (5), 746–750. https://doi.org/10.1134/1.1130862.

(375) Sujatha, B.; Viswanatha, R.; Nagabushana, H.; Narayana Reddy, C. Electronic and Ionic Conductivity Studies on Microwave Synthesized Glasses Containing Transition Metal Ions. *Journal of Materials Research and Technology* **2017**, *6* (1), 7–12. https://doi.org/10.1016/j.jmrt.2016.03.002.

(376) Prisner, T. F. Shaping EPR: Phase and Amplitude Modulated Microwave Pulses. *Journal of Magnetic Resonance* **2019**, *306*, 98–101. https://doi.org/10.1016/j.jmr.2019.07.023.

(377) Aasa, R.; Vänngård, T. EPR Signal Intensity and Powder Shapes: A Reexamination. *Journal of Magnetic Resonance (1969)* **1975**, *19* (3), 308–315. https://doi.org/10.1016/0022-2364(75)90045-1.

(378) Laguta, V.; Zorenko, Y.; Buryi, M.; Gorbenko, V.; Zorenko, T.; Mares, J. A.; Nikl, M. EPR Study of Ce3+ Luminescent Centers in the Y2SiO5 Single Crystalline Films. *Opt Mater (Amst)* **2017**, *72*, 833–837. https://doi.org/10.1016/j.optmat.2017.09.035.

(379) Buryi, M.; Laguta, V.; Nikl, M.; Gorbenko, V.; Zorenko, T.; Zorenko, Y. LPE Growth and Study of the Ce3+ Incorporation in LuAlO3:Ce Single Crystalline Film Scintillators. *CrystEngComm* **2019**, *21* (21), 3313–3321. https://doi.org/10.1039/c9ce00193j.

(380) Zayachuk, D.; Polyhach, Y.; Slynko, E.; Khandozhko, O.; Rudowicz, C. EPR and NMR in Powders of Doped and Undoped IV-VI Crystals. In *Spectrochimica Acta - Part A: Molecular and Biomolecular Spectroscopy*; Elsevier, 2004; Vol. 60, pp 1247–1256. https://doi.org/10.1016/j.saa.2003.10.023.

(381) Mollet, H. F.; Gerstein, B. C. An EPR Study of W5+ in a Recently Discovered Triclinic Tungsten Bronze, Na0.33WO3. *J Chem Phys* **1974**, *60* (4), 1420–1423. https://doi.org/10.1063/1.1681217.

(382) Rakhimov, R. R.; Aleksandrov, A. I. Electron Paramagnetic Resonance Study of W5+ Pairs in Lithium-Tungsten Phosphate Glasses. *Journal of Physical Chemistry B* **2000**, *104* (47), 10973–10977. https://doi.org/10.1021/jp000150w.

(383) Trombetta, J. M.; Watkins, G. D. Identification of An Interstitial Carbon – Interstitial Oxygen Complex in Silicon. *MRS Proceedings* **1987**, *104* (1), 93–98. https://doi.org/10.1557/proc-104-93.

(384) Seeman, V.; Lushchik, A.; Shablonin, E.; Prieditis, G.; Gryaznov, D.; Platonenko, A.; Kotomin, E. A.; Popov, A. I. Atomic, Electronic and Magnetic Structure of an Oxygen Interstitial in Neutron-

Irradiated Al2O3 Single Crystals. *Sci Rep* **2020**, *10* (1), 1–14. https://doi.org/10.1038/s41598-020-72958-9.

(385) McQuaid, S. A.; Newman, R. C.; Muñoz, E. The Role of Rapidly Diffusing Dimers in Oxygen Loss and the Association of Thermal Donors with Small Oxygen Clusters. In *C,H,N and O in Si and Characterization and Simulation of Materials and Processes*; Elsevier, 1996; pp 171–174. https://doi.org/10.1016/b978-0-444-82413-4.50044-5.

(386) Zang, L. -Y; Zhang, Z.; Misra, H. P. EPR STUDIES OF TRAPPED SINGLET OXYGEN (LO2) GENERATED DURING PHOTOIRRADIATION OF HYPOCRELLIN A. *Photochem Photobiol* **1990**, *52* (4), 677–683. https://doi.org/10.1111/j.1751-1097.1990.tb08666.x.

(387) Nakamura, T.; Ling, Y.; Amezawa, K. The Effect of Interstitial Oxygen Formation on the Crystal Lattice Deformation in Layered Perovskite Oxides for Electrochemical Devices. *J Mater Chem A Mater* **2015**, *3* (19), 10471–10479. https://doi.org/10.1039/c5ta01504a.

(388) Bodziony, T.; Kaczmarek, S. M.; Hanuza, J. EPR and Optical Properties of LiNbO 3 :Yb, Pr Single Crystals. In *Lasers and Applications*; Society of Photo-Optical Instrumentation Engineers, 2005; Vol. 5958, p 59580A. https://doi.org/10.1117/12.622510.

(389) Harris, E. A.; Mellor, J. H.; Parke, S. Electron Paramagnetic Resonance of Tetravalent Praseodymium in Zircon. *physica status solidi (b)* **1984**, *122* (2), 757–760. https://doi.org/10.1002/pssb.2221220241.

(390) Cristina de Oliveira, R.; Cabral, L.; Cabral, A. C.; Almeida, P. B.; Tibaldi, N.; Sambrano, J. R.; Simões, A. Z.; Macchi, C. E.; Moura, F.; Marques, G. E.; Ponce, M. A.; Longo, E. Charge Transfer in Pr-Doped Cerium Oxide: Experimental and Theoretical Investigations. *Mater Chem Phys* **2020**, *249*, ID-122967. https://doi.org/10.1016/j.matchemphys.2020.122967.

(391) Herrero-Martín, J.; García-Muñoz, J. L.; Valencia, S.; Frontera, C.; Blasco, J.; Barón-González, A. J.; Subías, G.; Abrudan, R.; Radu, F.; Dudzik, E.; Feyerherm, R. Valence Change of Praseodymium in Pr0.5Ca0.5CoO3 Investigated by x-Ray Absorption Spectroscopy. *Phys Rev B Condens Matter Mater Phys* **2011**, *84* (11), ID-115131. https://doi.org/10.1103/PhysRevB.84.115131.

(392) Kaczmarek, S. M.; Tomaszewicz, E.; Moszyński, D.; Jasik, A.; Leniec, G. DTA/TG, IR, EPR and XPS Studies of Some Praseodymium(III) Tungstates. *Mater Chem Phys* **2010**, *124* (1), 646–651. https://doi.org/10.1016/j.matchemphys.2010.07.028.

(393) Malhotra, V. M. EPR Spectrum of Gadolinium in Hydrated Praseodymium Sulphate. *Solid State Commun* **1976**, *18* (4), 499–503. https://doi.org/10.1016/0038-1098(76)90324-0.

(394) Koretsky, G. M.; Knickelbein, M. B. The Evolution of Electronic Structure in Lanthanide Metal Clusters: Threshold Photoionization Spectra of Cen and Prn. *European Physical Journal D* **1998**, *2* (3), 273–278. https://doi.org/10.1007/s100530050140.

(395) Schmidt, V. Photoionization of Atoms Using Synchrotron Radiation. *Reports on Progress in Physics* **1992**, *55* (9), 1483–1659. https://doi.org/10.1088/0034-4885/55/9/003.

(396) Pickup, B. T. On the Theory of Fast Photoionization Processes. *Chem Phys* **1977**, *19* (2), 193–208. https://doi.org/10.1016/0301-0104(77)85131-8.

(397) Endo, Y.; Doi, Y.; Hinatsu, Y. Magnetic Properties of Praseodymium-Containing Double Perovskites (Ba1-XSrx)2PrRuO6. *J Solid State Chem* **2018**, *267*, 1–5. https://doi.org/10.1016/j.jssc.2018.08.001.

(398) Ivanov, S. A.; Bush, A. A.; Stash, A. I.; Kamentsev, K. E.; Shkuratov, V. Y.; Kvashnin, Y. O.; Autieri, C.; Di Marco, I.; Sanyal, B.; Eriksson, O.; Nordblad, P.; Mathieu, R. Polar Order and Frustrated Antiferromagnetism in Perovskite Pb2MnWO6 Single Crystals. *Inorg Chem* **2016**, *55* (6), 2791–2805. https://doi.org/10.1021/acs.inorgchem.5b02577.

(399) Hou, D.; Qiu, Z.; Saitoh, E. Spin Transport in Antiferromagnetic Insulators: Progress and Challenges. *NPG Asia Materials*. Nature Publishing Group July 12, 2019, pp 1–6. https://doi.org/10.1038/s41427-019-0135-9.

(400) Battle, P. D.; Gibb, T. C.; Jones, C. W.; Studer, F. Spin-Glass Behavior in Sr2FeRuO6 and BaLaNiRuO6: A Comparison with Antiferromagnetic BaLaZnRuO6. *J Solid State Chem* **1989**, *78* (2), 281–293. https://doi.org/10.1016/0022-4596(89)90109-6.

(401) Zhao, Q.; Han, F.; Stoumpos, C. C.; Han, T. H.; Li, H.; Mitchell, J. F. New Insulating Antiferromagnetic Quaternary Iridates MLa10Ir4O24 (M=Sr, Ba). *Sci Rep* **2015**, *5* (1), ID-11705. https://doi.org/10.1038/srep11705.

(402) Sanders, J. P.; Gallagher, P. K. Kinetics of the Oxidation of Magnetite Using Simultaneous TG/DSC. In *Journal of Thermal Analysis and Calorimetry*; Springer, 2003; Vol. 72, pp 777–789. https://doi.org/10.1023/A:1025053828639.

(403) Zhong, X.; Chen, Y.; Dou, G.; Wang, D. Effect of Experimental Conditions on Parameters Derived from Micro Calorimeter Measurements of Coal Low-Temperature Oxidation. In *Applied Mechanics and Materials*; Springer, 2013; Vol. 316–317, pp 850–853. https://doi.org/10.4028/www.scientific.net/AMM.316-317.850.

(404) Huang, X.; Sun, S.; Tu, G. Investigation of Mechanical Properties and Oxidation Resistance of CVD TiB2 Ceramic Coating on Molybdenum. *Journal of Materials Research and Technology* **2020**, *9* (1), 282–290. https://doi.org/10.1016/j.jmrt.2019.10.056.

(405) Binder, K. Theory of First-Order Phase Transitions. *Reports on Progress in Physics* **1987**, *50* (7), 783–859. https://doi.org/10.1088/0034-4885/50/7/001.

(406) Degiorgio, V.; Scully, M. O. Analogy between the Laser Threshold Region and a Second-Order Phase Transition. *Phys Rev A (Coll Park)* **1970**, *2* (4), 1170–1177. https://doi.org/10.1103/PhysRevA.2.1170.

(407) Skotnicki, M.; Aguilar, J. A.; Pyda, M.; Hodgkinson, P. Bisoprolol and Bisoprolol-Valsartan Compatibility Studied by Differential Scanning Calorimetry, Nuclear Magnetic Resonance and X-Ray Powder Diffractometry. *Pharm Res* **2015**, *32* (2), 414–429. https://doi.org/10.1007/s11095-014-1471-7.

(408) Scussat, S.; Sensidoni, A. Structural Impact of Pre-Heating Treatments on Whey Proteins: Biophysical Studies from Macroscopic to Molecular Scale, University of Burgundy, Dion, France, 2010. https://doi.org/10.13140/2.1.4018.4965

(409) Niwa, E.; Nakamura, T.; Mizusaki, J.; Hashimoto, T. Analysis of Structural Phase Transition of Nd2NiO 4 + δ by Scanning Thermal Measurement under Controlled Oxygen Partial Pressure. *Thermochim Acta* **2011**, *523* (1–2), 46–50. https://doi.org/10.1016/j.tca.2011.04.031.

(410) Niwa, E.; Wakai, K.; Hori, T.; Yashiro, K.; Mizusaki, J.; Hashimoto, T. Thermodynamic Analyses of Structural Phase Transition of Pr 2NiO4+δ Involving Variation of Oxygen Content. *Thermochim Acta* **2014**, *575*, 129–134. https://doi.org/10.1016/j.tca.2013.10.025.

(411) Talik, P.; Piwowarczyk, J.; Muszyńska, B.; Hubicka, U. DSC Study of Hydration and Water-Holding Behaviour of Cultured in Vitro Mycelium and Naturally Grown Fruiting Bodies of Freeze-Dried Boletus Badius, Agaricus Bisporus and Cantharellus Cibarius. *J Therm Anal Calorim* **2021**, *143* (5), 3525–3532. https://doi.org/10.1007/s10973-020-09654-3.

(412) Kozlov, A. N.; Shamansky, V. A.; Donskoy, I. G.; Penzik, M. V.; Keiko, A. V. A DSC Signal for Studying Kinetics of Moisture Evaporation from Lignocellulosic Fuels. *Thermochim Acta* **2021**, *698*, ID-178887. https://doi.org/10.1016/j.tca.2021.178887.

(413) Dongshuai, H.; Zeyu, L.; Peng, Z.; Qingjun, D. Molecular Structure and Dynamics of an Aqueous Sodium Chloride Solution in Nano-Pores between Portlandite Surfaces: A Molecular Dynamics Study. *Physical Chemistry Chemical Physics* **2016**, *18* (3), 2059–2069. https://doi.org/10.1039/c5cp05884h.

(414) Svishchev, I. M.; Kusalik, P. G. Structure in Liquid Water: A Study of Spatial Distribution Functions. *J Chem Phys* **1993**, *99* (4), 3049–3058. https://doi.org/10.1063/1.465158.

(415) Jong, U. G.; Yu, C. J.; Ri, G. C.; McMahon, A. P.; Harrison, N. M.; Barnes, P. R. F.; Walsh, A. Influence of Water Intercalation and Hydration on Chemical Decomposition and Ion Transport in Methylammonium Lead Halide Perovskites. *J Mater Chem A Mater* **2018**, *6* (3), 1067–1074. https://doi.org/10.1039/c7ta09112e.

(416) Naganuma, T.; Traversa, E. Air, Aqueous and Thermal Stabilities of Ce3+ Ions in Cerium Oxide Nanoparticle Layers with Substrates. *Nanoscale* **2014**, *6* (12), 6637–6645. https://doi.org/10.1039/c3nr06662b.

(417) Noor, M.; Al Mamun, M. A.; Atique Ullah, A. K. M.; Matsuda, A.; Kawamura, G.; Hakim, M. A.; Islam, M. F.; Matin, M. A. Physics of Ce3+↔Ce4+ Electronic Transition in Phytosynthesized CeO2/CePO4 Nanocomposites and Its Antibacterial Activities. *Journal of Physics and Chemistry of Solids* **2021**, *148*, ID-109751. https://doi.org/10.1016/j.jpcs.2020.109751.

(418) Liu, X. J.; Li, H. L.; Xie, R. J.; Hirosaki, N.; Xu, X.; Huang, L. P. Cerium-Doped Lutetium Aluminum Garnet Optically Transparent Ceramics Fabricated by a Sol-Gel Combustion Process. *J Mater Res* **2006**, *21* (6), 1519–1525. https://doi.org/10.1557/jmr.2006.0183.

(419) Lv, P.; Zhang, L.; Koppala, S.; Chen, K.; He, Y.; Li, S.; Yin, S. Decomposition Study of Praseodymium Oxalate as a Precursor for Praseodymium Oxide in the Microwave Field. *ACS Omega* **2020**, *5* (34), 21338–21344. https://doi.org/10.1021/acsomega.0c00505.

(420) Ferro, S. Physicochemical and Electrical Properties of Praseodymium Oxides. *International Journal of Electrochemistry* **2011**, *2011*, ID-561204. https://doi.org/10.4061/2011/561204.

(421) Jung, W. G. Recovery of Tungsten Carbide from Hard Material Sludge by Oxidation and Carbothermal Reduction Process. *Journal of Industrial and Engineering Chemistry* **2014**, *20* (4), 2384–2388. https://doi.org/10.1016/j.jiec.2013.10.017.

(422) Qiao, D.; Wang, Y.; Li, F.; Wang, D.; Yan, B. Kinetic Study on Preparation of Substoichiometric Tungsten Oxide WO2.72 via Hydrogen Reduction Process. *J Therm Anal Calorim* **2019**, *137* (2), 389–397. https://doi.org/10.1007/s10973-018-7966-4.

(423) Kwon, Y. S.; Gromov, A. A.; Ilyin, A. P.; Ditts, A. A.; Kim, J. S.; Park, S. H.; Hong, M. H. Features of Passivation, Oxidation and Combustion of Tungsten Nanopowders by Air. *Int J Refract Metals Hard Mater* **2004**, *22* (6), 235–241. https://doi.org/10.1016/j.ijrmhm.2004.06.005.

(424) Pecquenard, B.; Castro-Garcia, S.; Livage, J.; Zavalij, P. Y.; Whittingham, M. S.; Thouvenot, R. Structure of Hydrated Tungsten Peroxides [WO2(O2)H2O]·nH2O. *Chemistry of Materials* **1998**, *10* (7), 1882–1888. https://doi.org/10.1021/cm980045n.

(425) Zhang, H.; Sun, S.; Liu, W.; Ding, H.; Zhang, J. Synthesis of Perovskite by Solid-Phase Method with Metatitanic Acid and Calcium Carbonate and Its Pigment Properties Investigation. *Materials* **2020**, *13* (7), 1516. https://doi.org/10.3390/ma13071508.

(426) Vedmid', L.; Fedorova, O.; Uporov, S.; Sterkhov, E. Structural and Magnetic Characteristics of Gadolinium Manganite Modified with Barium Gd0.9Ba0.1MnO3. *J Supercond Nov Magn* **2022**, *35* (5), 1141–1150. https://doi.org/10.1007/s10948-022-06159-y.

(427) Kamran, M. Thermodynamics for Renewable Energy Systems. In *Renewable Energy Conversion Systems*; Fazal, M. R., Ed.; Academic Press, 2021; pp 21–51. https://doi.org/10.1016/b978-0-12-823538-6.00004-x.

(428) Taarea, D.; Bakhtiyarov, S. I. General Physical Properties. In *Smithells Metals Reference Book*; Gale, W. F., Totemeier, T. C., Eds.; Butterworth-Heinemann, 2003; pp 1–45. https://doi.org/10.1016/B978-075067509-3/50017-8.

(429) Sahnoun, O.; Bouhani-Benziane, H.; Sahnoun, M.; Driz, M.; Daul, C. Ab Initio Study of Structural, Electronic and Thermodynamic Properties of Tungstate Double Perovskites Ba2MWO6 (M = Mg, Ni, Zn). *Comput Mater Sci* **2013**, *77*, 316–321. https://doi.org/10.1016/j.commatsci.2013.04.053.

(430) Bissengaliyeva, M. R.; Gogol, D. B.; Bespyatov, M. A.; Taimassova, S. T.; Bekturganov, N. S. Thermodynamic and Magnetic Properties of Compounds in the System MeO-Nd2O3-Mo(W)O3 (Me = Mg, Ca, Sr). *Mater Res Express* **2019**, *6* (10), ID-106109. https://doi.org/10.1088/2053-1591/ab3ae3.

(431) Robie, R. A.; Bin, Z.; Hemingway, B. S.; Barton, M. D. Heat Capacity and Thermodynamic Properties of Andradite Garnet, Ca3Fe2Si3O12, between 10 and 1000 K and Revised Values for ΔfGom (298.15 K) of Hedenbergite and Wollastonite. *Geochim Cosmochim Acta* **1987**, *51* (8), 2219–2224. https://doi.org/10.1016/0016-7037(87)90271-7.

(432) Wang, K.; Feng, X.; Feng, W.; Shi, S.; Li, Y.; Zhang, C. Effect of Trace Fe3+ on Luminescent Properties of CaWO4: Pr3+ Phosphors. *Zeitschrift fur Naturforschung - Section A Journal of Physical Sciences* **2016**, *71* (1), 21–25. https://doi.org/10.1515/zna-2015-0360.

(433) Christofilos, D.; Papagelis, K.; Ves, S.; Kourouklis, G. A.; Raptis, C. High-Pressure Raman Study and Lattice Dynamical Calculations for SrWO4. *Journal of Physics Condensed Matter* **2002**, *14* (47), 12641–12650. https://doi.org/10.1088/0953-8984/14/47/334.

(434) Bates, S.; Zografi, G.; Engers, D.; Morris, K.; Crowley, K.; Newman, A. Analysis of Amorphous and Nanocrystalline Solids from Their X-Ray Diffraction Patterns. *Pharm Res* **2006**, *23* (10), 2333–2349. https://doi.org/10.1007/s11095-006-9086-2.

(435) Maurya, R. S.; Laha, T. Effect of Rare Earth and Transition Metal Elements on the Glass Forming Ability of Mechanical Alloyed Al-TM-RE Based Amorphous Alloys. *J Mater Sci Technol* **2015**, *31* (11), 1118–1124. https://doi.org/10.1016/j.jmst.2015.09.007.

(436) Ansari, M. A.; Jahan, N. Structural and Optical Properties of BaO Nanoparticles Synthesized by Facile Co-Precipitation Method. *Materials Highlights* **2021**, *2* (1–2), 23. https://doi.org/10.2991/mathi.k.210226.001.

(437) Peyrovi, P.; Gillot, S.; Dacquin, J. P.; Granger, P.; Dujardin, C. The Activity of CeVO4-Based Catalysts for Ammonia-SCR: Impact of Surface Cerium Enrichment. *Catal Letters* **2021**, *151* (4), 1003–1012. https://doi.org/10.1007/s10562-020-03363-0.

(438) Yang, L.; Huang, Y.; Cheng, H.; Seo, H. J. Spectroscopy and Structural Characteristics of Eu3+-Activated Perovskite Tungstate Ba2La2ZnW2O12. *J Phys D Appl Phys* **2015**, *48* (43), ID-435107. https://doi.org/10.1088/0022-3727/48/43/435107.

(439) Sahmi, A.; Bensadok, K.; Zirour, H.; Trari, M. Physical and Photoelectrochemical Characterizations of SrWO4 Prepared by Thermal Decomposition. Application to the Photo Electro-Oxidation of Ibuprofen. *Journal of Solid State Electrochemistry* **2017**, *21* (10), 2817–2824. https://doi.org/10.1007/s10008-017-3599-y.

(440) Keskar, M.; Sali, S. K.; Vats, B. G.; Phatak, R.; Krishnan, K.; Kannan, S. Structural and Thermal Investigations of Sr2WO5. *J Alloys Compd* **2017**, *695*, 3639–3647. https://doi.org/10.1016/j.jallcom.2016.11.388.

(441) Bramnik, K. G.; Ehrenberg, H.; Buhre, S.; Fuess, H. Preparation, Crystal Structure and Magnetic Properties of the High-Pressure Phase MnReO4 with a Wolframite-Type Structure. *Acta Crystallogr B* **2005**, *61* (3), 246–249. https://doi.org/10.1107/S0108768105005380.

(442) Hubbard, C. R. A Review of the XRD Data of the Phases Present in the CaO-SrO-CuO System. *Powder Diffr* **1992**, *7* (3), 142–148. https://doi.org/10.1017/S0885715600018492.

(443) Roy, A.; Gauri, S. S.; Bhattacharya, M.; Bhattacharya, J. Antimicrobial Activity of CaO Nanoparticles. *J Biomed Nanotechnol* **2013**, *9* (9), 1570–1578. https://doi.org/10.1166/jbn.2013.1681.

(444) Gao, X.; Xu, D.; Du, J.; Li, J.; Yang, Z.; Sun, J. Tunability of Green–Red up-Conversion Emission of Co-Doped Ca3WO6:Yb3+/Er3+ Powders. *Journal of Materials Science: Materials in Electronics* **2017**, *28* (21), 16540–16546. https://doi.org/10.1007/s10854-017-7566-2.

(445) Chen, S. J.; Li, J.; Chen, X. T.; Hong, J. M.; Xue, Z.; You, X. Z. Solvothermal Synthesis and Characterization of Crystalline CaWO4 Nanoparticles. *J Cryst Growth* **2003**, *253* (1–4), 361–365. https://doi.org/10.1016/S0022-0248(03)01089-3.

(446) Wang, Y.; Ma, J.; Tao, J.; Zhu, X.; Zhou, J.; Zhao, Z.; Xie, L.; Tian, H. Synthesis of CaWO4 Nanoparticles by a Molten Salt Method. *Mater Lett* **2006**, *60* (2), 291–293. https://doi.org/10.1016/j.matlet.2005.08.037.

(447) Wang, S.; Yan, S.; Ma, X.; Gong, J. Recent Advances in Capture of Carbon Dioxide Using Alkali-Metal-Based Oxides. *Energy and Environmental Science*. The Royal Society of Chemistry September 27, 2011, pp 3805–3819. https://doi.org/10.1039/c1ee01116b.

(448) Yang, X.; Xia, C.; Xiong, X.; Mu, X.; Hu, B. Preparation and Catalytic Properties of Barium Cerate and Yttrium-Doped Barium Cerate Supported Ruthenium for Ammonia Synthesis. *Cuihua Xuebao/Chinese Journal of Catalysis* **2010**, *31* (4), 377–379. https://doi.org/10.1016/S1872-2067(09)60055-3.

(449) Scholten, M. J.; Schoonman, J.; van Miltenburg, J. C.; Oonk, H. A. J. Synthesis of Strontium and Barium Cerate and Their Reaction with Carbon Dioxide. *Solid State Ion* **1993**, *61* (1–3), 83–91. https://doi.org/10.1016/0167-2738(93)90338-4.

(450) Zhao, Y.; Weidner, D. J. Thermal Expansion of SrZrO3 and BaZrO3 Perovskites. *Phys Chem Miner* **1991**, *18* (5), 294–301. https://doi.org/10.1007/BF00200187.

(451) Jacobsson, T. J.; Schwan, L. J.; Ottosson, M.; Hagfeldt, A.; Edvinsson, T. Determination of Thermal Expansion Coefficients and Locating the Temperature-Induced Phase Transition in Methylammonium Lead Perovskites Using X-Ray Diffraction. *Inorg Chem* **2015**, *54* (22), 10678–10685. https://doi.org/10.1021/acs.inorgchem.5b01481.

(452) Biegalski, M. D.; Haeni, J. H.; Trolier-McKinstry, S.; Schlom, D. G.; Brandle, C. D.; Ven Graitis, A. J. Thermal Expansion of the New Perovskite Substrates DyScO3 and GdScO3. *J Mater Res* **2005**, *20* (4), 952–958. https://doi.org/10.1557/JMR.2005.0126.

(453) Howard, C. J.; Zhang, Z.; Carpenter, M. A.; Knight, K. S. Suppression of Strain Coupling in Perovskite La0.6 Sr0.1 Ti O3 by Cation Disorder. *Phys Rev B Condens Matter Mater Phys* **2007**, *76* (5), 054108. https://doi.org/10.1103/PhysRevB.76.054108.

(454) Wu, J.; Chen, L.; Song, T.; Zou, Z.; Gao, J.; Zhang, W.; Shi, S. A Review on Structural Characteristics, Lithium Ion Diffusion Behavior and Temperature Dependence of Conductivity in Perovskite-Type Solid Electrolyte Li3xLa2/3-x TiO3. *Functional Materials Letters* **2017**, *10* (3), ID-17300002. https://doi.org/10.1142/S179360471730002X.

(455) Yashima, M.; Ali, R. Structural Phase Transition and Octahedral Tilting in the Calcium Titanate Perovskite CaTiO3. *Solid State Ion* **2009**, *180* (2–3), 120–126. https://doi.org/10.1016/j.ssi.2008.11.019.

(456) Boström, H. L. B. Tilts and Shifts in Molecular Perovskites. *CrystEngComm* **2020**, *22* (5), 961–968. https://doi.org/10.1039/c9ce01950b.

(457) Zhao, T.; Daniels, L. M.; Slater, B.; Rosseinsky, M. J.; Corà, F. Effects of Octahedral Tilting on Band Structure and Thermoelectric Power Factor of Titanate Perovskites: A First-Principles Study on SrTiO3. *Journal of Physical Chemistry C* **2020**, *124* (24), 13045–13052. https://doi.org/10.1021/acs.jpcc.0c03513.

(458) Liao, Z.; Gauquelin, N.; Green, R. J.; Müller-Caspary, K.; Lobato, I.; Li, L.; Van Aert, S.; Verbeeck, J.; Huijben, M.; Grisolia, M. N.; Rouco, V.; El Hage, R.; Villegas, J. E.; Mercy, A.; Bibes, M.; Ghosez, P.; Sawatzky, G. A.; Rijnders, G.; Koster, G. Metal–Insulator-Transition Engineering by Modulation Tilt-Control in Perovskite Nickelates for Room Temperature Optical Switching. *Proc Natl Acad Sci U S A* **2018**, *115* (38), 9515–9520. https://doi.org/10.1073/pnas.1807457115.

(459) Herbstein, F. H.; Marsh, R. E. Changes in Space and Laue Groups of Some Published Crystal Structures. *Acta Crystallogr* **1982**, *B38* (Part 4), 1051–1055. https://doi.org/10.1107/s0567740882004956.

(460) Cao, R.; Zhang, W.; Chen, T.; Zheng, Y.; Ao, H.; Luo, Z.; Xie, S.; Wan, H. Perovskite Tungstate Ba2La2ZnW2O12:Mn4+ Phosphor: Synthesis, Energy Transfer and Tunable Emission. *Mater Res Bull* **2021**, *137*, 111200. https://doi.org/10.1016/j.materresbull.2020.111200.

(461) Bugaris, D. E.; Hodges, J. P.; Huq, A.; Zur Loye, H. C. Crystal Growth, Structures, and Optical Properties of the Cubic Double Perovskites Ba2MgWO6 and Ba2ZnWO6. *J Solid State Chem* **2011**, *184* (8), 2293–2298. https://doi.org/10.1016/j.jssc.2011.06.015.

(462) Huang, X.; Guo, H. Finding a Novel Highly Efficient Mn4+-Activated Ca3La2W2O12 Far-Red Emitting Phosphor with Excellent Responsiveness to Phytochrome PFR: Towards Indoor Plant Cultivation Application. *Dyes and Pigments* **2018**, *152*, 36–42. https://doi.org/10.1016/j.dyepig.2018.01.022.

(463) Groenink, J. A.; Blasse, G. Some New Observations on the Luminescence of $PbMoO_4$ and $PbWO_4$. *J Solid State Chem* **1980**, *32* (1), 9–20. https://doi.org/10.1016/0022-4596(80)90263-7.

(464) Van Oosterhout, A. B. Tungstate Luminescence in Ordered Perovskites. *physica status solidi (a)* **1977**, *41* (2), 607–617. https://doi.org/10.1002/pssa.2210410234.

(465) Pinatti, I. M.; Pereira, P. F. S.; de Assis, M.; Longo, E.; Rosa, I. L. V. Rare Earth Doped Silver Tungstate for Photoluminescent Applications. *J Alloys Compd* **2019**, *771*, 433–447. https://doi.org/10.1016/j.jallcom.2018.08.302.

(466) Wu, X.; Du, L.; Ren, Q.; Hai, O. A Far-Red Emission Ca3La2W2O12:XMn4+ Phosphor for Potential Application in Plant Growth LEDs. *J Lumin* **2022**, *249*, 118993. https://doi.org/10.1016/j.jlumin.2022.118993.

(467) Huang, X.; Guo, H. Finding a Novel Highly Efficient Mn4+-Activated Ca3La2W2O12 Far-Red Emitting Phosphor with Excellent Responsiveness to Phytochrome PFR: Towards Indoor Plant Cultivation Application. *Dyes and Pigments* **2018**, *152*, 36–42. https://doi.org/10.1016/j.dyepig.2018.01.022.

(468) Xie, Z.; Liu, X.; Zhao, W. Tunable Photoluminescence and Energy Transfer of Novel Phosphor Sr9La2W4O24:Sm3+, Eu3+ for near-UV White LEDs. *Journal of Materials Science: Materials in Electronics* **2020**, *31* (9), 7114–7122. https://doi.org/10.1007/s10854-020-03282-1.

(469) Jiao, Y.; Shao, C.; Guo, M.; Guzik, M.; Zhang, Y.; Yu, C.; Boulon, G.; Hu, L. Influence of Ce3+ Ion on Optical Properties and Radiation Resistance in Ce3+/Tm3+-Co-Doped Alumino-Silicate Glasses. *Optical Materials: X* **2022**, *13*, 100113. https://doi.org/10.1016/j.omx.2021.100113.

(470) Guan, R.; Cao, L.; You, Y.; Cao, Y. The Luminescence Properties and Energy Transfer from Ce3+ to Pr3+ for YAG:Ce3+Pr3+ Phosphors. *J Nanomater* **2015**, *2015*, ID-549208. https://doi.org/10.1155/2015/549208.

(471) Chewpraditkul, W.; He, X.; Chen, D.; Shen, Y.; Sheng, Q.; Yu, B.; Nikl, M.; Kucerkova, R.; Beitlerova, A.; Wanarak, C.; Phunpueok, A. Luminescence and Scintillation of Ce 3+-Doped Oxide Glass with High Gd 2O 3 Concentration. *Physica Status Solidi (A) Applications and Materials Science* **2011**, *208* (12), 2830–2832. https://doi.org/10.1002/pssa.201127365.

(472) Kucera, M.; Hanus, M.; Onderisinova, Z.; Prusa, P.; Beitlerova, A.; Nikl, M. Energy Transfer and Scintillation Properties of Ce3+ Doped (LuYGd)3(AlGa)5O12 Multicomponent Garnets. *IEEE Trans Nucl Sci* **2014**, *61* (1), 282–289. https://doi.org/10.1109/TNS.2013.2281234.

(473) Chen, P.; Yang, D.; Hu, W.; Zhang, J.; Wu, Y. Photoluminescence Properties and Structure of Double Perovskite Ba2ZnWO6:Eu3+, Li+ as a Novel Red Emitting Phosphor. *Chem Phys Lett* **2017**, *689*, 169–173. https://doi.org/10.1016/j.cplett.2017.10.006.

(474) Boutinaud, P. Rationalization of the Pr3+- to-Transition Metal Charge Transfer Model: Application to the Luminescence of Pr3+ in Titano-Niobates. *J Lumin* **2019**, *214*, 116557. https://doi.org/10.1016/j.jlumin.2019.116557.

(475) Legendziewicz, J.; Cybińska, J.; Guzik, M.; Boulon, G.; Meyer, G. Comparative Study of Crystal Field Analysis in Pr3+ and Yb3+-Doped K2LaX5 (X = Cl-, Br-) Ternary Halides and Yb3+-Doped A3Lu(PO4)2 (A = Na+, Rb+) Double Phosphates. Charge Transfer Band Observations of Yb3+-Doped Systems. *Opt Mater (Amst)* **2008**, *30* (11), 1655–1666. https://doi.org/10.1016/j.optmat.2007.11.005.

(476) Boutinaud, P.; Mahiou, R.; Cavalli, E.; Bettinelli, M. Red Luminescence Induced by Intervalence Charge Transfer in Pr3+-Doped Compounds. *J Lumin* **2007**, *122–123* (1–2), 430–433. https://doi.org/10.1016/j.jlumin.2006.01.198.

(477) Paul, A.; Mulholland, M.; Zaman, M. S. Ultraviolet Absorption of Cerium(III) and Cerium(IV) in Some Simple Glasses. *J Mater Sci* **1976**, *11* (11), 2082–2086. https://doi.org/10.1007/PL00020336.

(478) Portillo, M. C.; Moreno, O. P.; Mora-Ramírez, M. A.; Santiesteban, H. J.; Avendaño, C. B.; Bernal, Y. P. Optical and Structural Analysis of the Charge Transfer of Ce3++ E- →Ce4+ Ion in the Cerium Oxide (CeO2). *Optik (Stuttg)* **2021**, *248*, 168178. https://doi.org/10.1016/j.ijleo.2021.168178.

(479) Hoefdraad, H. E. Charge-Transfer Spectra of Tetravalent Lanthanide Ions in Oxides. *Journal of Inorganic and Nuclear Chemistry* **1975**, *37* (9), 1917–1921. https://doi.org/10.1016/0022-1902(75)80915-8.

(480) Zhang, S.; Li, C.; Pang, R.; Jiang, L.; Shi, L.; Su, Q. Energy Transfer and Excitation Wavelength Dependent Long-Lasting Phosphorescence in Pr3+ Activated Y3Al5O 12. *J Lumin* **2011**, *131* (12), 2730–2734. https://doi.org/10.1016/j.jlumin.2011.07.001.

(481) Xue, F.; Hu, Y.; Chen, L.; Ju, G.; Zhang, Q. Synthesis and Luminescence of Sr2Ta2O7:Pr3+: A Novel Blue Emission, Long Persistent Phosphor. *J Mater Res* **2016**, *31* (23), 3704–3711. https://doi.org/10.1557/jmr.2016.401.

(482) Wen, H.; Cheng, B. M.; Tanner, P. A. Optical Properties of Selected 4d and 5d Transition Metal Ion-Doped Glasses. *RSC Adv* **2017**, *7* (42), 26411–26419. https://doi.org/10.1039/c7ra04062h.

(483) Runowski, M.; Woźny, P.; Martín, I. R.; Lavín, V.; Lis, S. Praseodymium Doped YF3:Pr3+ Nanoparticles as Optical Thermometer Based on Luminescence Intensity Ratio (LIR) – Studies in Visible and NIR Range. *J Lumin* **2019**, *214*, ID-116571. https://doi.org/10.1016/j.jlumin.2019.116571.

(484) Rátiva, D. J.; De Araújo, C. B.; Messaddeq, Y. Energy Transfer and Frequency Upconversion Involving Triads of Pr3+ Ions in (Pr3+, Gd3+) Doped Fluoroindate Glass. *J Appl Phys* **2006**, *99* (8), ID-083505. https://doi.org/10.1063/1.2189207.

(485) Lazarowska, A.; Mahlik, S.; Krosnicki, M.; Grinberg, M.; Malinowski, M. Pressure-Induced Phase Transition in LiLuF 4:Pr 3+ Investigated by an Optical Technique. *Journal of Physics Condensed Matter* **2012**, *24* (11), 115502. https://doi.org/10.1088/0953-8984/24/11/115502.

(486) Adell, I.; Solé, R. M.; Pujol, M. C.; Lancry, M.; Ollier, N.; Aguiló, M.; Díaz, F. Single Crystal Growth, Optical Absorption and Luminescence Properties under VUV-UV Synchrotron Excitation of Type III Ce3+:KGd(PO3)4, a Promising Scintillator Material. *Sci Rep* **2018**, *8* (1), ID-11002. https://doi.org/10.1038/s41598-018-29372-z.

(487) Oliva, J.; De La Rosa, E.; Diaz-Torres, L. A.; Salas, P.; Torres, A.; Meza, O. Effect of Ammonia on Luminescent Properties of YAG:Ce 3+ ,Pr 3+ Nanophosphors. In *Nanophotonic Materials*; SPIE, 2010; Vol. 7755, pp 56–66. https://doi.org/10.1117/12.861049.

(488) Huang, C.-H.; Liu, W.-R.; Kuo, T.-W.; Chen, T.-M. A Study on the Luminescence and Energy Transfer of Green-Emitting Ca9Y(PO4)7:Ce3+,Tb3+ Phosphor for Fluorescent Lamp Application. *Chem* **2011**, *1* (1), 9–15. https://doi.org/10.5618/chem.2011.v1.n1.2.

(489) Van der Kolk, E.; Dorenbos, P.; Van Eijk, C. W. E. Vacuum Ultraviolet Excitation of 1S0 and 3P0 Emission of Pr3+ in Sr0.7La0.3Al11.7Mg0.3O 19 and SrB4O7. *Journal of Physics Condensed Matter* **2001**, *13* (23), 5471–5486. https://doi.org/10.1088/0953-8984/13/23/306.

(490) Katayama, Y.; Tanabe, S. Downconversion for 1 Mm Luminescence in Lanthanide and Yb3+ Co-Doped Phosphors. In *Solar Cells and Light Management*; Elsevier, 2019; pp 415–441. https://doi.org/10.1016/B978-0-08-102762-2.00012-4.

(491) Katayama, Y.; Tanabe, S. Spectroscopy and 1μm Luminescence by Visible Quantum Cutting in Pr3+-Yb3+ Codoped Glas. *Materials* **2010**, *3* (4), 2405–2411. https://doi.org/10.3390/ma3042405.

(492) Qin, W. P.; Liu, Z. Y.; Sin, C. N.; Wu, C. F.; Qin, G. S.; Chen, Z.; Zheng, K. Z. Multi-Ion Cooperative Processes in Yb3+ Clusters. *Light Sci Appl* **2014**, *3* (8), IDe193. https://doi.org/10.1038/lsa.2014.74.

(493) Liang, Y. J.; Liu, F.; Chen, Y. F.; Wang, X. J.; Sun, K. N.; Pan, Z. New Function of the Yb3+ Ion as an Efficient Emitter of Persistent Luminescence in the Short-Wave Infrared. *Light Sci Appl* **2016**, *5* (7), ID. https://doi.org/10.1038/lsa.2016.124.

(494) Huang, F.; Liu, X.; Ma, Y.; Kang, S.; Hu, L.; Chen, D. Origin of near to Middle Infrared Luminescence and Energy Transfer Process of Er3+/Yb3+ Co-Doped Fluorotellurite Glasses under Different Excitations. *Sci Rep* **2015**, *5* (1), 8233–8238. https://doi.org/10.1038/srep08233.

(495) Cao, Y.; Chen, S.; Shao, C.; Yu, C. Influence of F- on Stark Splitting of Yb3+ and the Thermal Expansion of Silica Glass. *J Appl Phys* **2018**, *123* (21), ID-215106. https://doi.org/10.1063/1.5030357.

(496) Demirkhanyan, G. G. Intensities of Inter-Stark Transitions in Activated Crystals. *Optics and Spectroscopy (English translation of Optika i Spektroskopiya)* **2006**, *101* (4), 546–548. https://doi.org/10.1134/S0030400X06100079.

(497) Zhang, L.; Xia, Y.; Shen, X.; Yang, R.; Wei, W. Investigations on the Effects of the Stark Splitting on the Fluorescence Behaviors in Yb3+-Doped Silicate, Tellurite, Germanate, and Phosphate Glasses. *Opt Mater (Amst)* **2018**, *75*, 1–6. https://doi.org/10.1016/j.optmat.2017.10.008.

(498) Nalumaga, H.; Schuyt, J. J.; Breukers, R. D.; Williams, G. V. M. Radiation-Induced Changes in the Photoluminescence Properties of NaMgF3:Yb Nanoparticles: Yb3+ → Yb2+ Valence Conversion and Oxygen-Impurity Charge Transfer. *Mater Res Bull* **2022**, *145*, ID-111562. https://doi.org/10.1016/j.materresbull.2021.111562.

(499) Khadiev, A.; Akhmetov, N.; Korableva, S.; Morozov, O.; Nizamutdinov, A.; Semashko, V.; Pudovkin, M.; Gafurov, M. The Impact of BiF3 Doping on the Yb3+ to Yb2+ Reduction during the LiYF4:Yb3+ Crystal-Growth Process. *Ceramics* **2022**, *5* (4), 1198–1206. https://doi.org/10.3390/ceramics5040085.

(500) Mahlik, S.; Diaz, F.; Boutinaud, P. Pressure-Induced Luminescence Quenching in KY(WO4)2:Pr3+. *Opt Mater (Amst)* **2017**, *74*, 41–45. https://doi.org/10.1016/j.optmat.2017.04.002.

(501) Mahlik, S.; Grinberg, M.; Cavalli, E.; Bettinelli, M.; Boutinaud, P. High Pressure Evolution of YVO4:Pr3+ Luminescence. *Journal of Physics Condensed Matter* **2009**, *21* (10), ID-105401. https://doi.org/10.1088/0953-8984/21/10/105401.

(502) Gupta, S. K.; Abdou, H.; Mao, Y. Pressure-Induced Site Swapping, Luminescence Quenching, and Color Tunability of Gd2Hf2O7:Eu3+ Nanoparticles. *Opt Mater (Amst)* **2021**, *112*, ID-110789. https://doi.org/10.1016/j.optmat.2020.110789.

(503) Zhu, C.; Yang, J.; Shan, P.; Zhao, M.-H.; Zhao, S.; Pei, C.; Zhang, B.; Deng, Z.; Croft, M.; Qi, Y.; Yang, L.; Wang, Y.; Kuang, X.; Jiang, L.; Yao, D.-X.; Cheng, J.-G.; Li, M.-R. Pressure-Induced Intermetallic Charge Transfer and Semiconductor-Metal Transition in Two-Dimensional AgRuO 3. *CCS Chemistry* **2022**, *5* (4), 934–946. https://doi.org/10.31635/ccschem.022.202201989.

(504) Shukla, A.; Rueff, J. P.; Badro, J.; Vanko, G.; Mattila, A.; de Groot, F. M. F.; Sette, F. Charge Transfer at Very High Pressure in NiO. *Phys Rev B Condens Matter Mater Phys* **2003**, *67* (8), ID-081101. https://doi.org/10.1103/PhysRevB.67.081101.

(505) Zhu, L.; Li, P.; Sun, H.; Han, X.; Xu, Y.; Wang, X.; Liu, B.; Ozaki, Y.; Zhao, B. An Investigation of the Effect of High-Pressure on Charge Transfer in Dye-Sensitized Solar Cells Based on Surface-Enhanced Raman Spectroscopy. *Nanoscale* **2022**, *14* (2), 373–381. https://doi.org/10.1039/d1nr06250f.

(506) Behrendt, M.; Szczodrowski, K.; Mahlik, S.; Grinberg, M. High Pressure Effect on Charge Transfer Transition in Y2O2S:Eu3+. *Opt Mater (Amst)* **2014**, *36* (10), 1616–1621. https://doi.org/10.1016/j.optmat.2013.11.013.

(507) Singh, Y. High Pressure Study of Charge Transfer Complexes and Radical Ion Salts: A Review. In *AIP Conference Proceedings*; AIP Publishing LLCAIP Publishing, 2016; Vol. 1728, p ID-020692. https://doi.org/10.1063/1.4946743.

(508) Blasse, G.; Kemmler-Sack, S. LOW-TEMPERATURE LUMINESCENCE IN Eu3 + -DOPED TUNGSTATES OF THE PEROVSKITE STACKING-VARIANT TYPE. *Berichte der Bunsengesellschaft/Physical Chemistry Chemical Physics* **1983**, *87* (4), 352–355. https://doi.org/10.1002/bbpc.19830870417.

(509) Blasse, G.; Bokkers, G. Low-Temperature Decay-Time Measurements on the Luminescence of Calcium Tungstate (CaWO4). *J Solid State Chem* **1983**, *49* (1), 126–128. https://doi.org/10.1016/0022-4596(83)90225-6.

(510) Ahmed, N.; Kraus, H.; Kim, H. J.; Mokina, V.; Tsiumra, V.; Wagner, A.; Zhydachevskyy, Y.; Mykhaylyk, V. B. Characterisation of Tungstate and Molybdate Crystals ABO4 (A = Ca, Sr, Zn, Cd; B = W, Mo) for Luminescence Lifetime Cryothermometry. *Materialia (Oxf)* **2018**, *4*, 287–296. https://doi.org/10.1016/j.mtla.2018.09.039.

(511) Kushnirenko, I. Y.; Moroz, Z. T.; Nagornaya, L. L.; Nedel'ko, S. G.; Stetsun, A. I.; Tupitsyna, I. A. Characteristics of Low-Temperature Luminescence of Cadmium Tungstate Single Crystal-Luminescence. *J Appl Spectrosc* **1992**, *56* (2), 160–164. https://doi.org/10.1007/BF00662270.

(512) Benoît, G.; Véronique, J.; Arnaud, A.; Alain, G. Luminescence Properties of Tungstates and Molybdates Phosphors: Illustration on ALn(MO4)2 Compounds (A = Alikaline Cation, Ln = Lanthanides, M = W, Mo). *Solid State Sci* **2011**, *13* (2), 460–467. https://doi.org/10.1016/j.solidstatesciences.2010.12.013.

(513) Randall, J. T. Luminescence of Solids at Low Temperatures. *Nature*. Nature Publishing Group 1938, pp 113–114. https://doi.org/10.1038/142113a0.

(514) Gourgout, A.; Leroux, M.; Smirr, J. L.; Massoudzadegan, M.; Lobo, R. P. S. M.; Vignolles, D.; Proust, C.; Berger, H.; Li, Q.; Gu, G.; Homes, C. C.; Akrap, A.; Fauqué, B. Magnetic Freeze-out and Anomalous Hall Effect in ZrTe5. *NPJ Quantum Mater* **2022**, *7* (1), 1–7. https://doi.org/10.1038/s41535-022-00478-y.

(515) Rao, V. L.; Vasudeva Reddy, Y.; Shekharam, T.; Nagabhushanam, M. First Report on Effect of Freezing of Charge Carriers on Conductivity of CoxZn1−xS Ternary Semiconductor Compounds at Low Temperatures. *Chem Phys Lett* **2022**, *796*, ID-139571. https://doi.org/10.1016/j.cplett.2022.139571.

(516) Meaney, S.; Pan, A. V.; Jones, A.; Fedoseev, S. A. Partial Carrier Freeze-out at the LaAlO3/SrTiO3 Oxide Interface. *APL Mater* **2019**, *7* (10), ID-101105. https://doi.org/10.1063/1.5112804.

(517) O'Donnell, K. P.; Chen, X. Temperature Dependence of Semiconductor Band Gaps. *Appl Phys Lett* **1991**, *58* (25), 2924–2926. https://doi.org/10.1063/1.104723.

(518) King, P. D. C.; Veal, T. D.; Fuchs, F.; Wang, C. Y.; Payne, D. J.; Bourlange, A.; Zhang, H.; Bell, G. R.; Cimalla, V.; Ambacher, O.; Egdell, R. G.; Bechstedt, F.; McConville, C. F. Band Gap, Electronic Structure, and Surface Electron Accumulation of Cubic and Rhombohedral In2 O3. *Phys Rev B Condens Matter Mater Phys* **2009**, *79* (20), 205211. https://doi.org/10.1103/PhysRevB.79.205211.

(519) De Boer, T.; Bekheet, M. F.; Gurlo, A.; Riedel, R.; Moewes, A. Band Gap and Electronic Structure of Cubic, Rhombohedral, and Orthorhombic In2 O3 Polymorphs: Experiment and Theory. *Phys Rev B* **2016**, *93* (15), 155205. https://doi.org/10.1103/PhysRevB.93.155205.

(520) Lacomba-Perales, R.; Ruiz-Fuertes, J.; Errandonea, D.; Martínez-García, D.; Segura, A. Optical Absorption of Divalent Metal Tungstates: Correlation between the Band-Gap Energy and the Cation Ionic Radius. *Europhys Lett* **2008**, *83* (3), 37002. https://doi.org/10.1209/0295-5075/83/37002.

(521) Kaczmarek, S. M.; Leniec, G.; Bodziony, T.; Fuks, H.; Kowalski, Z.; Drozdowski, W.; Berkowski, M.; Głowacki, M.; Witkowski, M. E.; Makowski, M. BaWO4:Ce Single Crystals Codoped with Na Ions. *Crystals (Basel)* **2019**, *9* (1), 38. https://doi.org/10.3390/cryst9010028.

(522) He, P.; Xu, H.; Lan, L.; Deng, C.; Wu, Y.; Lin, Y.; Chen, S.; Ding, C.; Li, X.; Xu, M.; Peng, J. The Effect of Charge Transfer Transition on the Photostability of Lanthanide-Doped Indium Oxide Thin-Film Transistors. *Commun Mater* **2021**, *2* (1), ID-86. https://doi.org/10.1038/s43246-021-00193-4.

(523) Nomiya, K.; Sugie, Y.; Amimoto, K.; Miwa, M. Charge-Transfer Absorption Spectra of Some Tungsten(VI) and Molybdenum(VI) Polyoxoanions. *Polyhedron* **1987**, *6* (3), 519–524. https://doi.org/10.1016/S0277-5387(00)81018-9.

(524) Yaffe, O.; Guo, Y.; Tan, L. Z.; Egger, D. A.; Hull, T.; Stoumpos, C. C.; Zheng, F.; Heinz, T. F.; Kronik, L.; Kanatzidis, M. G.; Owen, J. S.; Rappe, A. M.; Pimenta, M. A.; Brus, L. E. Local Polar Fluctuations in Lead Halide Perovskite Crystals. *Phys Rev Lett* **2017**, *118* (13), ID-136001. https://doi.org/10.1103/PhysRevLett.118.136001.

(525) Wasylishen, R. E.; Knop, O.; Macdonald, J. B. Cation Rotation in Methylammonium Lead Halides. *Solid State Commun* **1985**, *56* (7), 581–582. https://doi.org/10.1016/0038-1098(85)90959-7.

(526) Worhatch, R. J.; Kim, H. J.; Swainson, I. P.; Yonkeu, A. L.; Billinge, S. J. L. Study of Local Structure in Selected Organic-Inorganic Perovskites in the Pm3m Phase. *Chemistry of Materials* **2008**, *20* (4), 1272–1277. https://doi.org/10.1021/cm702668d.

(527) Hu, Y.; Anandkumar, M.; Joardar, J.; Wang, X.; Deshpande, A. S.; Reddy, K. M. Effective Band Gap Engineering in Multi-Principal Oxides (CeGdLa-Zr/Hf)Ox by Temperature-Induced Oxygen Vacancies. *Sci Rep* **2023**, *13* (1), 2362–2373. https://doi.org/10.1038/s41598-023-29477-0.

(528) Cristina de Oliveira, R.; Cabral, L.; Cabral, A. C.; Almeida, P. B.; Tibaldi, N.; Sambrano, J. R.; Simões, A. Z.; Macchi, C. E.; Moura, F.; Marques, G. E.; Ponce, M. A.; Longo, E. Charge Transfer in Pr-Doped Cerium Oxide: Experimental and Theoretical Investigations. *Mater Chem Phys* **2020**, *249*, 122967. https://doi.org/10.1016/j.matchemphys.2020.122967.

(529) Chen, P.; Baldwin, M.; Bandaru, P. R. Hierarchically Structured, Oxygen Deficient, Tungsten Oxide Morphologies for Enhanced Photoelectrochemical Charge Transfer and Stability. *J Mater Chem A Mater* **2017**, *5* (28), 14898–14905. https://doi.org/10.1039/c7ta04118g.

(530) Li, J.; Lazzari, R.; Chenot, S.; Jupille, J. Contributions of Oxygen Vacancies and Titanium Interstitials to Band-Gap States of Reduced Titania. *Phys Rev B* **2018**, *97* (4), 041403. https://doi.org/10.1103/PhysRevB.97.041403.

(531) Gómez-Pérez, J. F.; Correa, J. D.; Pravda, C. B.; Kónya, Z.; Kukovecz, Á. Dangling-to-Interstitial Oxygen Transition and Its Modifications of the Electronic Structure in Few-Layer Phosphorene. *Journal of Physical Chemistry C* **2020**, *124* (44), 24066–24072. https://doi.org/10.1021/acs.jpcc.0c06542.

(532) Kohout, J. Modified Arrhenius Equation in Materials Science, Chemistry and Biology. *Molecules* **2021**, *26* (23), 7162–7180. https://doi.org/10.3390/molecules26237162.

(533) Abderezzak, B. Charge Transfer Phenomena. In *Introduction to Transfer Phenomena in PEM Fuel Cell*; Elsevier, 2018; pp 53–83. https://doi.org/10.1016/b978-1-78548-291-5.50002-0.

(534) Vink, A. P.; Dorenbos, P.; De Haas, J. T. M.; Donker, H.; Rodnyi, P. A.; Avanesov, A. G.; Van Eijk, C. W. E. Photon Cascade Emission in SrAlF5:Pr3+. *Journal of Physics Condensed Matter* **2002**, *14* (38), 8889–8899. https://doi.org/10.1088/0953-8984/14/38/312.

(535) Xue, J.; Fujitsuka, M.; Majima, T. Shallow Trap State-Induced Efficient Electron Transfer at the Interface of Heterojunction Photocatalysts: The Crucial Role of Vacancy Defects. *ACS Appl Mater Interfaces* **2019**, *11* (43), 40860–40867. https://doi.org/10.1021/acsami.9b14128.

(536) Kao, K. C. Electrical Conduction and Photoconduction. In *Dielectric Phenomena in Solids*; Academic Press, 2004; pp 381–514. https://doi.org/10.1016/b978-012396561-5/50017-7.

(537) Vikas Dubey, Neha Dubey, Marta Domanska, M Jayasimhadri, S. J. D. Defects in Rare-Earth-Doped Inorganic Materials. In *Rare-Earth-Activated Phosphors: Chemistry and Applications*; Elsevier, 2022; pp 85–133. https://doi.org/10.1016/B978-0-323-89856-0.00004-3.

(538) Haneef, H. F.; Zeidell, A. M.; Jurchescu, O. D. Charge Carrier Traps in Organic Semiconductors: A Review on the Underlying Physics and Impact on Electronic Devices. *Journal of Materials Chemistry C*. The Royal Society of Chemistry January 23, 2020, pp 759–787. https://doi.org/10.1039/c9tc05695e.

(539) Khanna, R.; Das, M. B. Roles of Shallow and Deep Electron Traps Causing Backgating in GaAs Metal-Semiconductor Field-Effect Transistors. *Appl Phys Lett* **1986**, *48* (14), 937–939. https://doi.org/10.1063/1.96664.

(540) Van der Heggen, D.; Vandenberghe, D.; Moayed, N. K.; De Grave, J.; Smet, P. F.; Joos, J. J. The Almost Hidden Role of Deep Traps When Measuring Afterglow and Thermoluminescence of Persistent Phosphors. *J Lumin* **2020**, *226*, 117496. https://doi.org/10.1016/j.jlumin.2020.117496.

(541) Quickenden, T. I.; Hanlon, A. R.; Freeman, C. G. Activation Energy for the Emission of 420 Nm Luminescence from UV-Excited Polycrystalline H2O Ice. *Journal of Physical Chemistry A* **1997**, *101* (25), 4511–4516. https://doi.org/10.1021/jp9706036.

(542) Savchenko, S. S.; Vokhmintsev, A. S.; Weinstein, I. A. Activation Energy Distribution in Thermal Quenching of Exciton and Defect-Related Photoluminescence of InP/ZnS Quantum Dots. *J Lumin* **2022**, *242*, 118550. https://doi.org/10.1016/j.jlumin.2021.118550.

(543) Cui, J.; Zheng, Y.; Wang, Z.; Cao, L.; Wang, X.; Yao, Y.; Zhang, M.; Zheng, M.; Yang, Z.; Li, P. Improving the Luminescence Thermal Stability of Ca3Y2Ge3O12:Cr3+ Based on Cation Substitution and Its Application in NIR LEDs. *Mater Adv* **2022**, *3* (6), 2772–2778. https://doi.org/10.1039/d2ma00009a.

(544) Mehdi, S.; Yangpeng, L.; Hadrien, C.; Fabrice, L.; Xishi, W.; Guillaume, C. Fluorescence Lifetime Measurements Applied to the Characterization of the Droplet Temperature in Sprays. *Exp Fluids* **2021**, *62* (8), 174–192. https://doi.org/10.1007/s00348-021-03264-x.

(545) Irimpan, L.; Ambika, D.; Kumar, V.; Nampoori, V. P. N.; Radhakrishnan, P. Effect of Annealing on the Spectral and Nonlinear Optical Characteristics of Thin Films of Nano-ZnO. *J Appl Phys* **2008**, *104* (3), 033118. https://doi.org/10.1063/1.2949400.

(546) M Zawawi, S. M.; Yahya, R.; Hassan, A.; Mahmud, H. N. M. E.; Daud, M. N. Structural and Optical Characterization of Metal Tungstates (MWO4; M=Ni, Ba, Bi) Synthesized by a Sucrose-Templated Method. *Chem Cent J* **2013**, *7* (1), 80–89. https://doi.org/10.1186/1752-153X-7-80.

(547) Mazumdar, S.; Zhao, Y.; Zhang, X. Stability of Perovskite Solar Cells: Degradation Mechanisms and Remedies. *Frontiers in Electronics* **2021**, *2*, ID-712785. https://doi.org/10.3389/felec.2021.712785.

(548) Davies, M. L. Addressing the Stability of Lead Halide Perovskites. *Joule*. Cell Press August 19, 2020, pp 1626–1627. https://doi.org/10.1016/j.joule.2020.07.025.

(549) Zhou, Y.; Zhao, Y. Chemical Stability and Instability of Inorganic Halide Perovskites. *Energy and Environmental Science*. The Royal Society of Chemistry May 16, 2019, pp 1495–1511. https://doi.org/10.1039/c8ee03559h.

(550) Ivanov, S. A.; Ivanov, S. A.; Kumar, P. A.; Nordblad, P.; Mathieu, R.; Bush, A. A.; Behtin, M. A.; Ritter, C.; Cherepanov, V. M.; Autieri, C.; Kvashnin, Y. O.; Di Marco, I.; Sanyal, B.; Eriksson, O. Evolution of the Structural and Multiferroic Properties of PbFe2/3W1/3O3 Ceramics upon Mn-Doping. *Mater Chem Phys* **2017**, *187*, 218–232. https://doi.org/10.1016/j.matchemphys.2016.12.003.

(551) Mottaghinejad, E.; Shaafi, E.; Ghasemzadeh, Z. Barium Dichromate [BaCr2O7], a Mild Reagent for Oxidation of Alcohols to Their Corresponding Carbonyls in Non-Aqueous Polar Aprotic Media. *ChemInform* **2005**, *36* (9), no-no. https://doi.org/10.1002/chin.200509033.

(552) Fromm, E. Reduction of Metal Evaporation Losses by Inert Gas Atmospheres. *Metallurgical Transactions A* **1978**, *9* (12), 1835–1838. https://doi.org/10.1007/BF02663416.

(553) Rai, V. K. Temperature Sensors and Optical Sensors. *Appl Phys B* **2007**, *88* (2), 297–303. https://doi.org/10.1007/s00340-007-2717-4.

(554) Wang, X.; Liu, Q.; Bu, Y.; Liu, C. S.; Liu, T.; Yan, X. Optical Temperature Sensing of Rare-Earth Ion Doped Phosphors. *RSC Advances*. The Royal Society of Chemistry October 12, 2015, pp 86219–86236. https://doi.org/10.1039/c5ra16986k.

(555) Singh, A. K.; Singh, S. K.; Gupta, B. K.; Prakash, R.; Rai, S. B. Probing a Highly Efficient Dual Mode: Down-Upconversion Luminescence and Temperature Sensing Performance of Rare-Earth Oxide Phosphors. *Dalton Transactions* **2013**, *42* (4), 1065–1072. https://doi.org/10.1039/c2dt32054a.

(556) Yang, L.; Kruse, B. Revised Kubelka–Munk Theory I Theory and Application. *Journal of the Optical Society of America A* **2004**, *21* (10), 1933. https://doi.org/10.1364/josaa.21.001933.

(557) Vargas, W. E.; Niklasson, G. A. Applicability Conditions of the Kubelka–Munk Theory. *Appl Opt* **1997**, *36* (22), 5580. https://doi.org/10.1364/ao.36.005580.

(558) Zhu, Z.; Xiao, J.; Sun, H.; Hu, Y.; Cao, R.; Wang, Y.; Zhao, L.; Zhuang, J. Composition-Dependent Band Gaps and Indirect-Direct Band Gap Transitions of Group-IV Semiconductor Alloys. *Physical Chemistry Chemical Physics* **2015**, *17* (33), 21605–21610. https://doi.org/10.1039/c5cp02558c.

(559) Hayashi, S.; Nesterenko, D. V.; Rahmouni, A.; Sekkat, Z. Observation of Fano Line Shapes Arising from Coupling between Surface Plasmon Polariton and Waveguide Modes. *Appl Phys Lett* **2016**, *108* (5), ID-051101. https://doi.org/10.1063/1.4940984.

(560) Wang, Q.; Huang, Y.; Yao, Z.; Xu, X. Analysis of Transition from Lorentz Resonance to Fano Resonance in Plasmon and Metamaterial Systems. *Opt Quantum Electron* **2016**, *48* (2), 83–92. https://doi.org/10.1007/s11082-015-0358-0.

(561) Limonov, M. F.; Rybin, M. V.; Poddubny, A. N.; Kivshar, Y. S. Fano Resonances in Photonics. *Nat Photonics* **2017**, *11* (9), 543–554. https://doi.org/10.1038/NPHOTON.2017.142.

(562) Limonov, M. F. Fano Resonance for Applications. *Adv Opt Photonics* **2021**, *13* (3), 703–771. https://doi.org/10.1364/aop.420731.

(563) Chaurasiya, R.; Auluck, S.; Dixit, A. Cation Modified A2(Ba, Sr and Ca) ZnWO6 Cubic Double Perovskites: A Theoretical Study. *Computational Condensed Matter* **2018**, *14*, 27–35. https://doi.org/10.1016/j.cocom.2017.12.005.

(564) Sahnoun, O.; Bouhani-Benziane, H.; Sahnoun, M.; Driz, M.; Daul, C. Ab Initio Study of Structural, Electronic and Thermodynamic Properties of Tungstate Double Perovskites Ba2MWO6 (M = Mg, Ni, Zn). *Comput Mater Sci* **2013**, *77*, 316–321. https://doi.org/10.1016/j.commatsci.2013.04.053.

(565) Albert, J. P.; Jouanin, C.; Cassagne, D.; Monge, D. Photonic Crystal Modelling Using a Tight-Binding Wannier Function Method. *Opt Quantum Electron* **2002**, *34* (1–3), 251–263. https://doi.org/10.1023/A:1013393918768.

(566) Garrity, K. F.; Choudhary, K. Database of Wannier Tight-Binding Hamiltonians Using High-Throughput Density Functional Theory. *Sci Data* **2021**, *8* (1), 106–115. https://doi.org/10.1038/s41597-021-00885-z.

(567) Doll, B.; Hepp, J.; Hoffmann, M.; Schuler, R.; Buerhop-Lutz, C.; Peters, I. M.; Hauch, J. A.; Maier, A.; Brabec, C. J. Photoluminescence for Defect Detection on Full-Sized Photovoltaic Modules. *IEEE J Photovolt* **2021**, *11* (6), 1419–1429. https://doi.org/10.1109/JPHOTOV.2021.3099739.

(568) Yang, M. Y.; Kamiya, K.; Shiraishi, K. Interstitial Oxygen Induced Fermi Level Pinning in the Al2O 3-Based High-k MISFET with Heavy-Doped n-Type Poly-Si Gates. *AIP Adv* **2013**, *3* (10), 102113. https://doi.org/10.1063/1.4825071.

(569) Han, W. H.; Oh, Y. J.; Chang, K. J.; Park, J. S. Electronic Structure of Oxygen Interstitial Defects in Amorphous In-Ga-Zn-O Semiconductors and Implications for Device Behavior. *Phys Rev Appl* **2015**, *3* (4), 044008. https://doi.org/10.1103/PhysRevApplied.3.044008.

(570) Soma, T.; Yoshimatsu, K.; Horiba, K.; Kumigashira, H.; Ohtomo, A. Electronic Properties across Metal-Insulator Transition in β -Pyrochlore-Type CsW2 O6 Epitaxial Films. *Phys Rev Mater* **2018**, *2* (11), 115003. https://doi.org/10.1103/PhysRevMaterials.2.115003.

(571) Jiang, X.; Yang, C.; Lv, P.; Yao, Q.; Song, J. Superior Dielectric Tunability of High-Valence W6+-Doped Na0.5Bi0.5TiO3 Thin Films. *Journal of Materials Science: Materials in Electronics* **2017**, *28* (2), 1433–1437. https://doi.org/10.1007/s10854-016-5678-8.

(572) Zhou, L.; Yang, G.; Yang, D.; Xu, J.; Peng, Z.; Wu, D.; Wei, L.; Liang, P.; Chao, X.; Yang, Z. The Origin of Dielectric Relaxation Behavior in TiO2 Based Ceramics Co-Doped with Zn2+, W6+ Ions under a N2/O2 Sintering Atmosphere. *Physical Chemistry Chemical Physics* **2023**, *25* (10), 7373–7382. https://doi.org/10.1039/d2cp05514g.

(573) Menéndez, N.; García-Hernández, M.; Sánchez, D.; Tornero, J. D.; Martínez, J. L.; Alonso, J. A. Charge Transfer and Disorder in Double Perovskites. *Chemistry of Materials* **2004**, *16* (18), 3565–3572. https://doi.org/https://doi.org/10.1021/CM049305T.

(574) Seijo, L.; Barandiarán, Z. Intervalence Charge Transfer Luminescence: The Anomalous Luminescence of Cerium-Doped Cs2LiLuCl6 Elpasolite. *Journal of Chemical Physics* **2014**, *141* (21), ID-214706. https://doi.org/10.1063/1.4902384.

(575) Kang, S.-J. L. Initial Stage Sintering. In *Sintering*; Butterworth-Heinemann, 2005; pp 39–55. https://doi.org/10.1016/b978-075066385-4/50004-2.

(576) German, R. M. Mixed Powders and Composites. In *Sintering: from Empirical Observations to Scientific Principles*; Butterworth-Heinemann, 2014; pp 355–385. https://doi.org/10.1016/b978-0-12-401682-8.00011-2.

(577) Radha, S. K.; Lambrecht, W. R. L. Understanding the Crystallographic Phase Relations in Alkali-Trihalogeno-Germanates in Terms of Ferroelectric or Antiferroelectric Arrangements of the Tetrahedral GeX3 Units. *Adv Electron Mater* **2020**, *6* (2), 1900887. https://doi.org/10.1002/aelm.201900887.

(578) Eremeev, S. V.; Otrokov, M. M.; Chulkov, E. V. Competing Rhombohedral and Monoclinic Crystal Structures in MnPn2Ch4 Compounds: An Ab-Initio Study. *J Alloys Compd* **2017**, *709*, 172–178. https://doi.org/10.1016/j.jallcom.2017.03.121.

(579) Errandonea, D.; Martínez-García, D.; Segura, A.; Haines, J.; Machado-Charry, E.; Canadell, E.; Chervin, J. C.; Chevy, A. High-Pressure Electronic Structure and Phase Transitions in Monoclinic InSe: X-Ray Diffraction, Raman Spectroscopy, and Density Functional Theory. *Phys Rev B Condens Matter Mater Phys* **2008**, *77* (4), 045208. https://doi.org/10.1103/PhysRevB.77.045208.

(580) Radha, S. K.; Lambrecht, W. R. L. Understanding the Crystallographic Phase Relations in Alkali-Trihalogeno-Germanates in Terms of Ferroelectric or Antiferroelectric Arrangements of the Tetrahedral GeX3 Units. *Adv Electron Mater* **2020**, *6* (2), 1900887. https://doi.org/10.1002/aelm.201900887.

(581) Roy, S. Mott Insulators and Related Phenomena: A Basic Introduction. In *Mott Insulators*; IOP Publishing, 2019; Vol. 3, pp 1–35. https://doi.org/10.1088/2053-2563/ab16c9ch3.

Appendix

Warszawa, 08.06.2023

(miejscowość, data)

Damian Włodarczyk

(imię i nazwisko)

664264575, wlodar@ifpan.edu.pl, Uranowa 21B m.14, 81-160, Gdynia, Polska

(dane kontaktowe)

90020709254

(pesel)

OŚWIADCZENIE

Autora rozprawy doktorskiej

Jako autor rozprawy doktorskiej pod tytułem:

[PL]: *Synteza i właściwości fizykochemiczne nowych wolframianowych podwójnych perowskitów oraz ich pochodnych domieszkowanych wybranymi jonami ziem rzadkich.*

[ENG]: *Synthesis and physicochemical properties of novel, tungsten-oxide double perovskites and their derivatives doped with selected rare-earth ions.*

przygotowanej pod kierunkiem Prof. Dr hab. Andrzeja Suchockiego,

przedłożonej Radzie Naukowej Instytutu Fizyki Polskiej Akademii Nauk oświadczam, że:

1) rozprawa została napisana przeze mnie samodzielnie i nie zawiera treści uzyskanych w sposób niezgodny z obowiązującymi przepisami (ustawa z dnia 4 lutego 1994 r. o prawie autorskim i prawach pokrewnych – t.j. Dz. U. z 2006 r., Nr 90, poz. 631 z późn. zm.),

2) rozprawa nie była wcześniej przedmiotem procedur związanych z uzyskaniem stopnia naukowego w innym przewodzie doktorskim,

3) rozprawa doktorska w wersji cyfrowej umieszczona na załączonym nośniku danych jest tożsama z wersją wydrukowana i przedłożoną w moim przewodzie doktorskim,

4) udzielam Instytutowi Fizyki Polskiej Akademii Nauk licencji niewyłącznej na umieszczenie pełnego tekstu ww. rozprawy doktorskiej w wersji elektronicznej na stronie internetowej Instytutu w domenie ifpan.edu.pl i tym samym udostępnienie jej treści dla wszystkich w sieci.

Damian Włodarczyk

(podpis)

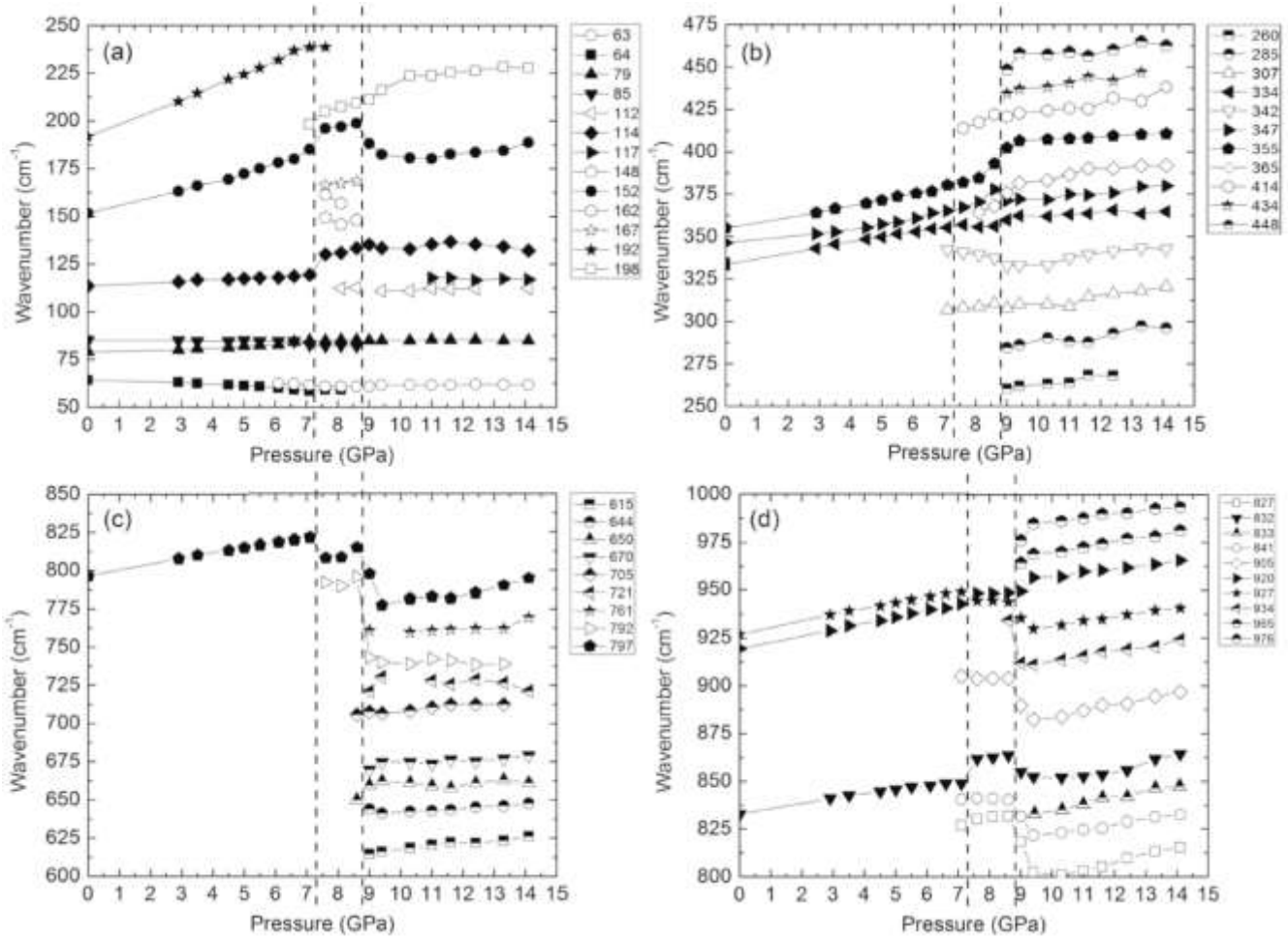

Figure A1 Pressure dependence of Raman scheelite modes (solid symbols), emerging fergusonite (open symbols), and the HP $BaWO_4$-II bands (semisolid symbols) up to 14.1 GPa. Dotted lines above 7 GPa show the onset of the scheelite-to-fergusonite phase transition, while dashed lines below 9 GPa the other related to the fergusonite - monoclinic $BaWO_4$-II change.

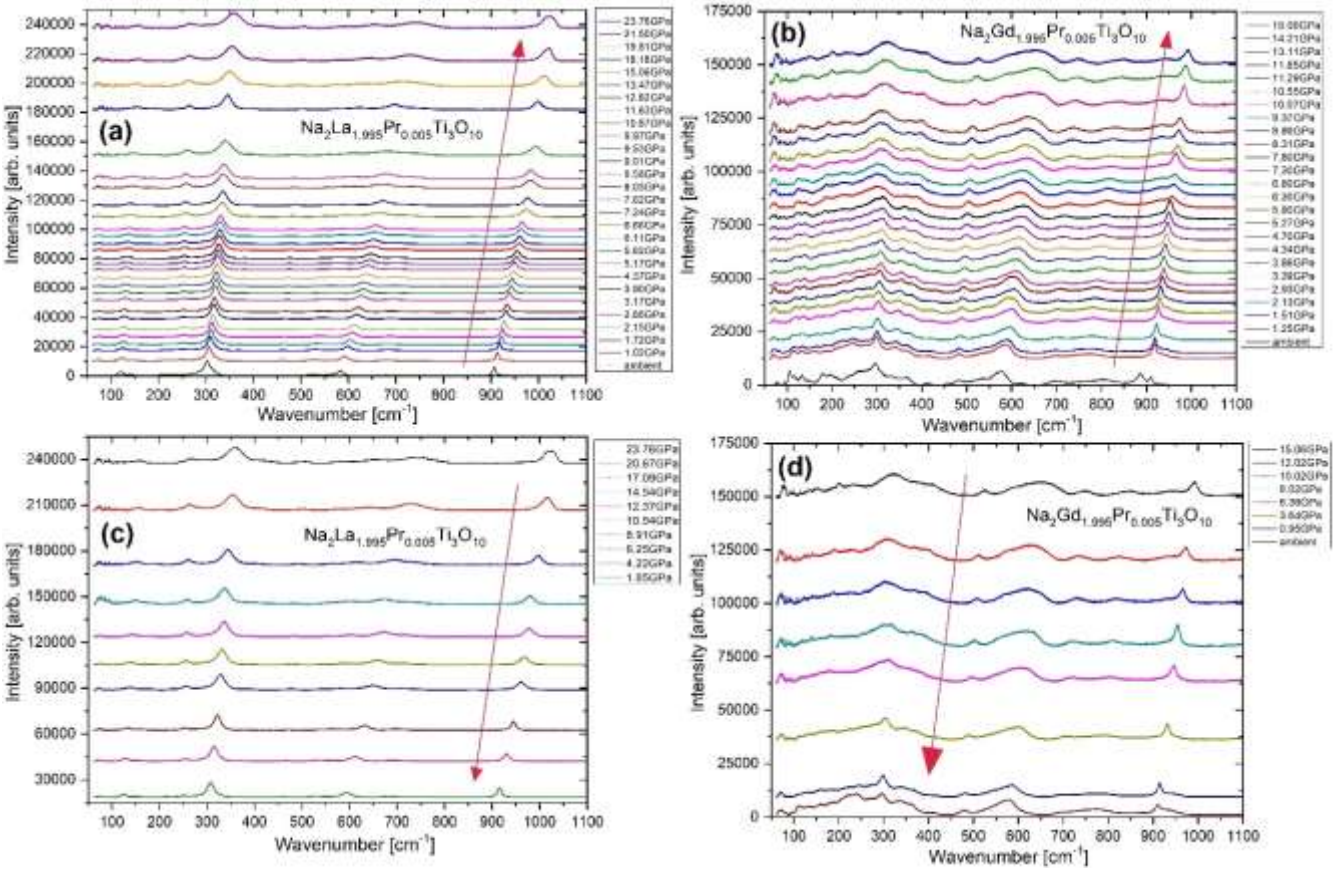

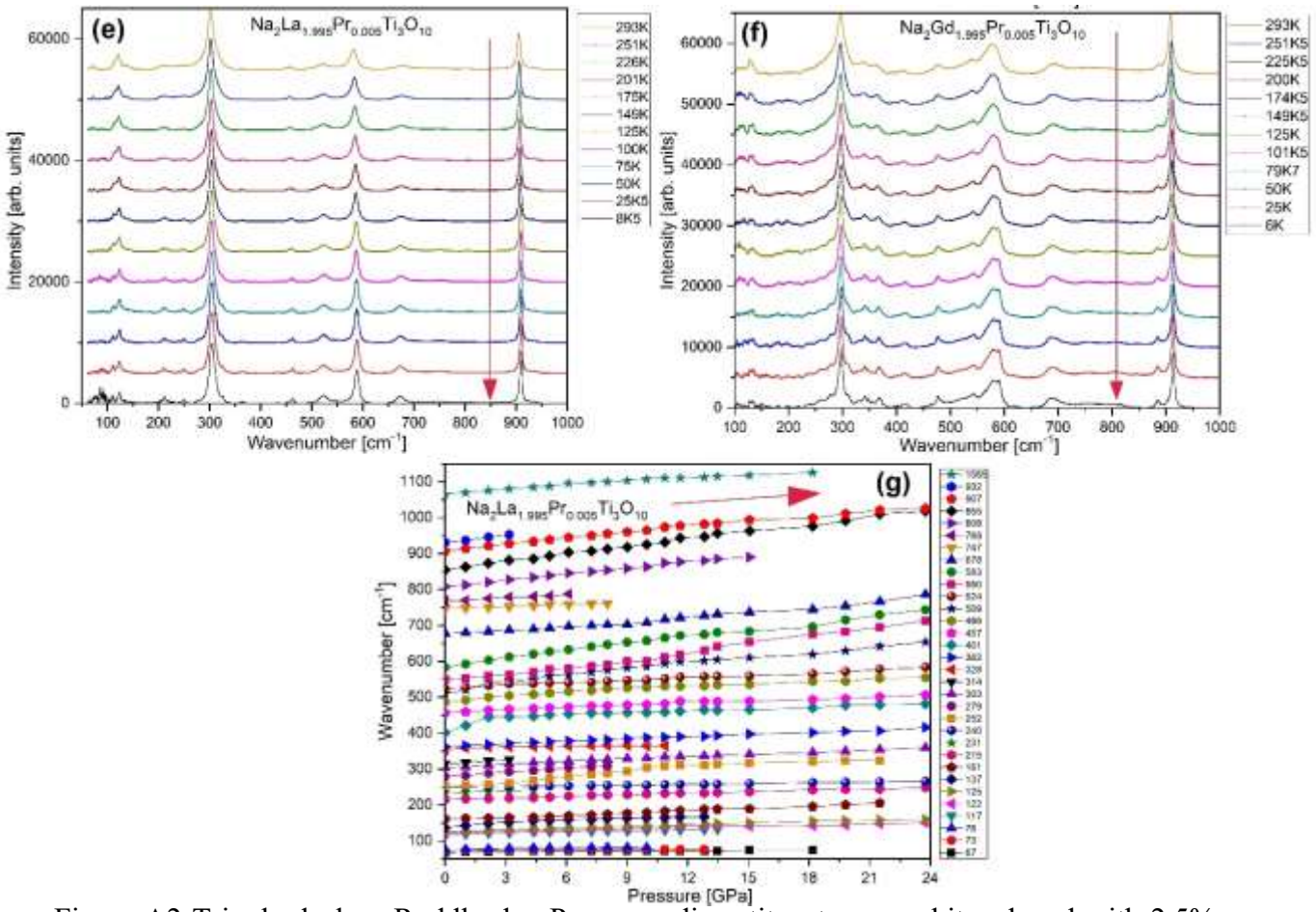

Figure A2 Tripple-decker, Ruddlesden-Popper sodium-titanate perovskites doped with 2.5% Pr^{3+} and their polymorphism viewed via Raman spectroscopy. The left figures relate to the $Na_2La_2Ti_3O_{10}$ matrix, while the right to $Na_2Gd_2Ti_3O_{10}$ in respective order: (a,b) compression, (c,d) decompression, (e,f) cooling from RT to cryogenic conditions. The bottom last graph (g) showcases peak versus pressure relations for lanthanide derivative solely to establish unique coefficients and calculate much-needed Grüneisen parameters.

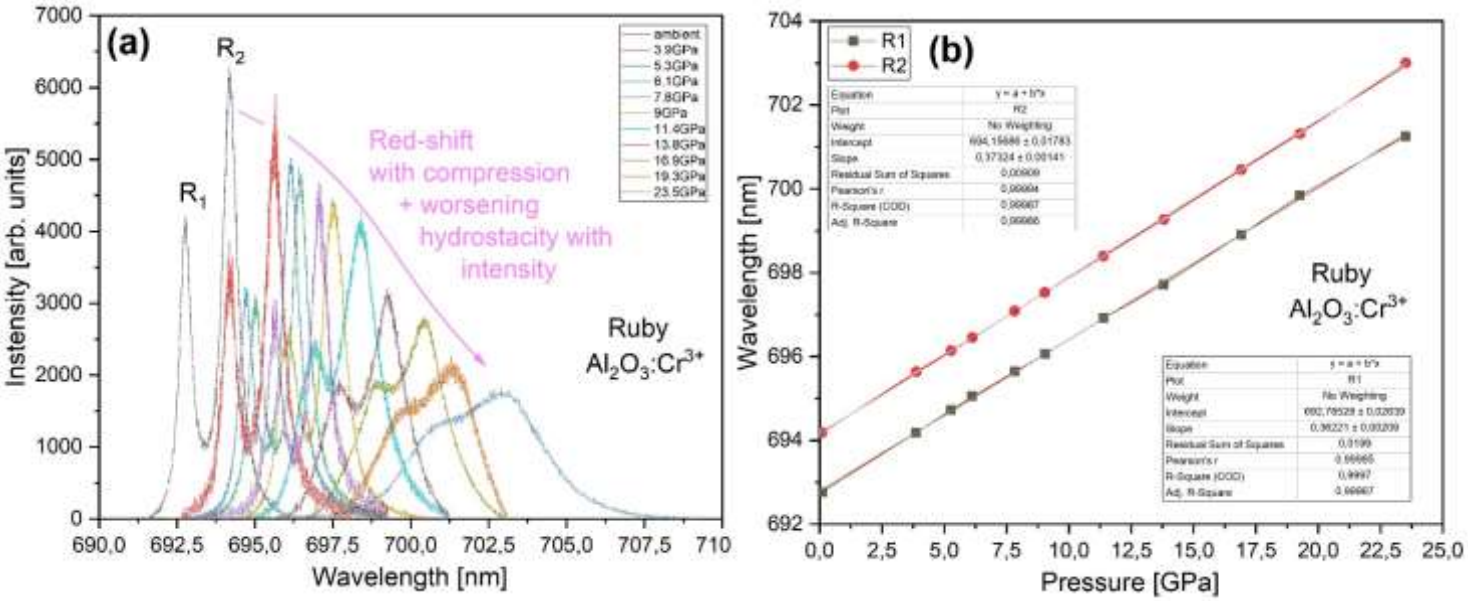

Figure A3 (a) An example of ruby fluorescence showcasing typical Cr^{3+} bands slowly red-shifting during compression. Pressure quenching and amorphization (loss of hydrostatic capabilities above 15 GPa) are also visible. Graph (b) depicts the position dependence of the exemplary R1 line and, more importantly, the R2 mode used as a reference for DAC interior pressure calculations provided by Syassen's and Mao's work.[149,150]

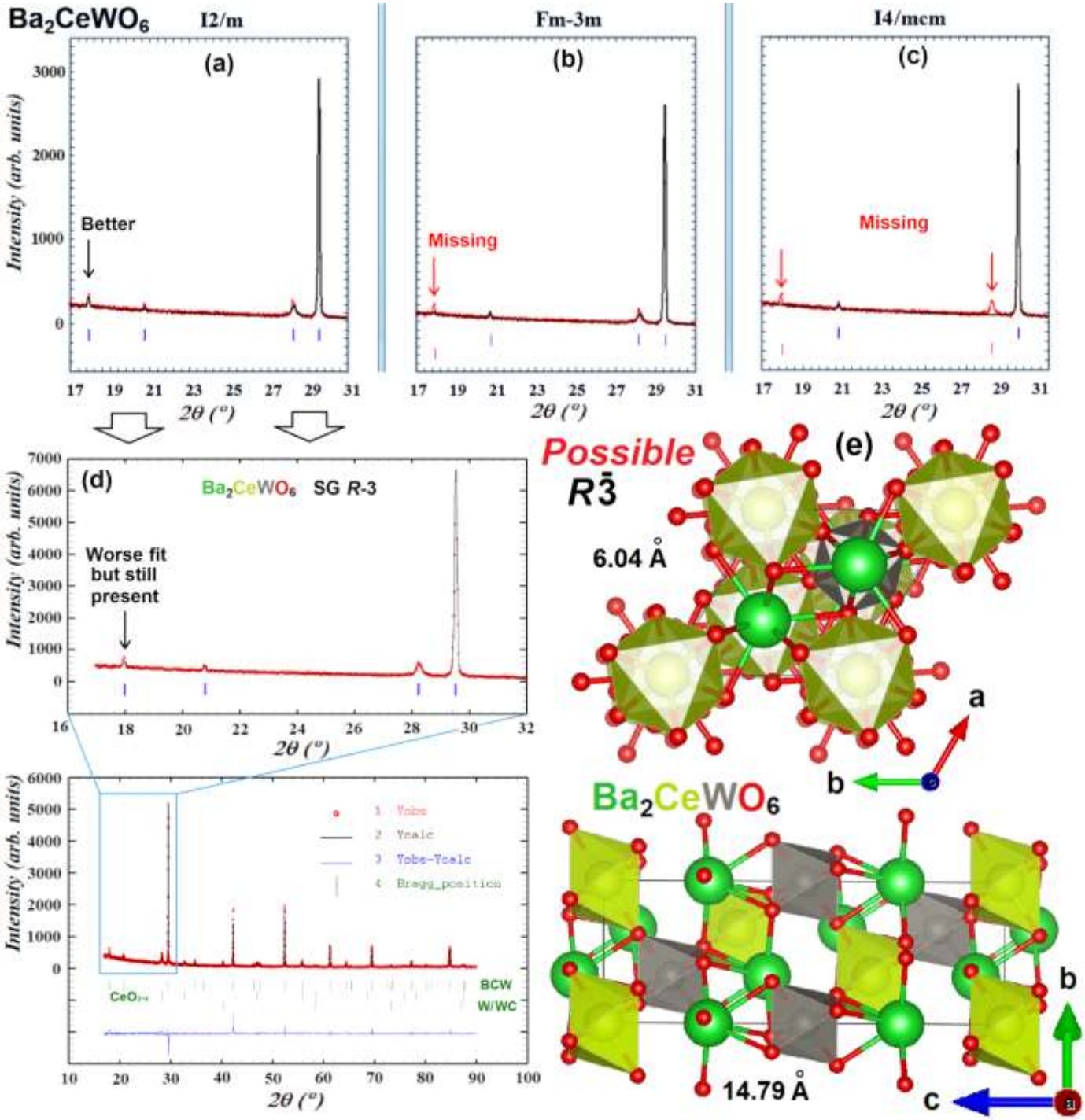

Figure A4 Case-specific powder XRD diffractograms showcasing a meticulous fitting process for the most possible SGs hosting BCW in a narrow 2θ region of interest. Red dots are the manifestation of an actual, observed pattern. A straight black line is a calculated fit. Blue and red vertical lines depict present and missing Bragg positions (green lines) compared to most ideal *I*2/*m* SG. As one can see, only pattern (a) for *I*2/*m* contains all four peaks, while cubic *Fm*-3*m* at (b) and *I*4/*mcm* in (c) came short of 1 or 2 positions, respectively. Figure (d) also matches all of them, however, a *hkl* at 18° (2θ) lacks in matters of intensity – closely associated with it, alternative *R*-3 unit cell is presented in mixed polyhedral/ball-stick convention to the right – Figure (e).

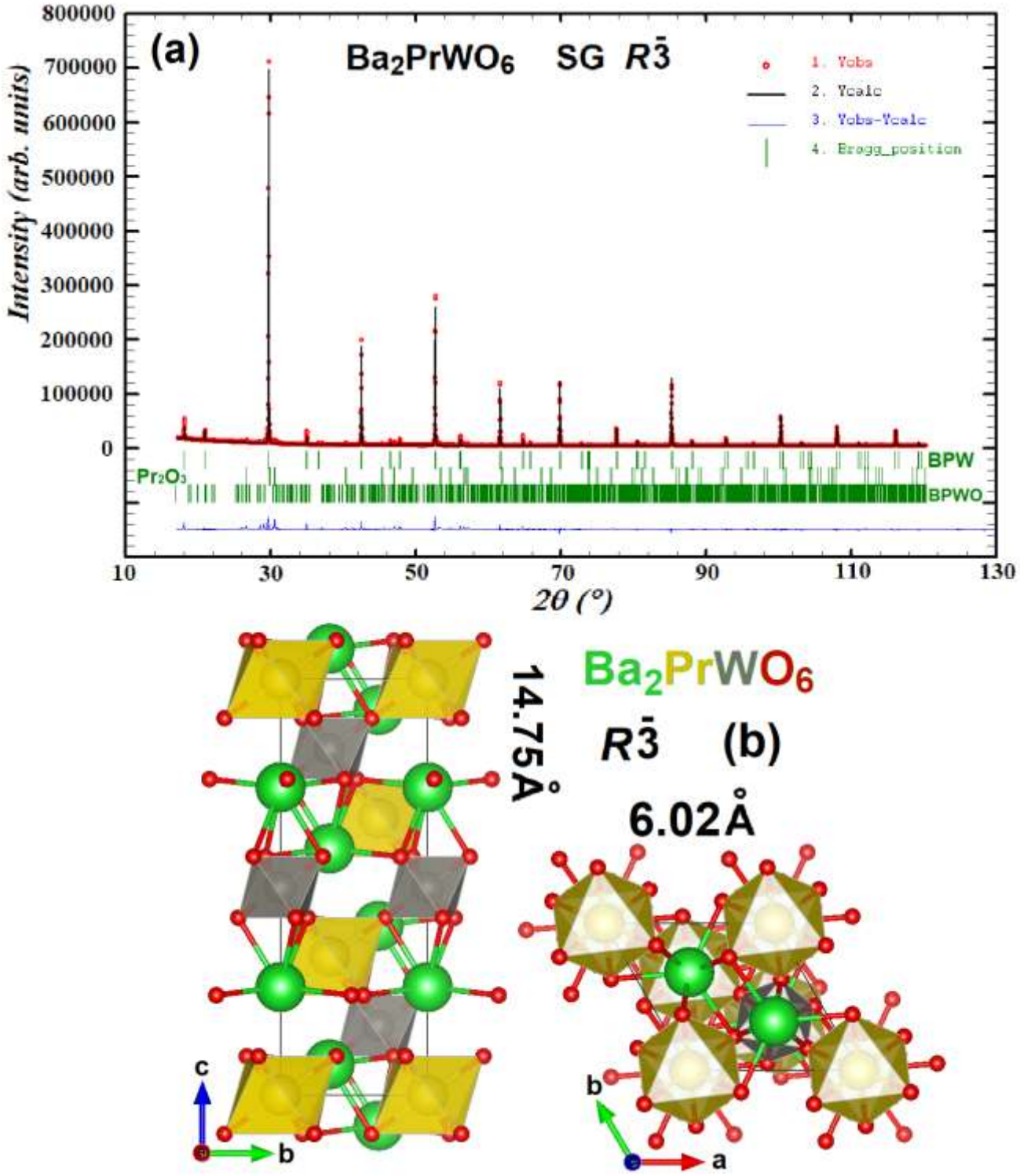

Figure A5 Alternate, almost identical XRD pattern fitting acquired post-Rietveld refinement to (a) *R*-3 phase for purest (~96%) Ba_2PrWO_6 (BPW) batch still containing traces of $BaPr_2WO_7$ and distorted Pr_2O_3 oxide impurities. Red dots are the manifestation of an actual, observed pattern. A straight black line is a calculated fit. The blue line depicts the difference between them. Green vertical lines are specific Bragg positions assigned to specific phases. The unit cell is shown in partially ball-stick, partially polyhedral conventions in (b) with some additional structural parameters alongside the c (right) and a (left) axes. Yellow spheres and polygons are Pr ions. Red is oxygen, and grey is assigned to tungsten space filling. Barium is depicted solely as green spheres to improve overall visibility since its dodecahedra would cover most of the view.

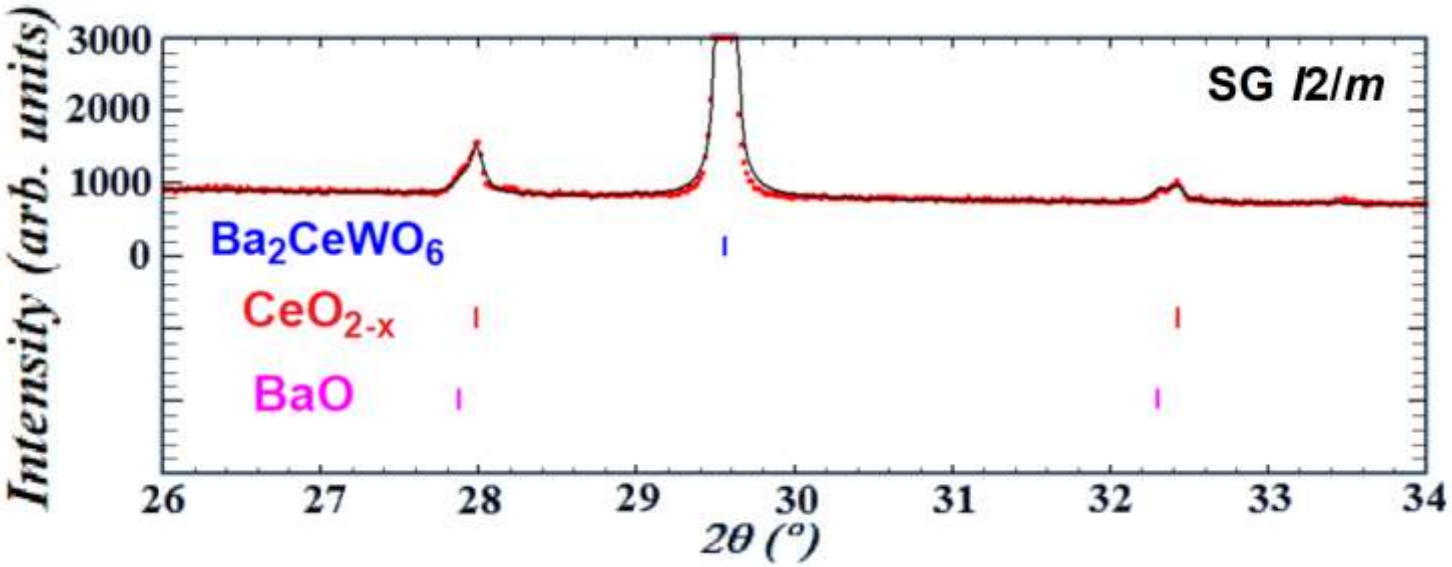

Figure A6 Powder XRD diffractogram showcasing a typical *I*2/*m* fit for one of the worse BCW batches. As seen, quite a few minor phases could form near crucial Bragg positions, such as here - highly-distorted CeO_{2-x} and BaO oxides are the culprits. Red dots are the manifestation of an actual, observed pattern. A straight black line is a calculated fit. The blue, red, and pink vertical lines relate to specific compounds and their Bragg positions – BCW, CeO_{2-x}, and BaO, respectively. Those impurities form due to the evaporation of 1 necessary reactant - WO_2.

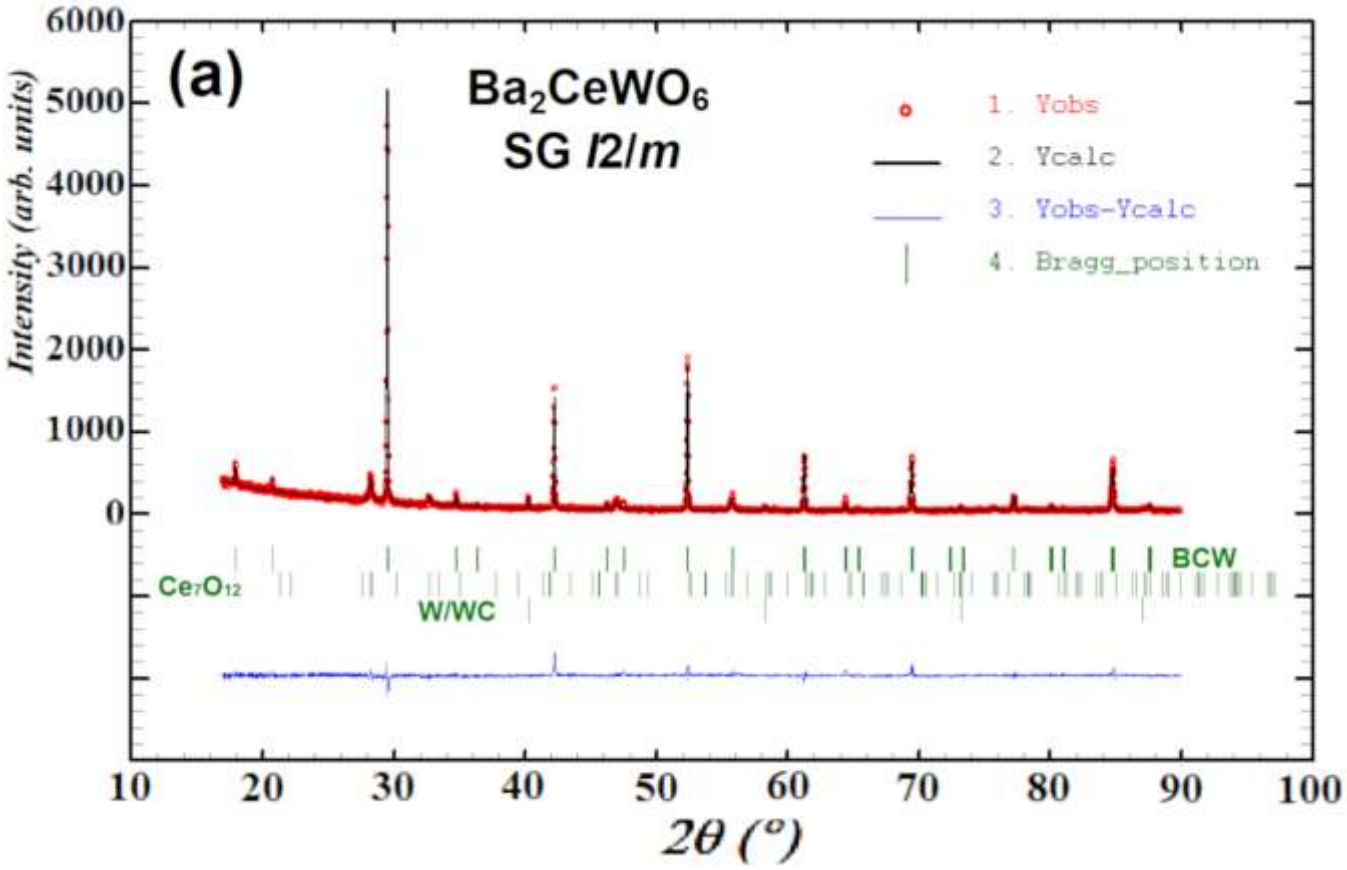

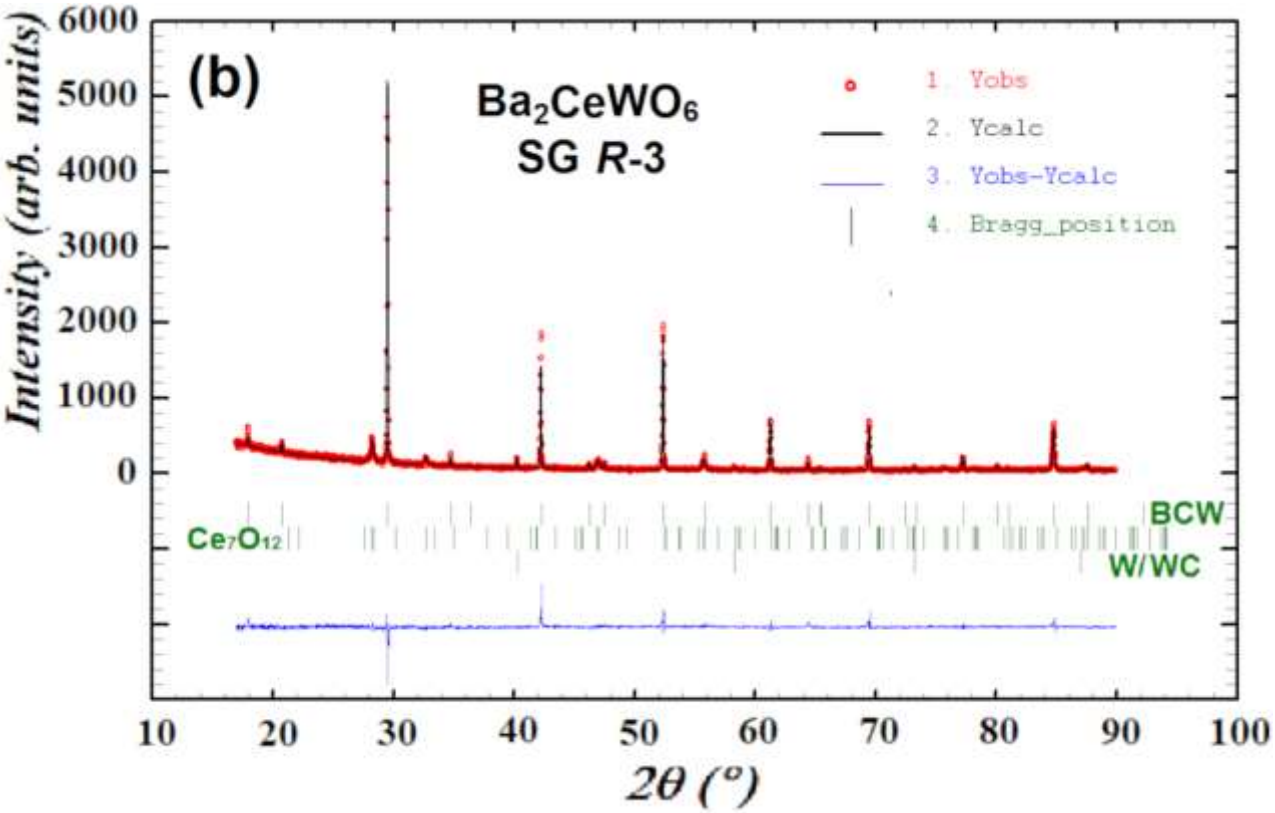

Figure A7 Powder XRD diffractogram fitting for one of the better BCW batches shows that in a few particular cases, a minor phase, such as highly-distorted $CeO_{2-x,}$ could form an almost perfect Ce_7O_{12} pattern. It is probably a targeted form of this undesired impurity concerning almost identical: (a) *I*2/*m* and (b) *R*-3 SG patterns. Red dots are the manifestation of an actual, observed pattern. A straight black line is a calculated fit. The green vertical lines relate to specific compounds and their Bragg positions.

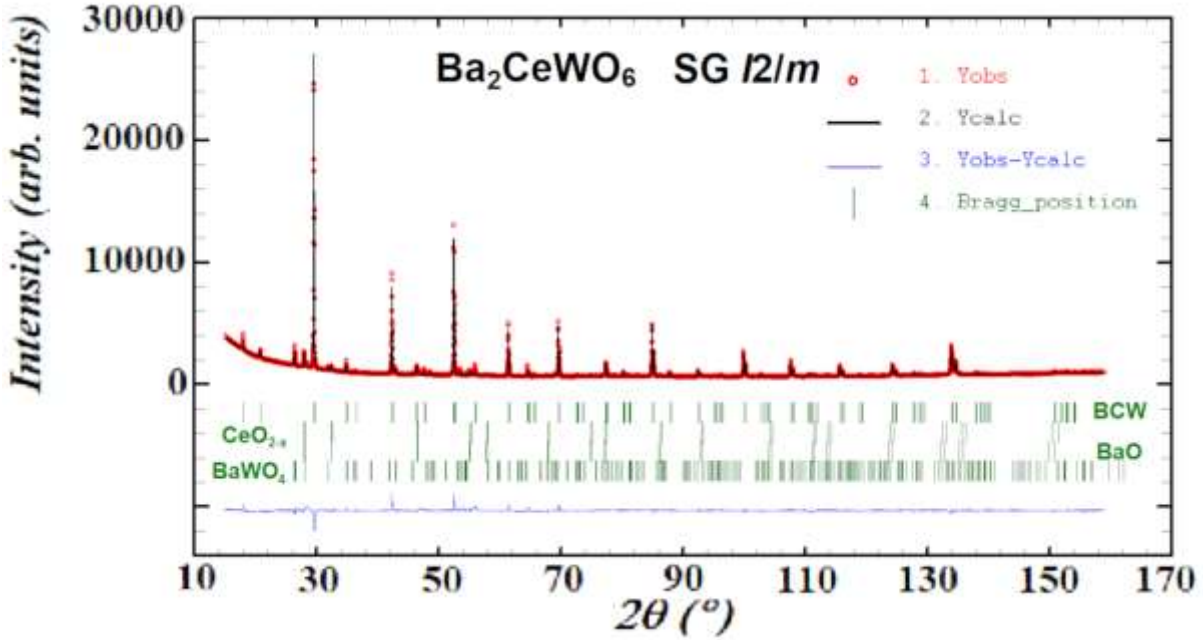

Figure A8 Powder XRD diffractogram fitting for one of the worst BCW batches showing that quite a few minor phases could form: not only highly-distorted CeO_{2-x} and BaO present due to WO_2 evaporation but also quite popular $BaWO_4$ created when an excessive amount of air is not removed from the furnace environment. Red dots are the manifestation of an actual, observed pattern. A straight black line is a calculated fit, and the green vertical lines relate to specific compounds and their Bragg positions – BCW, CeO_{2-x}, BaO, and $BaWO_4$.

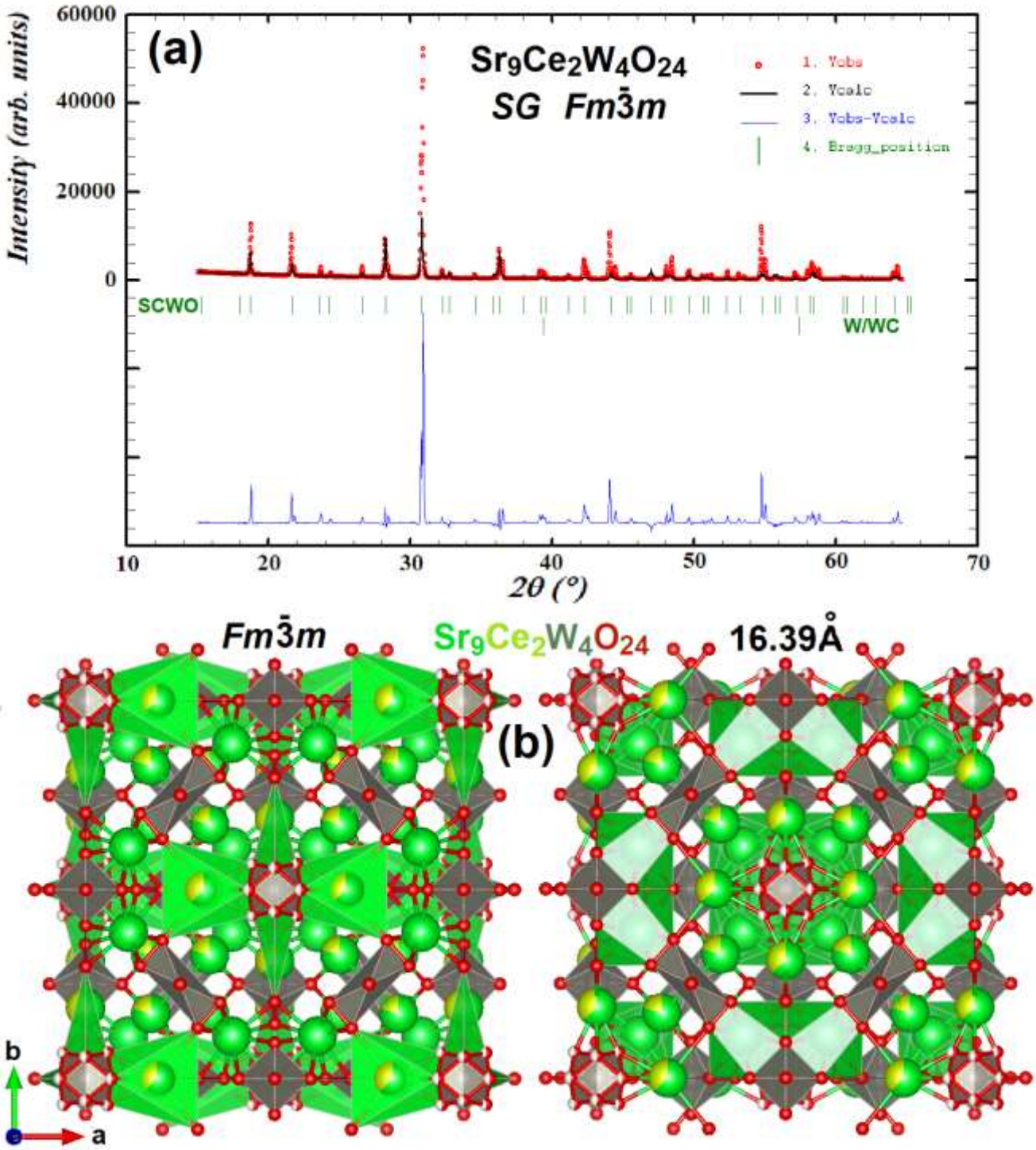

Figure A9 Alternate, closest XRD pattern fitting acquired post-Rietveld refinement for the most probable (a) *Fm*-3*m* phase of $Sr_9Ce_2W_4O_{24}$ (SCWO) still containing traces of W/WC ceramics as impurities (~99% pure batch). Red dots are the manifestation of an actual, observed pattern. A straight black line is a calculated fit. The blue line depicts the difference between them. Green vertical lines are specific Bragg positions assigned to specific phases. The unit cell is shown using partially ball-stick, partially polyhedral convention in figure (b), with additional structural parameters alongside the main axis. The right projection shows shared Sr/Ce polyhedral sites, while the left depicts only those specific for Sr. Green spheres and polygons are strontium atoms. Yellow is cerium. Red is oxygen, and grey is assigned to tungsten.

Table A1 Conventional Rietveld reliability factors for all the alternative space groups in investigated, undoped compounds and their minor phases present in the best possible batch. Data refers to diffractograms hosting Bragg contribution patterns corrected with the background concerning SG that will be disputed and deemed less plausible (but not entirely discarded) in the conclusions.

Formula	SG	Z	V [Å^3]	d_{cal} [g/cm^3]	R_B	R_P	R_{WP}	R_{EXP}	N_σ GoF	χ^2	Fract [%]
Ba_2CeWO_6	*R*-3	3	467.009	7.410	13.6						94.73
CeO_{2-x}	*Fm*-3*m*	4	164.207	6.962	42.3	23.7	20.9	4.41	1295.277	23.0	2.41
BaO	*Fm*-3*m*	4	168.007	6.062	37.0						2.55
W(/WC)	*Im*-3*m*	2	31.698	19.263	93.8						0.31
Ba_2PrWO_6	*R*-3	3	463.261	7.478	6.02						95.62
$BaPr_2WO_7$	*P*2$_1$/*b*	4	623.894	7.612	28.7	18.5	17.5	2.66	2736.675	43.1	3.98
Pr_2O_3	*P*-3*m*	1	77.682	7.050	57.9						0.40
$Sr_9Ce_2W_4O_{24}$	*Fm*-3*m*	8	4407.122	6.604	15.2	76.9	80.2	3.77	14242.9	45.2	99.34
W(/WC)	*Im*-3*m*	2	31.621	19.260	75.3						0.66
$Ca_3Ce_2W_2O_{12}$	*R*3*c*	18	4528.403	6.339	4.95	8.89	10.4	2.70	900.651	14.8	99.61
W(/WC)	*Im*-3*m*	2	31.678	19.257	70.8						0.39

Table A2 Crystallographic parameters obtained for all relevant, alternate, and undoped structures stored in the CIF CCDC database. Though R_{wp} suggests all mentioned rhombohedral SG are indistinguishable projections, they were moved to the appendix because the discussion renders them less plausible at the end, although not fully rejectable.

Formula	Main SG	Unit cell axis length [Å]			Angles [°]			Volume [Å^3]
		a [100]	b [010]	c [001]	α	β	γ	
Ba_2CeWO_6	*R*-3	6.03818(8)		14.7905(4)	90.000		120.000	467.00(9)
Ba_2PrWO_6	*R*-3	6.02194(4)		14.75098(2)	90.000		120.000	463.26(1)
$Sr_9Ce_2W_4O_{24}$	*Fm*-3*m*	16.395(3)			90.000			4407.12(2)
$Ca_3Ce_2W_2O_{12}$	*R*3*c*	9.72582(3)		55.2791(2)	90.000		120.000	4528.40(3)

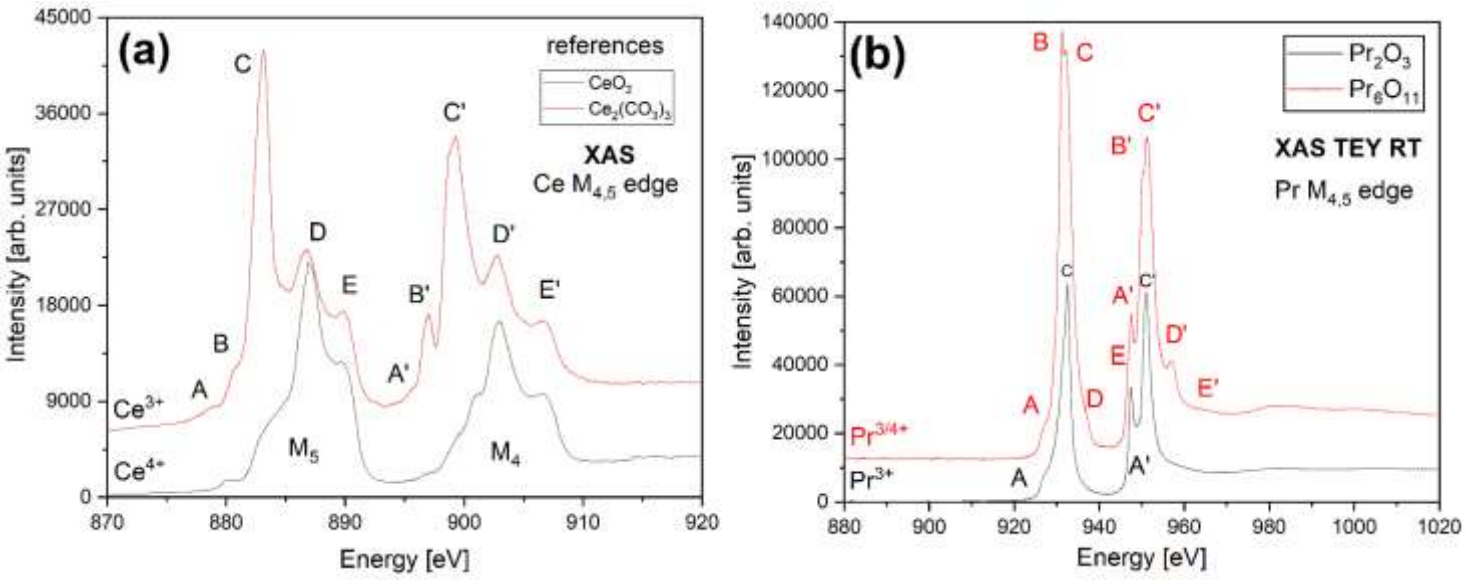

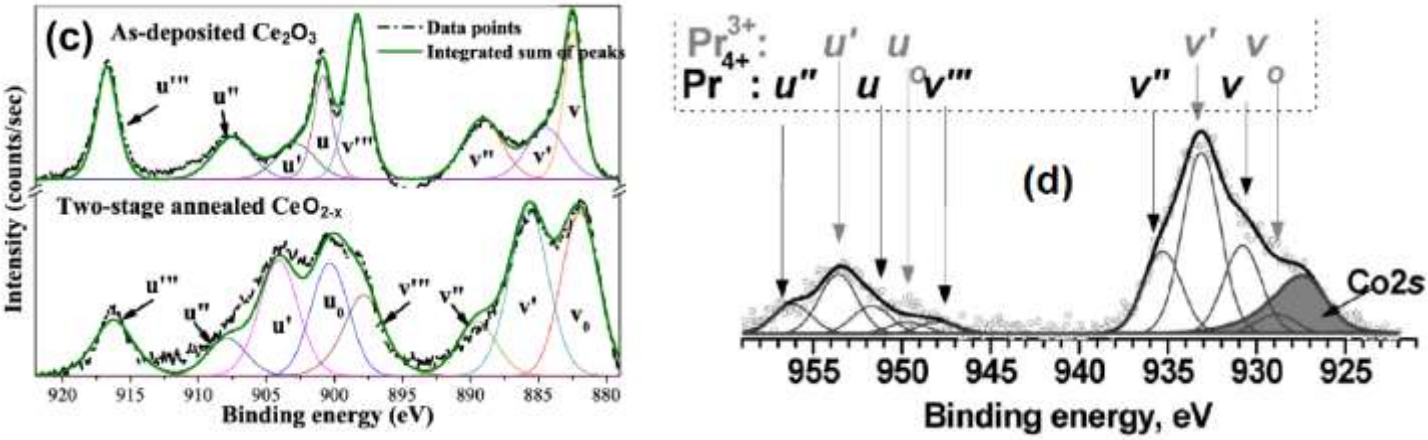

Figure A10 Reference XAS spectra taken at RT and ultra-high vacuum off 99.9%+ pure substrates used for synthesis: (a) cerium and (b) praseodymium oxides confronted with respective literature data shown in graphs (c) and (d) below.[219,220]

Figure (c) was obtained from R. K. Nachimuthu et al. research entitled '*Investigation of Cerium-Substituted Europium Iron garnets Deposited by Biased Target Ion Beam Deposition',* IEEE Transactions on Magnetics, 2014, **50** (12), pp. 1-7 copyrighted and licensed by IEEE. Figure (d) is borrowed from article E. Y. Konysheva and M. V. Kuznetsov '*Fluctuation of surface composition and chemical states at the hetero-interface in composites comprised of a phase with perovskite structure and a phase related to the Ruddlesden–Popper family of compounds*', RSC Adv. 2013, **3** (33), pp. 14114-14122, copyrighted and licensed by the Royal Society of Chemistry.

Table A3 Factor group analysis for all alternative-yet-relevant space groups assigned to all discussed tungstates.

Material (SG)	Ion	Wyckoff Positions	Point Symmetry	Red. Representation
BCW **BPW**	A^{2+} (Ba)	2c	C_3	$A_g+A_u+{}^1E_u+{}^2E_u+{}^1E_g+{}^2E_g$
	$B^{3+/4+}$ (Ce)	1a	C_{3i}	$A_u+{}^1E_u+{}^2E_u$
R*-3** ***(C_{3i})	$B'^{5+/4+}$ (W)	1b	C_{3i}	$A_u+{}^1E_u+{}^2E_u$
	O^{2-}	6f	C_1	$3A_g+3A_u+3{}^1E_u+3{}^2E_u+3{}^1E_g+3{}^2E_g$
$\Gamma_{TOTAL} = 4A_g+6A_u+6{}^1E_u+6{}^2E_u+4{}^1E_g+4{}^2E_g$; $\Gamma_{ACUSTIC} = A_u+{}^1E_u+{}^2E_u$; $\Gamma_{IR} = 5A_u+5{}^1E_u+5{}^2E_u$; $\Gamma_{Raman} = 4A_g+4{}^1E_g+4{}^2E_g$				
SCWO	$B^{6/5+}$ (W)	4a, 4b, 24d	D_{3d}, C_{2h}	$5T_{1u}$
	$B'^{3/4+}$ (Ce)	24e, 32f	C_{2v}, C_3	$2A_{1g}+2E_g+3T_{2g}+4T_{1u}$
Fm-3m ***(O_h)***	A^{2+} (Sr)	24e, 32f	C_{2v}, C_3	$2A_{1g}+2E_g+3T_{2g}+4T_{1u}$
	O^{2-}	24e, 48g, 48h	C_{2v}, C_2, C_{1h}	$3A_{1g}+4E_g+6T_{2g}+8T_{1u}$
$\Gamma_{TOTAL} = 5A_{1g}+8E_g+12T_{2g}+21T_{1u}$; $\Gamma_{ACUSTIC} = T_{1u}$; $\Gamma_{IR} = 20T_{1u}$; $\Gamma_{Raman} = 5A_{1g}+8E_g+12T_{2g}$				
CCWO	$B^{6/5+}$ (W)	2a, 6b	C_1, C_3	$4A_1+8E$
	$B'^{3/4+}$ (Ce)	2a, 6b	C_1, C_3	$4A_1+8E$
R3c ***(C_{3v})***	A^{2+} (Ca)	2a, 6b	C_1, C_3	$4A_1+8E$
	O^{2-}	6b	C_1	$3A_1+5E$
$\Gamma_{TOTAL} = 15A_1+29E$; $\Gamma_{ACUSTIC} = A_1+E$; $\Gamma_{IR} = 7A_1+14E$; $\Gamma_{Raman} = 7A_1+14E$				

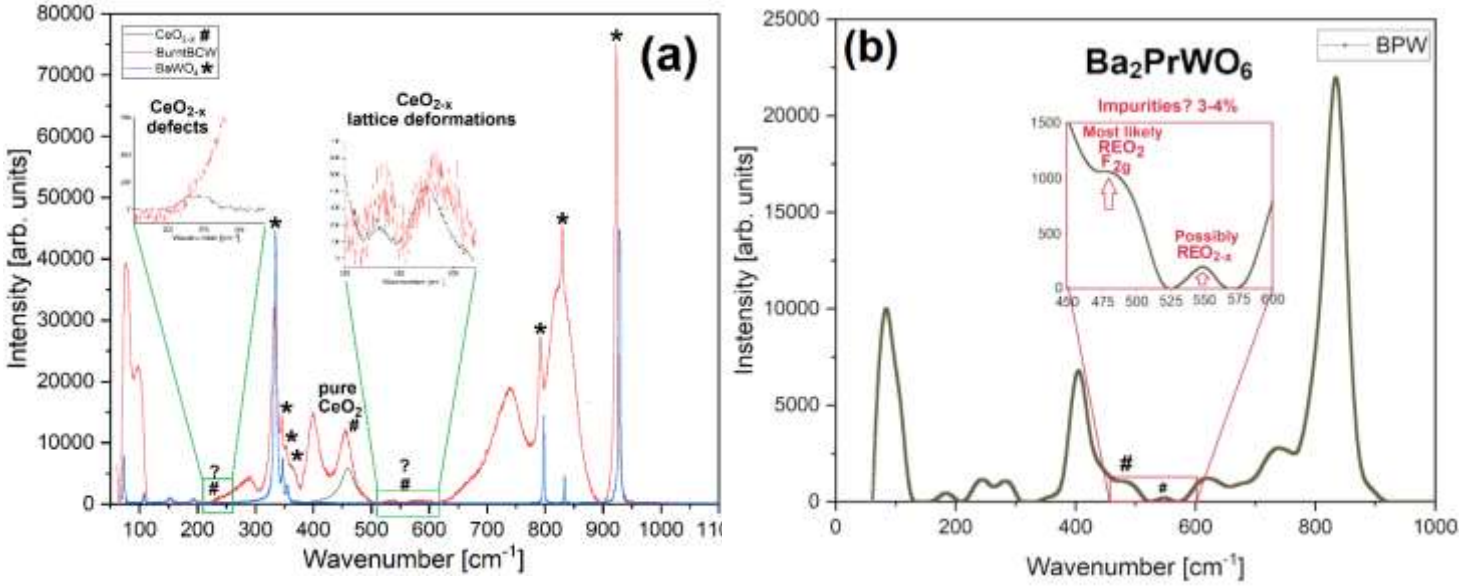

Figure A11 Raman spectra showcasing popular impurity referrals such as CeO_{2-x} (black) or $BaWO_4$ (blue lines) that can also transpire in worse or laser-burnt (a) BCW (red line) and (b) BPW batches analogically showcasing PrO_{2-x}. Visible peaks are pinpointed via hashtags (REO_{2-x}) and asterisks ($BaWO_4$) to guide the eye. One can also associate the former group with defective transverse $RE^{3/4+}O_x$ modes, which have similar scattering energy.

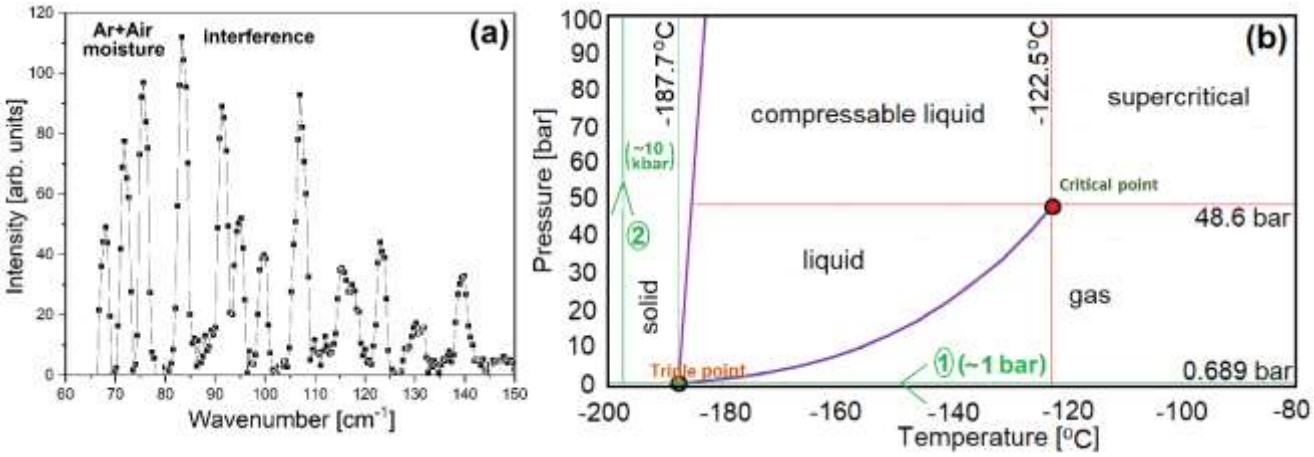

Figure A12 (a) Minor, static scattering interference registered at the beginning of each HP Raman scattering spectra with and without the sample in Ar-filled DAC and (b) a p(T) phase diagram of Argon featuring a way of preparing solid PTM after 1) DAC initial cooling and then 2) compressing it via hydraulic drive.

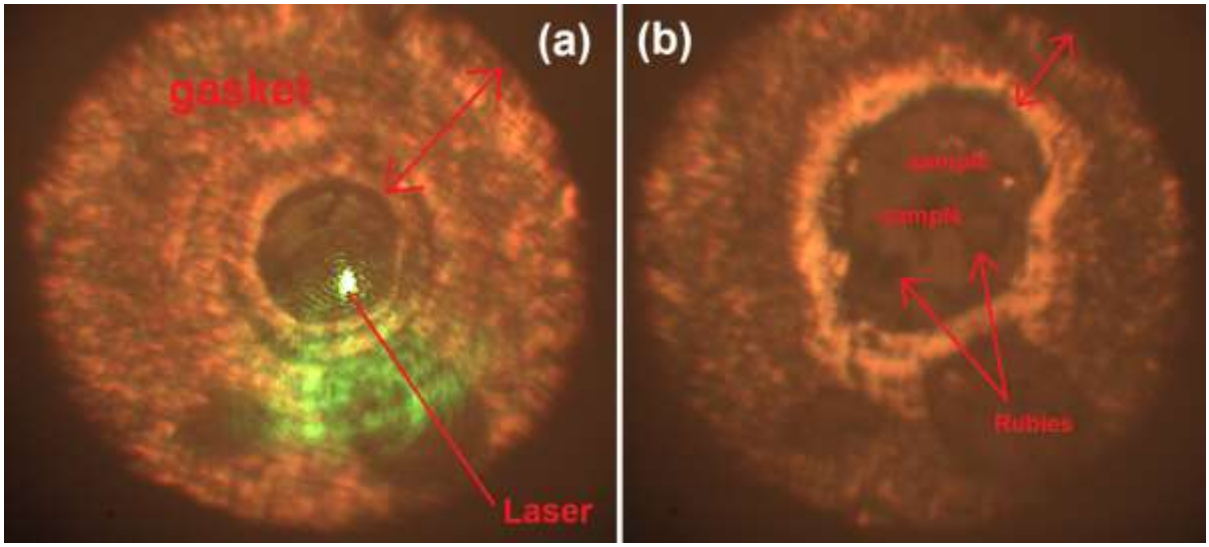

Figure A13 Digital microscopic photographs of DAC gasket filled with Ar PTM, referential (PL) pressure-gauging ruby, and powder from BCW at (a) the beginning and (b) end of the HP experiment (near its breaking point) featuring deformations and typically encountered laser size spot.

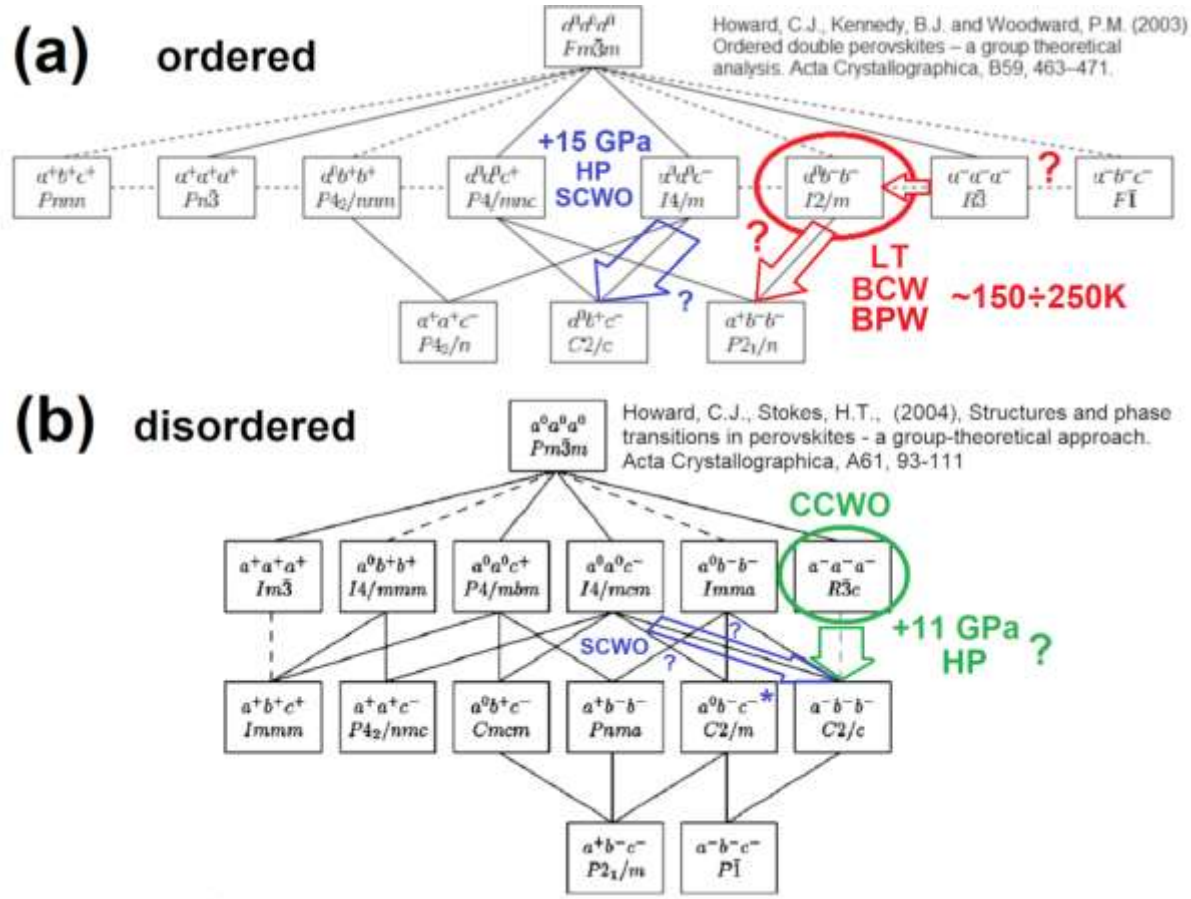

Figure A14 Particular group–subgroup relations associated with interchangeable $A_2BB'X_6$ tilt systems in (a) ordered (like BCW or BPW - red) and (b) disordered, perovskites-like materials (ilmenite CCWO - green) evaluated by Howard et al. between 1998-2005 using Landau DFT calculations.[71,72] Continuous black lines are second- and dashed first-order (Landau-Ginzburg) phase transitions. Possible sample placement has also been established artificially amongst possible SG. SCWO, as a disputable intermediate compound bearing similarities of both groups, is placed on both graphs (blue) despite not having any of the precisely mentioned SG ($I4_1/a$). Both graphics were partially adapted and reprinted with permissions from Howard C. J.; Kennedy B. J.; Woodward P. M. *Ordered double perovskites – a group-theoretical analysis*, Acta Crystallogr. **2003**, B59, pp. 463-471, and Howard C. J.; Stokes H. T. *Structures and phase transitions in perovskites – a group-theoretical approach*, Acta Crystallogr. **2004**, A61, pp. 93-111. They are copyrighted and licensed by IUCr Journals Publisher via Acta Crystallographica B journal after 2003 & 2004, respectively.

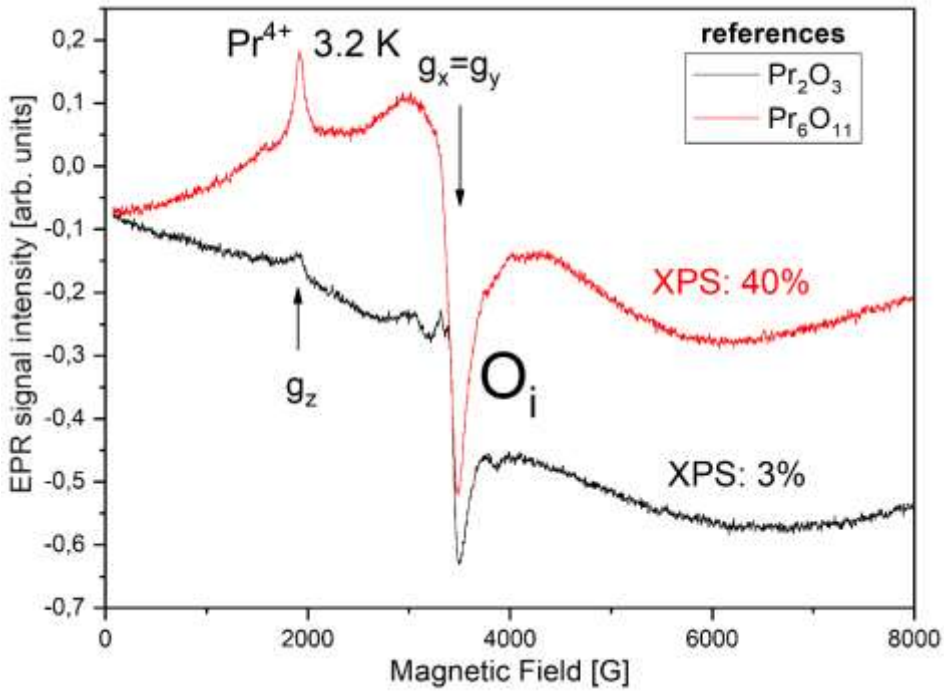

Figure A15 LT EPR spectra of Pr_6O_{11} & Pr_2O_3 substrates used as references for SSR synthesis showcasing the nature of both applied oxides. A weak Pr^{4+} response joins the place where O_i intrusions appear. It should emerge much more potent in perpendicular magnetic fields if there were no antiferromagnetic transitions and high enough concentration.

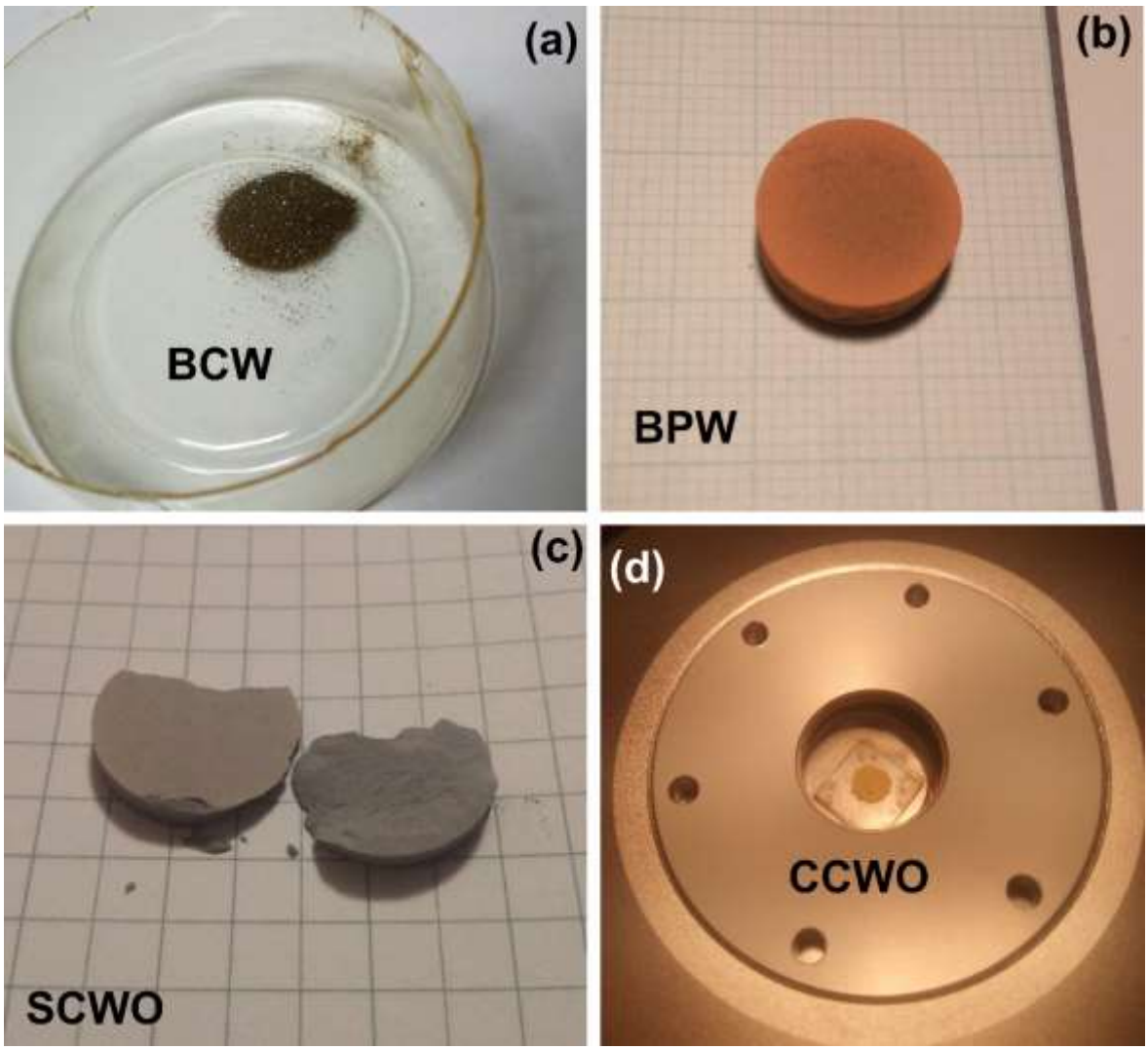

Figure A16 Macro photographs of all four investigated substances: (a) Ba_2CeWO_6, (b) Ba_2PrWO_6 double perovskites, and (c) $Sr_9Ce_2W_4O_{24}$ with (d) $Ca_3Ce_2W_2O_{12}$ derivatives after decomposition in the air at HT (above II stage of decomposition mentioned in *Figure 35*).

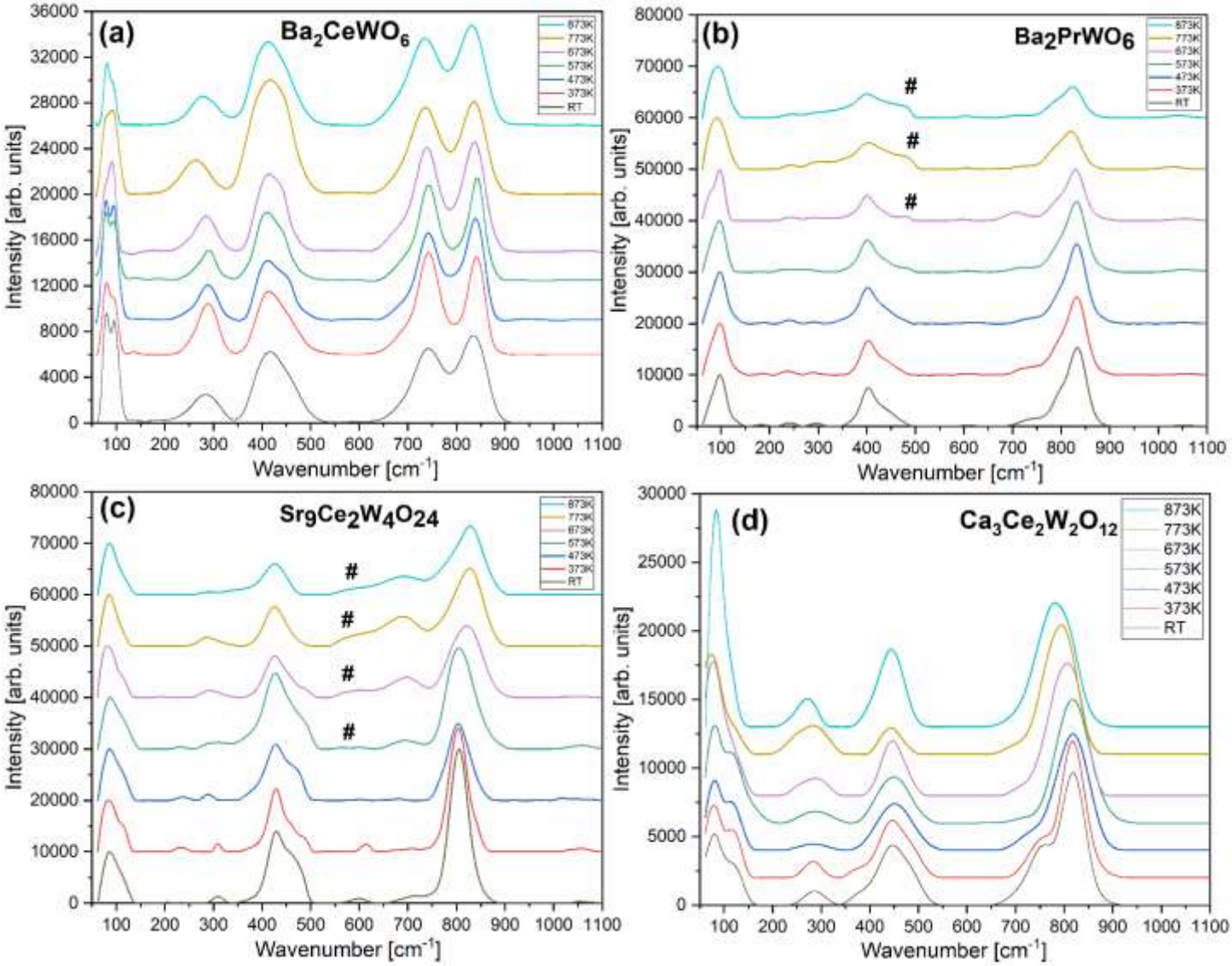

Figure A17 Raman spectra for all investigated compounds collected in the function of heating from room temperature up to 873K in a protective, inert N_2 atmosphere showing little to no change while subtle blue-shifts occur. Hashtags mark noticeable intensity changes in already denoted peaks within mostly defective materials, probably related to the internally stored O_i slowly creeping/integrating into the structures, creating many RE-O defects.

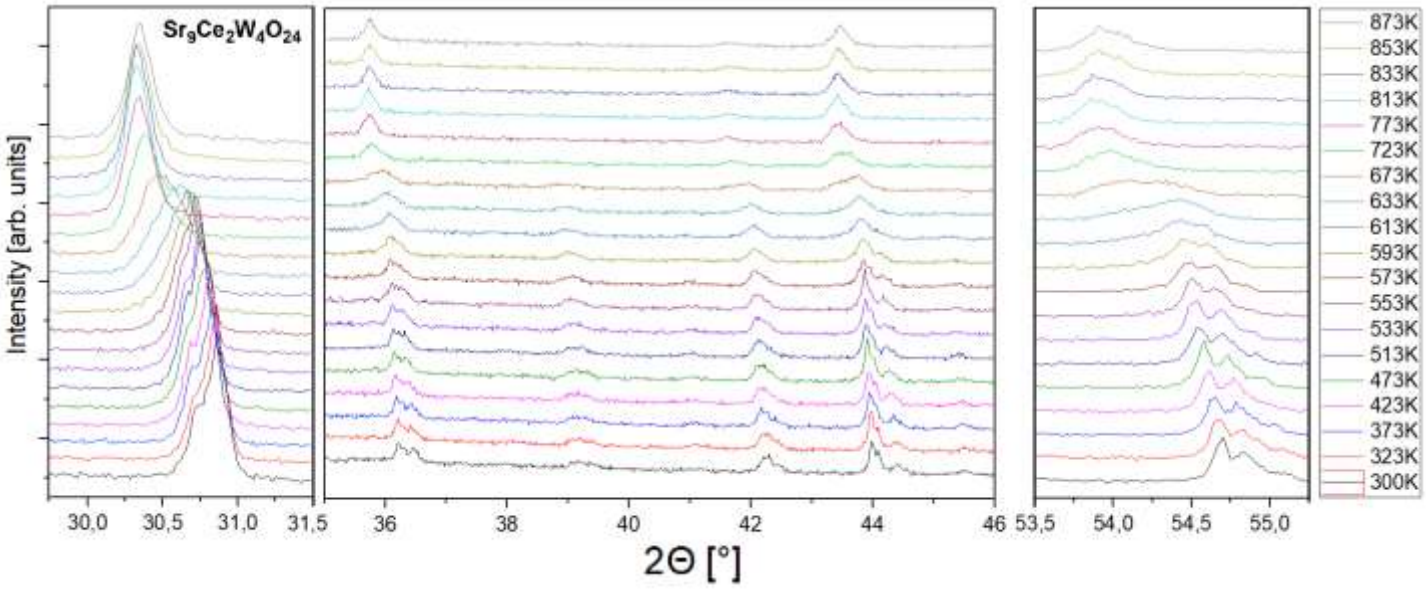

Figure A18 Close-ups on HT XRD powder diffractograms of SCWO quaternary perovskite done in the air. They feature some of the most prominent (decomposition) changes highlighted in densely packed *Figure 39d.*

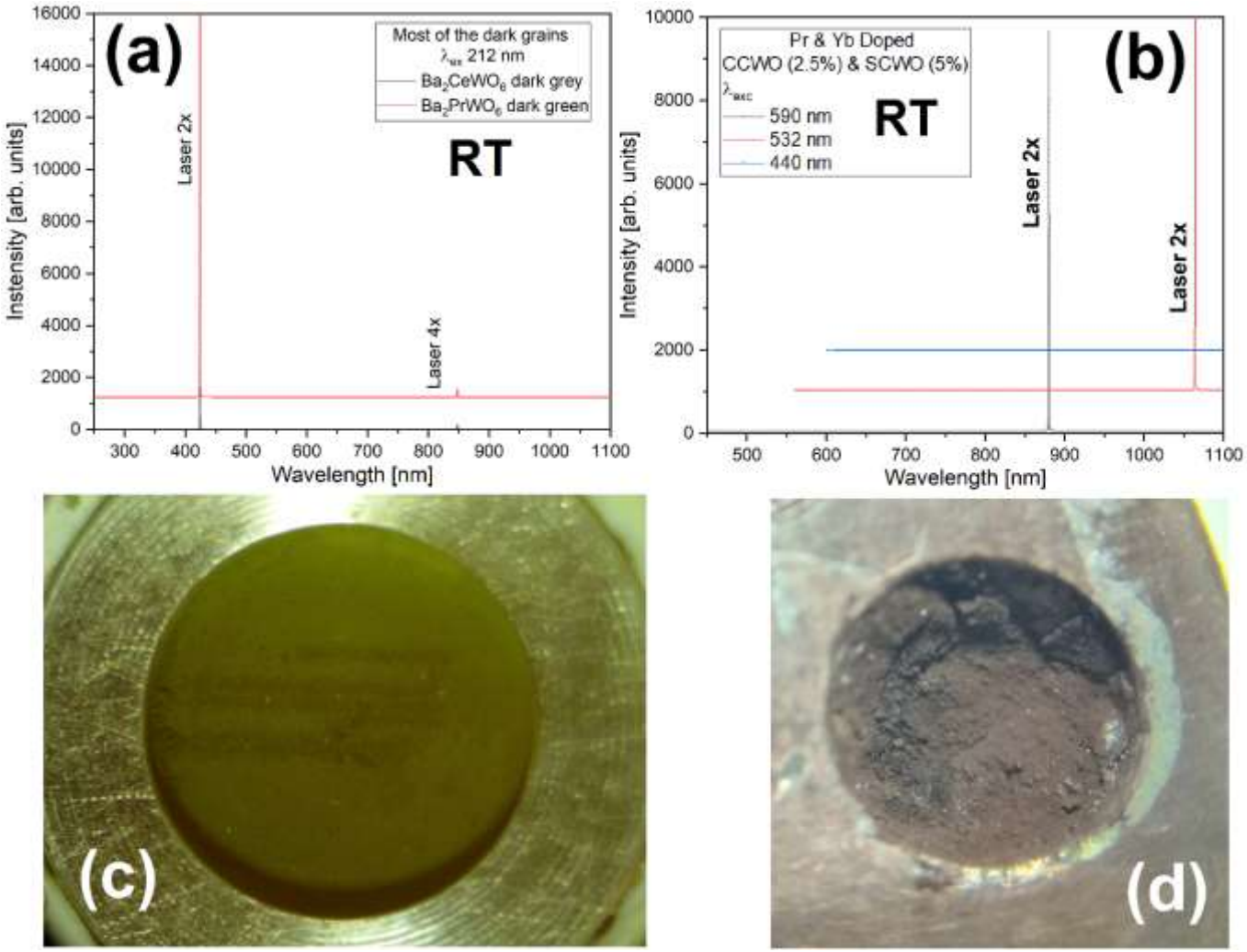

Figure A19 Inconsistent luminescence behavior of both: (a) undoped barium double perovskite materials, (b) doped tungstate derivatives given various excitation energies around possible absorption lines for typical RE^{3+} ions. Most samples tend to be physically drilled if exposed briefly to laser illumination (c) or respectively burned (d) due to disadvantageous dark coloring when exposed for a long time without any inert, protective atmospheres.

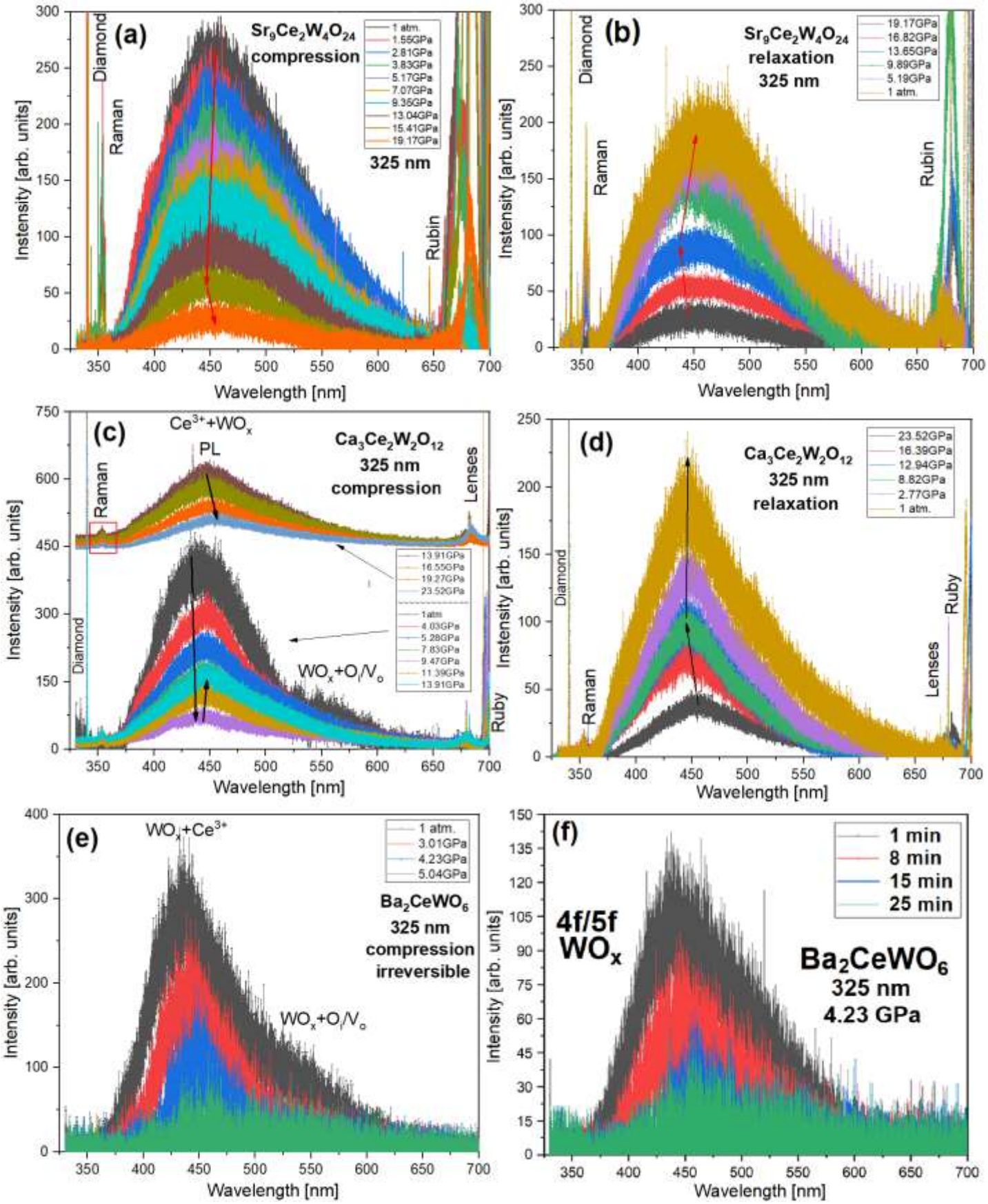

Figure A20 Alternating HP PL spectra of all undoped cerium tungstates presented in compression-decompression cycles respectively under NUV, 325 nm excitation: (a) & (b) for SCWO, (c) & (d) regarding CCWO, and irreversibly diminishing BCW light in (e) where it seems to be rather time- than pressure-resolved (f).

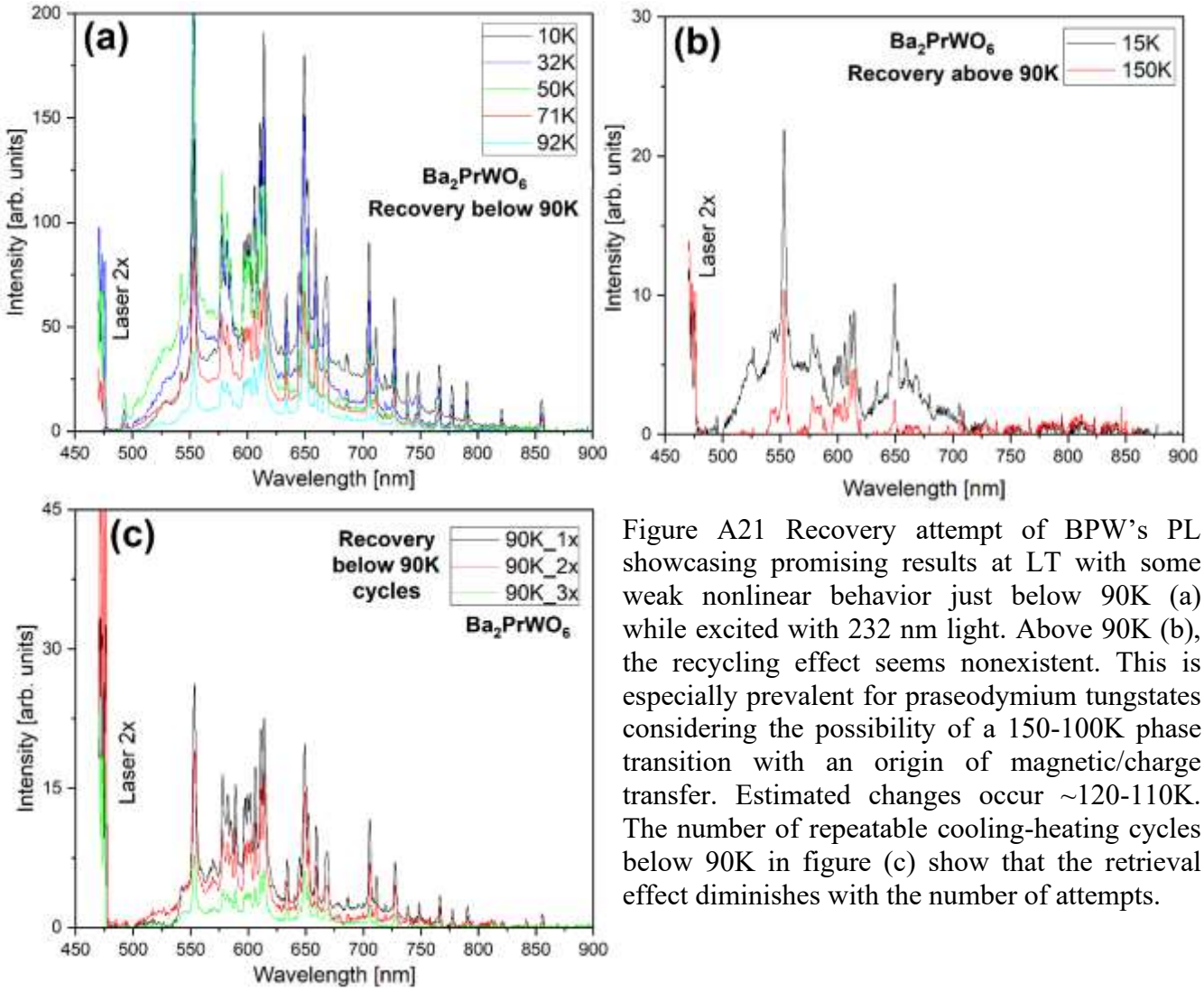

Figure A21 Recovery attempt of BPW's PL showcasing promising results at LT with some weak nonlinear behavior just below 90K (a) while excited with 232 nm light. Above 90K (b), the recycling effect seems nonexistent. This is especially prevalent for praseodymium tungstates considering the possibility of a 150-100K phase transition with an origin of magnetic/charge transfer. Estimated changes occur ~120-110K. The number of repeatable cooling-heating cycles below 90K in figure (c) show that the retrieval effect diminishes with the number of attempts.

Equations A1:

$$\frac{dN^*}{dt} = f(N - N^*) - (p + r(T))N^*$$

$$N = const.$$

$$\frac{dN}{dt} = -f(N - N^*) + (p + r(T))N^*$$

$$N^*(T) = \frac{fN}{(f + p + r(T))} \qquad N^*(T = 0) = \frac{fN}{(f + p)} = \frac{I_0}{p}$$

$$\frac{I_0}{I} - 1 = r(T)/(f + p)$$

where N - is the concentration of (e.g., Pr^{3+}); N* - occupation of the excited state (e.g., $^1S_0$); f – is excitation density; 'p' and 'r' are the probabilities of radiative and non-radiative recombination, respectively; In this case, dynamic equilibrium is established quickly (in the order of milliseconds or less), which means that with constant excitation $\frac{dN^*}{dt} = \frac{dN}{dt} = 0$

Equations A2:

$$\frac{dN^*}{dt} = f(N_0 - N^* - n) - (p + r)N^* - \beta N^* \exp\left(-{}^{E}/_{kT}\right)$$

$$\frac{dn}{dt} = \beta N^* exp\left(-{}^{E}/_{kT}\right) - wn^2$$

$$n = \sqrt{\frac{\beta}{w} N^* exp\left(-\frac{E}{kT}\right)} \qquad f(N_0 - n) = N^*\left[f + p + r + \beta exp\left(-\frac{E}{kT}\right)\right]$$

$$N^*(T) = \frac{N_0}{a} - \frac{\sqrt{(\beta exp(-E/kT)/w)^2 + 4N_0 a\beta exp(-E/kT)/w}}{2a^2}$$

$$a = \left(1 + \frac{p + r + \beta exp(-E/kT)}{f}\right)$$

$$N^*(T = 0) = \frac{N_0}{a(T = 0)}$$

N* - concentration of ionized dopant, always equal to the concentration of electrons in the n band; N_0 - total dopant concentration (= const.); $N_{(t,T)}+n_{(t,T)} = N_0$; β - the probability of ionization (contains the density of states in the conduction band); w – a cross-section of e^- capture.

Equations A3:

$$\frac{dN^*}{dt} = f(N - N^*) - (p + r)N^* - \beta N^* \exp\left(-{}^{E}/_{kT}\right)$$

$$\frac{dn}{dt} = \beta N^* exp\left(-{}^{E}/_{kT}\right) - w_M n(M_0 - M^-) - wn(N_0 - N)$$

$$\frac{dN}{dt} = -f(N - N^*) + (p + r)N^* + wn(N_0 - N)$$

$$\frac{dM^-}{dt} = w_M n(M_0 - M^-)$$

According to these equations, equilibrium will be reached after time 't' when N(t) = n(t) = 0 and $M^-(t)$ = N(t=0). This is a consequence of no trap ionization. It takes roughly 15 minutes at room temperature, as showcased in *Figures 50 & 55*. At low temperatures, it would be much longer. By measuring the luminescence, we measure the kinetics of Pr^{3+} decay, or rather its beginning, because the measurement lasts only about a minute.

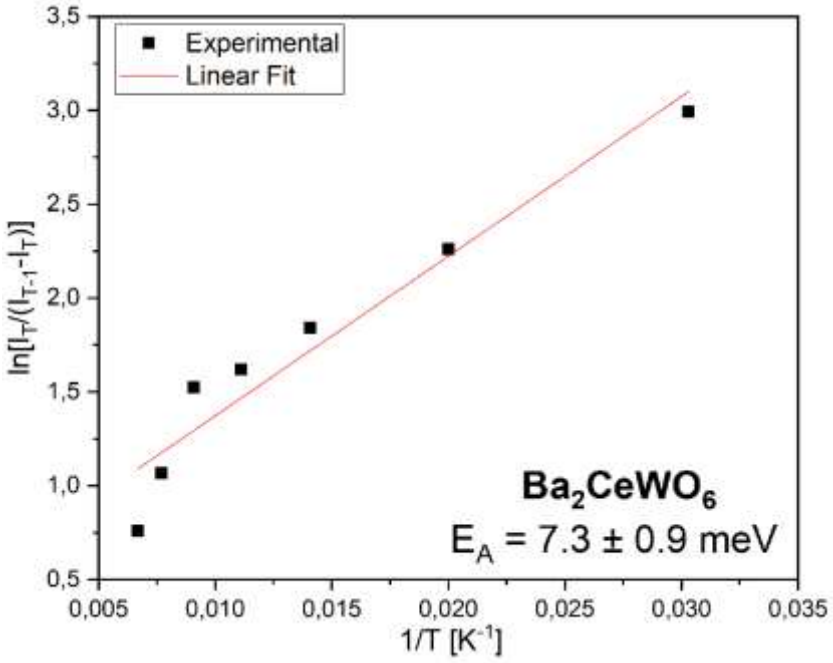

Figure A22 Activation energy estimate done for undoped BCW based on WO_x bands & modified Arrhenius equation. Measurements were done in the same pumped, helium-filled cryostat where no noticeable PL-related decomposition changes were observed under λ_{exc} = 232 nm.

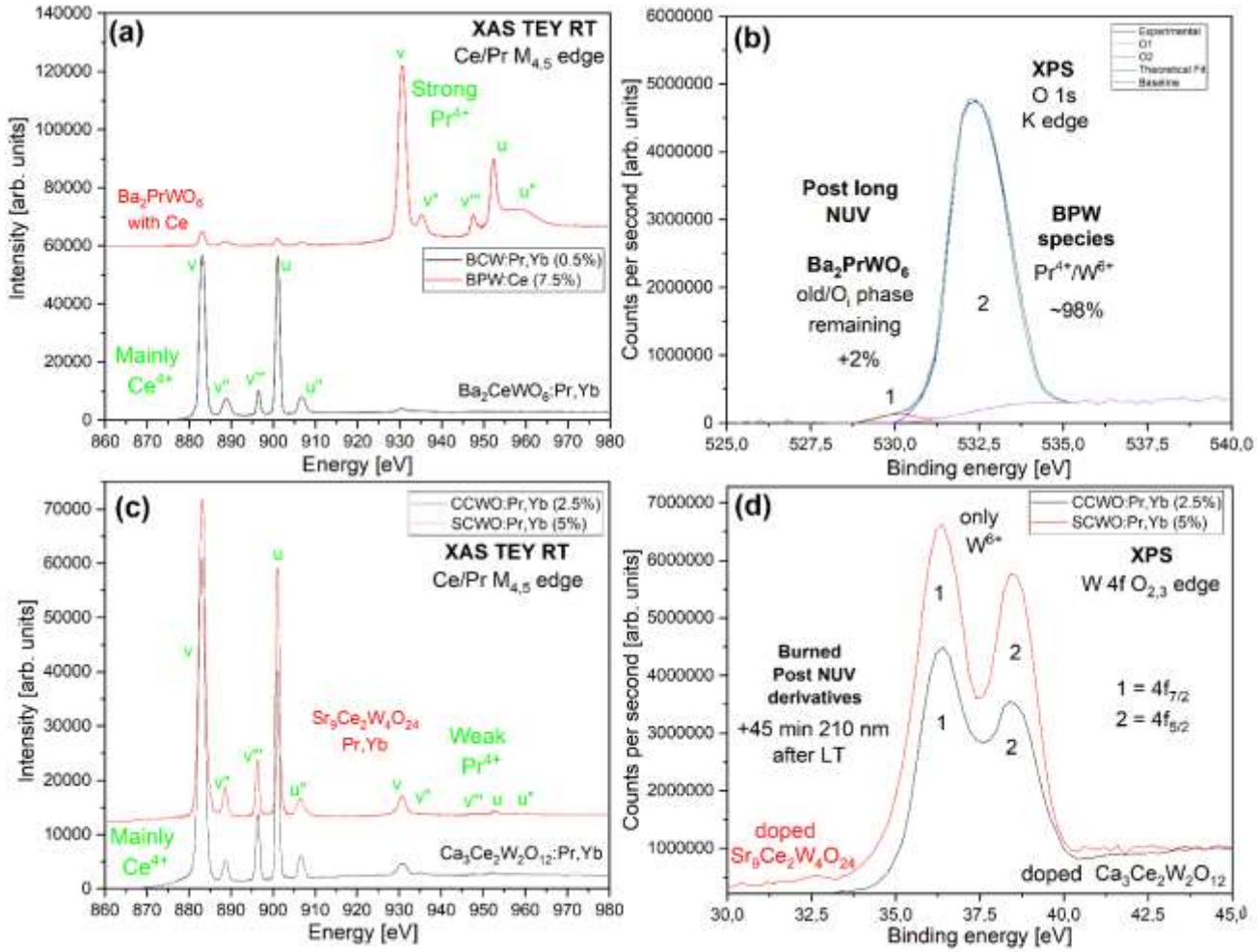

Figure A23 Supplementary, structural X-ray investigation of crucial atom sites after intense UV exposure featuring irreversible decomposition/oxidation signs in both doped double perovskites via complementary (a) Cerium, and (b) BCW's oxygen edges. Implanted derivatives also change with time after prolonged illumination (but through visual scorching), which fatally influences their PL capabilities and composition as seen on (c) RE & (d) W B-sites sells in comparison to Figures 19, 20 & 25. Intense excitation is needed to receive any response but with the most cautious approach.

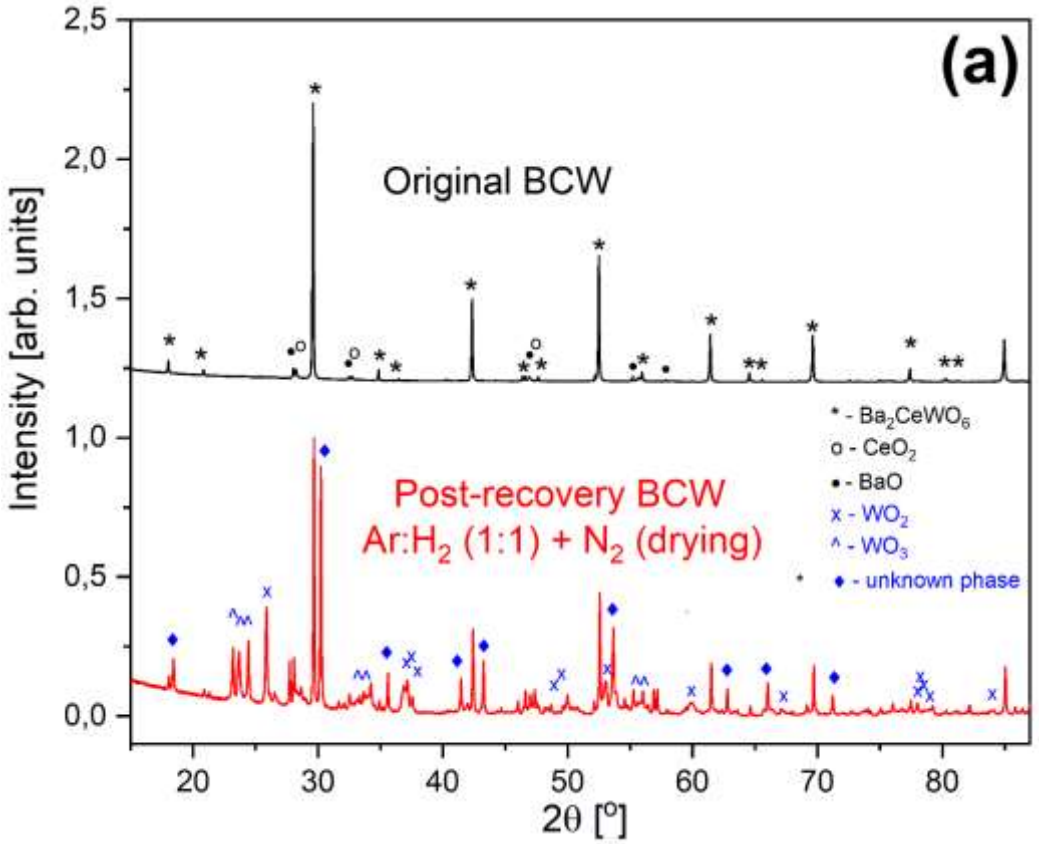

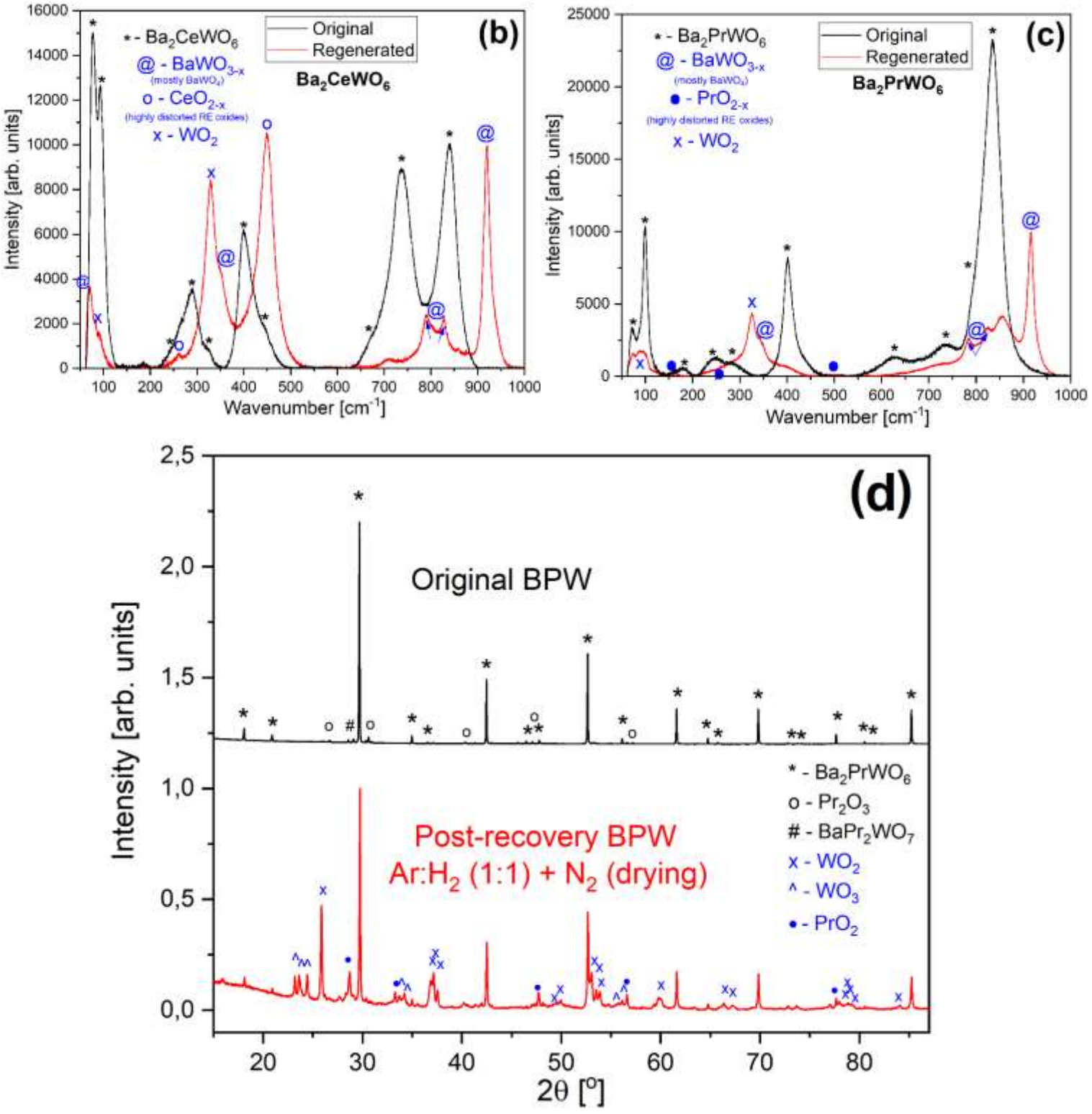

Figure A24 Ambient powder XRD diffraction patterns and complimentary Raman spectra of original (black) and theoretically regenerated (red) BCW (a,b) & BPW (c,d) barium double perovskites presented consecutively after HT SSR treatment in Ar:H_2 1:1 and N_2 drying. Latter samples feature partial decomposition of the main matrix and separation of the primary B/B' (RE/W)O_x components with eventual oxidation (highlighted in insets as blue), deeming the materials unrecoverable post deep-UV exposure. The unknown phase marked with a diamond (♦) in BCW figure (a) seems to be the main phase with smaller lattice constants (presumably shrunk due to missing, crucial, B-site components). No other reliable match regarding that last issue could be found in the crystallographic database.

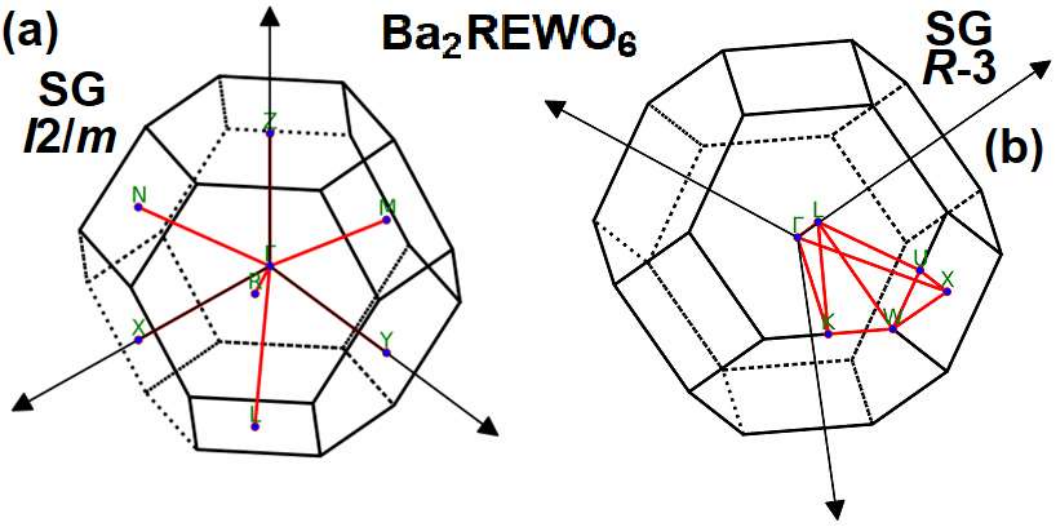

Figure A25 Depiction of Brillouin zone's high symmetry points referenced in Wannier/Tight binding equations for band gap calculations provided for barium RE tungstates' small unit cells in *Figures 59* and *A26*. Figure (a) showcases *I*2/*m* SG, and (b) alternate *R*-3.

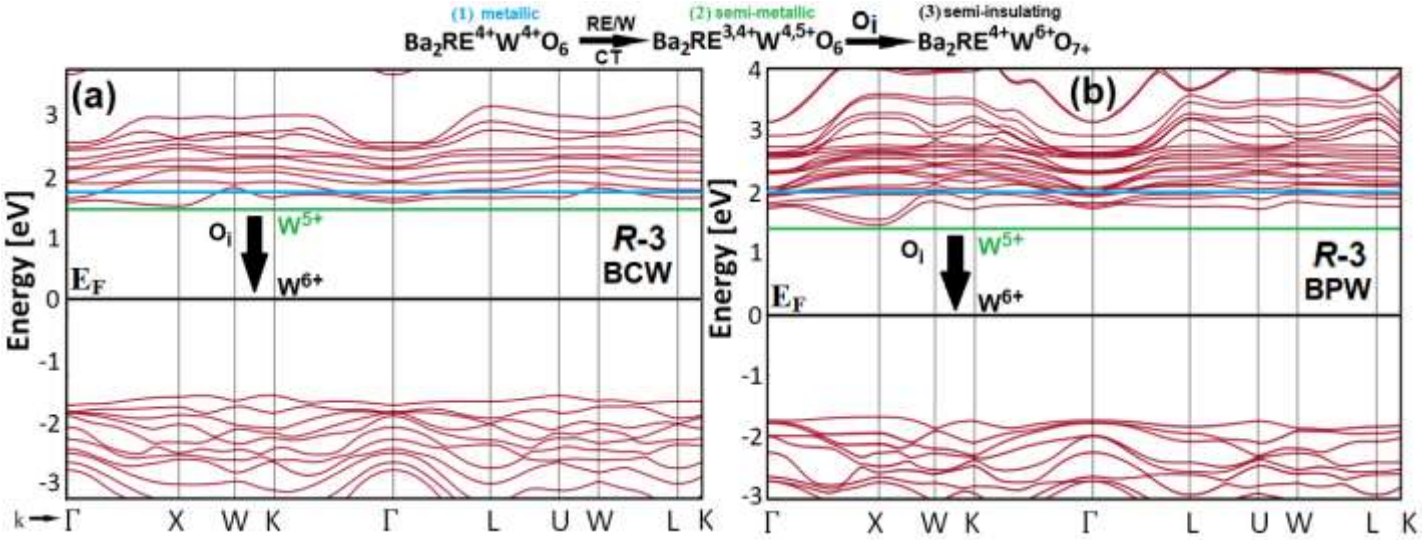

Figure A26 Tight-binding bandwidth estimations provided by VASP software using Wannier equations for both barium double perovskites (a) BCW & (b) BPW hosting alternate *R*-3 unit cells influenced by the O_i presence. As one can see, the evolving charge of W ions still does not account for such a broad emission which would require at least a 2× bigger gap.

\

ELSEVIER LICENSE
TERMS AND CONDITIONS

Apr 15, 2022

This Agreement between Damian Wlodarczyk ("You") and Elsevier ("Elsevier") consists of your license details and the terms and conditions provided by Elsevier and Copyright Clearance Center.

License Number	5290430532912
License date	Apr 15, 2022
Licensed Content Publisher	Elsevier
Licensed Content Publication	Progress in Solid State Chemistry
Licensed Content Title	A 2 B′B″O6 perovskites: A review
Licensed Content Author	Sami Vasala,Maarit Karppinen
Licensed Content Date	May 1, 2015
Licensed Content Volume	43
Licensed Content Issue	1-2
Licensed Content Pages	36
Start Page	1

Type of Use	reuse in a thesis/dissertation
Portion End Page	36
Format	figures/tables/illustrations
Number of figures/tables/illustrations	10
	both print and electronic
Title Are you the author of this Elsevier article?	No
Will you be translating?	No
	Synthesis and physicochemical properties of novel, tungsten-oxide double perovskites and their derivatives doped with selected rare-earth ions.
Institution name	Institute of Physics, Polish Academy of Science
Expected presentation date	Feb 2023
Order reference number	dis07021990
Portions	Figures 1, 2, 3, 6, 9, 10 & 11, Tables 2, 3 & 4
	Damian Wlodarczyk Al. Lotników 32/46
Requestor Location	
	Damian Wlodarczyk

Al. Lotników 32/46

Warsaw, Masovia 02-668
Poland
Attn: Damian Wlodarczyk

Total

Publisher Tax ID GB 494 6272 12

Billing Type Invoice

Billing Address

Warsaw, Poland 02-668
Attn: Damian Wlodarczyk

0.00 EUR

Terms and Conditions

Thesis/Dissertation: If your license is for use in a thesis/dissertation your thesis may be submitted to your institution in either print or electronic form. Should your thesis be published commercially, please reapply for permission. These requirements include permission for the Library and Archives of Canada to supply single copies, on demand, of the complete thesis and include permission for Proquest/UMI to supply single copies, on demand, of the complete thesis. Should your thesis be published commercially, please reapply for permission. Theses and dissertations which contain embedded PJAs as part of the formal submission can be posted publicly by the awarding institution with DOI links back to the formal publications on ScienceDirect.

ELSEVIER LICENSE
TERMS AND CONDITIONS
Dec 03, 2022

This Agreement between Damian Wlodarczyk ("You") and Elsevier ("Elsevier") consists of your license details and the terms and conditions provided by Elsevier and Copyright Clearance Center.

License Number	5441491172274
License date	Dec 03, 2022
Licensed Content Publisher	Elsevier
Licensed Content Publication	Nano Energy
Licensed Content Title	Dion-Jacobson and Ruddlesden-Popper double-phase 2D perovskites for solar cells
Licensed Content Author	Ping Fu,Yang Liu,Shuwen Yu,Heng Yin,Bowen Yang,Sajjad Ahmad,Xin Guo,Can Li
Licensed Content Date	Oct 1, 2021
Licensed Content Volume	88
Licensed Content Issue	n/a
Licensed Content Pages	1
Start Page	106249
End Page	0
Type of Use	reuse in a thesis/dissertation
Portion	figures/tables/illustrations
Number of figures/tables/illustrations	1
Format	both print and electronic
Are you the author of this Elsevier article?	No
Will you be translating?	No
Title	Synthesis and physicochemical properties of novel, tungsten-oxide double perovskites and their derivatives doped with selected rare-earth ions.
Institution name	Institute of Physics, Polish Academy of Science
Expected presentation date	Feb 2023
Order reference number	DwRefDys1
Portions	Graphical Abstract
Requestor Location	Damian Wlodarczyk Al. Lotników 32/46 Warsaw, Masovia 02-668 Poland

	Attn: Damian Wlodarczyk
Publisher Tax ID	GB 494 6272 12
Total	0.00 EUR
Terms and Conditions	

Thesis/Dissertation: If your license is for use in a thesis/dissertation, your thesis may be submitted to your institution in either print or electronic form. Should your thesis be published commercially, please reapply for permission. These requirements include permission for the Library and Archives of Canada to supply single copies, on demand, of the complete thesis and include permission for Proquest/UMI to supply single copies, on demand, of the complete thesis. Should your thesis be published commercially, please reapply for permission. Theses and dissertations which contain embedded PJAs as part of the formal submission can be posted publicly by the awarding institution with DOI links back to the formal publications on ScienceDirect.

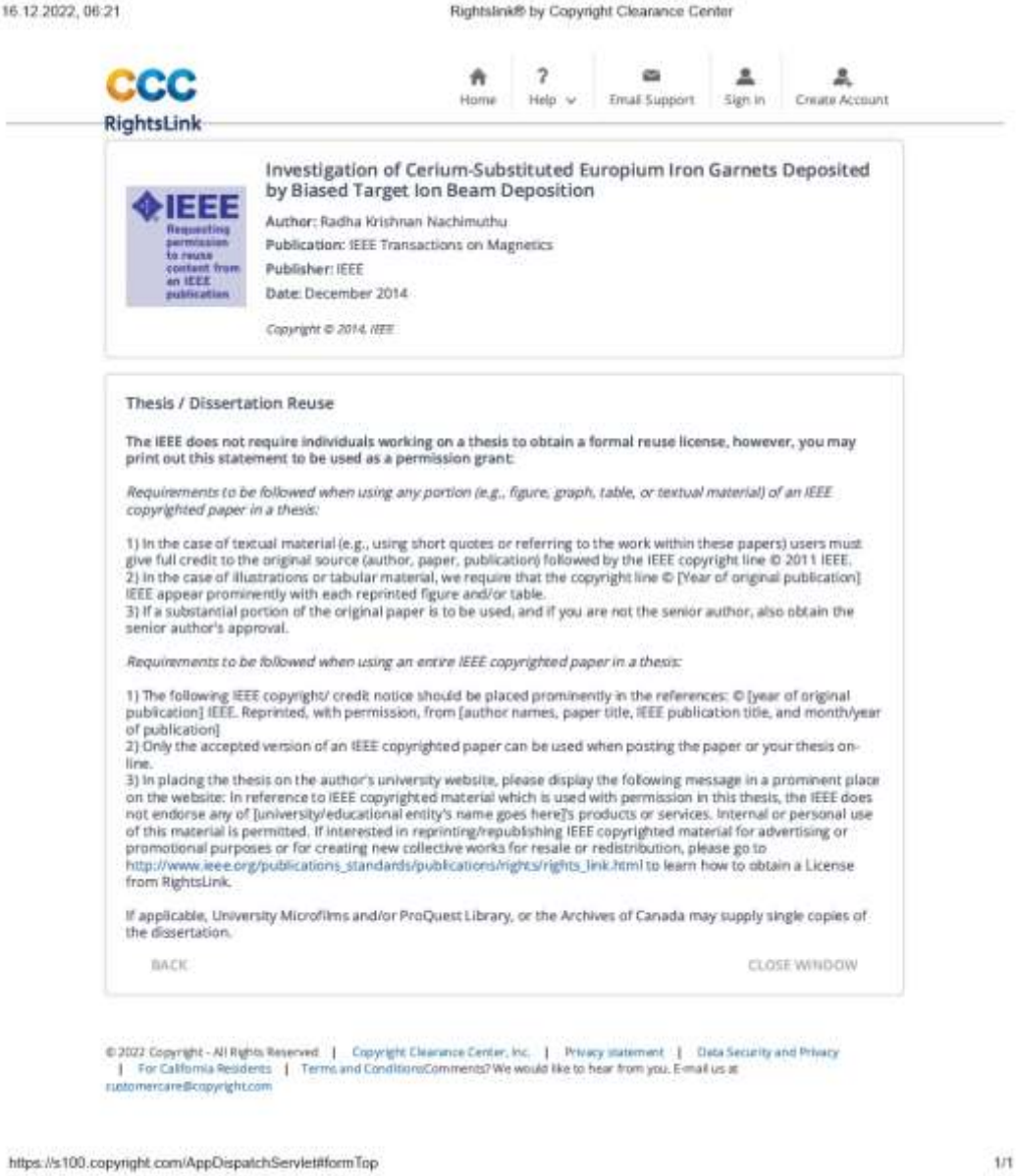

CCC Marketplace

Order Date	16-Dec-2022	Type of Use	Republish in a thesis/dissertation
Order License ID	1301381-1		
ISSN	2046-2069	Publisher	RSC Publishing
		Portion	Image/photo/illustration

LICENSED CONTENT

Publication Title	RSC advances	Publication Type	e-Journal
Article Title	Fluctuation of surface composition and chemical states at the hetero-interface in composites comprised of a phase with perovskite structure and a phase related to the Ruddlesden–Popper family of compounds	Start Page	14114
		Issue	33
		Volume	3
		URL	http://pubs.rsc.org/en/Journals/JournalIssues/RA
Date	01/01/2011		
Language	English		
Country	United Kingdom of Great Britain and Northern Ireland		
Rightsholder	Royal Society of Chemistry		

REQUEST DETAILS

Portion Type	Image/photo/illustration	Distribution	Worldwide
Number of Images / Photos / Illustrations	1	Translation	Original language of publication
Format (select all that apply)	Print, Electronic	Copies for the Disabled?	No
		Minor Editing Privileges?	Yes
Who Will Republish the Content?	Academic institution	Incidental Promotional Use?	No
Duration of Use	Life of current edition	Currency	EUR
Lifetime Unit Quantity	Up to 499		
Rights Requested	Main product		

NEW WORK DETAILS

Title	Synthesis and physicochemical properties of novel, tungsten-oxide double perovskites and their derivatives doped with selected rare-earth ions.	Institution Name	Institute of Physics PAS
		Expected Presentation Date	2023-06-30
Instructor Name	Prof. Andrzej Suchocki		

ADDITIONAL DETAILS

Order Reference Number	Dysert1	The Requesting Person/Organization to Appear on the License	Damian Wlodarczyk

REUSE CONTENT DETAILS

Title, Description or Numeric Reference of the Portion(s)	Figure 7	Title of the Article/Chapter the Portion Is From	Fluctuation of surface composition and chemical states at the hetero-interface in composites comprised of a phase with perovskite structure and a phase related to the Ruddlesden–Popper family of compounds
Editor of Portion(s)	Konysheva, Elena Yu.; Kuznetsov, Michail V.		
Volume of Serial or Monograph	3		
Page or Page Range of Portion	14114	Author of Portion(s)	Konysheva, Elena Yu.; Kuznetsov, Michail V.
		Issue, if Republishing an Article From a Serial	33
		Publication Date of Portion	2013-07-30

IUCr Journals

Terms and conditions of use of the article titled

Ordered double perovskites - a group-theoretical analysis

[Howard *et al.* (2003). *Acta Cryst.* B**59**, 463-471
https://doi.org/10.1107/S0108768103010073]

Permission to reprint Figure 1 from the above article in PhD thesis Synthesis and physicochemical properties of novel, tungsten-oxide double perovskites and their derivatives doped with selected rare-earth ions in Institute of Physics PAS, Ave. Lotnikow 32/46, PL02668, Warsaw, Poland. is granted to

Damian Wlodarczyk

provided that the reused material is not subject to additional explicit statements of copyright or prior reproduction permission from other organizations or individuals, and is accompanied by a citation of the original article and a statement that the material was reproduced with permission of the International Union of Crystallography, according to the terms and conditions of use of material published by the International Union of Crystallography.

Peter Strickland
Executive Managing Editor, IUCr Journals

IUCr Journals

Terms and conditions of use of the article titled

Structures and phase transitions in perovskites - a group-theoretical approach

[Howard & Stokes (2005). *Acta Cryst.* A**61**, 93-111
https://doi.org/10.1107/S0108767304024493]

Permission to reprint Figure 9 from the above article in PhD thesis Synthesis and physicochemical properties of novel, tungsten-oxide double perovskites and their derivatives doped with selected rare-earth ions in Institute of Physics PAS, Ave. Lotnikow 32/46, PL02668, Warsaw, Poland is granted to

Damian Wlodarczyk

provided that the reused material is not subject to additional explicit statements of copyright or prior reproduction permission from other organizations or individuals, and is accompanied by a citation of the original article and a statement that the material was reproduced with permission of the International Union of Crystallography, according to the terms and conditions of use of material published by the International Union of Crystallography.

Peter Strickland
Executive Managing Editor, IUCr Journals

Dear Dr. Wlodarczyk,

Thank you for contacting ACS Publications Support.

The requested article

"Synthesis Attempt and Structural Studies of Novel A2CeWO6 Double Perovskites (A2+ = Ba, Ca) in and outside of Ambient Conditions", ACS Omega 2022, 7, 22, 18382–18408, Publication Date:May 23, 2022
https://doi.org/10.1021/acsomega.2c00669

is published under the license:
https://creativecommons.org/licenses/by/4.0/
[https://creativecommons.org/licenses/by/4.0/]
Please consult the publisher that is to re-publish the content, to confirm if the license can be applied for the reuse.
If you require a clarification regarding the license, please contact the Creative Commons directly at: https://creativecommons.org/about/contact
[https://creativecommons.org/about/contact]

I hope you will find this useful.

Please let me know if you need any further assistance.

Sincerely,

Vojin Vucic
ACS Publications Support
Customer Services & Information
Website: https://acs.service-now.com/acs [https://acs.service-now.com/acs]
Email: support@services.acs.org
Phone: 800-227-9919 | 202-872-(HELP) 4357

Case Info:

Case Number : CSCSI0113659

Created On: 01-15-2023 10:28:28 PM EST

ACS Statement for Open Access CC BY 4.0 publication is presented on another page.

Attribution 4.0 International (CC BY 4.0)

This is a human-readable summary of (and not a substitute for) the license. Disclaimer.

You are free to:

Share — copy and redistribute the material in any medium or format

Adapt — remix, transform, and build upon the material for any purpose, even commercially.

The licensor cannot revoke these freedoms as long as you follow the license terms.

Under the following terms:

Attribution — You must give appropriate credit, provide a link to the license, and indicate if changes were made. You may do so in any reasonable manner, but not in any way that suggests the licensor endorses you or your use.

No additional restrictions — You may not apply legal terms or technological measures that legally restrict others from doing anything the license permits.

Notices:

You do not have to comply with the license for elements of the material in the public domain or where your use is permitted by an applicable exception or limitation.

No warranties are given. The license may not give you all of the permissions necessary for your intended use. For example, other rights such as publicity, privacy, or moral rights may limit how you use the material.

ELSEVIER LICENSE
TERMS AND CONDITIONS
Mar 25, 2023

This Agreement between Damian Wlodarczyk ("You") and Elsevier ("Elsevier") consists of your license details and the terms and conditions provided by Elsevier and Copyright Clearance Center.

License Number	5516210660516
License date	Mar 25, 2023
Licensed Content Publisher	Elsevier
Licensed Content Publication	Optical Materials
Licensed Content Title	Near-infrared downconversion in Pr3+–Yb3+ codoped oxyfluoride glass ceramics
Licensed Content Author	Yumiko Katayama,Setsuhisa Tanabe
Licensed Content Date	Dec 1, 2010
Licensed Content Volume	33
Licensed Content Issue	2
Licensed Content Pages	4
Start Page	176
End Page	179
Type of Use	reuse in a thesis/dissertation
Portion	figures/tables/illustrations
Number of figures/tables/illustrations	1
Format	both print and electronic
Are you the author of this Elsevier article?	No
Will you be translating?	No
Title	Synthesis and physicochemical properties of novel, tungsten-oxide double perovskites and their derivatives doped with selected rare-earth ions.
Institution name	Institute of Physics, Polish Academy of Science
Expected presentation date	Dec 2023
Order reference number	dw070219901
Portions	Figure 1
Requestor Location	Damian Wlodarczyk Al. Lotników 32/46

	Warsaw, Masovia 02-668 Poland Attn: Damian Wlodarczyk
Publisher Tax ID	GB 494 6272 12
Total	0.00 EUR

~~~~~~

RE: Permission for thesis request

Od Optica Publishing Group Copyright
Do wlodar, Optica Publishing Group Copyright
Data Wt 17:40

Ogólne Nagłówki HTML

Dear Damian Wlodarczyk,

Thank you for contacting Optica Publishing Group.

For the use of figure 1 from Xiaofeng Liu, Yu Teng, Yixi Zhuang, Junhua Xie, Yanbo Qiao, Guoping Dong, Danping Chen, and Jianrong Qiu, "Broadband conversion of visible light to near-infrared emission by Ce3+, Yb3+-codoped yttrium aluminum garnet," Opt. Lett. 34, 3565-3567 (2009):

Optica Publishing Group considers your requested use of its copyrighted material to be Fair Use under United States Copyright Law. We request that a complete citation of the original material be included in any publication.

While your publisher should be able to provide additional guidance, we prefer the below citation formats:

For citations in figure captions:

[Reprinted/Adapted] with permission from [ref #] © The Optical Society. (Please include the full citation in your reference list)

For images without captions:

Journal Vol. #, first page (year published) An example: Biomed. Opt. Express 6, 793 (2015)

Please let me know if you have any questions.

Kind Regards,
Hannah Greenwood

Hannah Greenwood
April 4, 2023
Authorized Agent, Optica Publishing Group
[Optica_logo_transitional_vt_black_rgb - 400]
~~~~~~

Scientific CV

- Personal Data:

Name & Surname: Damian (Roman) Włodarczyk
Division: Physics and Technology of Wide Band Gap Semiconductors
Group: High-pressure spectroscopy, IP PAS (ON 4.1)
Telephone.: +48 664 264 575
E-mail: wlodar@ifpan.edu.pl, damwloda@gmail.com

- Education:

2016 – 2023 – Institute of Physics PAS – PhD in Solid State Physics,

2014 – 2016r. – Gdansk University of Technology, a Ph.D. student in Chemical Technology – Polymer Technology and Anticorrosion (discontinued),

2013 – 2014r.– Gdansk University of Technology, Master's degree in Materials Engineering - anticorrosion & individual course studies chosen from Chemical Technology (organics),

2009 – 2013r.- Gdansk University of Technology, an Engineering degree in Chemical Technology – anticorrosion specialty (inorganic & physical chemistry).

- Employment: (including internships)

04.2022 – 02.2023 – Institute of Physics PAS – Technician: Physicist & Chemist,

02.2020 – 02.2023 – Institute of Physics PAS – Head of Preludium 17 ST5 grant,

08.09 – 08.10.2014 - Jotun Polska S.A – Quality control department – inspector anticorrosion assistant,

18.07 – 22.07.2014 - Polfarma S.A.– R&D – Statistical, pharmaceutical analysis,

01.04.2014 – 26.06.2014 & 1.08.2015 – 1.10.2015 – PPH Kamix Sp. z o.o. Sp. k. – Main Technologist assistant – Department of Production & quality control,

05.08.2013 – 18.08.2013 - FUO Rumia Sp. z o.o.– – Main Technologist assistant – Department of production & quality control,

06.08 – 20.08.2012 – Soda Polska Ciech Sp. z o.o. – Main Technologist assistant – 3-person team – Department of water treatment, carbonization & calcination.

- Responsibility and current scientific duties:

- Minor repairs, maintenance work, and calibration of spectroscopic devices for pressure and low-temperature luminescence, Raman, and FTIR measurements. Assistance in servicing optics and electronics (software-wise),

- Waste disposal and ordering chemicals experimental instruments in the docusafe invoice system with offer searching for grant purposes,

- Synthesizing, shaping, cutting, and polishing of metallic samples immersed in epoxy resins & those made into single crystals. Distillation & demineralization of water,

- High-temperature Solid State synthesis of inorganic compounds in inert and air conditions (mainly powders). Synthesis of organic compounds in enclosed glass systems involving tube furnaces, transformers, heating mantles, and other typical laboratory glassware,

- Research on numerous materials such as: clinopyroxenes doped with Eu and Mn; YAM, YAP, and LuAP oxides; $BaWO_4$ single crystals; Spectral mapping of graphene and black phosphorus structures; the topological character of rhenium sulfide; Research on GaN crystals doped with C, Mn, and Fe; Study of amorphization in vanadium and phosphorus whitlockites; Low-temperature measurements of gadolinium gallium garnets with cerium as a low-temperature sensor; Thermal diffusion studies of elements such as Ti, Cu, Cr, Co, Fe in lithium niobate and YIG; Spectral analysis of AgGaGeSe8 used for electronic purposes; Studies of unique structures and their subtle phase transitions of first or second order like martensitic type $Y_4Al_2O_9$:Ce; Specialty in researching perovskites and double perovskites – created four novel ones: cerium (3) and praseodymium (1) tungstates hosting Ba, Sr, and Ca.

♦ Hobbies & additional appliances:

- Courses and training as an internal auditor of the management systems: in the PN-EN ISO 17025:2005 laboratory; OHSAS 18001:2007; and environmental systems 14001:2004. Training from the State's Pharmaceutical Inspectorate regarding supervision of psychoactive, psychotropic, and addictive substances,
- Participant in projects: (subcontractor) Baltic TRAM (Leader: Prof. Jabłońska, IPPAS); NCN OPUS 9 (Leader: Prof. Suchocki, IPPAS), PUR-GRAF NCBiR (Leader: Prof. Strankowski, Gdańsk University of Technology); Project Manager of Preludium 17 ST5 panel (IPPAS),
- Operator of numerous spectrometers as part of MSc/Ph.D. work at the Gdańsk University of Technology and IMP PAN (Horiba Yobin Yvon and Renishaw apparatus) & visits at the Innovation Research Center of the State Higher School in Biała Podlaska - Ntegra Spectra C.

♦ Languages:

English – C1;
German – B1;
Swedish – A2

♦ Software skills:

- Microsoft Office, ISIS Draw, AutoCad, Mendeley, Origin, LaTeX, Grapher 9; Nanotechnologia: HyperChem Professional; ToupView. Gamry Framework, ZsimpWin, Labspec; VistaControl, GRAMS, Fityk & Wire.

♦ Additional skills:

- Cat. B driving license (cars)
- First-Aid CPR course (2013 r by PCK)

List of Publications

Before IP PAS PhD:

1. I. Żmuda-Trzebiatowska, M. Rudnicka, E. Miśta, M. Kolbadinejad, A. Lashkari, P. Kalbarczyk, D. Włodarczyk, G. Śliwiński, *Spectroscopic pigment identification in ornamentation tiles (XIII-XV ac) from Aveh, Qom, and Mashhad in Iran*, Photonic Letters of Poland, 06.2016, Vol **8** (2), pp. 57-59, doi: 10.4302/plp.2016.2.10
2. M. Strankowski, D. Wlodarczyk, Ł. Piszczyk, J. Strankowska, *Polyurethane Nanocomposites Containing Reduced Graphene Oxide, FTIR, Raman, and XRD Studies.* International Journal of Polymer Science, 07.2016, Vol. **2016**, Article ID 7520741, http://dx.doi.org/10.1155/2016/7520741
3. D. Wlodarczyk, M. Urban, M. Strankowski, *Chemical modifications of graphene and their influence on properties of polyurethane composites: a review,* Physica Scripta, 09.2016, Vol. **91** (10), Article ID 104003, doi:10.1088/0031-8949/91/10/104003 – Corresponding author
4. M. Strankowski, D. Wlodarczyk, Ł. Piszczyk, J. Strankowska, *Thermal and Mechanical Properties of Microporous Polyurethanes Modified with Reduced Graphene Oxide*, International Journal of Polymer Science, 09.2016, Vol. **2016,** Article ID 8070327, http://dx.doi.org/10.1155/2016/8070327

During IP PAS employment:

5. J. Barzowska, Z. Xia, D. Jankowski, D. Włodarczyk, K. Szczodrowski, Chong-Geng Ma, M. G. Brik, Ya. Zhydachevskii, A. Suchocki, *High-pressure studies of Eu^{2+} and Mn^{2+} doped $NaScSi_2O_6$ clinopyroxenes,* RSC Advances, 01.2017, Vol. **7** (1), pp. 275-284, doi: 10.1039/c6ra24854c
6. J. Kucińska-Lipka, I. Gubanska, O. Korchynskyi, K. Malysheva, M. Kostrzewa, D. Włodarczyk, J. Karczewski, H. Janik, *The influence of Calcium Glycerophosphate (GPCa) modifier on the physicochemical, mechanical and biological performance of polyurethanes applicable as biomaterials for bone tissue scaffold fabrication*, *Polymers,* 08.2017, *Vol.* ***9*** (8), pp. 329-350, doi:10.3390/polym9080329
7. Y. Wang, D. Włodarczyk, Li Li, A. Wittlin, H. Przybylinska, P. Sybilski, Ya Zhydachevskii, Chong-Geng Ma, M.G. Brik, M. Malinowski, Yu Zorenko, V. Gorbenko, A. Suchocki, *Electronic structure of Ce^{3+} in yttrium and lutetium ortho-aluminate crystals and single crystal layers*, Journal of Alloys and Compounds, 11.2017, Vol. **723** (1), pp. 157-163, http://dx.doi.org/10.1016/j.jallcom.2017.06.235
8. J. Urban, M. Baranowski, A. Surrente, D. Wlodarczyk, A. Suchocki, G. Long, Y. Wang, Ł. Kłopotowski, N. Wang, D. Maude, P. Plochocka, *Observation of A_g^1 Raman mode splitting in few layers black phosphorus encapsulated with hexagonal boron nitride,* Nanoscale, 11.2017, Vol. **9** (48), pp. 19298-19303, doi: 10.1039/C7NR05588A
9. D. Sugak, I.I. Syvorotka, U. Yakhnevych, O. Buryy, M. Vakiv, S. Ubizskii, D. Włodarczyk, Ya. Zhydachevskyy, A. Pieniążek, R. Jakiela, A. Suchocki, *Investigation of Co Ions Diffusion in $Gd_3Ga_5O_{12}$ Single Crystals,* Acta Physica Polonica A, 04.2018, Vol. **133** (4), pp. 959-964, doi:10.12693/APhysPolA.133.959
10. J. Urban, M. Baranowski, A. Kuc, Ł. Kłopotowski, A. Surrente, Y. Ma, D. Wlodarczyk, A. Suchocki, D. Ovchinnikov, T. Heine, D. Maude, A. Kis,

P. Plochocka; *Non-equilibrium anisotropic excitons in atomically thin ReS_2*; 2D Materials, 01.2019, Vol. **6** (1), Article ID 015012, doi: 10.1088/2053-1583/aae9b9

11. K. M. Kosyl, W. Paszkowicz, O. Ermakova, D. Wlodarczyk, A. Suchocki, R. Minikayev, J. Z. Domagala, A. N. Shekhovtsov, M. Kosmyna, C. Popescu, F. Fauth; *Equation of state and amorphization of $Ca_9R(VO_4)_7$ (R = La, Nd, Gd): A combined high-pressure X-ray diffraction and Raman spectroscopy study;* Inorganic Chemistry, 10.2018, Vol. **57** (21), pp. 13115-13127, doi: 10.1021/acs.inorgchem.8b01182
12. Y. Wang, R. Hrubiak, S. Turczynski, D. A. Pawlak, M. Malinowski, D. Wlodarczyk, K. M Kosyl, W. Paszkowicz, H. Przybylinska, A. Wittlin, A. Kaminska, Y. Zhydachevskyy, M. G. Brik, Li Li, Chong-Geng Ma, A. Suchocki; *Spectroscopic properties and martensitic phase transition of $Y_4Al_2O_9$:Ce single crystals under high pressure*; Acta Materialia, 02.2019, Vol. **165**. pp. 346-361, https://doi.org/10.1016/j.actamat.2018.11.057
13. M. Amilusik, D. Włodarczyk, A. Suchocki, M. Bockowski, *Micro-Raman studies of strain in bulk GaN crystals grown by hydride vapor phase epitaxy on ammonothermal GaN seeds*, Japanese Journal of Applied Physics, 05.2019, Vol. **58**, Article ID SCCB32 (11 pages), doi: 10.7567/1347-4065/ab1390
14. J. Kaszewski, J. Rosowska, B. S. Witkowski, Ł. Wachnicki, K. Wenelska, E. Mijowska, L-I. Bulyk, D. Włodarczyk, A. Suchocki, B. Kozankiewicz, M. Godlewski, *Shape control over microwave hydrothermally grown Y_2O_3:Eu by europium concentration adjustment*, Journal of Rare Earths, 11.2019, Vol. **37** (11), pp. 1206-1212, doi: 10.1016/j.jre.2019.04.011
15. D. Włodarczyk, L.-I. Bulyk, M. Berkowski, M. Głowacki, K. M. Kosyl, S. M. Kaczmarek, Z. Kowalski, A. Wittlin, H. Przybylińska, Ya. Zhydachevskyy, A. Suchocki, *High pressure low-temperature optical studies of $BaWO_4$:Ce, Na crystals*, Inorganic Chemistry, 04.2019, Vol. **58** (9), pp. 5617-5629, doi: 10.1021/acs.inorgchem.8b03606 – Corresponding author
16. D. Wlodarczyk, I. Zmuda-Trzebiatowska, J. Karczewski, M. Lubinska-Szczygel, M. Urban, A. Marciniak, A. Kaminska, P. Sikorska, M. K. Graczyk, M. Strankowki, *Structural evaluation of percolating, self-healing polyurethane-polycaprolactone blends doped with metallic, ferromagnetic and modified graphene fillers*, Polymers and Polymer Composites, 05.2020, Vol. **29** (5), pp. 541-552, doi:10.1177/0967391120923826 – Corresponding author
17. Y. Wang, D. Wlodarczyk, M. G. Brik, J. Barzowska, A. N. Shekhovtsov, K. N. Belikov, W. Paszkowicz, Li Li, X. Zhou, A. Suchocki, „*Effect of temperature and high-pressure on luminescence properties of Mn^{3+} ions in $Ca_3Ga_2Ge_3O_{12}$ single crystals*", Journal of Physical Chemistry C, 02.2021, Vol. **125** (9), pp. 5146−5157, doi: 10.1021/acs.jpcc.0c09845
18. L. Vasylechko, V. Sydorchuk, A. Lakhnik, Y. Suhak, D. Wlodarczyk, S. Hurskyy, U. Yakhnevych, Y. Zhydachevskyy, D. Sugak, I. I. Syvorotka, I. Solskii, O. Buryy, A. Suchocki, H. Fritze, *„Investigations of LiNb1-xTaxO3 nanopowders obtained with mechanochemical method",* Crystals, 06.2021, Vol. **11** (7), pp. 755-775, doi: 10.3390/cryst11070755
19. O. Buryy, L. Vasylechko, V. Sydorchuk, A. Lakhink, Yu.Suhak, D. Wlodarczyk, S. Hurskyj, U. Yakhnevych, Ya. Zhydachevskyy, D. Sugak, A. Suchocki, H. Fritze, *Crystal structure, Raman spectra and electrical conductivity of $LiNb_{1-x}Ta_xO_3$ nanopowders obtained with high-energy ball milling,* Journal of nano- and electronic physics, 2021, Vol. **13** (2), Article ID 020386cc, doi: 10.21272/jnep.13(2).02038

20. M. Amilusik, M. Zajac, T. Sochacki, B. Lucznik, M. Fijalkowski, M. Iwinska, D. Wlodarczyk, A. K. Somakumar, A. Suchocki, M. Bockowski, *Carbon and manganese in semi-insulating bulk GaN crystals*, Materials, 03.2022, Vol. **15** (7), Article ID 2389, doi: 10.3390/ma15072379
21. I. I. Syvorotka, D. Sugak, U. Yakhnevych, O. Buryy, D. Wlodarczyk, A. Pieniazek, Y. Zhydachevskyy, N. Levinant-Zayonts, H. Savytskyy, O. Bonchyk, S. Ubizskii, A. Suchocki, „*Investigation of the interface of $Y_3Fe_5O_{12}/Gd_3Ga_5O_{12}$ structure obtained by the liquid phase epitaxy*", Crystal Research & Technology, 05.2022, Vol. **57** (5), Article ID 2100180, doi: 10.1002/crat.202100180
22. D. Wlodarczyk, M. Amilusik, K. M. Kosyl, M. Chrunik, K. Lawniczak-Jablonska, M. Strankowski, M. Zajac, V. Tsiumra, A. Grochot, A. Reszka, A. Suchocki, T. Giela, P. Iwanowski, M. Bockowski, H. Przybylinska, *Synthesis attempt and structural studies of novel A_2CeWO_6 double perovskites (A^{2+}= Ba, Ca) in and outside of ambient conditions*, ACS Omega, 04.2022, Vol. **7** (22), pp. 18381-18408, doi: 10.1021/acsomega.2c00669 - Corresponding author.

List of conferences

Oral presentations

International conferences:

1. D. Włodarczyk, K. M. Kosyl, W. Paszkowicz, J. Z. Domagala, O. Ermakova, R. Minikayev, A. Suchocki, A. Shekhovtsov, M. Kosmyna, C. Popescu, F. Fauth – EURODIM 18 – Bydgoszcz, 8-13.07.2018 – *Structural studies focused on $Ca_9R(VO_4)_7$ (R = La, Nd, Gd) whitlockites under elevated pressure;*
2. D. Wlodarczyk, M. Berkowski, M. Głowacki, S. Kaczmarek, Z Kowalski, A. Wittlin,
H Przybylinska, L-I Bulyk, Ya. Zhydachevskii, A. Suchocki – Phosphor Safari & VI IWASOM – Gdansk, 9-14.07.2017 - *Optical studies of $BaWO_4$:Ce,Na;*
3. D. Wlodarczyk, M. Amilusik, M. J. Chrunik, K. M. Kosyl, V. Tsiumra, M . Strankowski, T. Giela, M. Zajac, A. Grochot, A. Reszka, P. Iwanowski, M. Boćkowski, K. Lawniczak-Jablonska, H. Przybylinska, A. Suchocki – LUMDETR XI – Bydgoszcz, 12-17.09.2021 – *Structural and optical studies of novel, cerium-tungstate double perovskites doped with rare-earth ions;*
4. D. Wlodarczyk, M. Amilusik, R. Islam, L-I. Bulyk, V. Tsiumra, M. Zajac, A. Suchocki, M. Bockowski, K. Jablonska, H. Przybylinska - FM&NT NIBS – Ryga, 3-6.07.2022 – *Novel double perovskites and their derivatives hosting rare earth ions – a prelude to charge transfer phenomenon;*
5. D. Wlodarczyk, M. Amilusik, R. Islam, L-I. Bulyk, V. Tsiumra, M. Zajac, A. Suchocki, M. Bockowski, K. Jablonska, H. Przybylinska - VII IWASOM – Gdansk, 1-15.07.2022 – *Spectral and X-ray comparison between novel double perovskites and their derivatives based on tungstates doped with rare earths;*

Polish Conferences:

1. D. Wlodarczyk, A. Feliniak, M. Lubinska, K. Kopczyńska, E. Nalborska, S. Krakowiak – IV Ogólnokrajowa Konferencja Naukowa Młodzi Naukowcy w Polsce, Badania i Rozwój – Gdansk, 27.11 2016 - *Korozja materiałów konstrukcyjnych w zbiornikach browarniczych;*
2. D. Wlodarczyk, E. A. Miśta, I. Żmuda-Trzebiatowska, P. Kalbarczyk, M. Kolbadinejad – IX Międzyuczelnianie Seminarium Kół Naukowych WAT – Warsaw, 19-20.05 2016 – *Analiza chemiczna dekoracyjnych kafelków naściennych z Iranu;*
3. D. Włodarczyk, L-I. Bulyk, M. Głowacki, M. Berkowski, A. Suchocki - IV Interdyscyplinarna Akademicka Konferencja Ochrony Środowiska - Gdansk 5-7.04.2019 - *High-pressure, and low-temperature optical studies of $BaWO_4$:Ce,Na single crystals;*
4. D. Wlodarczyk, M. Tomczyk, D. A. Pawlak, A. Suchocki - XII Międzyuczelniane Seminarium Kół Naukowych WAT - Warsaw, 4-5.06.2019 - *Comparison of optical and structural properties between Ba^{2+} and Zn^{2+} tungstates;*
5. D. Wlodarczyk, M. Amilusik, R. Islam, L-I. Bulyk, V. Tsiumra, M. Zajac, A. Suchocki, M. Bockowski, K. Jablonska, H. Przybylinska – VII Interdyscyplinarna Akademicka Konferencja Ochrony Środowiska – Gdansk, 21-23.09.2022 - *Synthesis and comparison of structural properties between tungstate double perovskites and their derivatives doped with rare earth ions;*

Posters

1. D. Wlodarczyk, K. M. Kosyl, K. Izdebska, W. Paszkowicz, M. Kosmyna, A. Shekhovtsov, A. Suchocki – OMEE 2017 – Lviv, 28.05-2.06 2017 - *High-pressure luminescence and Raman investigation of $Ca_9Nd(VO_4)_7$ whitlockite-like crystals*;
2. D. Wlodarczyk, K. M. Kosyl, V. Tsiumra, M. Amilusik, M. Chrunik, M. Zajac, R. Islam, M. Bockowski, H. Przybylinska, A. Suchocki - VII Interdyscyplinarna Akademicka Konferencja Ochrony Środowiska – Gdansk, 21-23.09.2022 - *Rare earth doped double perovskites & their tungstate derivatives created for UV detection;*
3. D. Wlodarczyk, K. M. Kosyl, M. Strankowski, M. Chrunik, M. Zając, A. Suchocki - XVI Ogólnokrajowa Konferencja Naukowa Młodzi Naukowcy w Polsce - Badania i Rozwój – Online conference, 28.11.2022 - *Polymorphism analysis of novel tungstate double perovskites and their derivatives doped with chosen rare earth ions;*
4. D. Wlodarczyk, M. Amilusik, V. Tsiumra, L-I. Bulyk, R. Islam, A. Suchocki - XVI Ogólnokrajowa Konferencja Naukowa Młodzi Naukowcy w Polsce - Badania i Rozwój – Online conference, 28.11.2022 - *Anomalous luminescent behavior of novel double perovskites and their rare-earth doped tungstate derivatives.*

Seminars and Workshops

1. ON4 seminar – IP PAS - 14.06.2016 - *Od pomysłu do przemysłu, czyli zastosowanie spoktroskopii ramanowskiej w praktyce;*

2. ON 4 seminar - IP PAS – 17.10.2017 - *Optical studies of $BaWO_4$:Ce, Na;*

3. ON 4 seminar - IP PAS – 13.11.2018 - *Structural studies focused on $Ca_9R(VO_4)_7$ (R = La, Nd, Gd) whitlockites under elevated pressure;*

5. X Symposium of PhD Students PAS - Bialobrzegi, 04.06.2018 – *"Optical studies of BaWO4:Ce,Na;*

6. XI Symposium of Ph.D. Students PAS – Serock, 28-30.05.2019 - *Phase-transition and energy-transfer phenomena in modeled double perovskites doped with rare-earth ions;*

7. ON4 Seminar - IP PAS - 13.10.2020 – *Structural and optical studies of novel, doped A_2CeWO_6 double perovskites (A=Ca, Sr or Ba^{2+}).*

Projects

Leader

1. 36-month project Preludium 17, NCN nr 2019/33/N/ST5/02317 (internal no. P-506/P) pt.: *Structural and optical studies of novel, doped A_2CeWO_6 double perovskites.*

Stipendist/Subcontractor

1. 31-month stipendist in project NCN OPUS-9, nr UMO-2015/17/B/ST5/01658 (internal no. P-441/0) pt.: *„Modification of solar energy through down-conversion on the basis of oxide materials doped with Ytterbium for photovoltaic applications"* under supervision of Prof. Andrzeja Suchocki.

2. Baltic TRAM; Project no. #R002; Financed by Interreg Baltic Sea Region Programme (85%) & IP PAS (15%); Supervisor – Prof. Krystyna Jabłońska; Partially employed as a subcontractor in between 04-10-2017 & 04-11-2018 regarding shungite research;

3. Subcontractor of PUR-GRAF NCBR project no. GRAF-TECH/NCBR/11/08/2013 regarding *Production of polyurethane nanocomposites doped with thermally reduced graphene oxide used towards shoe industry*; Project leader – Ph.D. hab. eng. Michał Strankowski; Time of employment 04.2015 to 04.2016;